

**AN EXPERIMENTAL AND THEORETICAL  
STUDY OF THE DARK CURRENT AND  
X-RAY SENSITIVITY OF AMORPHOUS  
SELENIUM X-RAY PHOTOCONDUCTORS**

A Thesis Submitted to the College of

Graduate Studies and Research

In Partial Fulfillment of the Requirements

For the Degree of Doctor of Philosophy

In the Department of Electrical and Computer Engineering

University of Saskatchewan

Saskatoon, SK, Canada

by

**JOEL BRANDON FREY**

Saskatoon, Saskatchewan, Canada

Copyright © December, 2011: J.B. Frey, All rights reserved.

# COPYRIGHT

The author has agreed that the library, University of Saskatchewan, may make this thesis freely available for inspection. Moreover, the author has agreed that permission for extensive copying of this thesis for scholarly purposes may be granted by the professor who supervised the thesis work recorded herein, or in his absence, by the Head of the Department or the Dean of the College in which this thesis work was done. It is understood that due recognition will be given to the author of this thesis and to the University of Saskatchewan in any use of the material in this thesis. Copying or publication or any other use of this thesis for financial gain without approval by the University of Saskatchewan and the author's written permission is prohibited.

Request for permission to copy or make any other use of the material in this thesis in whole or in part should be addressed to:

Head of the Department of Electrical and Computer Engineering

Engineering Building, 57 Campus Dr

University of Saskatchewan

Saskatoon, SK, S7N 5A9

Canada

# ABSTRACT

Recently, the world of diagnostic radiography has seen the integration of digital flat panel x-ray image detectors into x-ray imaging systems, replacing analog film screens. These flat panel x-ray imagers (FPXIs) have been shown to produce high quality x-ray images and provide many advantages that are inherent to a fully digital technology. Direct conversion FPXIs based on a photoconductive layer of stabilized amorphous selenium (a-Se) have been commercialized and have proven particularly effective in the field of mammography. In the operation of these detectors, incident x-ray photons are converted directly to charge carriers in the a-Se layer and drifted to electrodes on either side of the layer by a large applied field (10 V/ $\mu\text{m}$ ). The applied field causes a dark current to flow which is not due to the incident radiation and this becomes a source of noise which can reduce the dynamic range of the detector. The level of dark current in commercialized detectors has been reduced by the deposition of thin *n*- and *p*- type blocking layers between the electrodes and the bulk of the a-Se. Despite recent research into the dark current in metal/a-Se/metal sandwich structures, much is still unknown about the true cause and nature of this phenomenon. The work in this Ph.D. thesis describes an experimental and theoretical study of the dark current in these structures. Experiments have been performed on five separate sets of a-Se samples which approximate the photoconductive layer in an FPXI. The dark current has been measured as a function of time, sample structure, applied field, sample thickness and contact metal used. This work has conclusively shown that the dark current is almost entirely due to the injection of charge carriers from the contacts and the contribution of Poole-Frenkel enhanced bulk thermal generation is negligible. There is also evidence that while the dark current is initially controlled by the injection of holes from the positive contact, several minutes after the application of the bias, the dark current due to hole injection may decay to the point where the electron current becomes significant and even dominant. These conclusions are supported by numerical calculations of the dark current transients which have been calibrated to match experimental results.

Work detailed in this Ph.D. thesis also focuses on Monte Carlo modeling of the x-ray sensitivity of a-Se FPXIs. The higher the x-ray sensitivity of a detector, the lower the radiation dose required to acquire an acceptable image. FPXIs can experience a decrease in the x-ray sensitivity of the photoconductive layer with accumulating exposure, leading to a phenomenon known as “ghosting”. Modeling this decrease in sensitivity can uncover the reasons behind it. The Monte Carlo model described in this thesis is a continuation of a previous model which now considers the effects of the *n*- and *p*-like blocking layers and the flow of dark current between x-ray exposures. The simulation results explain how deep trapping of photogenerated charge carriers, and the resulting effect on the electric field distribution, contribute to sensitivity loss. The model has shown excellent agreement with experimental data and has accurately predicted a sensitivity recovery once exposure has ceased which is due to primarily to the relaxation of metastable x-ray-induced carrier trap states.

# ACKNOWLEDGEMENTS

I would like to humbly thank all those who made the completion of this work a reality, for without them, this simply would not have been possible. First, I would like to thank my ever-generous parents, Ron and Patti Frey, whose emotional and financial support has been essential (and seemingly endless) in my life. I would also like to thank my Grandpa, Henry Hryciw, for always inspiring me to pursue my academic dreams. I am greatly indebted to my Supervisor of the last seven years, Dr. Safa Kasap, whose wisdom and understanding have guided me academically, professionally and personally. Many thanks are due to Dr. George Belev, whose tireless efforts and insightful advice have been instrumental in shaping and carrying out this work. I also thank Dr. Habib Mani and Dr. Olivier Tousignant of ANRAD Corporation, Quebec, Canada, for help in facilitating much of the experimental work done and for many fruitful discussions. I thank the members of my advisory committee and many of the ECE faculty members and students for their guidance and friendship. I am grateful for the financial support provided by my supervisor, Dr. Safa Kasap, the Natural Science and Engineering Research Council of Canada, ANRAD Corporation, The Department of Electrical and Computer Engineering, The College of Engineering and The University of Saskatchewan. Last, but certainly not least, I want to thank my wife, Izabela, for her love, patience and support while I completed this journey and for giving me new reasons to reach for my goals.

# TABLE OF CONTENTS

COPYRIGHT.....	i
ABSTRACT.....	ii
ACKNOWLEDGEMENTS.....	iv
TABLE OF CONTENTS.....	v
LIST OF FIGURES.....	ix
LIST OF TABLES.....	xxvii
LIST OF ABBREVIATIONS.....	xxix
<b>1. INTRODUCTION.....</b>	<b>1</b>
1.1 PROJECTION RADIOGRAPHY.....	1
1.2 X-RAY IMAGE DETECTORS.....	3
1.2.1 X-ray Film.....	3
1.2.2 Flat Panel X-ray Image Detectors.....	4
1.2.3 General Requirements of X-ray Imaging Systems.....	9
1.2.4 The Future of a-Se FPXIs.....	10
1.3 RESEARCH OBJECTIVES.....	12
1.3.1 Dark Current.....	13
1.3.2 X-ray Sensitivity.....	14
1.4 SCOPE OF THESIS.....	15
<b>2. METRICS OF X-RAY IMAGE DETECTOR PERFORMANCE.....</b>	<b>17</b>
2.1 X-RAY SENSITIVITY.....	17
2.1.1 X-ray Interactions in the Photoconductive Layer.....	18
2.1.1.1 Rayleigh Scattering.....	21
2.1.1.2 Compton Scattering.....	21
2.1.1.3 Photoelectric Absorption.....	22
2.1.2 Photogeneration of Charge Carriers.....	23
2.1.3 Collection of Photogenerated Charge Carriers.....	25
2.1.4 X-ray Sensitivity Revisited.....	27
2.1.5 Ghosting.....	29
2.1.6 Modeling of X-ray Sensitivity in Amorphous Selenium.....	31
2.2 IMAGE RESOLUTION.....	33
2.3 NOISE POWER SPECTRUM.....	37
2.4 DETECTIVE QUANTUM EFFICIENCY.....	37
2.5 DYNAMIC RANGE.....	40
2.6 DARK CURRENT.....	41
2.6.1 Potential Sources of Dark Current.....	41
2.6.1.1 Carrier Injection.....	41

2.6.1.2	Carrier Diffusion.....	45
2.6.1.3	Bulk Thermal Generation .....	46
2.6.2	Acceptable Levels of Dark Current in Direct Conversion FPXIs .....	50
2.6.3	The Study of Dark Current in Amorphous Selenium Films.....	54
2.7	CONCLUSION.....	57
<b>3.</b>	<b>X-RAY PHOTOCONDUCTORS.....</b>	<b>59</b>
3.1	AN IDEAL X-RAY PHOTOCONDUCTOR .....	59
3.2	TYPES OF PHOTOCONDUCTORS .....	60
3.3	SELENIUM .....	62
3.3.1	Crystalline Selenium .....	62
3.3.2	Amorphous Selenium.....	65
3.3.2.1	Structure of Amorphous Selenium .....	65
3.3.2.2	Electronic Density of States of Amorphous Selenium.....	67
3.3.2.3	Structural Defects in Amorphous Selenium .....	75
3.3.2.4	Amorphous Selenium as an X-ray Photoconductor.....	79
3.3.2.4.1	Effects of Alloying with As.....	80
3.3.2.4.2	Effects of Doping with Cl .....	81
3.3.2.4.3	Effects of Doping with O .....	82
3.4	POLYCRYSTALLINE PHOTOCONDUCTOR CANDIDATES .....	84
3.4.1	Polycrystalline Mercuric Iodide (Poly-HgI <sub>2</sub> ) .....	85
3.4.2	Polycrystalline Lead Iodide (Poly – PbI <sub>2</sub> ).....	86
3.4.3	Polycrystalline Cadmium Zinc Telluride (Poly – Cd <sub>0.95</sub> Zn <sub>0.05</sub> Te).....	87
3.4.4	Polycrystalline Cadmium Telluride (Poly-CdTe) .....	88
3.4.5	Polycrystalline Lead Oxide (Poly – PbO).....	89
3.4.6	Polycrystalline Thallium Bromide (Poly-TlBr) .....	90
3.4.7	Polycrystalline Bismuth Tri-Iodide (Poly-BiI <sub>3</sub> ) .....	91
3.4.8	Polycrystalline Lead Bromide (Poly-PbBr <sub>2</sub> ) and Mercuric Bromide (Poly-HgBr <sub>2</sub> ).....	91
3.5	CONCLUSION.....	92
<b>4.</b>	<b>EXPERIMENTAL STUDY OF DARK CURRENT IN AMORPHOUS SELENIUM FILMS.....</b>	<b>93</b>
4.1	INTRODUCTION .....	93
4.2	EXPERIMENTAL TECHNIQUES.....	93
4.2.1	Sample Sets .....	93
4.2.1.1	Sample Preparation .....	94
4.2.1.2	Sample Set A .....	95
4.2.1.3	Sample Set B.....	96
4.2.1.4	Sample Set C.....	98
4.2.1.5	Sample Set D .....	98
4.2.1.6	Sample Set E.....	100
4.2.2	Dark Current Measurement Apparatus .....	101
4.3	RESULTS .....	103
4.3.1	Dark Current as a Function of Time.....	103
4.3.2	Dark Rest Tests .....	106
4.3.3	Contact Formation Process .....	107
4.3.4	Dark Current as a Function of Sample Structure .....	108
4.3.5	Dark Current as a Function of Applied Field.....	112
4.3.6	Space Charge Measurements .....	118

4.3.6.1	Control Experiment .....	119
4.3.6.2	Voltage Step Measurements .....	121
4.3.6.3	Discharge Measurements .....	124
4.3.7	Long Term Reproducibility .....	135
4.3.8	Dark Current as a Function of <i>i</i> -layer Thickness .....	135
4.3.8.1	Results From Sample Set B .....	136
4.3.8.2	Results From Sample Sets C and D .....	147
4.3.9	Dark Current as a Function of Contact Metal .....	151
4.3.10	Dark Current Measurements on Sample Set E .....	156
4.4	CONCLUSION .....	159

## **5. MODELING OF DARK CURRENT TRANSIENTS IN AMORPHOUS SELENIUM FILMS.....161**

5.1	MONTE CARLO SIMULATIONS .....	161
5.2	MODIFIED MONTE CARLO SIMULATIONS .....	162
5.2.1	Dimensional Slices .....	163
5.2.2	Time Steps .....	164
5.2.3	Charge Carrier Injection .....	164
5.2.4	Carrier Trapping .....	165
5.2.5	Carrier Recombination .....	166
5.2.6	Carrier Release .....	167
5.2.7	Electric Field Distribution .....	169
5.2.8	Random Number Generation .....	170
5.2.9	Results .....	170
5.3	NUMERICAL CALCULATIONS .....	175
5.3.1	Matching Similar Published Work .....	175
5.3.2	Removing Simplifying Assumptions of Published Work .....	177
5.3.3	Matching Experimental Results with the Published Model .....	179
5.4	CONCLUSION .....	186

## **6. MODELING OF X-RAY SENSITIVITY IN AMORPHOUS SELENIUM FILMS.....188**

6.1	PREVIOUS MODEL .....	188
6.2	PRESENT MODEL .....	192
6.3	SIMULATION RESULTS .....	198
6.3.1	Results for Single Layer Structures .....	198
6.3.2	Results for <i>n-i</i> and <i>n-i-p</i> Structures .....	201
6.3.2.1	<i>n-i</i> Structure .....	202
6.3.2.2	<i>n-i-p</i> Structure .....	204
6.3.2.2.1	Effect of <i>p</i> -layer Thickness .....	204
6.3.2.2.2	Effect of <i>n</i> -layer Thickness .....	205
6.3.2.2.3	Effect of Hole Lifetime in the <i>n</i> -layer .....	206
6.3.2.2.4	Effect of Electron Lifetime in the <i>n</i> -layer .....	208
6.3.3	Results for Negatively Biased Structures .....	210
6.3.3.1	Results for <i>i</i> -layer Structures .....	211
6.3.3.2	Results for <i>p-i-n</i> Structures .....	214
6.3.4	Effects of Dark Current .....	215
6.3.4.1	Effects of a Non-uniform Initial Electric Field Distribution .....	215
6.3.4.2	Effects of Dark Current Flowing Between X-ray Exposures .....	218

6.4	MATCHING EXPERIMENTAL RESULTS .....	221
6.4.1	Experimental Procedure .....	222
6.4.2	Simulation Parameters .....	224
6.4.3	Results.....	225
6.5	CONCLUSION .....	232
<b>7.</b>	<b>SUMMARY, CONCLUSIONS AND RECOMMENDATIONS .....</b>	<b>233</b>
7.1	INTRODUCTION .....	233
7.2	DARK CURRENT.....	233
7.2.1	Experimental Work .....	234
7.2.1.1	Dark Current as a Function of Time .....	234
7.2.1.2	Dark Current as a Function of Sample Structure .....	235
7.2.1.3	Dark Current as a Function of Applied Field .....	236
7.2.1.4	Dark Current as a Function of i-layer Thickness .....	236
7.2.1.5	Dark Current as a Function of Contact Metal.....	237
7.2.2	Modeling of Dark Current Transients .....	237
7.2.3	Conclusions on Dark Current.....	238
7.3	X-RAY SENSITIVITY.....	238
7.3.1	Effect of Blocking Layers on X-ray Sensitivity.....	239
7.3.2	Effect of Dark Current on X-ray Sensitivity .....	239
7.3.3	Matching X-ray Sensitivity Experiments.....	240
7.3.4	Conclusions on X-ray Sensitivity .....	240
7.4	RECOMMENDATIONS FOR FUTURE WORK.....	240
	<b>APPENDIX: Simplified Field Formula Derivation .....</b>	<b>243</b>
	<b>REFERENCES .....</b>	<b>247</b>

# LIST OF FIGURES

**Figure 1.1** Basic radiographic imaging technique; after [2]. An x-ray beam from a source is passed through the object of interest onto an image detector.....1

**Figure 1.2** A uniform distribution of x-rays passes through an object containing regions of varying density. As some regions attenuate x-rays more efficiently, the x-ray beam emerging from the object will have a modulated intensity distribution, which contains the information of interest; after [2]. .....2

**Figure 1.3** A digital radiography system; after [2]. When compared to an analog radiography system, the screen film detector has been replaced with a digital one which can immediately display the resultant image on a computer screen. ....5

**Figure 1.4** Schematic diagram of a few pixels of a self-scanning, thin-film transistor, active-matrix array. Each row of pixels is addressed sequentially while each pixel in the addressed row is read out simultaneously. The charge stored on each pixel capacitor is read out in parallel and amplified before being multiplexed into serial data and sent to the display device. The entire array is coated with a photoconductive layer of a-Se and a top metal electrode.. ....7

**Figure 1.5** A highly simplified cross-section of a single direct-conversion pixel. The charges generated by the absorption of x-rays drift towards their respective electrodes. The capacitor  $C_I$  integrates the induced current due to the drift of the carriers which results in a stored charge,  $Q_I$ , on  $C_I$ .  $n$ - and  $p$ -type blocking layers are deposited between the intrinsic layer of a-Se and the contacts to reduce dark current levels. Drawing is not to scale.....8

**Figure 1.6** a-Se based direct conversion x-ray image detectors without their protective, light proof cases.....9

**Figure 1.7** X-ray images taken of a phantom of a human skull: a-Se based direct conversion flat panel detector (left), conventional film technology (right); after [39].....10

**Figure 2.1** Mass attenuation and absorption coefficients for photons with energies from 10 keV to 100 MeV in air. The total absorption curve is the sum of Compton absorption, photoelectric absorption and pair production; after [1]. .....20

**Figure 2.2** Plot of the total attenuation, energy absorption, Rayleigh scattering, Compton scattering and photoelectric absorption coefficients for a-Se for photon energies of 10 – 200 keV; after [63,66]... .....20

**Figure 2.3** Schematic illustration of (a) Rayleigh scattering and (b) Compton scattering. In Rayleigh scattering, the trajectory of the photon is altered but the atom does not change. In Compton scattering, the trajectory of the photon is altered and its

energy is reduced from $E$ to $E'$ as an outer shell electron is ejected with kinetic energy $E''$ ; after [63,67].	21
<b>Figure 2.4</b> A schematic illustration of photoelectric absorption. The incident x-ray imparts all of its energy to an inner shell electron, ejecting it. An outer shell electron transitions down to fill the created vacancy, releasing a fluorescent x-ray photon; after [63].	22
<b>Figure 2.5</b> The charted dependence of $W_{\pm}$ in a-Se on the applied electric field and mean x-ray photon energy, $\varepsilon$ ; after [78]. The data was gathered through pulse height spectroscopy and the constant field lines were drawn with a quadratic interpolation.	25
<b>Figure 2.6</b> The effects of charge trapping on the x-ray sensitivity and resolution depends on the type of carriers that have been trapped; whether carriers were drifting to the top or bottom electrode. $C$ is the central (reference) pixel and $L$ and $R$ are the neighbouring left and right pixels. The transient currents flowing into the pixels are integrated and eventually yield the collected charges at the pixels. In the case of this positively biased detector, trapped holes have a greater effect on x-ray sensitivity than trapped electrons and tend to decrease resolution while trapped electrons actually improve resolution.	26
<b>Figure 2.7</b> Explanation of image lag. Charge generated during the initial x-ray exposure is trapped in the photoconductive layer, inducing charges on the pixels underneath that area, even after exposure. This is called a dark image; after [63].	27
<b>Figure 2.8</b> Appearance of a “ghost” image in a subsequent exposure as the area of the previous exposure has reduced sensitivity, $S'$ ; after [2].	30
<b>Figure 2.9</b> The initial image (a) is of a lead “X” shaped object. Images (b) and (c) are taken 1 and 2 minutes after image (a) respectively. The “ghost” of image (a) is clearly visible in images (b) and (c); after [87].	31
<b>Figure 2.10</b> Monte Carlo and numerical simulation and experimental results for relative sensitivity vs. cumulative x-ray exposure at applied fields of 6 and 10 V/ $\mu\text{m}$ . Experimental data is shown as circles, Monte Carlo simulation results as triangles and numerical calculations as the solid lines; after [62].	32
<b>Figure 2.11</b> Normalized x-ray sensitivity vs. cumulative exposure for both a single layer a-Se sample and an $n-i-p$ multilayer sample. The model shows that multilayer samples have a lower overall sensitivity but experience a very similar decrease in sensitivity with cumulative exposure; after [59].	32
<b>Figure 2.12</b> The x-ray incidence is a narrow line (a delta function in the $y$ direction). The resultant charge signal is spread out in the $y$ direction, representing the LSF; redrawn from [63].	33

<b>Figure 2.13</b> The MTF of this example detector is 100% at A, slightly lower at B and 0% at C. This detector can resolve images at 1 lp/mm, but not at 4 lp/mm. The inset at the lower right shows the MTF plotted as a function of spatial frequency, $f$ ; after [89].....	34
<b>Figure 2.14</b> (a) definition of pixel aperture width, $d$ , and pixel pitch, $a$ . (b) plot of $MTF_a(f)$ vs. spatial frequency, $f$ , where the first zero occurs at $1/d$ ; redrawn from [63].....	35
<b>Figure 2.15</b> The MTF of two detectors manufactured by Anrad: a mammographic detector with 85 $\mu\text{m}$ pixels and a fluoroscopic detector with 150 $\mu\text{m}$ pixels. The measured MTF of each detector is very close to the $MTF_a$ for the respective pixel size; after [90]. .....	36
<b>Figure 2.16</b> $DQE(f)$ vs. spatial frequency for a mammographic a-Se FPXI manufactured by Anrad operating in tomosynthesis mode for several exposures ranging from 0.19 mR to 0.8 mR. A good DQE value is maintained even at very low doses; after [90].....	38
<b>Figure 2.17</b> X-ray images of a breast from a mammographic a-Se x-ray detector operating in tomosynthesis mode; after [90]. These images are only 2 of 49 acquired for the complete scan. ....	38
<b>Figure 2.18</b> A block diagram showing a cascaded linear-system model of $DQE(0)$ for an a-Se FPXI; after [96].....	40
<b>Figure 2.19</b> Plot of $DQE(0)$ vs. exposure for a general radiographic a-Se detector. The circles represent experimental data for a 70 kVp x-ray spectrum with 23.5 mm Al filtration while the line gives the theoretical fit given by the model shown in Fig. 2.18; after [96]. ....	40
<b>Figure 2.20</b> Energy level diagram for a hole blocking contact between a metal and an intrinsic semiconductor; redrawn from [102]. $E_{Fm}$ and $\phi_m$ are the Fermi level and work function of the metal while $E_F$ , $E_v$ , $E_c$ , $E_g$ , $\phi$ , and $\chi$ are the Fermi level, valence band edge, conduction band edge, bandgap, work function and electron affinity of the semiconductor, respectively.....	42
<b>Figure 2.21</b> Energy band diagram incorporating the Schottky effect for an electron blocking contact on a semiconductor; combined from [103]. $\phi_e$ is the original barrier to electron injection from the metal into the semiconductor, while $\phi_B$ is the barrier lowered by the Schottky effect.....	44
<b>Figure 2.22</b> Depiction of the process of bulk thermal generation from states within the bandgap of a semiconductor (a) at mid-gap, (b) above mid-gap, (c) below mid-gap.....	47

<b>Figure 2.23</b> Schein's plot of the natural log of the dark current in an a-Se sample without a top contact on the square root of the electric field at three times after the application of the field. At all times, the relationship is linear with a slope characteristic of Poole-Frenkel enhanced bulk thermal generation; after [110].....	49
<b>Figure 2.24</b> Various voltages across $C_{px}$ as a function of dark current density; after [15]. Mammographic exposures used to calculate voltages corresponding to max. likely exposure, mean exposure, min. likely exposure and radiation noise signals are 240 mR, 12 mR, 0.6 mR and 60 $\mu$ R, respectively. ....	52
<b>Figure 2.25</b> Example of a <i>p-i-n</i> multilayer structure. As injected electrons become trapped in the <i>p</i> -layer and holes in the <i>n</i> -layer, the electric field distribution changes to be non-uniform, reducing the field at both contacts. ....	56
<b>Figure 2.26</b> The best reported values to date of dark current density for a-Se and polycrystalline photoconductive layers. Note that most of these are measured at relatively low applied electric fields where it is questionable that the charge collection efficiency is adequate. It is not possible to scale these to the same field as the field dependence of the dark current is rarely linear and in general is unknown. All polycrystalline layers are labeled as deposited by physical vapour deposition (PVD), screen printing (SP) or close space sublimation (CSS). Solid colors represent values obtained from films that have not yet been used to obtain x-ray images; hashed bars represent values from demonstrated x-ray imagers. The grey hashed area represents the acceptable range for dark current in an FPXI. Data have been taken from various sources, including the following: a-Se ( <i>i</i> -layer and <i>n-i-p</i> ) from [13], a-Se ( <i>i-n</i> ) from [119], HgI <sub>2</sub> (PVD at 0.25 V/ $\mu$ m and SP) from [120], HgI <sub>2</sub> (PVD at 0.4 V/ $\mu$ m) from [121], PbI <sub>2</sub> (PVD) from [122], PbI <sub>2</sub> (SP) from [123], Cd <sub>0.95</sub> Zn <sub>0.05</sub> Te from [124][125], PbO (PVD) from [125], PbO (SP) from [126], PbBr <sub>2</sub> and HgBr <sub>2</sub> from [127] and BiI <sub>3</sub> from [128]. ....	57
<b>Figure 3.1</b> The bonding configuration of selenium atoms; after [63].....	63
<b>Figure 3.2</b> Molecular structure of the main allotropes of crystalline Se; after [7]. ....	64
<b>Figure 3.3</b> Definition of important bonding parameters in a-Se. The dihedral angle, $\phi$ , is the angle between the bonding planes of atoms 1, 2, 3 and 2, 3, 4, while $\theta$ is the angle between the bonds formed by a given atom; after [118].....	65
<b>Figure 3.4</b> Proposed structure of a-Se, consisting of chain and ring segments defined by repetition of the same dihedral angle sign or alternating dihedral angle sign, respectively; after [118]. ....	67
<b>Figure 3.5</b> The density of electronic states in a-Se as proposed by Abkowitz [7,140]; after [7]. Peaks in concentration of shallow states exist at 0.25 eV above $E_v$ and	

0.35 eV below $E_c$ while peaks in deep states are located at 0.87 eV above $E_v$ and 1.22 eV below $E_c$ .	69
<b>Figure 3.6</b> Diagrammatic representation of electron and hole drift, with the microscopic mobilities in the transport bands reduced by short lived trapping and release events involving shallow traps. Carriers trapped by deep traps are essentially lost during the time scale of interest. The application of the electric field tilts the bands to demonstrate increased potential energy for electrons at the negative terminal of the source; after [63].	71
<b>Figure 3.7</b> The density of electronic states in a-Se as proposed by Adriaenssens [7,156,157]; after [7]. The solid lines represent data from the energy range that is accessible by the post transit time-of-flight experiments used. There are single peaks at 0.4 eV above $E_v$ and 0.52 eV below $E_c$ .	72
<b>Figure 3.8</b> The density of electronic states in a-Se as proposed by Koughia <i>et al.</i> [7,160-162]; after [7]. There are two peaks of shallow states at 0.3 eV and 0.5 eV below $E_c$ while there is a featureless decay in state concentration near $E_v$ . The exact location of deep states could not be resolved with the method used.	74
<b>Figure 3.9</b> Structure and energy of simple bonding configurations for selenium atoms. Straight lines represent bonding (B) orbitals, lobes represent lone-pair (NB) orbitals, and circles represent anti-bonding (AB) orbitals. The energy of a lone-pair is taken as zero; after [63]. (a) A normally bonded a-Se atom, $Se_2^0$ , (b) A neutral under-coordinated Se atom, $Se_1^0$ , (c) A negatively charged under-coordinated Se atom, $Se_1^-$ , (d) The lowest energy neutral defect in a-Se, an $Se_3^0$ atom, (e) A positively charged over-coordinated Se atom, $Se_3^+$ .	77
<b>Figure 3.10</b> Schematic representation of a possible atomic structure of a-Se, showing over- and under-coordinated defects; after [118].	78
<b>Figure 3.11</b> Comparison of x-ray images obtained with direct conversion detectors utilizing different photoconductive layers: (a) Hand phantom with a-Se, after [231], (b) Alarm clock with $HgI_2$ , after [211], (c) Foot phantom with $PbI_2$ , after [211], (d) Gastrointestinal phantom with CZT, after [124], (e) Chicken bone with CdTe, after [215], (f) Hand phantom and Huettner phantom with PbO, after [125].	92
<b>Figure 4.1</b> Schematic of the vacuum deposition system used to create sample sets B and D.	95
<b>Figure 4.2</b> A Photo of a sample from sample set A. The entire top surface of the sample is covered by a Cr contact.	96
<b>Figure 4.3</b> A photo of a sample from set B after two of the top contacts were deposited. From left to right the contacts are Cr, Al, and Au and Pt would be deposited in a similar fashion. The exposed area outside the contacts is the $n$ -layer of a-Se.	98

<b>Figure 4.4</b> Schematic representation of a sample from set D. The <i>i</i> -layer has two distinct regions of thickness while the <i>n</i> -layer thickness is as uniform as possible across the entire sample. Each thickness region has two top contacts allowing for two different metals in each region. Not to scale. ....	99
<b>Figure 4.5</b> A photo of a sample from sample set D with round Al (light) and Pt (dark) contacts on each side. The reflection of light from the ridge dividing the thick and thin sides can be seen. ....	100
<b>Figure 4.6</b> Schematic diagram of the dark current transient acquisition system. ....	102
<b>Figure 4.7</b> Schematic representation of a <i>p-i-n</i> sample reverse (negatively) biased. Regardless of bias, positive current direction is defined as flowing into the top contact from the power supply. ....	103
<b>Figure 4.8</b> Magnitude of typical dark current transients produced by a negatively biased <i>i</i> -layer sample at different fields. The dark current decays with time following the application of the bias in a non-exponential manner. ....	104
<b>Figure 4.9</b> Dark current density vs. time. (a) <i>n-i-p</i> sample from set D with an Al contact biased at 10 V/ $\mu$ m. The transient reaches a steady-state after $\sim$ 1000 s. (b) <i>n-i-p</i> sample from set A with a Cr contact biased at 10 V/ $\mu$ m. The transient seems to decay indefinitely. (c) <i>n-i-p</i> sample from set C with an Al contact biased at both 10 and 5 V/ $\mu$ m. At higher fields, most of the samples of set C display a temporary plateau before continuing to decay. (d) <i>n-i-p</i> sample from set B biased at 10 V/ $\mu$ m. Three different contacts of Cr, Al and Pt give quite differently shaped transients. ....	105
<b>Figure 4.10</b> Dark current transients produced by an <i>i</i> -layer sample of set A biased at 3 V/ $\mu$ m, after different rest periods, illustrating the need for adequate dark rest between measurements. A rest period of 12 hours produces transients which differ by at most 10% from very well rested samples. ....	106
<b>Figure 4.11</b> Typical evidence of a contact formation process during the first application of a high voltage bias to the Al contact of a sample from set B. For all samples, the second transient in the test was lower than the first with subsequent transients being similar to the second. All transients represent data from a sample which was rested for 12 hours before the voltage was applied. ....	108
<b>Figure 4.12</b> Typical dark current transients (magnitude shown) for all seven sample structures in set A. The <i>n-i-p</i> family of samples in (a) are all positively biased at 10 V/ $\mu$ m, while the <i>p-i-n</i> family of samples in (b) are all negatively biased at -10 V/ $\mu$ m. ....	109
<b>Figure 4.13</b> Comparison of the magnitude of the dark current level 300 s after the application of the 10 V/ $\mu$ m reverse bias for all seven sample structures of set A. The level of dark current deemed acceptable for detector operation [15] is given	

by the hashed area. Only samples which contain an $n$ -layer produce a dark current level below the acceptable range.....	110
<b>Figure 4.14</b> Magnitude of dark current density for a $p$ - $i$ - $n$ sample of set A forward biased at 3 different fields and negatively biased at $-10$ V/ $\mu\text{m}$ . Forward biasing a multilayer sample results in much higher dark current and the appearance of a characteristic “hump” which appears at earlier times at higher forward fields.....	112
<b>Figure 4.15</b> $J$ - $F$ characteristics for the positively biased $n$ - $i$ - $p$ family of sample set A, 1000 s after the application of the bias. A good fit is given for each sample by a power law expression, $J(F) \propto F^n$ , in which the value of $n$ varies between samples and is tabulated in Table 4.2.....	113
<b>Figure 4.16</b> $J$ - $F$ characteristics at 10, 100 and 1000 s after the application of the field for (a) an $n$ - $i$ - $p$ sample from set A and (b) an $i$ -layer sample from set A. The field dependence of the dark current in the $n$ - $i$ - $p$ sample decreases substantially with time following the application of the bias. This decrease is not nearly as substantial in the $i$ -layer sample. The point connecting lines are only a guide for the eye.....	114
<b>Figure 4.17</b> Dark current density as a function of applied field for (a) the Pt contact and (b) the Al contact on an $n$ - $i$ - $p$ sample from set C with a $74 \mu\text{m}$ $i$ -layer, 2 s after the application of the field. Also shown in each plot is a fit for injection of carriers over a Schottky barrier. An electron barrier of 0.85 eV is assumed in both cases, while a hole barrier of 0.83 eV is assumed for the Pt contact and 0.84 eV is assumed for the Al contact. The Schottky injection model gives a reasonable fit, more so for the Pt contact.....	115
<b>Figure 4.18</b> Dark current density as a function of applied field for (a) the Pt contact and (b) the Al contact on an $n$ - $i$ - $p$ sample from set C with a $74 \mu\text{m}$ $i$ -layer, 100 s after the application of the field. Also shown in each plot is a fit for injection of carriers over a Schottky barrier with the field reduced to 18% for the Pt contact and 15% for the Al contact due to trapping of charge carriers in the blocking layers. An electron barrier of 0.85 eV is assumed in both cases, while a hole barrier of 0.83 eV is assumed for the Pt contact and 0.84 eV is assumed for the Al contact. Best fit power law plots are shown for both the high and low field regions for each contact.....	116
<b>Figure 4.19</b> Plot of the natural log of the magnitude of the dark current vs. the square root of the magnitude of the applied field for an $n$ - $i$ - $p$ and $p$ - $i$ - $n$ sample from set A. The plots give slopes very similar to that expected for Schottky injection. Both one and three dimensional Poole-Frenkel treatments give slopes much higher than the data.....	118
<b>Figure 4.20</b> Expected $I$ - $t$ characteristics for samples in set A if large quantities of space charge due to trapped injected carriers control the dark current transients; redrawn	

from [240]. (a) gives the expected behaviour for a step up in voltage and (b) for a step down. ....	119
<b>Figure 4.21</b> (a) Schematic representation of a current reversal control experiment. At $t_1$ the applied voltage is switched from $V_A$ to the lower voltage, $V_B$ . (b) Expected transients for the voltage across the capacitor, $V(t)$ , and current through the RC circuit, $i(t)$ . ....	120
<b>Figure 4.22</b> Dark current density transients through a $p-i-n$ sample from sample set A in response to step-wise changes in the applied field. The transient at $t = 1000$ s has a peak value equal to the transient before it where the applied field was two times less. Steps down in voltage result in current spikes in the opposite direction. This could be evidence of space charge build up within the sample. ....	122
<b>Figure 4.23</b> Dark current density transients through an $i$ -layer sample from set A in response to step-wise changes in the applied field. The current scale is logarithmic to account for the large range of currents produced, as the $i$ -layer samples have a much greater field dependence than multilayer samples. ....	123
<b>Figure 4.24</b> Dark and discharge current density transients produced by applying $-10$ V/ $\mu\text{m}$ across a $p-i-n$ sample from set A for 1000 s followed by short-circuiting the sample through a resistor and measuring the discharge current for 2 hours (1000 s of discharge shown). ....	125
<b>Figure 4.25</b> Magnitudes of (a) the dark current density and (b) the discharge current density transients for the $p-i-n$ family of sample set A. The dark current depends strongly on the sample structure but the corresponding discharge current does not. ....	126
<b>Figure 4.26</b> Measured released charge as a function of sample structure and applied bias for (a) the $p-i-n$ family and (b) the $n-i-p$ family of sample set A. The values were obtained by using Matlab to numerically integrate the discharge currents over 2 hours, setting the initial current value to 0. The $p-i$ sample releases a larger amount of trapped charge than the other samples of the $p-i-n$ family while the samples of the $n-i-p$ family release an amount of trapped charge that is fairly consistent between samples. All samples store more charge at higher applied fields. ....	127
<b>Figure 4.27</b> Discharge measurements recorded during the observation of the contact formation process on the Al contact of an $n-i-p$ sample from set C. (a) Transients measured during the application of the bias, (b) discharge transients measured by short-circuiting the sample after the application of the bias for 1000 s. Very different dark current levels at the same applied field result in identical discharge transients. ....	129
<b>Figure 4.28</b> Schematic illustration of (a) an $i$ -layer sample with holes and electrons uniformly trapped throughout, (b) an $i-p$ sample with holes trapped in the $i$ -layer and electrons trapped in the $p$ -layer, (c) an $n-i$ sample with holes trapped in the $n$ -layer and electrons trapped in the $i$ -layer and (d) an $n-i-p$ sample with holes	

trapped in the <i>n</i> -layer and electrons trapped in the <i>p</i> -layer. The same amount of charge is stored in each sample, but the location of the charge has a varying effect on the electric field at the contacts.....	130
<b>Figure 4.29</b> Discharge currents for a <i>p-i-n</i> sample of set A after being forward biased at different voltages. At field above 1 V/ $\mu\text{m}$ , the discharge current is in the same direction as the current when the bias was applied.....	132
<b>Figure 4.30</b> Explanation of reversal of discharge current direction in a <i>p-i-n</i> sample when forward biased above a certain value. (a) Below an applied field of 1 V/ $\mu\text{m}$ , injected holes are trapped in the <i>p</i> -layer and injected electrons are trapped in the <i>n</i> -layer, creating an internal field in opposition to that applied. (b) Above 1 V/ $\mu\text{m}$ , injected holes drift through the <i>p</i> - and <i>i</i> -layer and are trapped in the <i>n</i> -layer and injected electrons drift through the <i>n</i> - and <i>i</i> -layer and are trapped in the <i>p</i> -layer, creating an internal field supporting that applied. ....	133
<b>Figure 4.31</b> Change in dark current transients with roughly one and two years of ageing of sample set A. (a) an <i>i</i> -layer sample biased at 10 V/ $\mu\text{m}$ , (b) an <i>n-i-p</i> sample, biased at 10 V/ $\mu\text{m}$ and (c) the same <i>n-i-p</i> sample biased at -10 V/ $\mu\text{m}$ (current magnitudes shown). Over two years, the dark current increased by roughly one order of magnitude in the <i>i</i> -layer sample. In the <i>n-i-p</i> sample, the dark current increased by roughly four orders of magnitude when reverse biased, but remained fairly consistent when forward biased. ....	135
<b>Figure 4.32</b> Dark current density as a function of <i>i</i> -layer thickness for the Pt contacts on samples of set B, 100 s and 1000 s after the application of the 10 V/ $\mu\text{m}$ bias. The solid lines give the best linear fit at both times. The points marked with an “x” represent the uncharacteristically low points from sample US5 (240 $\mu\text{m}$ <i>i</i> -layer), which are considered outliers.....	137
<b>Figure 4.33</b> Dark current density as a function of <i>i</i> -layer thickness for sample set B at 10 V/ $\mu\text{m}$ , 100 s after the application of the bias for (a) Al contacts, (b) Cr contacts and (c) Au contacts. The points marked with an “x” represent the uncharacteristically low points from sample US5 (240 $\mu\text{m}$ <i>i</i> -layer). The dashed lines are only a guide for the eye. The solid line in (b) is a power law fit to the Cr data, omitting the outlying point at 240 $\mu\text{m}$ .....	138
<b>Figure 4.34</b> Dark current density as a function of <i>i</i> -layer thickness for Pt contacts on samples of set B, 1000 s after the application of the 10 or 5 V/ $\mu\text{m}$ bias. The points marked with an “x” represent the uncharacteristically low points from sample US5 (240 $\mu\text{m}$ <i>i</i> -layer). The solid lines give the best linear fit at both applied fields.....	139
<b>Figure 4.35</b> A comparison of dark current density values for <i>n-i-p</i> family samples of set A (nominally 200 $\mu\text{m}$ thick) and Pt and Cr contacts on sample US2 (110 $\mu\text{m}$ <i>i</i> -	

layer) of sample set B, 1000 s after the application of the positive bias of 10 V/ $\mu\text{m}$ . .....	140
<b>Figure 4.36</b> $J$ - $F$ curve for the Pt contact on sample US2 of sample set B, 100 s after the application of the bias. There are two regions of different field dependence. The transition between the two occurs at $\sim 5$ V/ $\mu\text{m}$ .....	141
<b>Figure 4.37</b> Schematic diagram of the electric field distribution across an $n$ - $i$ - $p$ sample with properly functioning blocking layers. $L$ is the total thickness of the sample, $L_n$ is the thickness of the $n$ -layer and $L_p$ is the thickness of the $p$ -layer. ....	143
<b>Figure 4.38</b> (a) Electric field at the positive ( $F_1$ ) and negative ( $F_2$ ) contacts and (b) the corresponding hole, electron and total injection current as a function of sample thickness for an $n$ - $i$ - $p$ sample with working blocking layers, once the dark current has reached a steady-state. At practical thicknesses ( $> 100$ $\mu\text{m}$ ), the electric field at both contacts and the dark current are relatively independent of $i$ -layer thickness.....	144
<b>Figure 4.39</b> Schematic diagram of the electric field distribution across an $n$ - $i$ - $p$ sample with a leaky $n$ -layer.....	145
<b>Figure 4.40</b> (a) Electric field at the positive ( $F_1$ ) and negative ( $F_2$ ) contacts and (b) the corresponding hole, electron and total injection current as a function of sample thickness for an $n$ - $i$ - $p$ sample with a leaky $n$ -layer, once the dark current has reached a steady state. The field at the positive contact decreases with increasing $i$ -layer thickness, while the field at the negative contact increases. As a result, the electron current increases and so too does the total dark current. ....	145
<b>Figure 4.41</b> (a) Electric field at the positive ( $F_1$ ) and negative ( $F_2$ ) contacts and (b) the corresponding hole, electron and total injection current as a function of sample thickness for an $n$ - $i$ - $p$ sample with a leaky $n$ -layer when the applied voltage, not the applied field, is kept constant. (c) The total calculated current, scaled up by 1000 times, compared with experimental data for the Pt contacts of sample set B. When the applied voltage is kept constant, the leaky $n$ -layer model predicts a decrease in dark current with increasing $i$ -layer thickness that is similar to that observed experimentally. ....	146
<b>Figure 4.42</b> Dark current density transients for four samples of set C with the Al contacts biased at 5 V/ $\mu\text{m}$ . Samples at both thicknesses give identical transients, showing a lack of $i$ -layer thickness dependence.....	148
<b>Figure 4.43</b> Dark current density transients for the stabilized a-Se samples of set D with the Pt contacts biased at 10 V/ $\mu\text{m}$ . The 7 times thicker side gives currents slightly higher than the thin side, but the difference is not great enough to indicate the presence of a significant contribution from bulk thermal generation. ....	149

**Figure 4.44** A comparison of dark current levels 300 s after the application of the bias to samples of sets C and D. (a) Al contacts biased at 10 V/ $\mu\text{m}$ , (b) Al contacts biased at 5 V/ $\mu\text{m}$ , (c) Pt contacts biased at 10 V/ $\mu\text{m}$ , (d) Pt contacts biased at 5 V/ $\mu\text{m}$ . A change in *i*-layer thickness has no consistent effect on the dark current while an increase of 2  $\mu\text{m}$  in *n*-layer thickness decreases the dark current by roughly one order of magnitude at high applied fields. .... 150

**Figure 4.45** Dark current density levels 1000 s after the application of the 10 V/ $\mu\text{m}$  bias for *n-i-p* samples of sets C and D. The comparison clearly shows that the Pt contacts invariably give higher levels of dark current than the Al contacts for each sample. .... 152

**Figure 4.46** Dark current density vs. applied field for an 86  $\mu\text{m}$  thick sample of set C for both the Pt and Al contact, 1000 s after the application of the field. The solid lines give the power law fits. The Pt contact gives higher dark current levels and exhibits a stronger field dependence. .... 153

**Figure 4.47** Dark current transients produced by samples of set B. All samples are *n-i-p* structures and were biased at 10 V/ $\mu\text{m}$ . (a) 60  $\mu\text{m}$  *i*-layer sample with Cr, Al and Pt contacts, (b) 110  $\mu\text{m}$  *i*-layer sample with Cr, Au and Pt contacts, (c) 310  $\mu\text{m}$  *i*-layer sample with Cr, Al, Au and Pt contacts, (d) 35  $\mu\text{m}$  *i*-layer sample with Cr, Al, Au and Pt contacts, (e) 240  $\mu\text{m}$  *i*-layer sample with Cr, Al, Au and Pt contacts, (f) legend. Cr consistently gives the highest level of dark current while Pt often results in the lowest. .... 154

**Figure 4.48** Dark current density as a function of positive contact work function for sample US4 of sample set B, 1000 s after the application of two different fields, 5 and 10 V/ $\mu\text{m}$ . The lines are only a guide for the eye. There is a general trend of decreasing dark current with increasing work function of positive contact metal... .. 156

**Figure 4.49** Dark current density vs. time for non-chlorinated *i*-layer sample, 549-5, and chlorinated *i*-layer sample, 544-6, both biased at 3 V/ $\mu\text{m}$ . The chlorinated sample initially gives a higher dark current than the non-chlorinated sample but as time goes by the difference becomes much less. This potentially suggests that the dark current changes from being dominated by hole drift to electron drift as time passes after the application of the bias. .... 158

**Figure 4.50** Dark current density vs. time for chlorinated *i*-layer sample, 544-6, chlorinated *n-i-p* sample, 531-5 and non-chlorinated *p-i-n* sample, 553-5. The *n-i-p* sample produces a transient which does reach a steady-state after roughly 100 s. The dark current produced is lower than that produced by the *i*-layer sample until roughly 2000 s even though the *n-i-p* sample is biased at a much higher field. The forward biased *p-i-n* sample produces a transient with a hump at around 1000 s, similar to the transients produced by forward biased multilayer samples of other sample sets. .... 159

<b>Figure 5.1</b> Experimental results for the first 20 s of an <i>i</i> -layer dark current measurement along with two pure Monte Carlo simulation results using different values of deep hole trap concentration, $N_{th}$ .....	162
<b>Figure 5.2</b> An illustration of an <i>n-i-p</i> sample divided into dimensional slices.....	164
<b>Figure 5.3</b> Diagrammatic representation of the carrier release array. The bottom axis represents the time in the simulation while the top axis shows the corresponding steps in the release array. The vertical axis represents the trapped carrier concentration. (a) A carrier trapped 0.1 s into the simulation is randomly assigned a release time of 10 s. Therefore, one trapped carrier is added to step 100 of the release array, corresponding to 10 s of simulation time. (b) By 10 s of simulation time, 500 carriers have been trapped which have been assigned a release time between 10 and 10.1 s. At that point, the number of trapped carriers in step 100 of the release array is reduced to 0. A corresponding amount of trapped carriers are released from each step in the dimensional array. ....	169
<b>Figure 5.4</b> Dark current density transient for an <i>i</i> -layer sample of set A biased at 10 V/ $\mu$ m compared with the result of a corresponding modified Monte Carlo simulation. The simulated transient appears to reach a steady state at roughly 100 s while the experimental transient does not. ....	171
<b>Figure 5.5</b> Trapped hole and electron concentration distribution across the <i>i</i> -layer sample after 300 s of simulation. The resulting electric field distribution is also shown and compared to the original, uniform field. ....	172
<b>Figure 5.6</b> Dark current density transient for an <i>i</i> -layer sample of set A biased at 5 V/ $\mu$ m compared with the result of a modified Monte Carlo simulation. The correlation is not nearly as good as for the transient produced at 10 V/ $\mu$ m.....	173
<b>Figure 5.7</b> Dark current density transients produced by modified Monte Carlo simulations. The simulation which produced the lowest curve has slightly higher values for deep trap concentrations than the simulation which produced the middle curve. The curve which ends at the highest level corresponds to a slightly lower energy depth for deep hole traps as compared to the middle curve. While these results are intuitive, the number of adjustable parameters makes it very difficult to match simulation results with experimental results through trial and error adjustment of those parameters. ....	174
<b>Figure 5.8</b> Comparison of simulation results for a 1 mm thick <i>n-i-p</i> a-Se layer with published results (replotted from [57]). Using the same equations and parameters, the results were matched almost perfectly at fields of 10, 7 and 5 V/ $\mu$ m. ....	176
<b>Figure 5.9</b> (a) Representation of published model [57] where injected holes immediately fill the entire n-layer. (b) With the theoretical sample divided into dimensional slices much thinner than the <i>n</i> -layer, injected holes now fill the slice closest to the	

positive contact. Holes which are not trapped in the first slice drift into neighbouring slices in subsequent time steps. ....	178
<b>Figure 5.10</b> Dark current transients obtained by adding in Monte Carlo style features to the simulations of Mahmood and Kabir, compared with their results (bottom theoretical curve and experimental data selectively replotted from [57]). The top curve was obtained by reducing the deep hole trap concentration by an order of magnitude from that quoted in [57]. The shape of the decay is now unlike that of the experimental transient. ....	178
<b>Figure 5.11</b> Simulation results using the model of [57] to simulate the dark current density in three <i>n-i-p</i> structures with varying <i>i</i> -layer thicknesses of 60, 110 and 310 $\mu\text{m}$ . The change in thickness makes almost no difference, in agreement with the most reliable experimental results from Chapter 4. ....	180
<b>Figure 5.12</b> Dark current density transients experimentally measured (circles) and calculated (lines) for the Pt contact on an <i>n-i-p</i> sample of set C for applied fields of (a) 10 $\text{V}/\mu\text{m}$ , (b) 7 $\text{V}/\mu\text{m}$ , (c) 5 $\text{V}/\mu\text{m}$ , (d) 3 $\text{V}/\mu\text{m}$ . The matching is quite good at all fields except at 10 $\text{V}/\mu\text{m}$ where the plateau at 100 s is not accurately predicted by the model. The “wavy” appearance of the theoretical curves is due to the fact that only 2 discrete deep hole trap states were assumed. A smoother transient could be produced by assuming many deep hole trap states to approximate a continuous distribution in energy. ....	182
<b>Figure 5.13</b> Dark current density transients experimentally measured (circles) and simulated (lines) for the Pt contact on an <i>n-i-p</i> sample of set C at 5 $\text{V}/\mu\text{m}$ . The total simulated current is the sum of the simulated hole and electron currents. The electron current becomes dominant after roughly 200 s. The eventual increase in the hole current is due to an increasing field at the positive contact as the trapped carrier concentration distribution across the sample continues to change. This effect could be eliminated through the inclusion of several finely tuned deep hole trap states. ....	184
<b>Figure 5.14</b> Comparison of the dark current levels produced by the Pt and Al contacts on an <i>n-i-p</i> sample of set C, 2 s and 1000 s after the application of the 10 $\text{V}/\mu\text{m}$ bias. At 2 s, the Pt contact produces a larger current, which would be expected if hole injection is dominant as Pt has a larger work function than Al, providing a smaller barrier to hole injection. After 1000 s, the current levels are much closer, possibly due to a decreased relative contribution of holes to the dark current, as electrons will face the same barrier to injection in both cases. ....	185
<b>Figure 5.15</b> Dark current density transients experimentally measured (circles) and simulated (lines) for the Pt contact on an <i>n-i-p</i> sample of set C at 10 $\text{V}/\mu\text{m}$ . The temporary plateau exhibited experimentally is not well reproduced by the model. ....	186
<b>Figure 6.1</b> An illustration of an <i>n-i-p</i> sample divided into dimensional slices, with holes and electrons drifting from their point of photogeneration due to the applied field. ....	192

<b>Figure 6.2</b> The exponentially decaying carrier generation profile results in the majority of photogenerated carriers being created near the radiation receiving electrode. ....	195
<b>Figure 6.3</b> Single <i>i</i> -layer sample used in initial sensitivity simulations. ....	199
<b>Figure 6.4</b> (a) The CCE, PGR and normalized sensitivity as a function of cumulative exposure, (b) initial, mid-simulation and final electric field distribution and (c) final trapped carrier concentration distributions for a mammographic exposure, single layer simulation. The PGR increases with cumulative exposure due to trapped electrons near the positive contact which increase the electric field in that region, lowering $W_{\pm}$ . However, $s_x$ decreases with cumulative exposure as the CCE decreases more than the PGR increases due to the continued creation of x-ray induced, metastable trap states. ....	201
<b>Figure 6.5</b> Three layer, <i>n-i-p</i> structured sample used in sensitivity simulations involving blocking layers. <i>n-i</i> structure results use the same structure with no <i>p</i> -layer. ....	202
<b>Figure 6.6</b> Comparison of normalized x-ray sensitivity vs. cumulative exposure for <i>i</i> -layer, <i>n-i</i> and <i>n-i-p</i> structures. $s_x$ decreases at the same rate for all structures but is roughly 2% lower at any given cumulative exposure for the <i>n-i</i> and <i>n-i-p</i> structures than for the <i>i</i> -layer structure. The addition of the <i>p</i> -layer makes very little difference in the result. ....	203
<b>Figure 6.7</b> Trapped hole and electron concentration distributions in the <i>n-i</i> sample after 0.36 R of exposure. The area of the sample between 0 and 10 $\mu\text{m}$ where there is increased hole trapping is the <i>n</i> -layer. ....	204
<b>Figure 6.8</b> Normalized x-ray sensitivity vs. cumulative exposure for an <i>n-i-p</i> mammographic structure with three different thicknesses of <i>p</i> -layer. Due to the positive bias, the thickness of the <i>p</i> -layer has almost no effect on $s_x$ . ....	205
<b>Figure 6.9</b> Normalized sensitivity vs. cumulative exposure for an <i>n-i-p</i> structure in which the thickness of the <i>n</i> -layer varied from 5 to 20 $\mu\text{m}$ . $s_x$ decreases linearly with increasing <i>n</i> -layer thickness. ....	206
<b>Figure 6.10</b> Comparison of normalized sensitivity vs. cumulative exposure for <i>n-i-p</i> structures with a hole lifetime in the <i>n</i> -layer of 4.8 $\mu\text{s}$ , 0.48 $\mu\text{s}$ and 0 s. The shorter the hole lifetime in the <i>n</i> -layer, the lower the overall sensitivity. An ideal <i>n</i> -layer, with a hole lifetime of 0 s, produces a very low normalized sensitivity due to the immediate trapping of all holes photogenerated in the <i>n</i> -layer, next to the radiation receiving electrode. ....	208
<b>Figure 6.11</b> Comparison of normalized sensitivity vs. cumulative exposure for two <i>n-i-p</i> structures with different electron lifetimes in the <i>n</i> -layer. $s_x$ is reduced by only 0.4% after 0.36 R of exposure when the electron lifetime in the <i>n</i> -layer is decreased by one order of magnitude. ....	209

<b>Figure 6.12</b> The electric field distribution after 0.36 R for an <i>n-i-p</i> structure. When the electron lifetime in the <i>n</i> -layer is decreased by an order of magnitude, the increased trapped electron concentration near the positive contact causes a sharp increase in the electric field. ....	210
<b>Figure 6.13</b> Example of a negatively biased <i>p-i-n</i> sample used in sensitivity simulations. Single <i>i</i> -layer simulations use the same set up, without the <i>p</i> - and <i>n</i> -like blocking layers. ....	211
<b>Figure 6.14</b> A comparison of PGR, CCE and $s_x$ vs. cumulative exposure for a single <i>i</i> -layer sample when biased either positively or negatively. The notation of bias refers to the polarity of the top, radiation receiving contact with respect to the substrate, <i>i.e.</i> negative bias refers to the case where the radiation receiving electrode is negative with respect to the substrate electrode as shown in Fig. 6.13. The normalized sensitivity of the positively biased sample is considerably higher and more consistent with exposure. ....	212
<b>Figure 6.15</b> Trapped hole and electron concentrations across an <i>i</i> -layer sample biased negatively after 0.36 R of exposure. Trapped electron concentration increases away from the negative contact (right of graph), as most of the photogeneration will take place there and electrons will drift to the positive contact (left of graph). Holes will drift to the negative contact and few will be generated close to the positive contact leading to an increasing trapped hole concentration near the negative contact. ....	213
<b>Figure 6.16</b> A comparison of the electric field distribution across an <i>i</i> -layer sample biased either positively or negatively after 0.36 R of exposure. In the case of positive bias, the electric field increases near the positive contact (region of most photogeneration for positive bias), increasing the PGR. In the case of negative bias, the electric field decreases near the negative contact (region of most photogeneration for negative bias), decreasing the PGR. ....	213
<b>Figure 6.17</b> A comparison of normalized sensitivity vs. cumulative exposure between a negatively biased, single layer sample, a negatively biased, three layer sample and a positively biased, three layer sample. Regardless of structure, the positively biased sample has a higher normalized sensitivity which is more consistent with cumulative exposure when compared with the negatively biased samples. ....	215
<b>Figure 6.18</b> Example of a positively biased, <i>n-i-p</i> sample with a non-uniform initial electric field distribution used in the simulation. The field (shown as a dashed line) at both the positive and negative contacts is reduced by the trapping of holes in the <i>n</i> -layer and electrons in the <i>p</i> -layer due to the initial rush of dark current after the bias is applied. ....	216
<b>Figure 6.19</b> PGR, CCE and $s_x$ vs. cumulative exposure for an <i>n-i-p</i> structure resulting from both a simulation which considers a non-uniform initial electric field distribution due to dark current and one which does not (assumes an initially	

uniform electric field distribution). The initial reduction in sensitivity due to the trapped holes in the $n$ -layer and trapped electrons in the $p$ -layer is quickly neutralized by recombination with drifting photogenerated carriers.....	217
<b>Figure 6.20</b> PGR, CCE and $s_x$ vs. cumulative exposure for an $n-i-p$ structure resulting from simulations which assume no dark current (solid lines) and trapped holes in the $n$ -layer and trapped electrons in the $p$ -layer before each exposure as a result of the flow of dark current (dashed lines). The effect of the dark current flowing between each exposure is an overall reduction in the normalized sensitivity. ....	219
<b>Figure 6.21</b> Comparison of the electric field distribution across an $n-i-p$ sample after 0.36 R of exposure simulated both with and without the effect of dark current flowing between exposures. The field is greatly reduced at the contacts when the dark current effects are considered due to trapped holes in the $n$ -layer and trapped electrons in the $p$ -layer.....	220
<b>Figure 6.22</b> PGR, CCE and $s_x$ vs. cumulative exposure for an $n-i-p$ structure resulting from a simulation which assumes trapped holes in the $n$ -layer and trapped electrons in the $p$ -layer before each exposure as a result of the flow of dark current (solid lines) and a simulation which also assumes recombination of injected carriers with oppositely charged carriers trapped in the blocking layers (dashed lines). The inclusion of the recombination effect makes very little difference. ....	221
<b>Figure 6.23</b> Schematic diagram of the x-ray sensitivity data acquisition system. The 80 kVp X-ray source provided a spectrum with a mean beam energy of 54.5 keV and had an intrinsic filtration of 23.5 mm Al. ....	222
<b>Figure 6.24</b> X-ray sensitivity experimental sequencing. The 200 ms ghost doses will create enough charge within the sample to cause ghosting through a decrease in the x-ray sensitivity. The 20 ms read doses will be small enough to allow for a measurement of the sensitivity without affecting it. Therefore, once the ghosting period ends, only read doses will be administered and sensitivity recovery should be observed. ....	223
<b>Figure 6.25</b> $p-i-n$ sample used in x-ray sensitivity experiments. ....	223
<b>Figure 6.26</b> A comparison of experimentally measured and simulated values of x-ray sensitivity vs. time, during the ghosting phase, for three different applied electric fields with the sample described in Fig. 6.25 with the simulation parameters listed in Table 6.3. ....	226
<b>Figure 6.27</b> A comparison of experimentally measured and simulated values of x-ray sensitivity vs. time, during the ghosting phase, at an applied field of 5 V/ $\mu$ m, for 3 different values of $f_{recomb}$ . A value of 0.8 gives the best result.....	227
<b>Figure 6.28</b> A comparison of experimentally measured and simulated values of x-ray sensitivity vs. time, during both the ghosting and recovery phases, at an applied	

field of 5 V/ $\mu\text{m}$ . Simulated results are shown with and without relaxation of metastable deep traps and with and without electron release with  $\tau_{re} = 1$  hour. Significant recovery is observed only if the relaxation effect is considered and electron release is ignored..... 228

**Figure 6.29** Simulated PGR, CCE and  $s_x$  vs. cumulative exposure ignoring the release of trapped electrons (solid lines) and including the release of trapped electrons with a release time of 1 hour (dashed lines). The inclusion of electron release causes recovery in the PGR but prevents recovery in the CCE.. ..... 230

**Figure 6.30** Simulated electric field distribution across the  $p-i-n$  sample initially, at the end of the ghosting period and at the end of the recovery period. The applied electric field was 5 V/ $\mu\text{m}$ . Metastable deep trap relaxation was included in the simulation but electron release was not. As trapped holes are released, the space charge throughout the sample becomes increasingly negative, driving the field lower near the negative contact. This prevents substantial recovery of the PGR as shown in Fig. 6.29..... 230

**Figure 6.31** A comparison of experimentally measured and simulated values of x-ray sensitivity vs. time, during both the ghosting and recovery phases, for three different applied electric fields with the sample described in Fig. 6.25. Good agreement is achieved at all three fields, however the reasons behind the occurrence of the recovery in sensitivity differ from those found by Manouchehri et al. [82]. All simulation parameters are the same as those listed in Table 6.3. Equation 6.23 was used to model the relaxation of the metastable x-ray induced trap states with  $\beta = 0.5$  and  $\tau_{sr} = 10$  hours..... 231

**Figure A.1** (a) The trapped carrier concentration in each layer of a multilayer a-Se sandwich structure. Uniform trapped carrier concentrations are assumed in each layer. Trapped hole concentrations in the  $n$ -layer and  $i$ -layer are given by  $p_m$  and  $p_{ti}$ , respectively and trapped electron concentrations in the  $i$ -layer and  $p$ -layer are given by  $n_{ti}$  and  $n_{ip}$ , respectively. (b) The electric field distribution across the structure due only to the trapped carrier concentrations. The field at the positive contact is denoted as  $F_{\rho 1}$ , the field at the  $n$ - and  $i$ -layer interface is  $F_{\rho n}$ , the field at the  $i$ - and  $p$ -layer interface is  $F_{\rho p}$  and the field at the negative contact is  $F_{\rho 2}$ . ..... 244

# LIST OF TABLES

<b>Table 1.1</b> Parameters for digital x-ray imaging systems. The maximum energy of the emitted x-ray is equal to the kVp value (data taken from Rowlands and Yorkston [11]).....	10
<b>Table 3.1</b> Allotropic forms of Se as summarized in [135].....	64
<b>Table 3.2</b> Properties of stabilized a-Se (a-Se:0.2-0.5%As + 10-40 ppm Cl) films at room temperature (data taken from [65]).....	79
<b>Table 3.3</b> The influence of As alloying and Cl and O doping on charge transport in vacuum deposited a-Se films (summarized from [7]). .....	83
<b>Table 3.4</b> Some typical or expected properties of selected x-ray photoconductors for large area applications. PVD is physical vapor deposition; SP is screen printed. $\delta$ is the attenuation depth at the shown photon energy, either 20 keV or 60 keV. $\mu\tau$ represents the carrier range. From various references and combined selectively, including [28,29,196] and those listed in the table. ....	85
<b>Table 4.1</b> Summary of characteristics for sample sets A, B, C, D, and E. The notation used to describe the sample structure uses the first letter to represent the top layer, or what would be the layer next to the radiation receiving electrode. ....	101
<b>Table 4.2</b> Values of $n$ in the relation $J(F) \propto F^n$ for all sample structures and corresponding $R^2$ (confidence in the fit of the power law). Applied voltages are positive for $i$ - $p$ , $n$ - $i$ and $n$ - $i$ - $p$ samples, negative for $p$ - $i$ , $i$ - $n$ and $p$ - $i$ - $n$ samples and both for $i$ -layer samples. Current values are taken 1000 s after the application of the bias. ....	113
<b>Table 4.3</b> Results for the control experiment described by Fig. 4.21. Observed charges were calculated using Matlab to numerically integrate the measured current transients, setting initial values to zero.....	121
<b>Table 4.4</b> Results for voltage step measurements on sample set A. The $p$ - $i$ - $n$ samples display behaviour which is most indicative of large amounts of trapped charge carriers within the sample. ....	124
<b>Table 4.5</b> Electric field at the positive ( $F_1$ ) and negative ( $F_2$ ) contacts of the samples shown in Fig. 4.28, calculated using Eqs. 4.3 and 4.4 with assumed values of $L = 200 \mu\text{m}$ , $L_p = 2 \mu\text{m}$ , $L_n = 5 \mu\text{m}$ , a total trapped hole concentration of $2 \times 10^{12} \text{ cm}^{-3}$ and a total trapped electron concentration of $1 \times 10^{12} \text{ cm}^{-3}$ .....	132

<b>Table 4.6</b> Material and structural properties assumed for calculations of the electric field at the contacts and the corresponding hole and electron injection currents in an <i>n-i-p</i> a-Se sandwich structure using Eqs. 4.3 – 4.5.....	143
<b>Table 4.7</b> Sample numbers and corresponding characteristics, including hole and electron schubwegs for samples of set E. ....	157
<b>Table 5.1</b> Material properties assumed for the numerical calculations done to match dark current transients measured experimentally. ....	181
<b>Table 5.2</b> Values of <i>n</i> -layer deep hole trap concentrations assumed for dark current simulations at different applied fields.....	182
<b>Table 6.1</b> Important material properties assumed in the initial x-ray sensitivity results. Deep trap concentrations are denoted as $N_{th(e)}$ for holes (electrons), $\tau_{0h(e)}$ are the carrier lifetimes, $\tau_{rh(e)}$ are the release times and $N_{x_{0h(e)}}$ are the constants used in calculating x-ray generated metastable traps. ....	199
<b>Table 6.2</b> Material properties of the <i>n</i> - and <i>p</i> -like blocking layers. A double subscript of <i>n</i> refers to properties in the <i>n</i> -like layer, while a double subscript of <i>p</i> refers to properties in the <i>p</i> -like layer. ....	202
<b>Table 6.3</b> Material properties assumed for the simulations done to match x-ray sensitivity experimental results. A double subscript of <i>n</i> refers to properties in the <i>n</i> -like layer, while a double subscript of <i>p</i> refers to properties in the <i>p</i> -like layer and a double subscript of <i>i</i> refers to properties in the <i>i</i> -layer. ....	224

# LIST OF ABBREVIATIONS

AB	Anti-Bonding
AMA	Active Matrix Array
APS	Active Pixel Sensor
a-Se	Amorphous Selenium
a-Si:H	Hydrogenated Amorphous Silicon
B	Bonding
CCD	Charge Coupled Device
CCE	Charge Collection Efficiency
CCS	Close Space Sublimation
CZT	Cadmium Zinc Telluride
DC	Direct Current
DOS	Density Of States
DQE	Detective Quantum Efficiency
DR	Dynamic Range
EHP	Electron-Hole Pair
ESR	Electron Spin Resonance
FF	Fill Factor
FPXI	Flat Panel X-ray Imager
GPIB	General Purpose Interface Bus
HARP	High-gain Avalanche Rushing Photoconductor structure
IFTOF	Interrupted Field Time-Of-Flight
IR	Infrared
ITO	Indium-Tin-Oxide
IVAP	Intimate Valence Alternation Pair
lp	line pair
LP	Lone Pair
LSF	Line Spread Function
MRI	Magnetic Resonance Imaging

MTF	Modulation Transfer Function
NB	Non-Bonding
NPS	Noise Power Spectrum
PDF	Probability Density Function
PE	Potential Energy
PGR	Photogeneration Ratio
ppm	parts-per-million
PPS	Passive Pixel Sensor
PSF	Point Spread Function
PVD	Physical Vapour Deposition
QE	Quantum Efficiency
SCLC	Space-Charge-Limited Current
SNR	Signal to Noise Ratio
SP	Screen Printing
TFT	Thin Film Transistor
TOF	Time-Of-Flight
VAP	Valence Alternation Pair

# 1. INTRODUCTION

## 1.1 Projection Radiography

Within weeks of their discovery in 1895 by Wilhelm Röntgen, x-rays were being used for medical imaging and diagnostics, leading to the field of diagnostic radiology. X-rays are a form of electromagnetic radiation with the spectrum of frequencies from  $3 \times 10^{16}$  to  $3 \times 10^{19}$  Hz. X-rays used in diagnostic radiology are generated by an x-ray tube in which a high applied voltage accelerates electrons, which are emitted from a hot cathode, through a vacuum, impinging on the anode which is a metal target [1]. The sudden deceleration of the electrons results in the emission of x-ray photons. The target is commonly made of tungsten for general radiography, but a molybdenum target is often used for mammography where lower energy x-rays are required. In the imaging process, the generated x-rays are passed through an object and onto a detector as shown in Fig. 1.1. An x-ray tube is essentially a point source of radiation so that in projection radiography the acquired image is a shadow of the object of interest.

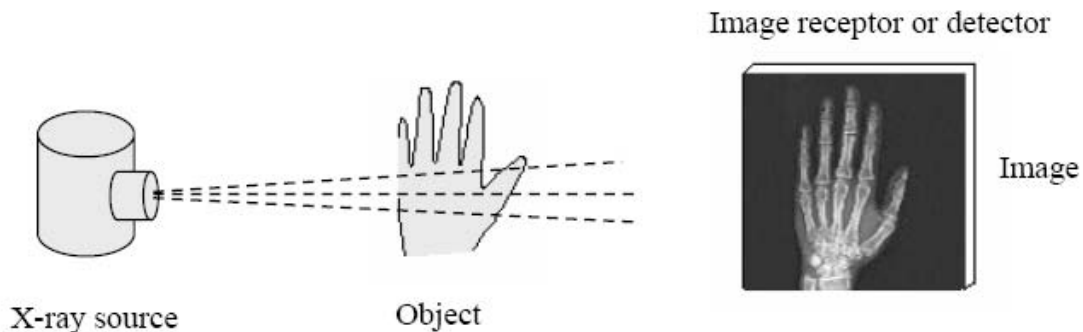


**Figure 1.1 Basic radiographic imaging technique; after [2]. An x-ray beam from a source is passed through the object of interest onto an image detector.**

The creation of the image is due to the differential attenuation of the x-rays by the object being analyzed, that is, different materials within the object will attenuate x-rays differently. Relatively denser material, such as bone within the human body, will attenuate more x-rays than surrounding tissues. If the x-rays incident upon the object are of uniform intensity, then the radiation which passes through will have a modulated intensity distribution and this remnant radiation will contain information about the internal structure of the object, as seen in Fig. 1.2.

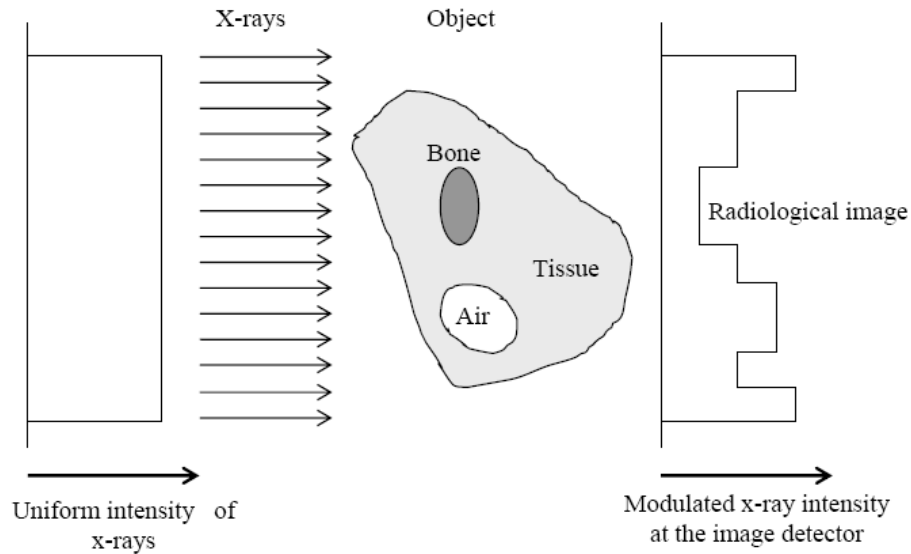


**Figure 1.2** A uniform distribution of x-rays passes through an object containing regions of varying density. As some regions attenuate x-rays more efficiently, the x-ray beam emerging from the object will have a modulated intensity distribution, which contains the information of interest; after [2].

An important example of projection radiography is mammography, which is the soft tissue imaging of human breasts to screen for breast cancer by imaging for abnormal masses or microcalcifications. Mammography is currently the most effective tool for the early screening of breast cancer [3], a disease of which 194,280 new cases were estimated in the United States alone in 2009 [4]. This makes up 27% of new cancer cases for women and in 2009 there were an estimated 40,610 deaths from breast cancer in the U.S., accounting for 15% of cancer related deaths of women [4]. It has been shown that mammographic screening reduces the mortality rate of breast cancer patients by roughly 30% through early detection [5]. The field of mammography presents interesting challenges as the radiologist must be able to distinguish between several types of soft tissue with very similar x-ray absorption properties. Further, the images must have a very high resolution, as microcalcifications of interest can be only 80 – 100  $\mu\text{m}$  wide [6].

While projection radiography is an excellent method of “looking” inside of something non-invasively, one must keep it mind that x-rays are ionizing radiation and can cause damage to living tissue [1]. As such, the lowest possible dose for any application is always used and reducing the value of the lowest required dose is a continual design challenge in the world of medical imaging physics and engineering [7].

In spite of its potential side effects, projection radiography is one of the most commonly used modalities of diagnostic imaging [1]. While other modalities have evolved over time, most still suffer from significant drawbacks. Computed Tomography (CT) scans which are now very commonly used, while able to reconstruct three dimensional images of body parts, actually require a much larger dose (tens of times larger) than the corresponding imaging using projection radiography [8]. Magnetic Resonance Imaging (MRI) requires no exposure to ionizing radiation, but the techniques are expensive and are not yet readily accessible. Further, MRI exposes patients to a very large static magnetic field (up to 4 T for clinical imaging), the long term health implications of which have not been studied [1,9]. The field of endoscopy remains a valuable diagnostic tool, but is invasive, uncomfortable and potentially dangerous for the patient [10].

## **1.2 X-ray Image Detectors**

As shown in Figs. 1.1 and 1.2, the concept of projection radiography depends on a detector to receive and decipher the information contained in the modulated distribution of x-rays. This section will discuss the evolution of x-ray image detectors used in projection radiography from photographic film to the digital detectors which are the focus of the research presented in this thesis.

### **1.2.1 X-ray Film**

Historically, diagnostic radiography has been an analog technology as it has been film based. The image detector used to receive the x-rays is a cassette containing fluorescent screens on either side of a photographic film. The fluorescent screens convert the remnant radiation that is incident upon them into visible light. This light forms a latent image on the film, which is sensitive to light in the visible spectrum. The film itself is comprised of either a cellulose acetate or polyester resin base with an emulsion of silver halide granules on either one or both sides of the base. Sites on the emulsion layer which absorb radiation experience a build up of mobile silver ions. These sites accumulate more metallic silver upon chemical development in a dark room. The more radiation absorbed at a site, the more silver which accumulates and the darker the area of the film becomes. In this way, an image is formed [1].

This analog procedure has many inherent flaws. It is inconveniently inefficient as only 2 – 6% of the incident x-rays are absorbed in the emulsion of an x-ray film, though this can be increased by as much as an order of magnitude through the use of intensifying screens [1]. While the film emulsion has a very high resolution (up to several hundred lp/mm), the use of an intensifying screen causes visible photons to be emitted in all directions, greatly reducing the resolution (10 - 15 lp/mm) [7]. There is a time delay involved with the development of the film and as a result, real-time imaging is not possible. The images produced are not electronically captured which means that image processing is not possible without first digitizing the picture. Also, the developed films must be physically archived and cannot be stored in a compact, electronic format [11]. Given these drawbacks and the related evolution of film photography into digital photography, it was only a matter of time until projection radiography advanced into the digital realm.

### **1.2.2 Flat Panel X-ray Image Detectors**

As many new imaging modalities are inherently digital, *e.g.* MRI, projection radiography is advancing into the digital world as well. An ideal replacement for analog film technology would create quality images immediately after exposure, doing away with film development times and the uncertainty that a proper image was obtained, and at the same time meet the requirements for real-time imaging. It would also allow the image to be displayed on a computer screen, facilitating computer aided diagnosis, and would allow the image to be transmitted via the internet for immediate second opinions and stored electronically, doing away with space consuming physical archives. Further, an ideal x-ray image detector would have increased sensitivity to x-rays, reducing the necessary dose to patients as x-rays are ionizing radiation and can cause mutations in living cells [1]. Finally, this system must be implementable with a minimum disruption to current imaging system parameters and physical set up to avoid overhead conversion costs and mass retraining of personnel.

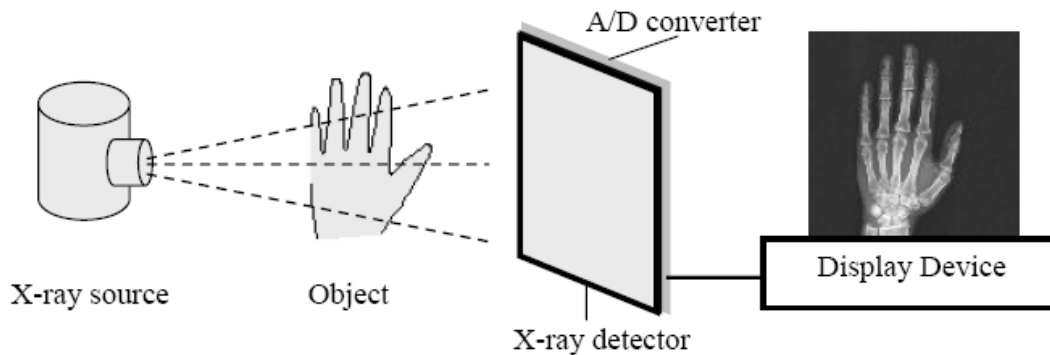


**Figure 1.3 A digital radiography system; after [2]. When compared to an analog radiography system, the screen film detector has been replaced with a digital one which can immediately display the resultant image on a computer screen.**

The answer to this problem comes in the form of digital radiography systems, as schematically shown in Fig. 1.3. Historically, many varied attempts have been made to devise a purely digital radiography system. The most successful were based on x-ray stimulated storage phosphors which trapped electrons excited by the incident radiation to store a latent image. This image was then subsequently read out using photostimulated luminescence [11]. Phillips Medical Imaging Systems used xeroradiographic concepts (essentially the photo-copying of the internal structure of a body part) combined with an electronic readout technique in a digital radiography system known as Thoravision [12,13]. However, it was not until the development of hydrogenated amorphous silicon (a-Si:H) thin film transistor (TFT) based active matrix arrays (AMAs) in the early 1990's that a suitable electronic readout technique rose to the forefront. It was this development which truly revolutionized digital radiography, leading to the advent of flat panel, digital x-ray image detectors.

Digital flat panel x-ray imagers (FPXIs) are a technology which represents the ideal imaging system [11,14-24]. They are digital systems which create x-ray images directly on computer screens and can be used for mammography, chest radiography and fluoroscopy. Flat panel detectors are sized appropriately to directly replace the cassettes used in current analog systems, making them easily integrated. Further, digital, flat panel detectors make it possible to view combined x-ray and magnetic resonance images to more accurately guide medical diagnosis and treatment [25]. There are essentially two types of FPXIs, distinguished by the technique used

to detect the x-rays [11,26]. In indirect conversion based FPXIs, the x-rays are first converted to light via a phosphor layer, such as  $\text{Gd}_2\text{O}_2\text{S:Tb}$ , or a structured scintillating phosphor, such as  $\text{CsI:Tl}$ , which absorbs the incident x-rays. The light emitted from the scintillator is subsequently detected by an array of photodiodes [27]. In direct conversion FPXIs, an x-ray photoconductor, such as a-Se, is used as the principal detecting element to convert the absorbed x-ray photons directly to collectable charge carriers, which represent the signal [13-15,28-30]. While both direct and indirect detection technologies face their own developmental and operational challenges, which one eventually dominates the digital radiography market may depend on advancements in the understanding of the underlying physical principles of their operation that are based on current research. a-Se based direct conversion detectors have been shown to have better resolution than indirect detectors [11] and the direct approach requires a simpler TFT array structure that can be manufactured in a standard facility for active matrix liquid crystal displays [7].

Both detection systems rely on the same technological idea for the readout of the electrical charge created. Just as the created image is displayed on a computer screen in pixels, the image must be captured in pixels. Therefore, the radiation receiving area must be divided up into small areas, each of which records the intensity of radiation incident upon it. Obviously, like with a common television screen, smaller pixels (more pixels in a given area), means better resolution and a better picture. This pixilated system has been realized using a large-area, TFT-AMA, illustrated in Fig. 1.4. An AMA is a two dimensional array of pixels in which each pixel has a TFT that can be externally addressed. The TFT-AMA technology was pioneered by Peter Brody using CdSe TFTs in the early 1970s [31]. As shown in the figure, each pixel is identical with its TFT gate connected to a particular address line and the source to a particular data line. The AMA has  $M \times N$  number of gate and data lines (Fig. 1.4) in which M and N can be very large, *i.e.*  $2816 \times 3584$ , in the sensor shown in the upper right of Fig. 1.4.

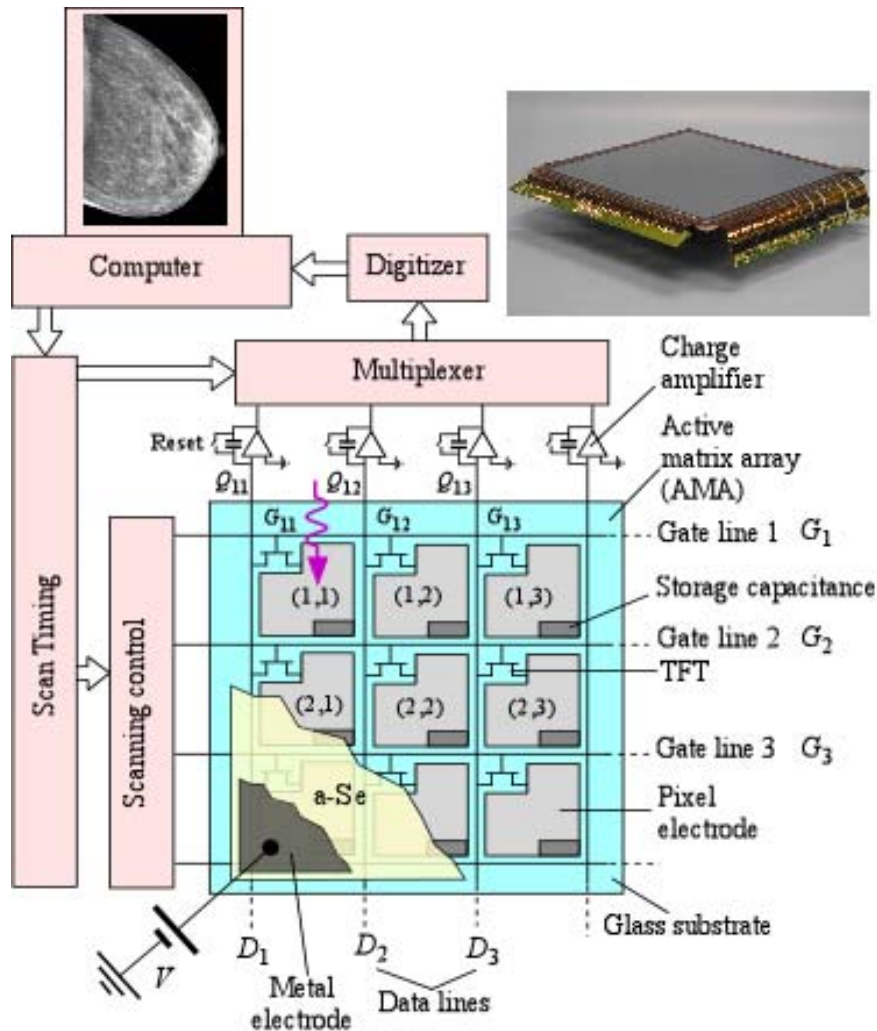


**Figure 1.4 Schematic diagram of a few pixels of a self-scanning, thin-film transistor, active-matrix array. Each row of pixels is addressed sequentially while each pixel in the addressed row is read out simultaneously. The charge stored on each pixel capacitor is read out in parallel and amplified before being multiplexed into serial data and sent to the display device. The entire array is coated with a photoconductive layer of a-Se and a top metal electrode.**

In an a-Se based FPXI, the active matrix array is coated with a-Se, which is then electroded on its surface to allow for the application of a bias voltage. Thus, each pixel acts as an individual x-ray detector and has a biased photoconductor as illustrated in the schematic cross section of a pixel depicted in Fig. 1.5. There is a storage capacitor at each pixel to collect charges that are generated by the photoconductor. The applied bias voltage establishes an electric field inside the photoconductor so that the charge carriers released by the absorption of an x-ray photon can be drifted and "collected" in the sense that they result in the deposition of charge on the storage capacitor,  $C_1$ .  $C_1$  integrates the current induced by the drift of the carriers and the integrated current, the charge on  $C_1$ , represents what appears to be collected from the

photogenerated carriers. In the example shown in Figs. 1.4 and 1.5, Pixel 1 receives the radiation, and the photogenerated charge in the photoconductor is collected on  $C_1$ . Fig. 1.5 shows an a-Si:H TFT switch, which allows the charge,  $Q_1$ , on  $C_1$  to be read out into the external circuit that has a charge amplifier as indicated in Fig. 1.4. When the gate,  $G_1$ , of TFT<sub>1</sub> is activated, TFT<sub>1</sub> switches on, and the charge on  $C_1$  is readout as  $MQ_1$  where  $M$  is the amplifier gain. The amount of charge,  $Q_1$ , that is generated depends on the incident radiation,  $X_1$ , on that particular pixel inasmuch as the number of electron and hole pairs generated in the photoconductor is proportional to the photon flux and the photon energy. One can therefore represent the x-ray image in terms of the charges residing on the pixel storage capacitors of the FPXI. The gates of all the TFTs in a row are connected to the same control line so that the charges are read off on parallel data lines,  $D_1, D_2, etc.$  and amplified separately. The information is then multiplexed into serial data, digitized and sent to a computer through image correction hardware. The next row is then accessed and so on until all of the rows in the AMA are read out. The system is then ready for another exposure [15].

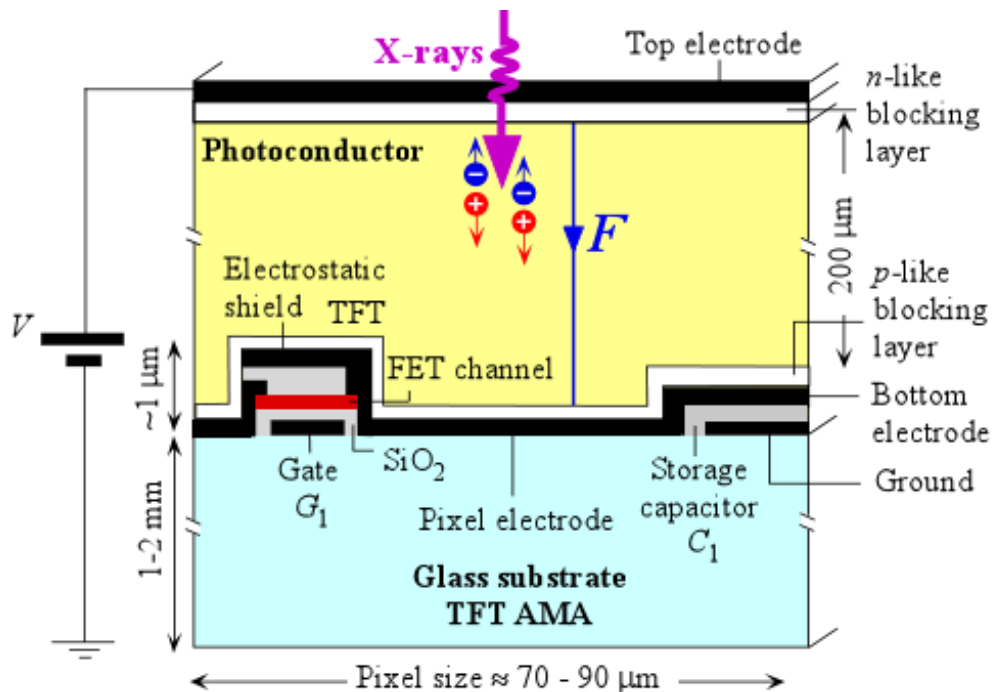


**Figure 1.5** A highly simplified cross-section of a single direct conversion pixel. The charges generated by the absorption of x-rays drift towards their respective electrodes. The capacitor  $C_1$  integrates the induced current due to the drift of the carriers which results in a stored charge,  $Q_1$ , on  $C_1$ .  $n$ - and  $p$ -type blocking layers are deposited between the intrinsic layer of a-Se and the contacts to reduce dark current levels. Drawing is not to scale.

Prototype a-Se based FPXIs were first demonstrated by Rowlands and coworkers [32-36] and by Lee, Cheung and Jeromin [37,38] in the mid-nineties. Since the first demonstration of the a-Se based FPXI, much research has been done in characterizing and understanding the imaging properties of a-Se, as will be discussed in detail in Chapters 2 and 3. The work presented in this thesis focuses solely on a-Se based FPXIs and has been carried out in partnership with ANRAD, a Quebec, Canada based producer of such detectors. Two examples of these detectors can be seen in Fig. 1.6 with the x-ray sensitive area and related electronics exposed.



**Figure 1.6 a-Se based, direct conversion x-ray image detectors without their protective, light proof cases.**

### **1.2.3 General Requirements of X-ray Imaging Systems**

An FPXI must be able to meet certain requirements in order to be used for different imaging tasks, including mammography, chest radiography and fluoroscopy. Table 1.1 summarizes these requirements.

Of course, the most important metric of system performance is image quality, whether this is defined qualitatively or quantitatively. A digital system cannot replace an analog one if the images it produces are of lower quality. This is not the case, as digital systems have been shown to provide images as good as or better than analog systems [39]. One can make the qualitative comparison for oneself using Fig. 1.7.

**Table 1.1 Parameters for digital x-ray imaging systems. The maximum energy of the emitted x-ray is equal to the kVp value (data taken from Rowlands and Yorkston [11]).**

Clinical Task	Chest Radiography	Mammography	Fluoroscopy
Detector Size	35 cm x 35 cm	18 cm x 24 cm	25 cm x 25 cm
Pixel Size	200 $\mu\text{m}$ x 200 $\mu\text{m}$	50 $\mu\text{m}$ x 50 $\mu\text{m}$	250 $\mu\text{m}$ x 250 $\mu\text{m}$
Number of Pixels	1750 x 2150	3600 x 4800	1000 x 1000
Readout Time	$\sim 1$ s	$\sim 1$ s	1/30 s
X-ray Spectrum	120 kVp	30 kVp	70 kVp
Mean Exposure	300 $\mu\text{R}$	12 mR	1 $\mu\text{R}$
Exposure Range	30 – 3000 $\mu\text{R}$	0.6 – 240 mR	0.1 – 10 $\mu\text{R}$

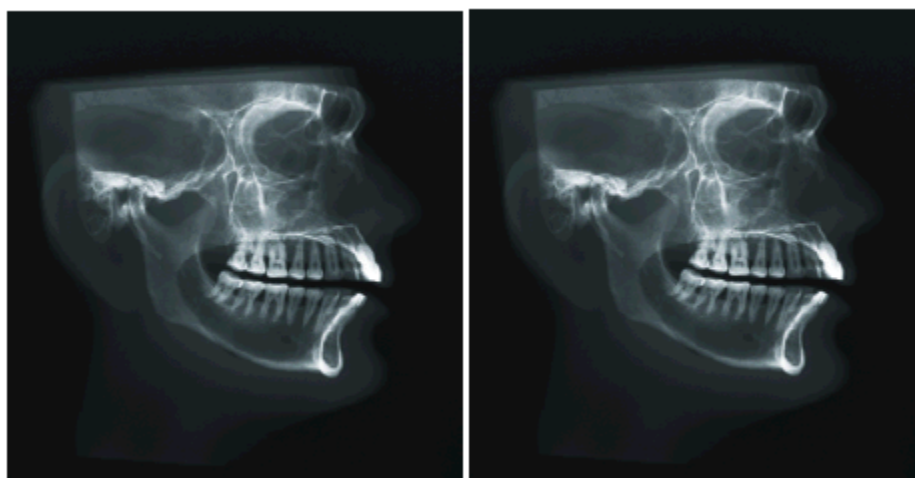


**Figure 1.7 X-ray images taken of a phantom of a human skull: a-Se based, direct conversion, flat panel detector (left), conventional film technology (right); after [39].**

#### 1.2.4 The Future of a-Se FPXIs

Though the image in Fig. 1.6 is a good indication of the high quality of images that can be obtained with currently commercially available a-Se based FPXIs, there is always room for improvement. Besides the improvement in the general understanding of the electronic and photoconductive properties of a-Se, which is the focus of this thesis, other avenues of advancing the technology are currently being explored. Please note that many of the terms used in this

section, such as modulation transfer function and x-ray sensitivity, will be described in detail in Chapter 2.

In the last decade, efforts have been made to replace the AMA readout technique with an array of charge coupled devices (CCDs) for very high resolution mammographic detectors [40]. This high resolution is due to the very small pixel sizes ( $20\ \mu\text{m} \times 20\ \mu\text{m}$ ) that are easily achievable with current CCD devices with total areas of  $11\ \text{cm} \times 1\ \text{cm}$ . Two or three of these devices can be combined to form a slot detector where the detector is mechanically scanned synchronously with a narrowly collimated x-ray source along the object being imaged, acquiring pieces of the whole image as they go [7]. While this complicates the imaging process, it does reduce the x-ray scatter which can be a significant problem in mammography [7]. A prototype CCD detector with an a-Se photoconductive layer has shown very low dark current and high resolution with a modulation transfer function above 0.5 at spatial frequencies of 11 – 14 lp/mm [41].

In the interest of improving the x-ray sensitivity and signal-to-noise ratio of the detector, signal gain can be implemented at the pixel level of the AMA [42]. Current commercial detectors use the single TFT passive pixel structure (PPS) described in Section 1.2.2. This can be replaced by an active pixel structure (APS) architecture where 2, 3, or 4 TFTs are used to provide signal gain at each pixel [43-45]. These architectures often use polycrystalline silicon (poly-Si) in place of a-Si:H to improve charge transfer times at the cost of increased noise and a less developed, and therefore less readily available, technology [46]. A  $64 \times 64$  APS 4 a-Si:H transistor array has been demonstrated with a photoconductive layer of a-Se and using the same readout electronics as commercially available a-Se FPXIs [47]. Extremely low exposures (as low as  $1.5\ \mu\text{R}$ ) were measurable with this prototype.

Another recently investigated method of improving x-ray sensitivity of these detectors is to improve the sensitivity of the a-Se layer by utilizing avalanche multiplication [48]. a-Se is the only evidenced amorphous semiconductor in which the primary charge carriers (holes) can acquire enough energy from the applied field to initiate impact ionization and secondary charge creation [49-51]. Therefore, each hole created by an incident photon can create many more

electron-hole pairs (EHPs) during its drift across the a-Se layer and each of those secondary holes can do the same. This leads to an “avalanche” of holes, generating much more charge per photon than is possible with commercial a-Se detectors. An explanation of how this can occur in low mobility amorphous semiconductors is given by the “lucky drift” model [49,52]. A maximum avalanche gain of  $10^3$  has been demonstrated for a 30  $\mu\text{m}$  thick a-Se layer at an applied field of 92 V/ $\mu\text{m}$  [49]. Of course, special blocking layers are needed to prevent massive charge injection at the electrodes used to apply the high electric field. This has been done successfully in high sensitivity television cameras based on HARPs (High-gain Avalanche Rushing Photoconductor structures) which use a scanning electron beam to read out the photogenerated charge distribution [53]. A modified HARP structure has been developed for applications in FPXIs [54], but the challenge of uniformly applying a field as high as 92 V/ $\mu\text{m}$  (for a 200  $\mu\text{m}$  thick a-Se layer, this corresponds to a voltage of 18.4 kV) over an area as large as 18 cm  $\times$  24 cm is indeed daunting.

While each of the potential improvements discussed above has promise for the future of a-Se FPXIs, it should be clear that each also introduces a unique set of complicated barriers to their implementation. While possibly not as dramatic as the improvements discussed above, simpler improvements in detector performance can be achieved through an improved understanding of the issues involved in using an a-Se conversion layer. Of course, another possible solution comes in the form of replacing the a-Se layer with another photoconductor, such as HgI<sub>2</sub> or PbO. The reason that a-Se has been the photoconductor of choice thus far, and the problems with using any of the potential replacements, will be discussed in Chapter 3. It stands to reason that a-Se based FPXIs will dominate the direct conversion market for the foreseeable future and the contribution to the understanding of the photoconductive layer by work such as that presented in this thesis will be invaluable for the future of this technology.

### **1.3 Research Objectives**

The research presented in this thesis focuses on developing a deeper understanding of the x-ray sensitivity and dark current present in multilayer metal/a-Se/metal (“sandwich structure”) devices used in direct conversion, digital x-ray image detectors. These two aspects of detector operation have a unique relationship in that a high x-ray sensitivity is desired, which requires a large bias to be applied across the structure, while a low dark current is required, the level of

which increases with the applied bias. The work presented in this thesis contains both experimental measurement and computer modeling of both x-ray sensitivity and dark current in a-Se sandwich structures.

### 1.3.1 Dark Current

The term dark current refers to an unwanted electrical current which flows through a photoconductor due to a necessary electrical potential placed across the photoconductive layer and not due to the photogeneration of electrical carriers due to incident radiation, which is normally the desired signal. Since the information used by flat panel detectors to create an image is the integration of pixel current, dark current is a source of noise in the system and decreases the dynamic range of the detector. There has been some recent effort to characterize and explain the dark current transients in metal/a-Se/metal sandwich structures [7,41,55-57], as detailed in Section 2.6.3. Yet, the understanding is far from complete. The dark current level in intrinsic stabilized a-Se layers is simply too high for use in flat panel detectors [13]. In a practical detector, thin *n*-type and *p*-type blocking layers are deposited between the intrinsic a-Se layer and the metal contacts, as shown in Fig. 1.5, to trap charge carriers injected from the contacts and reduce the dark current to acceptable levels [58]. The implementation of this *n-i-p* photodiode-like structure was based on the assumption that the dark current is dominated by the injection of carriers from the contacts. However, the actual effectiveness of each blocking layer and its position in the structure has never been systematically evaluated. Furthermore, it has long been assumed that the injection of charge carriers from the contacts is the dominant contributor to the dark current in these structures, while other possible contributions, such as thermal generation of charge carriers in the bulk, have been assumed to be negligible [57,59]. This has never been proven experimentally.

Experimental *I-t* and *I-V* curves from five separate sets of a-Se sandwich structure samples have been recorded. This work compares the measurements taken on different sample structures to determine the effectiveness of each blocking layer in reducing the dark current and looks for evidence of space charge in both the blocking layers and the intrinsic layer of the samples. Measurements on samples of varying thickness are compared to search for evidence of

generation of dark current in the bulk of the sample. Collective analysis of this data provides new insight into the true source of dark current in a-Se sandwich structures used in commercial FPXIs.

In addition to an exhaustive experimental investigation, computer modeling of the dark current was carried out. Matching the simulated dark current transients to the experimental results has allowed for the calibration of the physical parameters assumed in the model and gives evidence that the source of dark current assumed in the model, injection from the contacts or bulk thermal generation, is, in fact, the dominant contributor.

### 1.3.2 X-ray Sensitivity

The x-ray sensitivity of an FPXI is the collected charge per unit area per unit exposure of radiation. A high x-ray sensitivity allows for the detection of low doses of radiation, increasing the dynamic range of a detector and decreasing the required dose to the patient. Sensitivity depends on the fraction of the incident radiation that is absorbed in the detector, the amount of charge generated per unit of absorbed radiation and the amount of that generated charge that is collected. In the case of FPXIs based on an a-Se photoconductive layer, both of the latter two factors depend on the applied field; the higher the field, the greater the x-ray sensitivity [60].

Previous work has modeled the x-ray sensitivity of a-Se sandwich structures using Monte Carlo methods [2,61] and numerical methods solving continuity equations utilizing the backward Euler method [62,63]. These models assumed that the a-Se layer was homogenous and neglected the potential effects of dark current on the x-ray sensitivity. In the work presented here, the Monte Carlo methods used by Yunus [2] have been extended to model the effects of the blocking layers on the x-ray sensitivity of these *n-i-p* photodiode-like structures. Also considered are the effects on x-ray sensitivity of the dark current which flows through these structures before and in between x-ray exposures.

The results of the x-ray sensitivity modeling are compared with x-ray sensitivity experimental measurements taken with a *p-i-n* structured a-Se sample typical of those used in

general radiography detectors. This allowed for calibration and validation of the sensitivity model.

## **1.4 Scope of Thesis**

This first chapter has focused on introducing the basics of projection radiography and discusses the evolution of x-ray image detectors from film screen to direct and indirect conversion, digital, flat panel detectors, focusing on a-Se based direct conversion detectors currently used for mammography and the possible future improvements thereof.

The remainder of this thesis is divided into 6 chapters. Chapter 2 covers the metrics of x-ray image detector performance which are used to compare one detector against another. The metrics outlined include: x-ray sensitivity, image resolution, detective quantum efficiency, dynamic range and levels of dark current, with particular detail included in the discussion of x-ray sensitivity and dark current.

Chapter 3 discusses the properties of x-ray photoconductors that can be used in direct-conversion flat panel detectors. The majority of the chapter is devoted to a discussion on the understanding to date of the physical and electronic structure of Se in all of its phases, but particularly in its amorphous state. Progress in the development of competing photoconductors is also outlined.

Chapter 4 reports on the experimental work done to study the dark current in a-Se sandwich structures. The chapter begins with an outline of the experimental methods used, including a discussion on the preparation of the five sets of a-Se samples studied. Results from all five sets are given, showing the dark current as a function of time, applied field, sample structure, contact metal and sample thickness. Experimental investigations of charge stored in the samples during the application of an external field and the short and long term reproducibility of dark current transients are also presented. Analysis of this data is used to reach a conclusion on the dominant source of dark current in a-Se sandwich structures.

Chapter 5 focuses on the results of computer simulations modeling the dark current in a-Se sandwich structures. The results and challenges of using different simulation methods including Monte Carlo, modified Monte Carlo and numerical modalities are discussed. Simulation results are compared with experimental results to calibrate and validate the models.

Chapter 6 includes the results of Monte Carlo computer modeling of the x-ray sensitivity of multilayer a-Se structures, focusing on the effects of the blocking layers and the dark current on the x-ray sensitivity. Experimental results are presented and compared against the results of the theoretical model.

Chapter 7 contains the conclusions drawn from the work presented throughout the preceding chapters and suggestions for future work on the topics discussed.

## 2. METRICS OF X-RAY IMAGE DETECTOR PERFORMANCE

There are several metrics used to describe and compare the performance of x-ray image detection systems. Important characteristics of x-ray image detectors include the sensitivity of the detector to the x-ray radiation used, to allow for the lowest possible dose of radiation to a patient, and the image resolution that the detector is capable of producing, so that fine details can be observed. Furthermore, digital, direct conversion detectors have unique issues that do not arise in analog, film based detection systems. These issues include a dark current which creates a higher baseline of detectable signal and x-ray fatigue effects in the photoconductive layer due to repeated use of the detector. This chapter discusses the most important metrics used in diagnostic radiography and, specifically, digital, direct conversion detectors. While the parameters featured here can be applied to any digital x-ray image detector, specific examples and values will be included for a-Se based flat panel detectors, as these are the focus of this thesis.

### 2.1 X-ray Sensitivity

One of the most important metrics of any x-ray detection system is its sensitivity to x-ray photons,  $S_x$ , in the energy range of interest. The higher the sensitivity of the detector, the lower the dose needed to acquire an acceptable image and, hence, a lower dose is received by the patient. X-ray sensitivity is defined as the collected charge per unit area per unit exposure of radiation:

$$S_x = \frac{Q}{AX} \quad (2.1)$$

where  $Q$  is the collected charge in Coulomb (C),  $A$  is the radiation receiving area in  $\text{cm}^2$  and  $X$  is the radiation exposure in Roentgen (R), making the units of sensitivity  $\text{C cm}^{-2} \text{R}^{-1}$  [64,65]. One Roentgen is the quantity of radiation that creates a total free charge of  $2.58 \times 10^{-4}$  C per kg of air [1].

The sensitivity of a detector is almost entirely determined by the photoconductive layer of a direct conversion, flat panel detector and the sensitivity of the photoconductive layer is governed by three distinct processes [64]. First is the attenuation of the x-rays in the photoconductor and the absorption of the radiation energy per attenuated photon. The second process is the conversion of absorbed radiation to electron-hole pairs. The third process is the collection of the photogenerated charge carriers. These three factors will be discussed in detail separately and then brought back together to discuss the overall effect of each on the x-ray sensitivity at the end of the section.

### 2.1.1 X-ray Interactions in the Photoconductive Layer

When discussing the x-ray sensitivity of a detector, one must consider that only a portion of the x-ray photons which are incident on the detector surface will actually be attenuated by the photoconductive layer [63]. Furthermore, only some of those attenuated photons will deposit energy in the layer. The fraction of x-ray photons that are attenuated is called the quantum efficiency,  $\eta$  (commonly abbreviated QE), and depends on the linear attenuation coefficient of the photoconductor,  $\alpha$ , and the photoconductor thickness,  $L$ , as

$$\eta = 1 - \exp(-\alpha L) \quad (2.2)$$

so that the beam penetrating the photoconductive layer is given by

$$\Phi = \Phi_0 \exp(-\alpha L) \quad (2.3)$$

where  $\Phi_0$  is the incident photon fluence [1].  $\alpha$  depends on the atomic number,  $Z$ , of the photoconductor and the energy of radiation,  $E_{ph}$ , as  $Z^3/E_{ph}^3$  [1], so high  $Z$  photoconductors are desirable. The attenuation depth,  $\delta$ , is  $1/\alpha$ , and is the distance into the photoconductive layer at which the intensity of the incident beam is reduced by 63% [65].

Also commonly used is the mass attenuation coefficient,  $\alpha/\rho$ , which is obtained by dividing  $\alpha$  by the density,  $\rho$ , of the medium [1]. Both the linear and mass attenuation coefficients

refer to the total attenuation of radiation, but not necessarily to the energy absorbed. For this, the energy absorption coefficient,  $\alpha_{en}$ , is used and is defined as

$$\alpha_{en} = \alpha \frac{E_a}{E_{ph}} \quad (2.4)$$

where  $E_a$  is the average energy absorbed per photon interaction and  $E_{ph}$  is the photon energy. Similarly, one can define a mass energy absorption coefficient,  $\alpha_{en}/\rho$  [1].

Several possible processes can occur once an incident photon enters the photoconductive layer and the attenuation coefficient is actually comprised of several coefficients, one for each process:

$$\alpha = \omega + \tau + \sigma + \kappa + \pi \quad (2.5)$$

where the coefficients represent attenuation by coherent (Rayleigh) scattering ( $\omega$ ), photoelectric absorption ( $\tau$ ), Compton scattering ( $\sigma$ ), pair production ( $\kappa$ ) and photodisintegration ( $\pi$ ) [1]. Pair production and photodisintegration only occur at energies greater than 1.02 MeV, far greater than those used in diagnostic imaging (16 – 140 keV) [1,7]. Therefore, one must only be concerned with  $\omega$ ,  $\tau$  and  $\sigma$ . The contribution from each process can be seen in Fig. 2.1 when the attenuating medium is air. Fig. 2.2 shows the mass attenuation and mass absorption coefficients, and their important components, for a-Se in the energy range of diagnostic x-ray imaging.

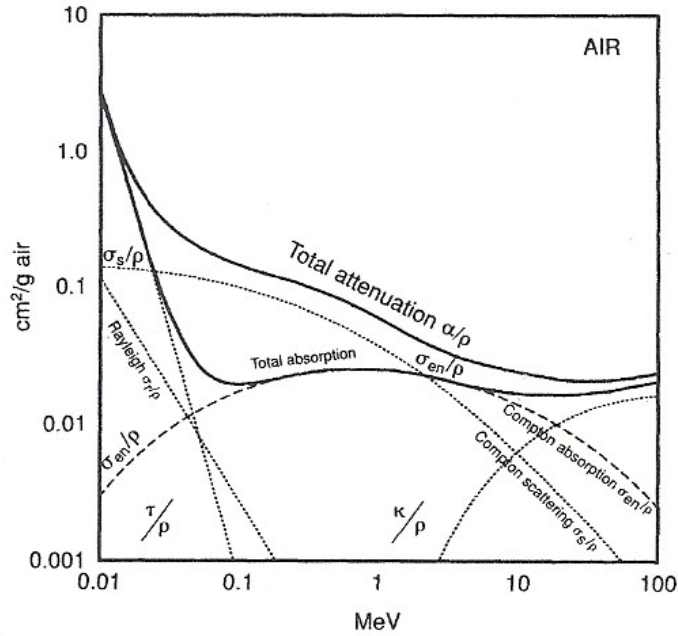


Figure 2.1 Mass attenuation and absorption coefficients for photons with energies from 10 keV to 100 MeV in air. The total absorption curve is the sum of Compton absorption, photoelectric absorption and pair production; after [1].

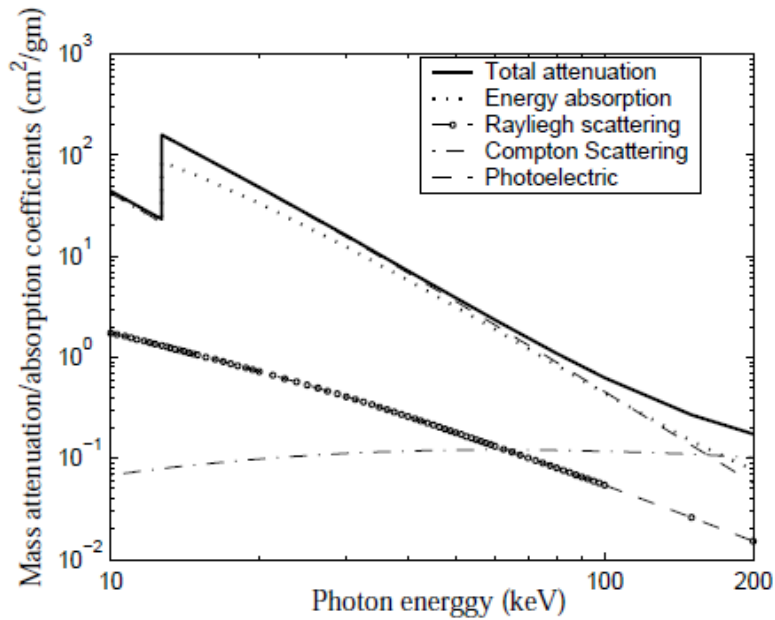


Figure 2.2 Plot of the total attenuation, energy absorption, Rayleigh scattering, Compton scattering and photoelectric absorption coefficients for a-Se for photon energies of 10 – 200 keV; after [63,66].

### 2.1.1.1 Rayleigh Scattering

Rayleigh scattering is coherent (or elastic) scattering where the incident photon is scattered by an atomic electron, but no energy is imparted to the particle; only the trajectory of the photon is changed, as shown in Fig. 2.3 (a) [1]. This can cause problems with image blurring, as the scattered x-rays will also be detected.

### 2.1.1.2 Compton Scattering

Compton scattering is incoherent (or inelastic) scattering and can occur when a photon has energy greater than the binding energy of the atomic electron it interacts with. The electron is ejected from an outer shell, resulting in an ionized atom, as seen in Fig. 2.3 (b). The x-ray's trajectory is altered, the angle of the change depending on the amount of energy imparted to the electron [1].

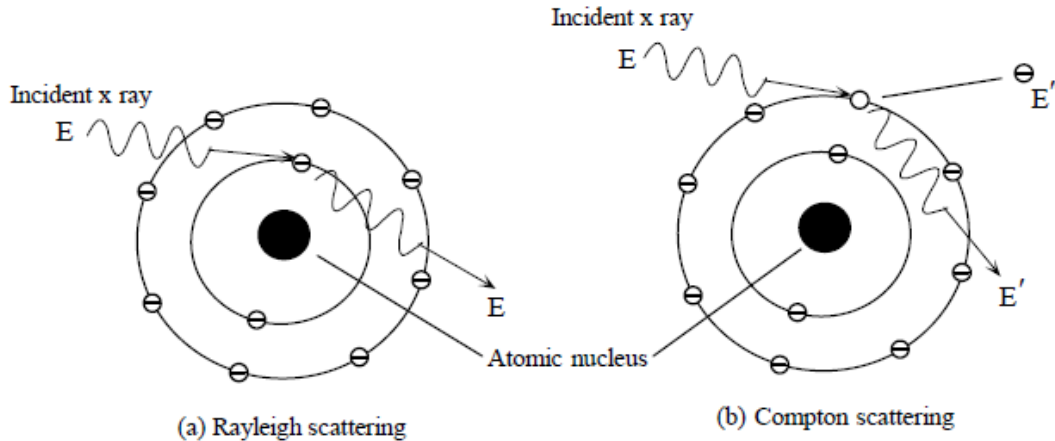


**Figure 2.3 Schematic illustration of (a) Rayleigh scattering and (b) Compton scattering. In Rayleigh scattering, the trajectory of the photon is altered but the atom does not change. In Compton scattering, the trajectory of the photon is altered and its energy is reduced from  $E$  to  $E'$  as an outer shell electron is ejected with kinetic energy  $E''$ ; after [63,67].**

### 2.1.1.3 Photoelectric Absorption

In photoelectric absorption, the incident photon imparts all of its energy to an atomic electron, ejecting it from its shell [1,63]. The kinetic energy of the excited electron is the difference between the photon's initial energy and the binding energy of the electron, assuming that the photon's energy is the greater of the two. Electrons in an inner shell are more tightly bound than outer shell electrons and, hence, have a greater binding energy. The innermost shell, K, will have an associated bonding energy referred to as the "K edge" and so too for the other shells: L, M, *etc.* As seen in Fig. 2.4, in the case of an excited innermost shell electron, outer shell electrons can transition to fill the remaining hole, producing one or more characteristic (or fluorescent) x-rays. The excess energy can also be imparted to another electron in the atom, ejecting it. This is called an Auger electron [1].

The energetic electron ejected from the photoconductor atom travels through the photoconductive layer, imparting energy to atoms, ionizing them and creating many EHPs along its track [65]. The energetic electron can also interact with the nucleus of another atom, partially orbiting it, decelerating in the process and creating bremsstrahlung (or breaking) radiation [63]. This breaking radiation and characteristic photons can also cause blurring of the image due to reabsorption in the photoconductive layer over adjacent pixels.

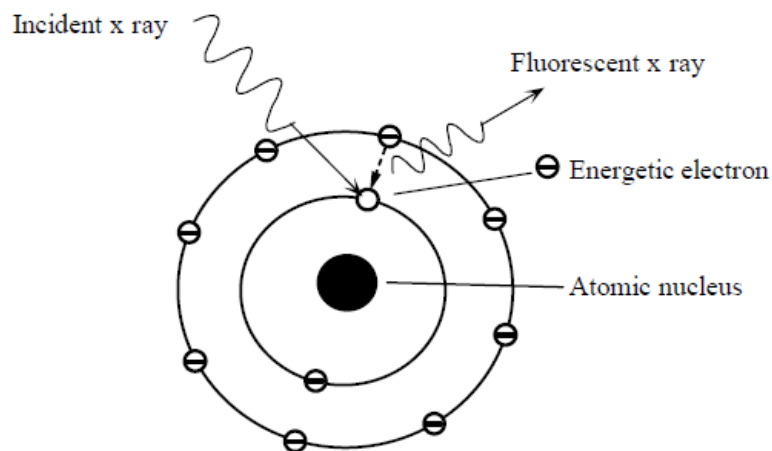


**Figure 2.4 A schematic illustration of photoelectric absorption. The incident x-ray imparts all of its energy to an inner shell electron, ejecting it. An outer shell electron transitions down to fill the created vacancy, releasing a fluorescent x-ray photon; after [63].**

## 2.1.2 Photogeneration of Charge Carriers

Once the energy of an incident photon is absorbed photoelectrically, the energetic primary electron travels through the photoconductor creating ionization. This conversion process is the second factor which can affect the x-ray sensitivity. The energy required to create a single free EHP is denoted as  $W_{\pm}$ . Many semiconductors (*e.g.* crystalline Si) have a value of  $W_{\pm}$  which depends on the Klein rule [68,69],

$$W_{\pm} \approx 2.8E_g + E_{phonon} \quad (2.6)$$

where  $E_g$  is the bandgap of the semiconductor and the phonon energy term is small ( $\sim 0.5$  eV). In many crystalline semiconductors,  $W_{\pm}$  is field independent and very well defined. Que and Rowlands [70] have argued that if one relaxes the conservation of  $k$  rule as required for amorphous semiconductors, then  $W_{\pm}$  is given by a slightly modified relation:

$$W_{\pm} \approx 2.2E_g + E_{phonon} \quad (2.7)$$

For example, a-Si:H and PbI<sub>2</sub> seem to follow this modified rule [39]. Unfortunately, due to the scatter in experimental data, it is difficult to confine a-Se to one model or the other. In a-Se, as with other low mobility solids,  $W_{\pm}$  has a strong dependence on the applied field. This has been demonstrated in work by Kasap *et al.* [71] which has shown that the lowest, or saturated  $W_{\pm}$ ,  $W_{\pm}^0$ , can be estimated by extrapolation to very high fields and is 5 – 6 eV, which actually does not discriminate against either of the models given by Eqs. 2.6 and 2.7.

The exact reason for the field dependence of  $W_{\pm}$  is still debated. If we assume none of the created EHPs are lost to trapping, then there are three sources of possible carrier loss: bulk recombination between drifting holes and electrons, geminate recombination and columnar recombination [65]. The recombination rate for bulk recombination is proportional to both the hole and electron concentrations so that the collected charge has a square root dependence on

radiation intensity. This rules out the process of bulk recombination, as experiments have shown that the collected charge actually has a linear dependence on radiation intensity [60].

The remaining possible processes are then geminate or columnar recombination. Geminate recombination involves the recombination of an electron and hole generated at the same time due to their coulombic attraction to one another. It is governed by the Onsager model for recombination which essentially calculates the probability that an EHP will diffuse apart for a given electric field and temperature [72]. Columnar recombination involves the recombination of non-geminate electrons and holes in the columnar track of the primary electron [73]. Both of the theories predict a linear dependence on radiation intensity, as experimentally observed. Electron-bombardment-induced transient conductivity measurements by Hirsch and Jahankhani [74] give results supporting the columnar theory as does the general lack of temperature dependence of  $W_{\pm}$  over the range of 263 – 300 K [60]. However, it has been argued that geminate recombination is the governing process at higher radiation energies [75].

Further complicating the situation is an unclear dependence of  $W_{\pm}$  on radiation energy. Theoretical treatments have shown that  $W_{\pm}$  should decrease with increasing photon energy [76]. The work by Kasap mentioned above [71] has shown that  $W_{\pm}$  has very little dependence on photon energy while earlier work by Rowlands *et al.* has shown virtually no energy dependence [77] and yet other work by Blevis *et al.* has shown what is described as a clear energy dependence [78]. The pulse height spectroscopy method used by Blevis yielded the results for the electric field and mean x-ray energy dependence of  $W_{\pm}$  shown in Fig. 2.5. Given the contradictory results of these separate works, it is clear that more systematic measurements are needed over wider ranges of energies, fields and temperatures.

For diagnostic radiography, the following rule has been applied to  $W_{\pm}$  for a-Se [60,79]:

$$W_{\pm} = W_{\pm}^0 + \frac{B}{F^n} \quad (2.8)$$

where  $B$  is a constant that weakly depends on photon energy,  $F$  is the applied field and  $n$  is between 0.7 and 1. In the 20 – 40 keV range, if  $W_{\pm}^0$  is taken to be 6 eV and  $B$  to be  $4.4 \times 10^2$  eV V/ $\mu$ m, then  $W_{\pm}$  is roughly 50 eV at 10 V/ $\mu$ m in a-Se.

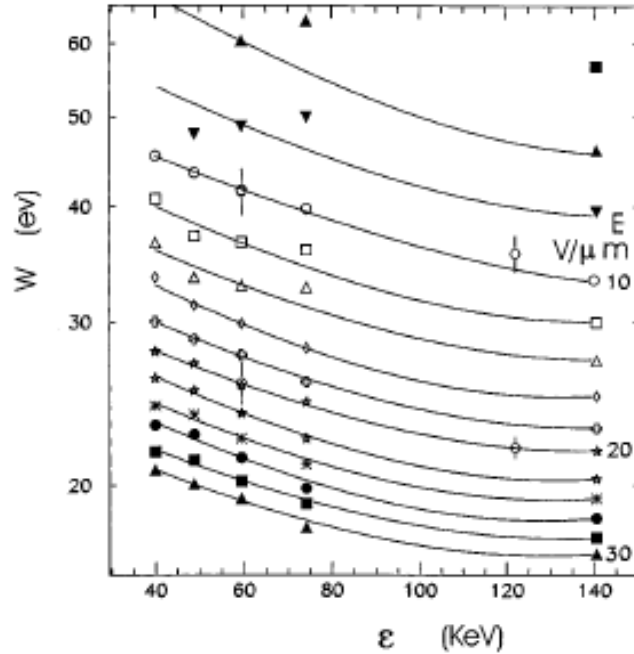


**Figure 2.5** The charted dependence of  $W_{\pm}$  in a-Se on the applied electric field and mean x-ray photon energy,  $\varepsilon$ ; after [78]. The data was gathered through pulse height spectroscopy and the constant field lines were drawn with a quadratic interpolation.

### 2.1.3 Collection of Photogenerated Charge Carriers

The third and final factor that can reduce the x-ray sensitivity of a detector is that less than 100 % of created EHPs may be collected by the electrodes on either side of the photoconductive layer. The charge collection efficiency,  $\eta_{CC}$  (commonly abbreviated CCE), of the photoconductive layer is the fraction of photogenerated charge carriers which are actually collected [65]. A large electric field is applied across the photoconductive layer to drift the carriers but they can still be deeply trapped in a localized state from which the release time is longer than the inter-frame time. The mean distance a carrier drifts before it is trapped is called the schubweg [65] and is given by  $\mu\tau F$  where  $\mu$  is the carrier drift mobility,  $\tau$  is the mean carrier lifetime and  $F$  is the applied field. To ensure the trapping of drifting carriers is negligible, it is important that the schubweg of both types of carriers be much greater than the photoconductive

layer thickness,  $L$ , so that  $\mu\tau F \gg L$ . This can be achieved by ensuring good carrier transport (high  $\mu\tau$  product or carrier range) and applying a large electric field [65].

The effect of carrier trapping on x-ray sensitivity becomes quite complicated when the bottom electrode is pixellated, as in a flat panel detector. As shown in Fig. 2.6, carriers trapped above a central pixel,  $C$ , will induce charges on neighbouring pixels,  $L$  and  $R$ . An analysis using the Shockley-Ramo theorem [80,81] shows that as the pixel size becomes smaller with respect to the photoconductor thickness, the sensitivity becomes much more sensitive to the trapping of the carrier drifting towards the bottom, pixellated electrode (holes in the case of Fig. 2.6). However, the sensitivity also becomes less sensitive to trapping of the carrier drifting in the other direction (electrons in Fig. 2.6). Therefore, it is imperative that if the transport of one carrier must be sacrificed to improve the transport of the other, it should be ensured that the carrier which drifts towards the pixellated electrode has the longer schubweg. It is important to note that a-Se detectors have been shown to have negligible pixel-to-pixel sensitivity variation [64].

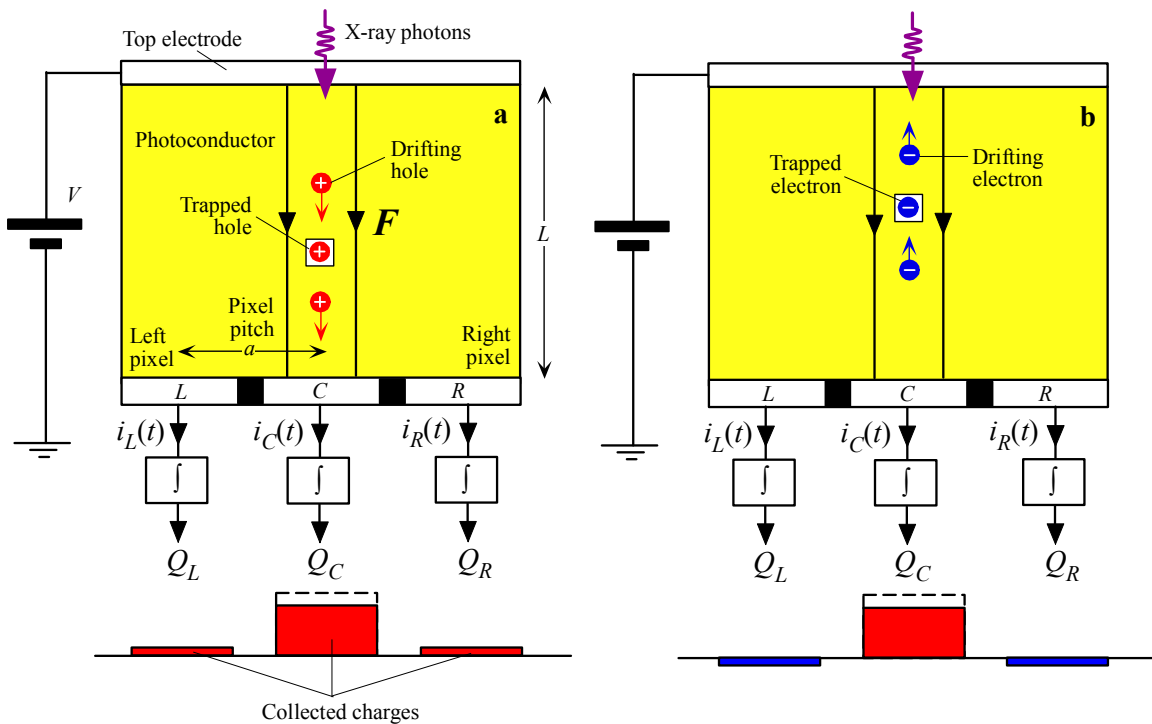


**Figure 2.6** The effects of charge trapping on the x-ray sensitivity and resolution depends on the type of carriers that have been trapped; whether carriers were drifting to the top or bottom electrode.  $C$  is the central (reference) pixel and  $L$  and  $R$  are the neighbouring left and right pixels. The transient currents flowing into the pixels are integrated and eventually yield the collected charges at the pixels. In the case of this positively biased detector, trapped holes have a greater effect on x-ray

sensitivity than trapped electrons and tend to decrease resolution while trapped electrons actually improve resolution.

Related to poor charge collection efficiency is a phenomenon known as image lag [63,65]. Image lag is the carry over of image charge generated by previous exposures and results in dark images, *i.e.*, increased pixel values at previously exposed areas, when there is no current exposure, as shown in Fig. 2.7. Image lag is due to trapping of photogenerated charge carriers during transit and the creation of deep carrier traps by radiation exposure (especially in the case of large doses) [82]. The occurrence of image lag is a sign of low carrier mobilities. In a-Se detectors, the image lag is under 2% after 33 ms and less than 1% after 0.5 s in the fluoroscopic mode of operation [83] and is considered as negligible.

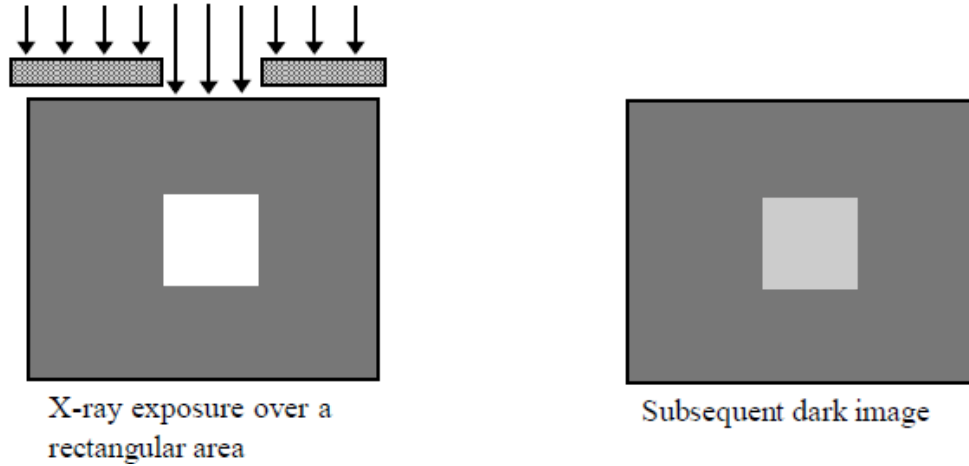


**Figure 2.7** Explanation of image lag. Charge generated during the initial x-ray exposure is trapped in the photoconductive layer, inducing charges on the pixels underneath that area, even after exposure. This is called a dark image; after [63].

#### 2.1.4 X-ray Sensitivity Revisited

As discussed,  $\alpha/\rho$ ,  $W_{\pm}$  and  $\eta_{CC}$  all contribute to x-ray sensitivity, the exact relationship is given in Eq. 2.9 [13]:

$$S_x = \left( \frac{5.45 \times 10^{13} e}{E_{ph} (\alpha_{en} / \rho)_{air}} \right) \times \eta \times \left( \frac{(\alpha_{en} / \alpha) E_{ph}}{W_{\pm}} \right) \times \eta_{CC} \quad (2.9)$$

where the first term gives the charge corresponding to the incident photon fluence per unit Roentgen ( $(\alpha_{en}/\rho)_{air}$  is the energy absorption coefficient for air), the second term is the quantum efficiency, the third term is the number of EHPs created per absorbed radiation energy and the fourth term is the charge collection efficiency. For most semiconductors, only the final term,  $\eta_{CC}$ , depends on the applied field, but for a-Se, the third term also has a field dependence due to the field dependence of  $W_{\pm}$  in a-Se, as discussed in Section 2.1.2.

Computer modeling of the x-ray sensitivity of photoconductive layers often uses a form of x-ray sensitivity called normalized sensitivity,  $s_x = S_x/S_0$  where  $S_0$  is the maximum sensitivity possible if all incident radiation is absorbed ( $\eta = 1$ ) and all created EHPs are collected ( $\eta_{CC} = 1$ ) and is given by [64]

$$S_0 = \left( \frac{5.45 \times 10^{13} e}{(\alpha_{en}/\rho)_{air} W_{\pm}} \right) \times \left( \frac{\alpha_{en}}{\alpha} \right) \quad (2.10)$$

If  $\eta_{CC}$  is not unity, then one must express  $s_x$  as

$$s_x = \frac{S_x}{S_0} = \frac{Q_{coll}}{Q_0} \quad (2.11)$$

where  $Q_{coll}$  is the charge that is actually collected while  $Q_0$  is the maximum collectable charge that is photogenerated and is given by

$$Q_0 = \frac{5.45 \times 10^{13} eAX}{W_{\pm_0} (\alpha_{en}/\rho)_{air}} \left( \frac{\alpha_{en}}{\alpha} \right) \quad (2.12)$$

where  $A$  is the area of exposure,  $X$  is the x-ray exposure in R and  $W_{\pm_0}$  is the EHP creation energy at the uniform applied field (not to be confused with  $W_{\pm}^0$ , the saturated EHP creation energy discussed in Section 2.1.2).

If  $\eta$  is not unity, then  $s_x$  is given by

$$s_x = \frac{S_x}{S_0} = \frac{Q_{coll}}{Q_{gen}^0} \times \eta \quad (2.13)$$

where  $Q_{gen}^0$  is the photogenerated charge when the field inside the photoconductive layer is uniform, or  $Q_0 \times \eta$ . However, if the field distribution across the photoconductor is not uniform, due to trapped charge carriers inside the photoconductor, then

$$s_x = \frac{S_x}{S_0} = \frac{Q_{gen}}{Q_{gen}^0} \times \frac{Q_{coll}}{Q_{gen}} \times \eta = PGR \times CCE \times QE \quad (2.14)$$

where  $Q_{gen}$  is the charge generated when the field inside the photoconductor is not uniform. The  $Q_{gen}/Q_{gen}^0$  term is called the photogeneration ratio (PGR) and can be calculated as follows:

$$PGR = \frac{\int_0^L \frac{\exp(-\alpha x)}{W_{\pm}(x)} dx}{\int_0^L \frac{\exp(-\alpha x)}{W_{\pm_0}} dx} = \frac{\alpha}{\eta} \int_0^L \frac{W_{\pm_0}}{W_{\pm}(x)} \exp(-\alpha x) dx \quad (2.15)$$

Equation 2.15 will clearly yield unity if  $W_{\pm}$  is equal to  $W_{\pm_0}$  throughout the photoconductor and as  $W_{\pm}(x)$  depends on the field at  $x$ , this implies the uniform field condition.

Computer simulations of  $s_x$  often calculate the factors PGR, CCE and QE separately and then combine them to determine the normalized sensitivity as shown in Eq. 2.14 [2].

### 2.1.5 Ghosting

An important problem that arises in digital radiography system operation is a change in the x-ray sensitivity of a detector in a subsequent exposure as the result of accumulated previous exposures [84]. This problem is known as ghosting and is explained in Fig. 2.8.

Ghosting is usually the result of a reduction in sensitivity. An exposure leaves an area of the detector with a lower sensitivity than the rest of the detector. A subsequent exposure, which involves a larger area than the first, produces an image which contains a “ghost” of the first image, as the sensitivity of the detector in the area of the first exposure has been reduced. The study of ghosting is an ongoing process, as the exact origins of ghosting are not fully understood [61,84-86]. A good example of ghosting can be seen in Fig. 2.9. It has been shown that ghosting is not significant in the clinical dose range but it becomes a large problem at higher doses [84].

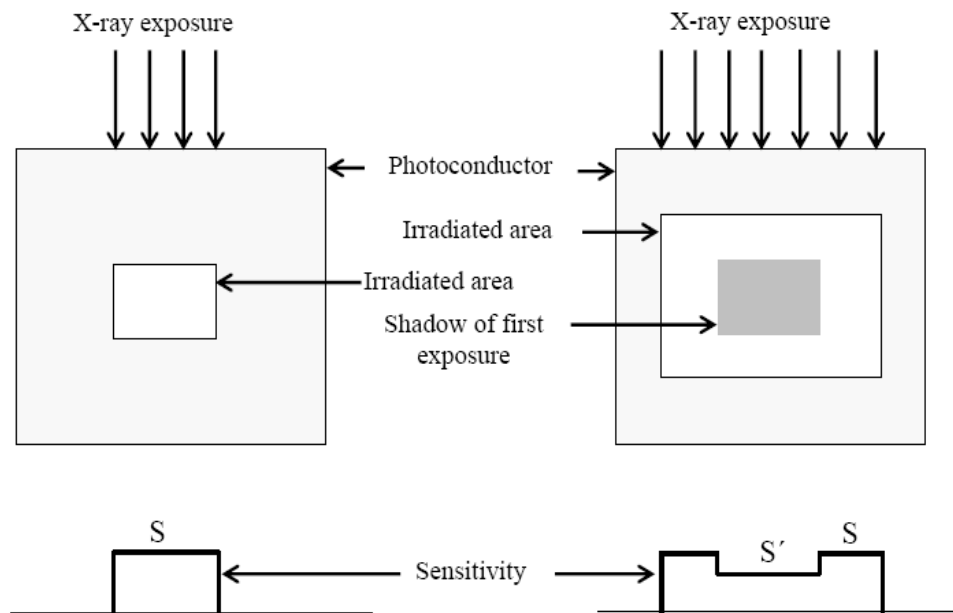


**Figure 2.8** Appearance of a “ghost” image in a subsequent exposure as the area of the previous exposure has reduced sensitivity,  $S'$ ; after [2].

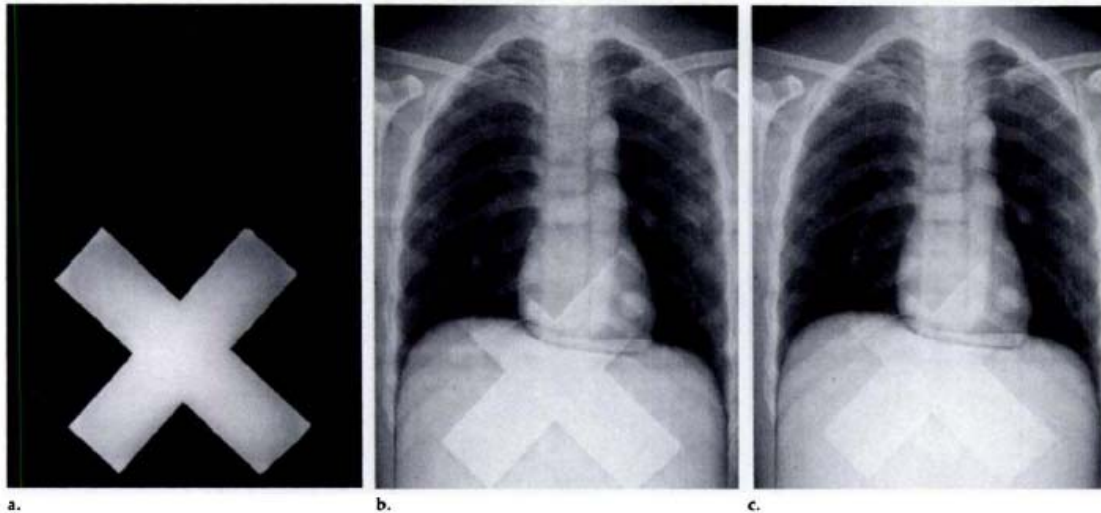


**Figure 2.9** The initial image (a) is of a lead “X” shaped object. Images (b) and (c) are taken 1 and 2 minutes after image (a) respectively. The “ghost” of image (a) is clearly visible in images (b) and (c); after [87].

### 2.1.6 Modeling of X-ray Sensitivity in Amorphous Selenium

Prior to 2008, work was done to model the change in x-ray sensitivity with cumulative exposure, which is believed to lead to ghosting, using Monte Carlo (MC) simulations [2,61] and numerical calculations which solve partial differential equations using the backward Euler finite difference method [62,63]. The results of these models have shown good agreement with experimental data measuring the decrease in sensitivity with exposure, as shown in Fig. 2.10 for a 1 mm thick a-Se detector at a photon energy of 55 keV, by considering the following factors: deep trapping of carriers, recombination between trapped and drifting carriers, trap filling effects, non-uniform electric field effects, effects of x-ray induced deep trap generation and release of trapped carriers.

These models assume a uniform photoconductive layer and did not account for the altered properties of the blocking layers used to reduce dark current as discussed in Sections 1.4 and 2.6. However, work done concurrently with research presented in this thesis by Kabir *et al.* [59,82] used numerical calculations to model the change in sensitivity with cumulative exposure for multilayer samples containing *n*- and *p*-type blocking layers and found good agreement with experimental data. As can be seen in Fig. 2.11, it was shown that a multilayer structure achieves

lower sensitivity than the modeled single layers. This model was also based on the factors listed above. Similar work, using MC simulations, will be presented in Chapter 6 of this thesis.

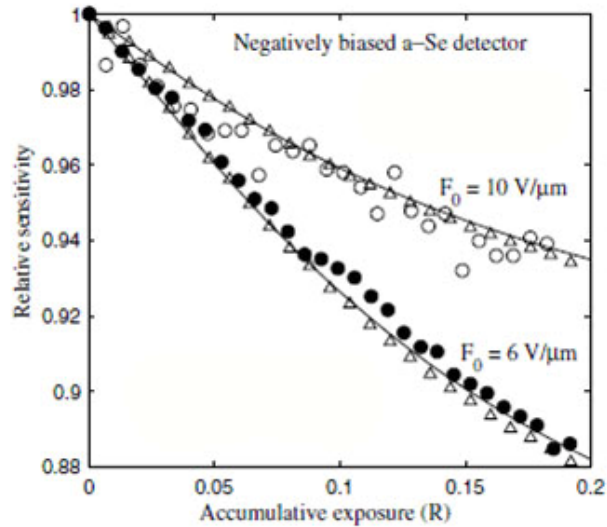


Figure 2.10 Monte Carlo and numerical simulation and experimental results for relative sensitivity vs. cumulative x-ray exposure at applied fields of 6 and 10 V/μm. Experimental data is shown as circles, Monte Carlo simulation results as triangles and numerical calculations as the solid lines; after [62].

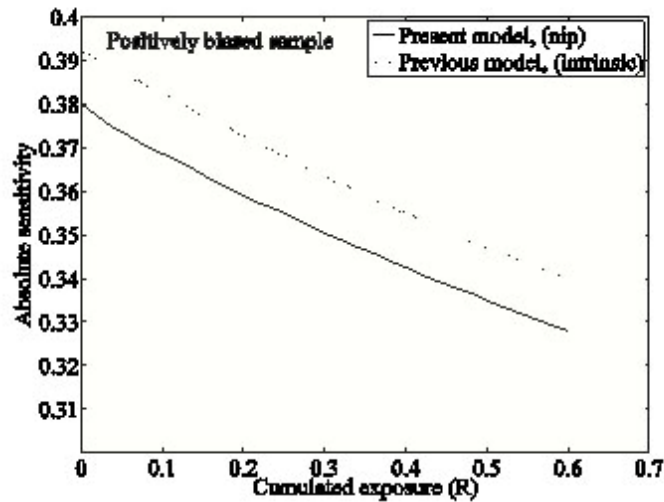
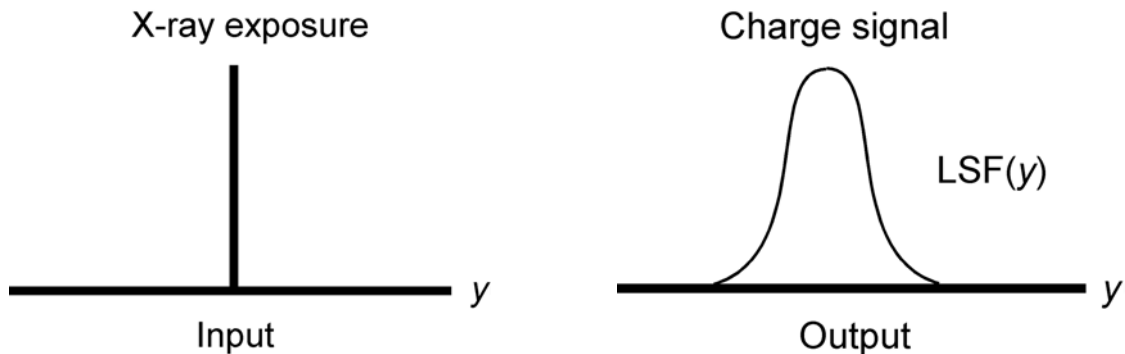


Figure 2.11 Normalized x-ray sensitivity vs. cumulative exposure for both a single layer a-Se sample and an *n-i-p* multilayer sample. The model shows that multilayer samples have a lower overall sensitivity but experience a very similar decrease in sensitivity with cumulative exposure; after [59].

## 2.2 Image Resolution

Resolution, or the resolving power of the detector, is the ability to record separate images of small objects that are placed very closely together [64]. Each component of an imaging system will affect the resolution of the system by spreading (blurring) or compressing the recorded image. This can be demonstrated in the response of a system to a delta function, called the point spread function (PSF) [63]. In practice, this is usually replaced with what is called the line spread function (LSF), as shown in Fig. 2.12.



**Figure 2.12** The x-ray incidence is a narrow line (a delta function in the  $y$  direction). The resultant charge signal is spread out in the  $y$  direction, representing the LSF; redrawn from [63].

The overall response of the system can be determined by a convolution of the LSF of each component of the system. However, this convolution can be replaced by a simpler multiplication operation if one works in the domain of spatial frequencies, just as convolutions in the time domain are equivalent to multiplications in the frequency domain when working with signal processing [88]. For this reason the modulation transfer function (MTF) has become the standard for describing and comparing the resolution of imaging systems. The MTF is the two dimensional Fourier transform of the PSF or, as is more commonly used, the one dimensional Fourier transform of the LSF.  $MTF(f)$  describes the ability of a detector to resolve an image as a function of spatial frequency [11]. A clear explanation of the MTF is given by Fig. 2.13. In the spatial frequency domain, a cycle of light and dark bars is called a line pair (lp), the number of which occurring in a specific distance (typically 1 mm) is the spatial frequency. It can be seen in the example in Fig. 2.13 that at 1 lp/mm (A) the system is able to 100% resolve the image, but at

2 lp/mm (B), the MTF has decreased and at 4 lp/mm (C), the MTF is 0% and the information in the image is completely lost.

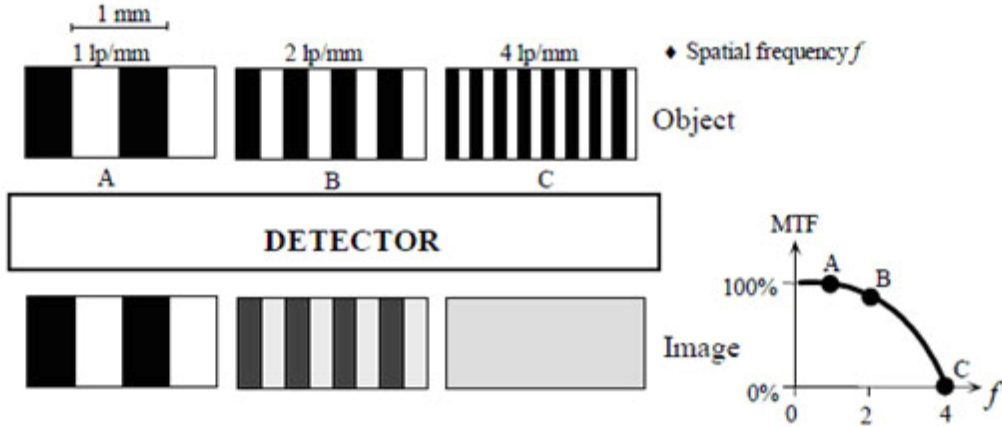


Figure 2.13 The MTF of this example detector is 100% at A, slightly lower at B and 0% at C. This detector can resolve images at 1 lp/mm, but not at 4 lp/mm. The inset at the lower right shows the MTF plotted as a function of spatial frequency,  $f$ ; after [89].

The presampling MTF of a detector can be expressed as

$$MTF(f) = MTF_m(f) \times MTF_a(f) \quad (2.16)$$

where  $MTF_m(f)$  is the MTF due to the photoconductive layer while  $MTF_a(f)$  is the MTF associated with the aperture function of the pixel electrodes [11]. If square pixels are assumed, as shown in Fig. 2.14 (a), the pixel aperture width is  $d$ , while the pixel pitch (center to center distance) is  $a$ . The active portion of the pixels determines  $MTF_a(f)$ , so that for square pixels,

$$MTF_a(f) = |Sinc(df)| = \left| \frac{\sin(\pi df)}{\pi df} \right| \quad (2.17)$$

which is plotted in Fig. 2.14 (b) where the first zero of the sinc function occurs at a spatial frequency of  $1/d$  [63].

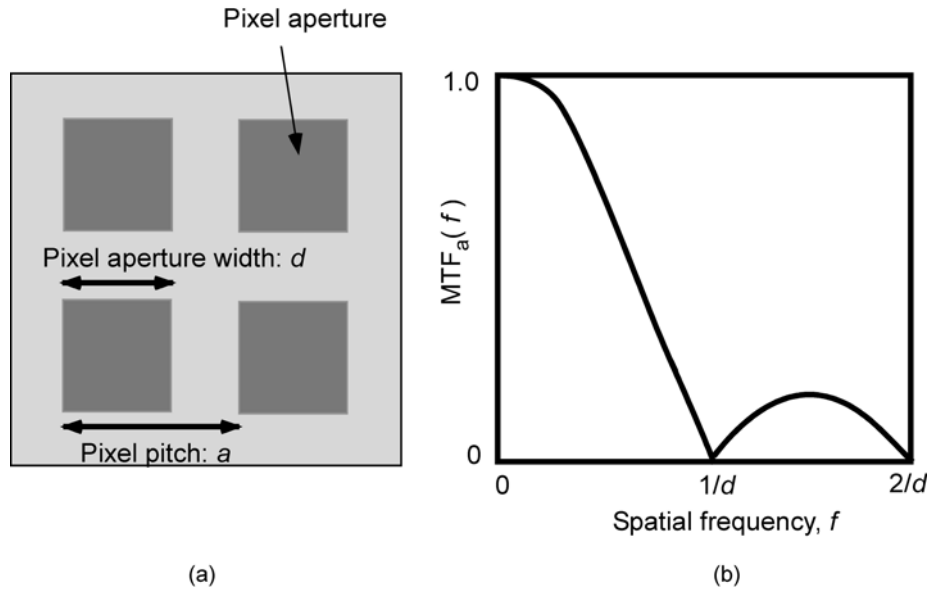


**Figure 2.14 (a) definition of pixel aperture width,  $d$ , and pixel pitch,  $a$ . (b) plot of  $MTF_a(f)$  vs. spatial frequency,  $f$ , where the first zero occurs at  $1/d$ ; redrawn from [63].**

The highest spatial frequency that can be imaged without aliasing (the misinterpretation of higher frequencies as lower frequencies [88]) is called the Nyquist frequency,  $f_{ny}$ , and is determined by  $a$ :

$$f_{ny} = \frac{1}{2a} \quad (2.18)$$

so that aliasing will occur for spatial frequencies between  $1/2a$  and  $1/d$  [63].

One might notice from Fig. 2.14 that  $d < a$  so that not all of the detector area is useful in absorbing radiation. The percentage of the total detector area that is useful is represented by the fill factor (FF). For direct conversion FPXIs, the FF is 75 – 85% but the effective FF is nearly 100% because the electric field in the “dead zones” bends towards the pixel electrodes allowing for almost all of the photogenerated charge carriers to be collected [11,24].

The MTF associated with the photoconductive layer,  $MTF_m(f)$ , represents the loss of spatial resolution due to the reabsorption of K-fluorescent x-ray photons and trapping of photogenerated charge carriers [81]. Direct conversion FPXIs have much higher  $MTF_m(f)$  than

indirect detectors [64]. a-Se based detectors have an excellent MTF, almost equal to  $MTF_a(f)$  as shown in Fig. 2.15 for two detectors with different pixel sizes [90]. Explanations for these impressive MTF values come from Monte Carlo simulations of the photoionization process in a-Se [91], which have shown that even for a photon with an energy as high as 140 keV, all of the EHPs are created in a volume of a-Se only  $8 \times 8 \times 8 \mu\text{m}^3$ , much smaller than typical pixel dimensions. Furthermore, the lateral diffusion of photogenerated carriers drifting towards their respective collection electrodes can be considered as negligible for a-Se FPXIs [92,93].

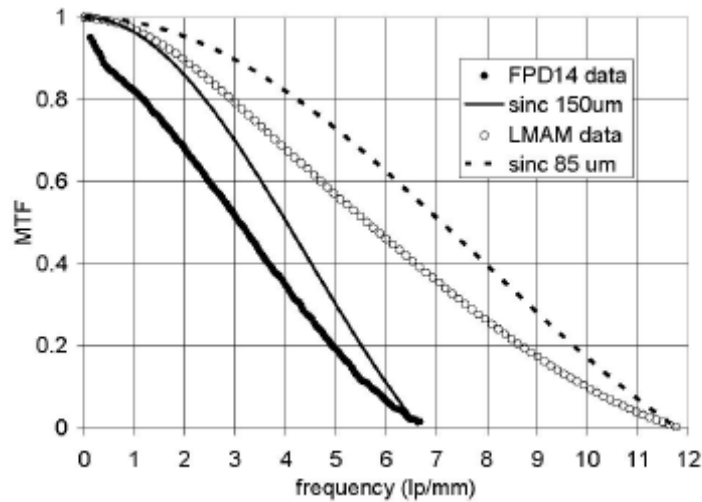


**Figure 2.15** The MTF of two detectors manufactured by Anrad: a mammographic detector with 85  $\mu\text{m}$  pixels and a fluoroscopic detector with 150  $\mu\text{m}$  pixels. The measured MTF of each detector is very close to the  $MTF_a$  for the respective pixel size; after [90].

The effect of charge carrier deep trapping during transit in a direct conversion FPXI can actually be rather complicated and is described in Fig. 2.6. The charge built up on neighbouring pixels,  $L$ ,  $C$  and  $R$  is due to the integration of the photogenerated currents,  $i_L(t)$ ,  $i_C(t)$  and  $i_R(t)$ , respectively. If holes generated above  $C$  which are drifting towards the pixellated electrode are trapped during transit, the charge built up on pixels  $L$  and  $R$  is of the same sign as that on  $C$ , causing a spreading of the image information. However, if an electron generated above  $C$  drifting to the top electrode is trapped, the charge induced on  $L$  and  $R$  is of the opposite sign, causing compression, or squeezing of the information towards  $C$ , actually improving the MTF at high spatial frequencies [81,94,95].

## 2.3 Noise Power Spectrum

The noise power spectrum (NPS) is the Fourier transform of the covariance of a random process and is the power of the noise signal present in a certain spatial frequency interval [63]. X-ray images are a distribution of quanta and the uniform distribution of x-rays coming from an x-ray tube is uncorrelated so that the  $NPS = \overline{\Phi}_0$ , where  $\overline{\Phi}_0$  is the mean incident x-ray fluence. As these uncorrelated photons are incident on a detector, they create secondary quanta (charge carriers for direct conversion detectors and visible photons for indirect conversion detectors) which may have a correlated component [63].

Direct conversion detectors have a relatively “white” (independent of spatial frequency) NPS due to minimal blurring in the photoconductive layer and aliasing of frequencies above  $f_{ny}$ . Indirect detectors have an NPS which decreases considerably with increasing spatial frequency due to presampling blurring in the phosphor layer [11].

## 2.4 Detective Quantum Efficiency

Detective Quantum Efficiency (DQE) is the most commonly compared metric of imaging systems. DQE is the ability of a detector to transfer signal relative to noise from its input to its output and is unity for an ideal detector [96].  $DQE(f)$  represents the signal-to-noise ratio (SNR) transfer efficiency as a function of spatial frequency through various stages of an imaging system as

$$DQE(f) = \frac{SNR_{out}^2(f)}{SNR_{in}^2(f)} \quad (2.19)$$

where  $SNR_{in}$  and  $SNR_{out}$  are the signal-to-noise ratios at the input and output of the detector, respectively [64]. Figure 2.16 shows the measured  $DQE(f)$  of a mammographic a-Se detector as a function of spatial frequency. Good DQE is preserved over a range of doses much lower than the normal mammographic dose; this detector was operating in tomosynthesis mode (the three dimensional reconstruction of an object using several x-ray images taken at different angles),

showing good DQE for this application. An example of an image taken by tomosynthesis from this detector can be seen in Fig. 2.17.

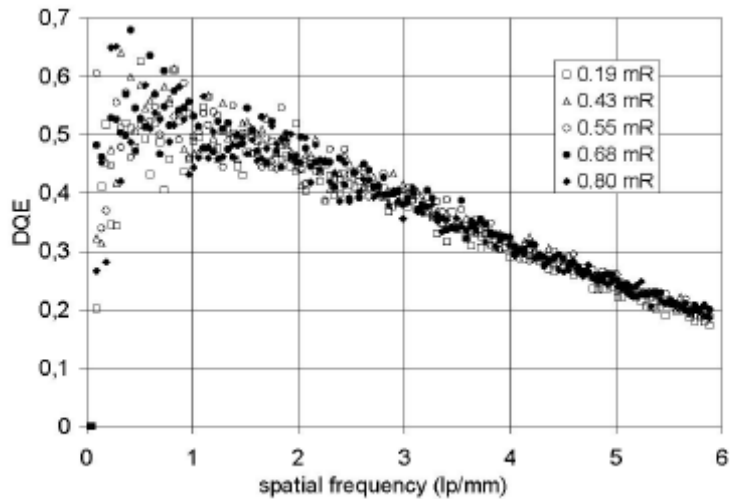


Figure 2.16 DQE( $f$ ) vs. spatial frequency for a mammographic a-Se FPXI manufactured by Anrad operating in tomosynthesis mode for several exposures ranging from 0.19 mR to 0.8 mR. A good DQE value is maintained even at very low doses; after [90].

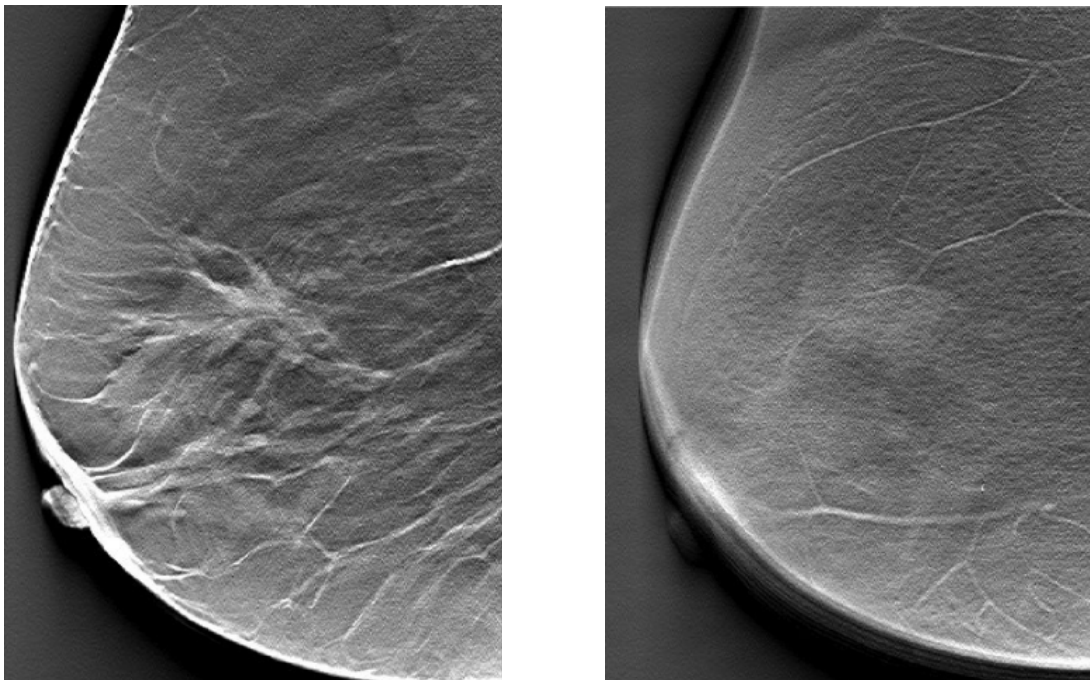


Figure 2.17 X-ray images of a breast from a mammographic a-Se x-ray detector operating in tomosynthesis mode; after [90]. These images are only 2 of 49 acquired for the complete scan.

Also often discussed is the DQE(0) of detectors. DQE(0) is the zero spatial frequency DQE (DQE( $f=0$ )), which represents signal quality degradation due to signal and noise transfer characteristics of the system without considering signal spreading [96]. The relationship between DQE( $f$ ) and DQE(0) is

$$DQE(f) = \frac{DQE(0)MTF^2(f)}{NPS_0(f)} \quad (2.20)$$

where  $NPS_0(f)$  is the noise power spectrum normalized to unity as  $f$  approaches 0 [63].

A cascaded linear-system model has been used to characterize the performance of many imaging systems in terms of signal and noise transfer relationships from input to output through various stages, taking into account significant noise sources [96-100]. In these models, the system is described as cascades of simple, independent elementary stages representing five different possible processes: gain, stochastic blurring, deterministic blurring, aliasing and the addition of noise. A model incorporating all of these effects for a PbO detector can be found in [101], but a simpler model which considers only DQE(0) of an a-Se detector is shown here in Fig. 2.18 [96]. The input and output are distributions of quanta, the random nature of which allows the noise in the number of incident x-rays to be given by a Poisson fluctuation. This means that if  $\bar{\Phi}_0$  is the mean incident x-ray photon fluence on a detector, then the input NPS in the number of photons incident on the detector is  $S_{N_0} = \bar{\Phi}_0$ . The output signal and noise are represented by  $\bar{\Phi}_4$  and  $S_{N_4}$ . The attenuation of x-ray photons, conversion to charge carriers and charge collection are all represented by gain stages, while the addition of electronic noise is obviously an addition stage. Blurring and aliasing are ignored, as this is a model for DQE(0). The results of calculations based on this model can be seen in Fig. 2.19 along with experimental data. It can be seen that the DQE(0) increases at higher exposures where the electronic noise,  $S_{N_e}$  (often reported as 1000 – 3000 electrons per pixel for an a-Si:H AMA [96]), becomes less important and the SNR increases with the square root of exposure [90].

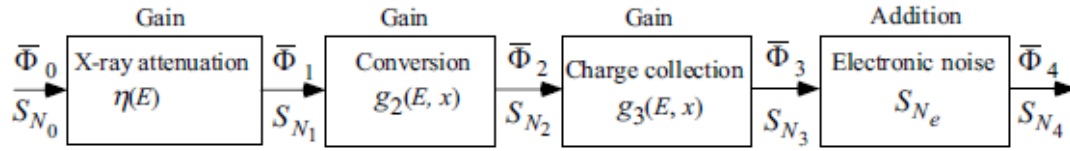


Figure 2.18 A block diagram showing a cascaded linear-system model of DQE(0) for an a-Se FPXI; after [96].

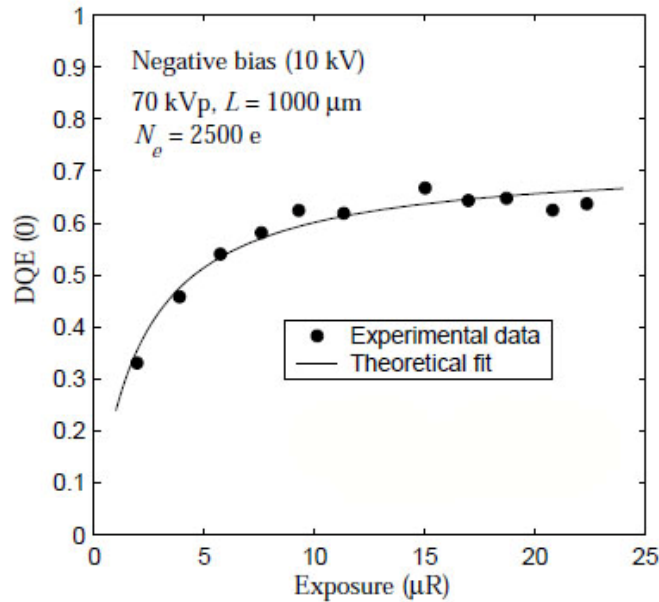


Figure 2.19 Plot of DQE(0) vs. exposure for a general radiographic a-Se detector. The circles represent experimental data for a 70 kVp x-ray spectrum with 23.5 mm Al filtration while the line gives the theoretical fit given by the model shown in Fig. 2.18; after [96].

## 2.5 Dynamic Range

The dynamic range (DR) of an imaging system is essentially an expression of the contrast resolution possible in images produced by the system [11]. DR is best described by the following simple relation:

$$DR = \frac{X_{\max}}{X_{\text{noise}}} \quad (2.21)$$

where  $X_{max}$  is the maximum signal that a detector can handle and  $X_{noise}$  is the signal representing the quadrature sum of the detector noise and x-ray quantum noise. A DR of 100:1 tends to be sufficient for chest radiography, but 400:1 is required for mammography, where the objects of interest do not attenuate x-rays much differently than their surroundings, *e.g.* a tumour in a breast [63]. It should be noted that a DR of 100:1 means a range of  $X_{mean}/10$  to  $10 \times X_{mean}$  and not something like  $X_{mean}/50$  to  $2 \times X_{mean}$ , where  $X_{mean}$  is the average exposure that the detector will experience [11].

## 2.6 Dark Current

The term dark current refers to an unwanted electrical current which flows through a photoconductor due to a necessary electrical potential placed across the photoconductive layer and not due to the photogeneration of electrical carriers due to incident radiation, which is normally the desired signal. Since the information used by flat panel detectors to create an image is the integration of pixel current, dark current is a source of noise in the system and decreases the dynamic range of the detector.

### 2.6.1 Potential Sources of Dark Current

#### 2.6.1.1 Carrier Injection

Metal electrodes must be present on both sides of the photoconductive layer in an FPXI to apply an electric bias to drift photogenerated carriers. Dark current can arise when charge carriers are emitted from the metal contacts into the photoconductor.

When a metal contact is made to a semiconductor, the Fermi level of the metal,  $E_{Fm}$ , and the Fermi level of the semiconductor,  $E_F$ , must be the same distance from the vacuum level. If  $E_{Fm}$  is closer to the vacuum level than  $E_F$ , meaning the work function of the metal,  $\phi_m$ , is less than the work function of the semiconductor,  $\phi$ , then it is easier to remove electrons from the metal than from the semiconductor. Therefore, when the two are brought together, as depicted in Fig. 2.20, electrons will move from the metal into the semiconductor, reducing the potential energy of

electrons in the conduction band near the junction. This is demonstrated by a downward bending of the band edges. This scenario results in what is called a hole blocking contact, as a hole will have to gain energy equal to  $E_g - \phi_B$  to move from the metal into the semiconductor, where  $\phi_B = \phi_m - \chi$ , the difference between the work function of the metal and the electron affinity of the semiconductor [102]. A hole blocking contact is likely to be what is formed on an a-Se layer as typical contact metals such as Cr and Al have work functions of around 4.5 eV, while the work function of Se is  $\sim 6$  eV [103].

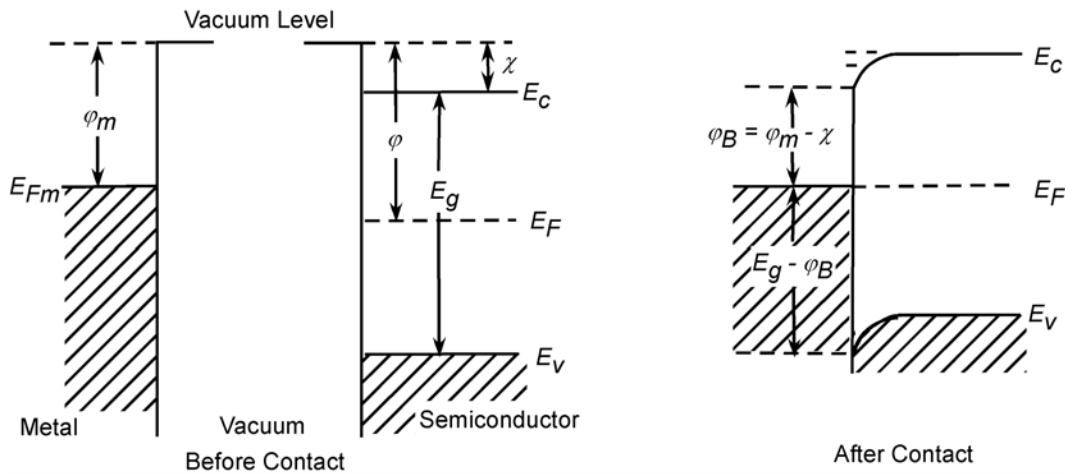


**Figure 2.20 Energy level diagram for a hole blocking contact between a metal and an intrinsic semiconductor; redrawn from [102].  $E_{Fm}$  and  $\phi_m$  are the Fermi level and work function of the metal while  $E_F$ ,  $E_v$ ,  $E_c$ ,  $E_g$ ,  $\phi$ , and  $\chi$  are the Fermi level, valence band edge, conduction band edge, bandgap, work function and electron affinity of the semiconductor, respectively.**

The situation is not quite as ideal as described in Fig. 2.20, especially in the case of amorphous semiconductors which have a large concentration of localized states near the Fermi level, as will be discussed for the case of a-Se in Chapter 3. The concentrations of states near  $E_F$  will accept electrons from the metal or supply electrons to the metal, depending on  $\phi_m - \phi$ , as it is brought into contact with the Se. This will result in a slight shifting of  $E_F$ , but its level will remain relatively pinned due to the presence of a large amount of available localized states. The picture can be further complicated by surface states, resulting from the abrupt termination of the solid or from the adsorption of impurities [7].

Regardless of the complicating factors, Fig. 2.20 serves to illustrate the potential barrier to charge carrier injection created when a metal and semiconductor are brought together. This

barrier can be lowered when an electric field is applied to the contact due to the Schottky effect [103]. When an electron is at a distance,  $x$ , from the metal, a positive charge, called the image charge, will be induced on the metal surface. The attractive force between the electron and the positive image charge will be

$$R = \frac{-e^2}{4\pi(2x)^2 \epsilon} \quad (2.22)$$

where  $\epsilon$  is the permittivity of the semiconductor ( $\epsilon_0\epsilon_r$ ) and  $e$  is the elementary charge. Integrating from infinity to  $x$  gives the potential energy of the electron as:

$$PE(x) = \frac{e^2}{16\pi\epsilon x} + eF_0x \quad (2.23)$$

where  $F_0$  is an applied field, giving the potential energy in eV. This is shown in Fig. 2.21, where the potential energy barrier is decreased by the applied field. The maximum of the potential energy barrier is determined by finding the point where  $d[PE(x)]/dx = 0$ . This gives:

$$x_m = \sqrt{\frac{e}{16\pi\epsilon F_0}} \quad (2.24)$$

$$\Delta\phi = \sqrt{\frac{eF_0}{4\pi\epsilon}} = \beta_s \sqrt{F_0} \quad (2.25)$$

where  $\Delta\phi$  is the barrier lowering in V and  $\beta_s$  is the Schottky coefficient, given by  $(e/4\pi\epsilon)^{1/2}$  in V and  $(e^3/4\pi\epsilon)^{1/2}$  in eV [103,104].

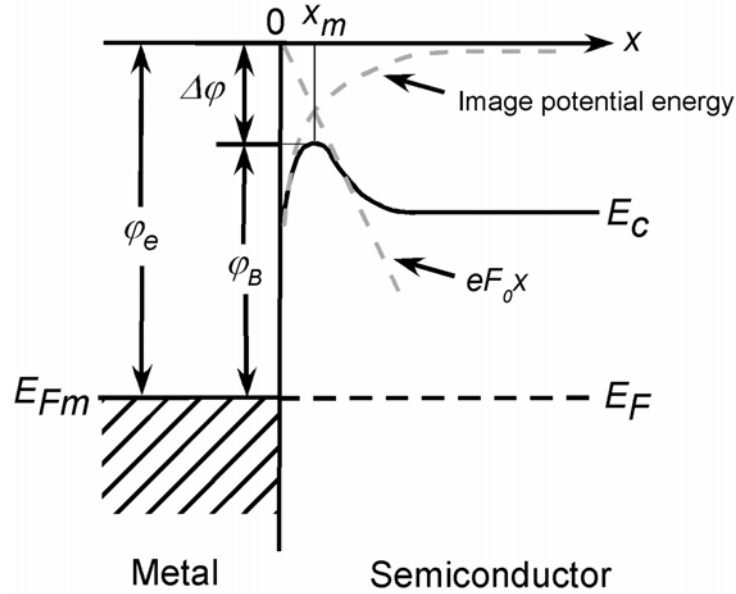


**Figure 2.21** Energy band diagram incorporating the Schottky effect for an electron blocking contact on a semiconductor; combined from [103].  $\phi_e$  is the original barrier to electron injection from the metal into the semiconductor, while  $\phi_B$  is the barrier lowered by the Schottky effect.

The concentration of electrons injected over a Schottky barrier is then given by [59]

$$n = N_c \exp\left(-\frac{\phi_e - \beta_s \sqrt{F_0}}{kT}\right) \quad (2.26)$$

where  $N_c$  is the effective concentration of states at the conduction band edge,  $k$  is the Boltzmann constant and  $T$  is the temperature. The corresponding current due to the drift of those electrons is given by:

$$J_{e_{drift}} = e\mu_e F_0 n \quad (2.27)$$

where  $\mu_e$  is the drift mobility of the electrons.

### 2.6.1.2 Carrier Diffusion

Carriers injected into a semiconductor can move both by drift due to the applied electric field and due to diffusion. If there is a concentration gradient of charge carriers, there will be a net diffusional motion of carriers in the direction of decreasing concentration [105]. Considering electrons injected from the negative contact, there will be an electron drift current given by equation 2.27 as well as a diffusion component given by

$$J_{e_{diff}} = -eD_e \frac{dn}{dx} \quad (2.28)$$

where  $dn/dx$  is the concentration gradient of electrons in the  $x$  direction (distance into the semiconductor).  $D_e$  is the diffusion coefficient for electrons which depends on the drift mobility of electrons in the semiconductor. According to the Einstein Relation [105],

$$D_e = \mu_e \frac{kT}{e} \quad (2.29)$$

It can be shown that the contribution of carrier diffusion to the dark current in a-Se sandwich structures, as used in FPXIs, is negligible when compared with the drift component of the current [106]. Assuming that holes are the dominant contributor to current in a-Se, as holes are injected into the a-Se from the positive contact, trapping will result in a free hole concentration which is reduced away from the contact. For simplicity's sake, the free hole distribution will be assumed to be exponential:

$$p(x) = p_0 \exp\left(-\frac{x}{\mu_h \tau_h F_0}\right) \quad (2.30)$$

where  $p_0$  is the carrier concentration at  $x = 0$ . Taking  $F_0$  as  $V_0/L$  where  $V_0$  is the applied voltage, Eqs. 2.27, 2.28, 2.29 (modified for holes) and 2.30 give the ratio of the diffusion current to the drift current as

$$\frac{J_{h_{diff}}}{J_{h_{drift}}} = \left( \frac{L}{\mu_h \tau_h F_0} \right) \left( \frac{V_t}{V_0} \right) \quad (2.31)$$

where  $V_t$  is the thermal voltage,  $kT/e$ . For FPXI operation, it is ideal that the hole schubweg be larger than the thickness of the photoconductor, so that the first term in Eq. 2.31 is less than unity. In the case of very poor hole transport,  $L/\mu_h \tau_h F_0 = 100$ . For a 200  $\mu\text{m}$  thick a-Se layer, the applied voltage would be 2000 V. The value of the thermal voltage at room temperature is  $\sim 0.025$  V, giving a ratio of diffusion current to drift current of  $1.25 \times 10^{-4}$ . So even in the case of poor hole drift, the diffusion current is roughly 4 orders of magnitude smaller than the drift current and is indeed negligible in FPXI operation.

### 2.6.1.3 Bulk Thermal Generation

Bulk thermal generation refers to the generation of charge carriers from localized states in the bandgap of a semiconductor, as depicted in Fig. 2.22 [103]. At temperatures above 0 K, a solid will experience lattice vibrations. Some of these vibrations may impart enough energy to a trapped carrier to allow it reach a transport band. A typically assumed value for the frequency of these lattice vibrations (also called the attempt-to-escape frequency),  $\nu_0$ , is  $1 \times 10^{12} \text{ s}^{-1}$  [59]. This process can be from the middle of the bandgap, where holes and electrons face an equal barrier to generation, and hence both a hole and electron are generated, as in Fig. 2.22 (a). But this can also occur above mid-gap where an electron will escape to the conduction band, leaving behind a positive space charge (Fig. 2.22 (b)), or below mid-gap where a hole will escape to the valence band, leaving behind a negative space charge (Fig. 2.22 (c)). Stabilized a-Se is inherently *p*-type, meaning that the Fermi level is below mid-gap, making it more likely that holes will be generated by thermal vibrations, as in Fig. 2.22 (c).

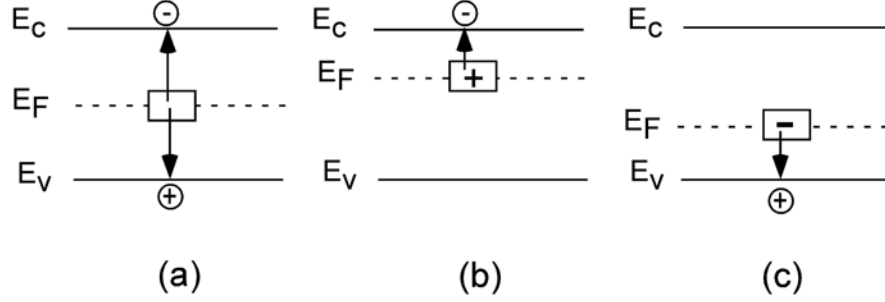


**Figure 2.22** Depiction of the process of bulk thermal generation from states within the bandgap of a semiconductor (a) at mid-gap, (b) above mid-gap, (c) below mid-gap.

The potential barrier faced by a trapped carrier can be reduced in a manner similar to the Schottky effect. This is known as the Poole-Frenkel effect and is the field-enhanced thermal excitation of trapped carriers into the transport bands [103]. Similar to the case of Schottky emission, the reduction in the potential energy of the barrier is given by

$$\Delta\phi = \sqrt{\frac{eF_0}{\pi\epsilon}} = \beta_{pF}\sqrt{F_0} \quad (2.32)$$

where the coefficient is now  $\beta_{pF}$ , the Poole-Frenkel coefficient, which is given by  $(e/\pi\epsilon)^{1/2}$  in V and  $(e^3/\pi\epsilon)^{1/2}$  in eV [102,103].  $\beta_{pF}$  is a factor of 2 larger than  $\beta_s$  as the charge attracting the released carrier is now immobile, doubling the amount of barrier reduction. It should be noted that the Poole-Frenkel barrier reduction is only applicable to traps which are neutral when filled and charged when empty, so that there is a coulombic attraction between the trap and the released carrier. If this is the case, then the rate of generation of carriers (as an example, holes are assumed) can then be determined by [107,108]

$$g = N(E)\nu_0 \exp\left(-\frac{E - E_v - \beta_{pF}\sqrt{F_0}}{kT}\right) dE \quad (2.33)$$

where  $N(E)$  is the concentration of localized states per eV. Equation 2.33 must be integrated over the energy range,  $dE$ , from which carriers are generated. But if  $dE$  is small ( $\sim kT$ ) and  $N(E)$  is constant over that small range, the generation rate can be closely approximated by

$$g = N(E_F)kTv_0 \exp\left(-\frac{E - E_v - \beta_{pF}\sqrt{F_0}}{kT}\right) \quad (2.34)$$

If it is assumed that all of the generated holes are collected, then the thermal generation current can be given by

$$I_{th} = egAL = eN(E_F)kTv_0 \exp\left(-\frac{E - E_v - \beta_{pF}\sqrt{F_0}}{kT}\right)AL \quad (2.35)$$

where  $A$  is the cross sectional area of the semiconductor and  $L$  is the thickness. It can be seen from Eq. 2.35 that the current due to bulk thermal generation depends linearly on the volume of the semiconductor and, for a given  $A$ , linearly on  $L$ .

If some of the generated holes are re-trapped before being collected, the Hecht formula must now be used and the equation for the hole current now becomes [109]

$$I_{th} = e\mu_h\tau_hF_0g\left[1 - \frac{\mu_h\tau_hF_0}{L}\left(1 - \exp\left(-\frac{L}{\mu_h\tau_hF_0}\right)\right)\right]A \quad (2.36)$$

where  $\mu_h$  is the hole drift mobility and  $\tau_h$  is the hole lifetime in the semiconductor.

Experimental work by Schein [110] has shown that the dark discharge of surface potential in xerographic a-Se samples is due to Poole-Frenkel enhanced bulk thermal generation. Schein observed a linear increase in dark discharge rate with sample thickness at several fields. Furthermore, he has plotted the natural log of the rate of decay of the surface potential (proportional to the natural log of the dark current) vs. the square root of the applied field, as shown in Fig. 2.23. As Eq. 2.35 would predict, this yielded a linear plot with a slope close to  $\beta_{pF}/kT$ , roughly  $1.2 \times 10^{-3} \text{ (m/V)}^{1/2}$ . Work on other materials has given similar plots with slopes which do not agree with the Poole-Frenkel model nor the model for Schottky injection, which would have a slope of  $6 \times 10^{-4} \text{ (m/V)}^{1/2}$ , but fell somewhere in between. As a result, several

authors have developed a more thorough treatment of the Poole-Frenkel model taking into account the reduction of the potential barrier in three dimensions, instead of considering only one dimension, as was done in the original model [102,111]. One such treatment by Hartke [111] predicts an increase in conductivity given by

$$\frac{\sigma}{\sigma_0} = \left( \frac{kT}{\beta_{pF} \sqrt{F_0}} \right)^2 \left\{ 1 + \left[ \left( \frac{\beta_{pF} \sqrt{F_0}}{kT} \right) - 1 \right] \exp \left( \frac{\beta_{pF} \sqrt{F_0}}{kT} \right) \right\} + \frac{1}{2} \quad (2.37)$$

where  $\sigma_0$  is the initial conductivity and  $\sigma$  is the Poole-Frenkel enhanced conductivity. While much more complex than in the one dimensional case, this can be reduced to a theoretical plot of the natural log of the current vs. the root of the field described earlier and the expected slope is  $\sim 7 \times 10^{-4} \text{ (m/V)}^{1/2}$ , between that for the one dimensional Poole-Frenkel model and the Schottky emission model.

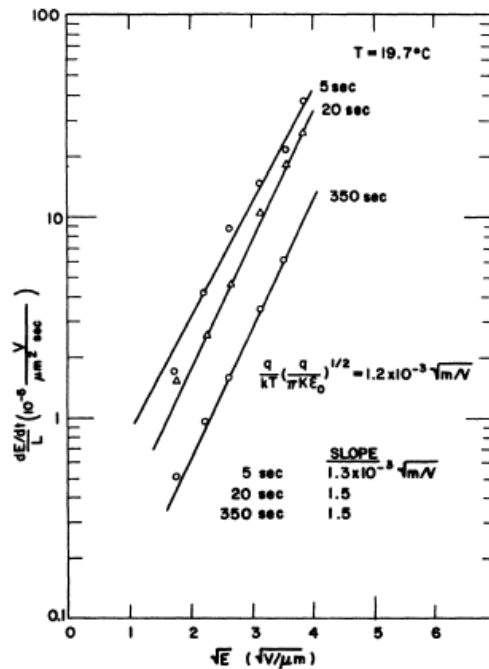


Figure 2.23 Schein's plot of the natural log of the dark current in an a-Se sample without a top contact on the square root of the electric field at three times after the application of the field. At all times, the relationship is linear with a slope characteristic of Poole-Frenkel enhanced bulk thermal generation; after [110].

## 2.6.2 Acceptable Levels of Dark Current in Direct Conversion FPXIs

The importance of low dark current levels in the successful operation of direct conversion FPXIs cannot be stressed enough. Without an acceptably low level of dark current, digital x-ray imagers lose all of their advantages over screen films and this single barrier has prevented many photoconductors from being viable candidates for use in FPXIs. But what exactly is an acceptable level of dark current for FPXI operation? The upper tolerable limit of dark current density is typically quoted at around  $10 \text{ pA mm}^{-2}$ , but is also often given as a range of 1-  $10 \text{ pA mm}^{-2}$  [15,56]. This is due to the fact that results of calculations of acceptable dark current levels vary depending on the criteria used. Generally, one wants the noise due to the dark current to be less than other sources of noise in the detector, but the source of noise chosen changes the acceptable level and these calculations have been explained by Kasap and Rowlands [15].

In FPXI operation, the dark current density,  $J_d$ , will accumulate a charge,  $Q_{dark}$ , on the pixel capacitance,  $C_{px}$ . This charge is given by

$$Q_{dark} = J_{dark} A \Delta t \quad (2.38)$$

where  $\Delta t$  is the pixel readout time (typically 1 s in mammographic applications) and  $A$  is the radiation receiving area. There will also be noise in the dark current signal due to stochastic fluctuations in the number of carriers collected on the pixel capacitance and this produces a charge  $Q_{noise}$ , given by

$$Q_{noise} = e \sqrt{\frac{Q_{dark}}{e}} = e \sqrt{\frac{J_{dark} A \Delta t}{e}} \quad (2.39)$$

These two signals must be compared with other sources of noise in the FPXI to ensure that they are not the dominate source of noise in the system. One such competing noise source is the quantum noise in the radiation. In mammography, the mean photon energy is 20 keV and the level of the quantum noise,  $X_{noise}$ , is around 60  $\mu\text{R}$  in an exposure. The radiation noise signal,  $Q_{x-noise}$ , is the charge collected on  $C_{px}$  due to the quantum noise and is given by

$$Q_{x-noise} = \frac{eAE_{1R}X_{noise}}{W_{\pm}} \quad (2.40)$$

where  $X_{noise}$  is in R and  $E_{1R}$  is the energy per unit area equivalent of 1 R of radiation. In contrast, the minimum likely exposure in mammography,  $X_{min}$ , is 0.6 mR and this exposure produces a collected charge on  $C_{px}$  given by

$$Q_{signal} = \frac{eAE_{1R}X_{min}}{W_{\pm}} \quad (2.41)$$

Another noise source in an FPXI is the thermal, or  $kTC$ , noise due to the TFT switch system used in the AMA. When the TFT is on, its resistance is small and thermal fluctuations in this resistance create charge fluctuations on  $C_{px}$ . Once the TFT is turned off, some charge is left stored on  $C_{px}$  and this leads to a noise signal given by

$$Q_{thermal} = \sqrt{2kTC_{px}} \quad (2.42)$$

Figure 2.24 shows all of these signals plotted as voltages developed across the pixel capacitance (*i.e.*  $V_{signal} = Q_{signal}/C_{px}$ ) vs. the dark current density. Values assumed in the plots in Fig. 2.24 are  $W_{\pm} = 5 \text{ eV}$ ,  $A = 50 \times 50 \text{ }\mu\text{m}$ ,  $C_{px} = 1 \text{ pF}$  and  $\Delta t = 1 \text{ s}$ .

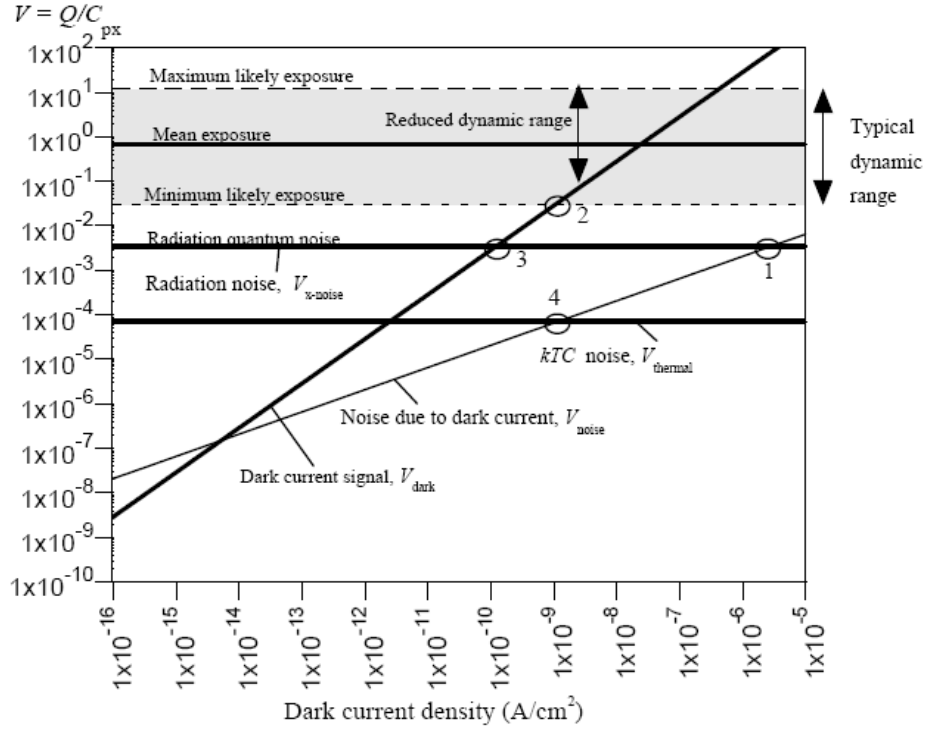


**Figure 2.24** Various voltages across  $C_{px}$  as a function of dark current density; after [15]. Mammographic exposures used to calculate voltages corresponding to max. likely exposure, mean exposure, min. likely exposure and radiation noise signals are 240 mR, 12 mR, 0.6 mR and 60  $\mu$ R, respectively.

If the limit on the dark current is set by requiring that the noise due to the dark current is less than the quantum noise,  $V_{noise} \leq V_{x-noise}$  (shown as point 1 in Fig. 2.24), then the dark current is allowed to be as high as  $1 \times 10^{-6} \text{ A cm}^{-2}$ . However, this would reduce the dynamic range of the detector to zero. To maximize the dynamic range,  $V_{dark}$  must be less than  $V_{signal}$ . They are equal at point 2 in Fig. 2.24 and an increase in the dark current past this point reduces the dynamic range. This sets the upper limit on the dark current as

$$J_{dark} A \Delta t \leq \frac{e A E_{1R} X_{min}}{W_{\pm}} \quad (2.43)$$

giving  $J_{dark} \leq 1.3 \times 10^{-9} \text{ A cm}^{-2}$ .

If the limit on dark current is set by requiring the dark current signal to be lower than the quantum noise signal,  $V_{dark} \leq V_{x-noise}$ , corresponding to point 3 in Fig. 2.24, then

$$J_{dark} A \Delta t \leq \frac{e A E_{1R} X_{noise}}{W_{\pm}} \quad (2.44)$$

setting the limit on dark current at  $1.3 \times 10^{-10} \text{ A cm}^{-2}$ . If the  $kTC$  noise is chosen as the limiting factor, such that  $V_{noise} \leq V_{thermal}$ , then

$$J_{dark} A \Delta t \leq \frac{C_{px} kT}{e} \quad (2.45)$$

which gives  $J_{dark} \leq 1 \times 10^{-9} \text{ A cm}^{-2}$  at point 4 in Fig. 2.24. The lowest range for the upper limit on the dark current, allowing for no degradation of dynamic range, is given by points 3 and 4:  $0.1 - 1 \text{ nA cm}^{-2}$  or  $1 - 10 \text{ pA mm}^{-2}$ .

A final consideration is the electronic noise in the AMA,  $N_e$ . If one considers a fairly conservative range for the carrier equivalent of this noise (500 – 1000 carriers), then

$$\sqrt{\frac{J_d A \Delta t}{e}} \leq N_e \quad (2.46)$$

and  $J_d \leq 4 - 16 \text{ pA mm}^{-2}$ , around the top of the quoted range.

There is, however, one further complication in that the fluctuations in the dark current are not actually due to shot noise alone. There is a  $1/f$  contribution that can be quite significant and more than the shot noise [112]. Since  $1/f$  spectral power density scales with  $I_d^2$ , the current should be even lower than the estimate above. Some  $1/f$  noise measurements have been reported on a-Se films and  $1/f$  noise has been shown to be more dominant than shot noise over the frequencies of interest [112]. The variance can be up to one hundred times larger, which puts the upper limit on dark current closer to around  $1 \text{ pA mm}^{-2}$ .

### 2.6.3 The Study of Dark Current in Amorphous Selenium Films

Much work done during the 1960s and 1970s focused on measuring the dark current in metal/a-Se/metal sandwich structures, but no general conclusion has been reached on the origin of the I-V characteristics of these structures.

Some researchers have interpreted the steady-state  $I$ - $V$  characteristics of a-Se layers as those of space charge limited currents (SCLC) [113,114]. By illuminating one or both contacts with intense light to create a reservoir of carriers at the electrode, Pfister and Lakatos found that the steady-state photogenerated currents obeyed the SCLC theories:  $J \propto V^2 / L^3$  (Child's Law) for one carrier and  $J \propto V^3 / L^5$  for two carriers [115]. They also found that the current scaled with the SCLC scaling law:  $J/L = f(V/L^2)$ . However, their observed levels of dark current were much higher than typical levels observed in a-Se films.

Mort and Lakatos studied photoemission from one of the contacts into the a-Se layer and concluded that there clearly exists an electrode material dependent potential barrier against carrier injection [116]. Müller and Müller proposed that this potential barrier can be interpreted as a Schottky barrier [117], while work done by Johanson *et al.* showed that the carrier injection does not follow such well established models [55]. They found no simple correlation between the work function of the contact material studied and dark current levels. Their results also suggest that hole injection from the positive contact dominates the dark current and this is intuitive, as the hole range in a-Se can be as much as an order of magnitude larger than the electron range (see Table 3.2).

It has been well documented that the dark current in metal/a-Se/ITO (indium tin oxide) devices decays in a non-exponential manner with time after the application of bias [7,55]. To further complicate the matter, it has been shown that the dark current through metal/a-Se/metal devices is not symmetrical even when the device has been designed to be symmetrical [56].

The rather unpredictable nature of these transients makes it very difficult to correct for the charge built up on a pixel capacitance by the flow of dark current. As a result, the presently

utilized solution has been to reduce the dark current in the a-Se layer to below the calculated acceptable level of 1 - 10 pA/mm<sup>2</sup>. This is not possible at the required applied field of 10 V/μm with a single intrinsic layer of a-Se, despite the relatively large dark resistivity of a-Se (~ 10<sup>14</sup> Ω cm) [64]. Rather, this has been achieved through the use of a thin *n*-type layer of alkali-doped a-Se to trap holes injected from the positive contact and a thin *p*-type layer of a-As<sub>2</sub>Se<sub>3</sub> to trap electrons injected from the negative contact [58]. As will be mentioned in Section 3.3.2.4.3, alkali-doped a-Se tends to behave as *n*-type and As<sub>2</sub>Se<sub>3</sub>, well known for its poor electron transport characteristics [118], can act as a *p*-type layer. The performance of this *n-i-p* structure has been matched by a simple *i-n* structure in which the *n*-layer is simply undoped stabilized a-Se deposited on a 7°C substrate, *i.e.* through “cold deposition” [56].

Recent theoretical work, done concurrently with the work in this thesis, by Kabir and Mahmood [57,59] has used numerical calculations to model the dark current transients in 1000 μm thick *n-i-p* a-Se samples approximating the photoconductive layer in flat panel detectors used in general radiography. Their results have shown good agreement with selected experimental results provided by Anrad in which the dark current reaches a steady-state within 1000 s after the application of the bias, however this is not always the case as some transients can decay seemingly indefinitely [7]. These simulations operate on the principle that the dark current transient is controlled entirely by the injection of carriers from the contacts over a Schottky barrier and the build up of space charge near the contacts due to carrier trapping in the blocking layers reduces the electric field at the contacts, as illustrated in Fig. 2.25. This reduces dark current with time until the rates of trapping and release of charge carriers reach an equilibrium, at which point the current reaches a steady-state. These results rely on some basic assumptions to reduce computation time: i) the dark current transient only depends on injected holes interacting with the *n*-layer, *i.e.* all injected holes are trapped immediately in the *n*-layer, ii) the current and space charge due to injected electrons is negligible, and iii) the dark current due to the bulk thermal generation of charge carriers is negligible. The assumptions used in this model and the results of this work will be discussed in much greater detail in Chapter 5 of this thesis.

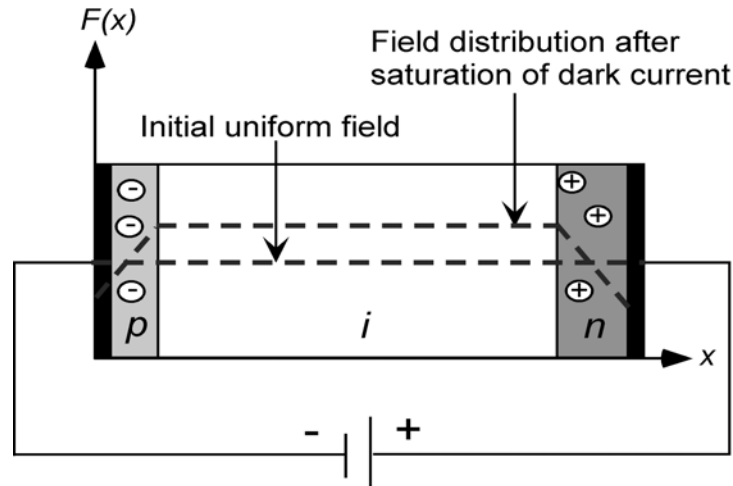


**Figure 2.25** Example of a *p-i-n* multilayer structure. As injected electrons become trapped in the *p*-layer and holes in the *n*-layer, the electric field distribution changes to be non-uniform, reducing the field at both contacts.

Experimental work on reverse biased a-Si:H *p-i-n* structures has shown that the dark current is due to Poole-Frenkel assisted bulk thermal generation [107,108] and recent models of the dark current in these structures has confirmed this [109]. Even though the contribution to the dark current from bulk thermal generation might be less in a-Se than in a-Si:H because of the larger bandgap in a-Se, bulk thermal generation has been found to control xerographic dark discharge in a-Se layers without a top contact, which were commonly used in xerography [110]. Very recently published simulations by Mahmood and Kabir [106] have estimated that the dark current due to bulk thermal generation in metal/a-Se/metal sandwich structures, such as that shown in Fig. 2.25, is roughly two orders of magnitude lower than the calculated current due to carrier injection from the contacts. While it is possible that the contribution from thermal generation is negligible, this has never been proven experimentally.

While the true source and nature of the dark current in a-Se detectors has not yet been determined, its low value has been one of the keys in the implementation of a-Se FPXIs. A comparison of the dark current levels in stabilized a-Se films with different structures and films of other potential x-ray photoconductors, which will be discussed in Chapter 3, can be seen in Fig. 2.26.

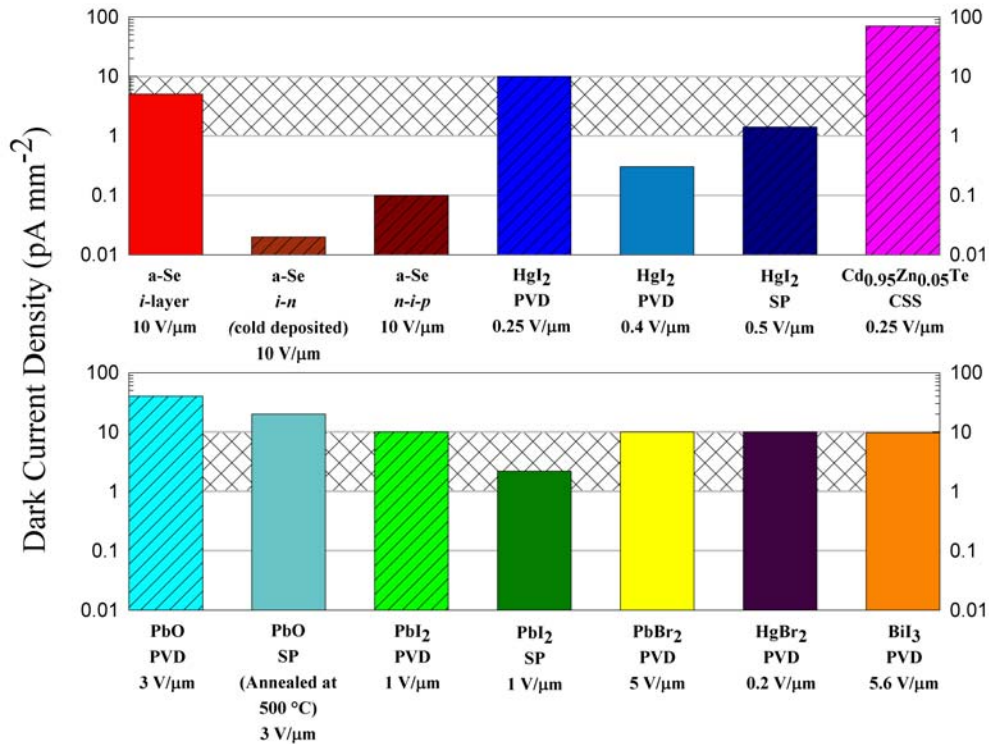


Figure 2.26 The best reported values to date of dark current density for a-Se and polycrystalline photoconductive layers. Note that most of these are measured at relatively low applied electric fields where it is questionable that the charge collection efficiency is adequate. It is not possible to scale these to the same field as the field dependence of the dark current is rarely linear and in general is unknown. All polycrystalline layers are labeled as deposited by physical vapour deposition (PVD), screen printing (SP) or close space sublimation (CSS). Solid colors represent values obtained from films that have not yet been used to obtain x-ray images; hashed bars represent values from demonstrated x-ray imagers. The grey hashed area represents the acceptable range for dark current in an FPXI. Data have been taken from various sources, including the following: a-Se (*i*-layer and *n*-*i*-*p*) from [13], a-Se (*i*-n) from [119], HgI<sub>2</sub> (PVD at 0.25 V/ $\mu\text{m}$  and SP) from [120], HgI<sub>2</sub> (PVD at 0.4 V/ $\mu\text{m}$ ) from [121], PbI<sub>2</sub> (PVD) from [122], PbI<sub>2</sub> (SP) from [123], Cd<sub>0.95</sub>Zn<sub>0.05</sub>Te from [124], PbO (PVD) from [125], PbO (SP) from [126], PbBr<sub>2</sub> and HgBr<sub>2</sub> from [127] and BiI<sub>3</sub> from [128].

## 2.7 Conclusion

This chapter has provided an in depth discussion of many of the metrics used to describe and compare the performance of digital x-ray image detectors including x-ray sensitivity, MTF, NPS, DQE, DR, and dark current, with particular emphasis being placed on the value of these metrics in a-Se based FXPIs. A solid understanding of these terms and their underlying meanings is crucial when comparing the performance of different x-ray imaging systems,

especially those based on different x-ray photoconductors. Chapter 3 of this thesis will compare the performance of many potential candidate photoconductors using these terms and it will become obvious that only a-Se has been developed to the point of commercialization. Therefore, furthering the understanding of the performance of a-Se in FXPIs is very important. The results presented in this thesis will focus on both experimental and theoretical explorations of the x-ray sensitivity and dark current levels in a-Se films used in FXPIs.

## 3. X-RAY PHOTOCONDUCTORS

In direct conversion flat panel detectors, the first step in creating the final product (the image) is the conversion of the incident x-ray radiation to electrical charge and this is done by a layer of x-ray photoconductor coated onto the AMA. Therefore, if the choice of x-ray photoconductor is not optimal, the performance of the system will suffer greatly.

### 3.1 An Ideal X-ray Photoconductor

Given the operating principles of direct conversion detectors, one can write a “wish list” of the properties that an ideal x-ray photoconductor would have [15,64]:

1. The photoconductor should have a large attenuation coefficient,  $\alpha$ , over the energy range of interest so that most of the incident radiation is absorbed in a layer of practical thickness. This implies that the attenuation depth,  $\delta$ , must be much less than the thickness of the layer,  $L$ .
2. The material should have high x-ray sensitivity. This implies that the electron-hole pair creation energy,  $W_{\pm}$ , should be as low as possible and that the material has a small band gap.
3. There should be negligible recombination between drifting photogenerated carriers of opposite charge.
4. There should be negligible deep trapping of photogenerated charge carriers as this has a detrimental effect on image lag and ghosting. This means that the Schubweg,  $\mu\tau F$ , for both carriers should be greater than  $L$ .
5. Diffusion of photogenerated carriers should be negligible compared to their drift along the applied field lines. This will ensure that carriers created above one pixel are not collected

by a neighbouring pixel, reducing resolution. This is especially important in detectors with very small pixels.

6. The dark current should be as small as possible. Ideally, the dark conductivity of the material would be zero. This implies a large bandgap photoconductor, in opposition to point 2 above.
7. The longest transit time of photogenerated carriers should be less than the image readout time or the inter-frame time in fluoroscopy.
8. The material should exhibit negligible x-ray fatigue and damage with continued exposure to x-ray radiation.
9. The photoconductor should be easily coated onto large area AMAs at a temperature compatible with a-Si:H TFTs (less than 300 °C).
10. When coated over a large area, the material must exhibit uniform characteristics over the whole area.

It is obvious that most, if not all potential photoconductor candidates, will be unable to meet the all of the demands of this list, especially since certain points are contradictory (such as points 2 and 6). However, several photoconductors have been developed to the point where prototype imagers have been developed and, in the case of amorphous selenium, commercialized. The important properties of these materials will be discussed in this chapter.

### **3.2 Types of Photoconductors**

Photoconductors can exist in three main states: crystalline, polycrystalline and amorphous. A crystalline material has a regular spatial arrangement of atoms giving it a long range order with a periodic structure. This means that each atom in a crystal has the same interatomic spacing, coordination (number of bonds formed) and bond length and angle. Single

crystals of photoconductors are used in radiation spectroscopy where the input of interest is the photon energy and not a radiation intensity distribution [129,130]. Images taken with projection radiography are essentially the shadow of the subject and since x-rays cannot be focused, a detector used in projection radiography must be at least as large as the object being imaged. As listed in Table 1.1, for human chest radiography, the detector size is 35 cm by 35 cm. This large size immediately rules out the use of crystalline semiconductors as the growth of crystals that large is exceedingly difficult and requires temperatures not compatible with a-Si:H AMAs. As a result, only polycrystalline and amorphous photoconductors are considered as potential candidates for use in flat panel detectors [11].

A polycrystalline material is made of many small crystals, called grains, that are arranged randomly throughout the solid. The boundaries between grains have stretched bonds, broken bonds, voids, high concentrations of impurities, misplaced atoms and just a general disorder [105]. This can lead to many problems in their application to flat panel detectors such as high dark current levels, poor transport of radiation induced charge carriers and non-homogeneity of responsiveness across the surface of the detector [63]. Nonetheless, much research has recently been focused on developing several polycrystalline photoconductors in the hopes that one or more may become usable in flat panel detectors. This work and the specific benefits and problems associated with some of these materials will be highlighted in Section 3.4.

An amorphous solid has no long range atomic order. There does exist some short range order because the individual atoms must satisfy their valence bonding requirements. However, each bond can have just a slight deviation in the bond angle and length and this leads to a continuous random network of atoms [105,131]. This lack of long range order allows amorphous materials to be coated over large areas with very good homogeneity and hence is ideal for large area displays and detectors. While a-Si has been studied at great length and its properties are well understood [132], its small bandgap doesn't allow for adequate attenuation of x-ray photons. To date, only direct conversion detectors based on a stabilized a-Se photoconductive layer have been commercialized [16] and the optical and electronic properties of a-Se will be discussed in detail in Section 3.3.

### 3.3 Selenium

The only commercialized direct conversion, flat panel detectors are based on a photoconductive layer of amorphous selenium [16]. What is interesting is that despite the in-depth work done to understand the electronic properties of a-Se in the 1970s as a result of its use in photocopying technology [13], much is still left to discover. This section will discuss the properties of amorphous selenium, as well as those of other forms of selenium, including a brief discussion of the crystalline forms. While crystalline Se is not suitable for use in an FPXI, it is instructive to include this discussion as theories on the structure of a-Se are based on knowledge of the crystalline structure of Se. Furthermore, a-Se has a tendency to revert to its crystal form over time (months to years) [65].

#### 3.3.1 Crystalline Selenium

Se is a member of Group VI of the periodic table and is called a chalcogen. Its atomic number,  $Z$ , is 34 and its electronic configuration can be represented as  $[\text{Ar}]3d^{10}4s^2p^4$ . The bonding configuration of selenium atoms can be seen in Fig. 3.1. The two 4s electrons and two of the 4p electrons form lone pairs (LP) which do not participate in bonding while the other two 4p electrons are involved in forming covalent bonds, leading to a coordination number of 2 with an optimum bond angle of  $105^\circ$  [133].

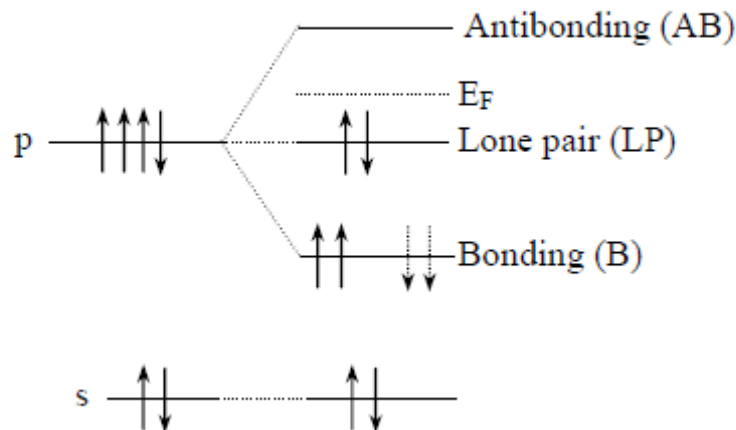


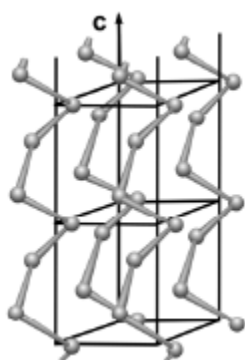
**Figure 3.1** The bonding configuration of selenium atoms; after [63].

Forming only 2 bonds per atom leads to a rather flexible structure and as a result several crystalline modifications have been described [134-136]. Crystalline Se is often said to have two main allotropes:  $\alpha$ -monoclinic, which is made up of  $\text{Se}_8$  rings, and trigonal ( $\gamma$ -Se), which is made of chains of many (n) Se atoms ( $\text{Se}_n$ ) [118]. However, a lengthy review by Minaev *et al.* [135], outlines the other forms, including:  $\beta$ -monoclinic (made of  $\text{Se}_8$  rings), rhombohedral (made of  $\text{Se}_6$  rings), orthorhombic (possibly made of  $\text{Se}_7$  rings), and  $\alpha$ - and  $\beta$ - cubic, which are produced in films. A summary of the characteristics of these allotropes can be found in Table 3.1.

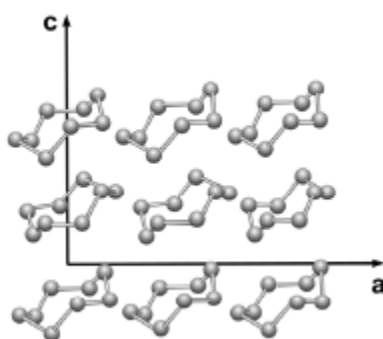
Trigonal Se is the thermodynamically stable allotropic modification. It has a melting temperature of roughly 217 °C and a bond length of 237 pm and is made of long chains of Se atoms as shown in Fig. 3.2 (a). Trigonal Se has a dihedral angle of 100.6 ° (see Fig. 3.3 for an explanation of the dihedral angle).  $\alpha$ - and  $\beta$ - monoclinic Se turn into trigonal Se above 140 °C. Their unit cells contain 4  $\text{Se}_8$  molecules with the arrangement differing between the forms as shown in Fig. 3.2 (b) and (c) [135].

**Table 3.1 Allotropic forms of Se as summarized in [135].**

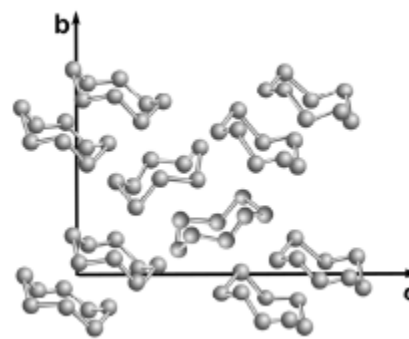
Name	Molecular composition	Bond length (pm)	Bond angle (deg.)	Coordination number $K_1$	Unit cell constants			Transformation temperature T (°C)	Density (g cm <sup>-3</sup> )
					a	b	c		
					(pm)	(pm)	(pm)		
<b>Crystalline</b>									
Trigonal	Spiral chains $Se_n$	237	103.1	2	436.6	-	495.4	Melting 217 – 221	4.819
$\alpha$ -monoclinic	Rings $Se_8$	232	105.9	2	905.4	908.3	1160.1	Transformation into trigonal 140 – 160	4.390
$\beta$ -monoclinic	Rings $Se_8$	234	105.5	2	1285	807	931	Transformation into trigonal 140 – 180	
$\alpha$ -cubic	-	297	-	6	297.0	-	-	-	
$\beta$ -cubic	-	248	-	4	575.5	-	-	-	
Rhombohedral	Rings $Se_6$	235	101.1	-	1136.2	-	442.9	Transformation into trigonal 120 – 135	4.710
Ortho-rhombic	-	-	-	-	2632	688	434	Transformation into trigonal 105	
<b>Non-crystalline</b>									
Red amorphous	Rings	233		~2.4	-	-	-	~ $T_{room}$	4.270
Black amorphous	-	-		-	-	-	-		
Vitreous	Chains and rings	233 246	105	2 – 2.2	-	-	-	Softening 30	4.280
Melt									4.010



**(a) Trigonal Se**



**(b)  $\beta$ -monoclinic Se**



**(c)  $\alpha$ -monoclinic Se**

**Figure 3.2 Molecular structure of the main allotropes of crystalline Se; after [7].**

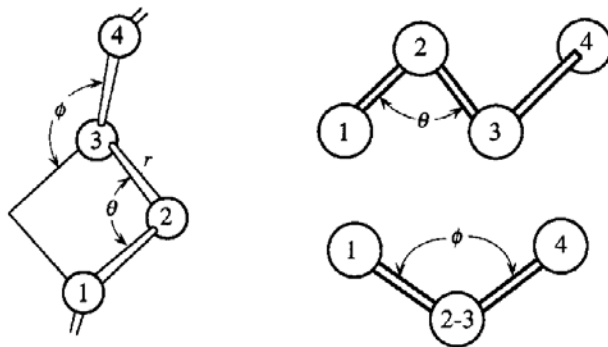


**Figure 3.3 Definition of important bonding parameters in a-Se. The dihedral angle,  $\phi$ , is the angle between the bonding planes of atoms 1, 2, 3 and 2, 3, 4, while  $\theta$  is the angle between the bonds formed by a given atom; after [118].**

### 3.3.2 Amorphous Selenium

As mentioned earlier, amorphous Se is the only photoconductor which has seen commercialization in a direct conversion x-ray image detector. As the work presented in this thesis focuses on a-Se films, the structure, electronic density of states, structural defects and important optical and electronic properties of a-Se with regards to its use as an x-ray photoconductor will be reviewed in detail in this subsection.

#### 3.3.2.1 Structure of Amorphous Selenium

In many works, the terms “vitreous” and “amorphous” are used synonymously to describe different phases of Se. In his review, Minaev [135] makes a distinction between the two. Vitreous Se is regarded as being the bulk material cooled from the melt. The critical cooling rate to avoid crystallization is 20 °C/min [134] and the glass transition temperature is ~ 40 °C [7]. Much effort has been expended trying to determine the structure of vitreous Se, but as summarized by Minaev [135], many of these results have been contradictory. It is no surprise that this is a somewhat difficult problem to solve. Given the large number of possible polymorphs of crystalline Se outlined in the previous section, more than 4 liquid forms can be obtained by melting crystalline Se. Obviously, the structure of the vitreous Se being studied will depend on the structure of the liquid quenched. Minaev concludes that the structure of vitreous

Se consists mainly of tangled chains of  $\text{Se}_8$  and  $\text{Se}_6$  ring fragments and chains of trigonal Se with a smaller amount of separate  $\text{Se}_8$  and  $\text{Se}_6$  rings.

Minaev classifies “amorphous” Se as being non-crystalline, non-vitreous and uses the term “ultra-dispersive” to refer to this powder- and film-like non-vitreous form [135]. He subdivides this category into red, black and brown a-Se and a-Se deposited by vacuum deposition. Red a-Se can be prepared through precipitation of Se from acidic selenic solutions [134] and is thought to consist of rings of Se atoms [135]. Less is known about black and brown a-Se, but the IR spectra of red and black are almost identical and red a-Se turns into black a-Se at  $\sim 37\text{ }^\circ\text{C}$  [134].

The films of a-Se studied in the work presented in this thesis are created through vacuum deposition techniques. The composition of the vapour used to create these films can vary greatly depending on temperature and, of course, the structure of the vitreous material used. It is thought that Se vapours consist of a mixture of  $\text{Se}_6$ ,  $\text{Se}_5$ ,  $\text{Se}_8$ ,  $\text{Se}_2$  and  $\text{Se}_7$  molecules around  $330\text{ }^\circ\text{C}$  while the amount of smaller particles (*i.e.*  $\text{Se}_2$ ) increases with the vapour temperature [137]. Thus the structure, and hence electronic properties, of a-Se films depend on the evaporation conditions used to create them (*i.e.* source and substrate temperature).

Popescu has proposed that there are two classes of a-Se thin films: films deposited onto low temperature substrates, called a-Se-I, and films produced at high temperatures and bulk vitreous Se, deemed a-Se-II [135]. a-Se-I is primarily made up of  $\text{Se}_8$  rings as a low substrate temperature would cause the structure of the Se vapour to be locked in immediately after contact with the substrate. a-Se-II is thought to consist mostly of polymer chains. Popescu found a maximum chains-to-rings ratio at a substrate temperature of  $50\text{ }^\circ\text{C}$  and stated that a-Se-I can be annealed into a-Se-II [135].

Takahashi has proposed a structural model in which the films are made of short ( $\sim 10$  atom) chains of Se with dihedral angles inside the chains similar to  $\gamma$ -Se, while chains are linked by different dihedral angles [138].

A similar interpretation is given by Lucovsky's "random chain model" in which all atoms are in a twofold coordinated chain structure with a dihedral angle that is constant in magnitude but changes in sign randomly [133,134,139,140]. A series of consistently-signed dihedral angles leads to a chain-like segment while an alternating sign results in a ring-like segment as shown in Fig. 3.4. This model accounts for both  $Se_8$  and  $Se_n$  chain-like features in IR absorption and Raman scattering spectra and is generally supported by several studies [141-143].

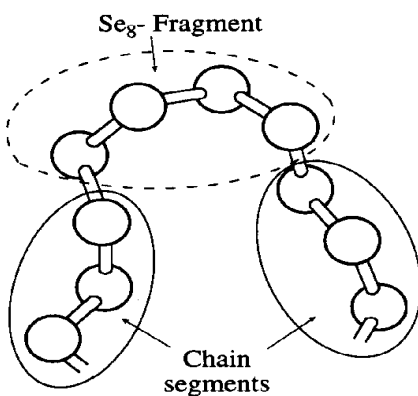


**Figure 3.4 Proposed structure of a-Se, consisting of chain and ring segments defined by repetition of the same dihedral angle sign or alternating dihedral angle sign, respectively; after [118].**

Clearly, no consensus has been reached on the true structure of a-Se, in that no one model has been shown to completely account for all measured properties. Given the variation in some of the properties reported for different a-Se films, it could be very likely that there is no unique answer, each film having a slightly different structure, dependent upon deposition conditions and techniques, the starting material used and the history of the film.

### 3.3.2.2 Electronic Density of States of Amorphous Selenium

One of the most important tools in understanding a material's electronic properties is the density of states (DOS) in the energy band model. The lack of long range order in amorphous solids suggests that the energy band model used to describe the electrical properties of crystalline semiconductors may not necessarily apply. However, one must start somewhere. Thus this well understood and tested model is extended to amorphous semiconductors, the lack of long range

order causing tailing of the transport bands into the forbidden bandgap which contains deep localized states due to defects.

Looking at the energy band of a-Se through the bond orbital model shows that the two 4p electrons which form covalent bonds (in a ring or chain) make  $\sigma$ -type bands 3 – 7 eV below the valence band edge while the top of the valence band (0 – 3 eV below the edge) is made of the lone pair 4p electrons. The conduction band is made of  $\sigma^*$  antibonding states from the 4p electrons involved in covalent bonding. This proposed model has been examined and confirmed by calculations and photoemission experiments on all phases of Se [144,145]. This model suggests a narrow valence band edge with only  $\sim 0.1$  eV of tailing. This makes sense, as the lone pairs which form the top of the valence band would not be affected much by the structural disorder of a-Se. This model estimated an upper limit of  $10^{20}$  eV<sup>-1</sup> cm<sup>-3</sup> states in the bandgap of vacuum deposited films [144].

One of the most commonly accepted models for the DOS of a-Se was put forth by Abkowitz in 1988 [140]. It is an extension of the Owen-Marshall model for As<sub>2</sub>Se<sub>3</sub> [146]. This model can be seen in Fig. 3.5 and features quickly decaying band tails with four narrow peaks of localized states in the bandgap. The locations of the shallow hole and electron traps at 0.25 eV above  $E_v$  and 0.35 eV below  $E_c$  were derived by analysis of the temperature dependence of carrier mobility in time-of-flight (TOF) transient photoconductivity measurements [147]. The deep traps in this model near the Fermi level were placed through the analysis of time-resolved xerographic measurements.

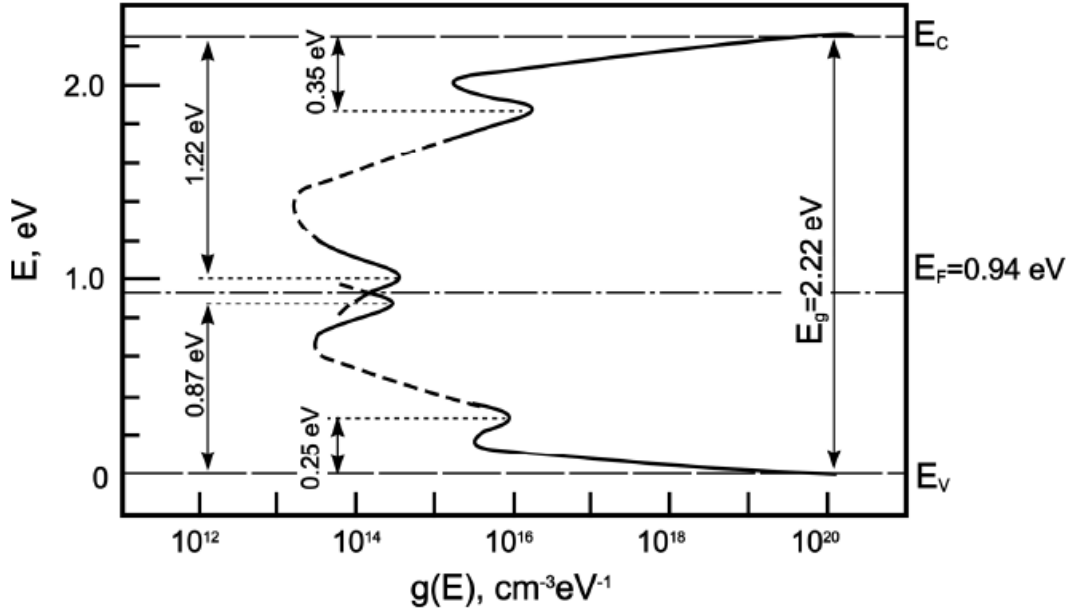


**Figure 3.5** The density of electronic states in a-Se as proposed by Abkowitz [7,140]; **after** [7]. Peaks in concentration of shallow states exist at 0.25 eV above  $E_v$  and 0.35 eV below  $E_c$  while peaks in deep states are located at 0.87 eV above  $E_v$  and 1.22 eV below  $E_c$ .

The terms “shallow” and “deep” when used to refer to carrier traps in the DOS are really relative terms. Deep means that the release time ( $\tau_r$ ) of a carrier trapped at this level is longer than the time scale of the experiment. A carrier trapped here is essentially “lost” to the observer. The shallow traps determine the observed carrier mobilities ( $\mu_e$  and  $\mu_h$ ) as short lived trapping and release events involving these traps during carrier drift lead to a reduction of the microscopic drift mobility in the extended states,  $\mu_0$ , as shown in Fig. 3.6, as was originally proposed by Spear [148]. This leads to the following relationship for holes:

$$\mu = \mu_0 \left[ 1 + \frac{N_{t_s}}{N_v} \exp\left(\frac{E_t}{kT}\right) \right]^{-1} \approx \mu_0 \frac{N_v}{N_{t_s}} \exp\left(-\frac{E_t}{kT}\right) \quad (3.1)$$

where  $N_{t_s}$  is the shallow trap concentration and  $N_v$  is the DOS at the valence band edge ( $E_v$ ). Equation 3.1 assumes a discrete, monoenergetic set of deep traps which predicts a microscopic hole mobility of 0.3 – 0.4  $\text{cm}^2 \text{V}^{-1} \text{s}^{-1}$  [147,149], while the microscopic electron drift mobility has

been reported to be  $0.1 \text{ cm}^2 \text{ V}^{-1} \text{ s}^{-1}$  [147]. This relates to simply multiplying the microscopic drift mobility by a transport parameter,  $\theta$ , to get the effective drift mobility,

$$\mu = \theta\mu_0 \quad (3.2)$$

The value of  $\theta$  is 0.4 for holes and about an order of magnitude smaller for electrons in a-Se [150]. It should be noted that a carrier trapped in a shallow state cannot be deeply trapped, therefore, the lifetime ( $\tau_e$  or  $\tau_h$ ) of a carrier depends on  $\theta$  and the concentration of deep traps,  $N_{td}$ , as

$$\tau = \frac{1}{C_t N_{td} \theta} = \frac{1}{C_r v_{th} N_{td} \theta} \quad (3.3)$$

where  $C_t$  is the capture coefficient given by the product of the capture cross section,  $C_r$ , and the thermal velocity of the carrier,  $v_{th}$ . Even a carrier trapped in a deep center will eventually be released and this release time is given by

$$\tau_r = \frac{1}{\nu_0} \exp\left(\frac{E_t}{kT}\right) \quad (3.4)$$

where  $\nu_0$  is the attempt to escape frequency (typically  $10^{12} \text{ s}^{-1}$ ),  $k$  is the Boltzmann constant and  $E_t$  is the energy depth of the traps from the band edge.

The DOS model by Abkowitz is supported by other experimental evidence. Carrier mobility vs. temperature data has been shown to have the form of Eq. 3.1 with a trap level of  $\sim 0.29 \text{ eV}$  above  $E_v$ . This gave the relation:  $\mu_0 \sim T^{-n}$  where  $n \sim 1$  [147]. Furthermore, the value for the microscopic hole mobility predicted by Eq. 3.1 is similar to values reported from Hall effect measurements [151]. A similar argument leads to an electron shallow trap level of  $0.35 \text{ eV}$  below  $E_c$  [65], in agreement with Fig. 3.5. Also in support of the model in Fig. 3.5, sharply (exponentially) decaying shallow trap densities from the transport bands have been suggested by the microwave stripline experiments of Orłowski and Abkowitz [152].

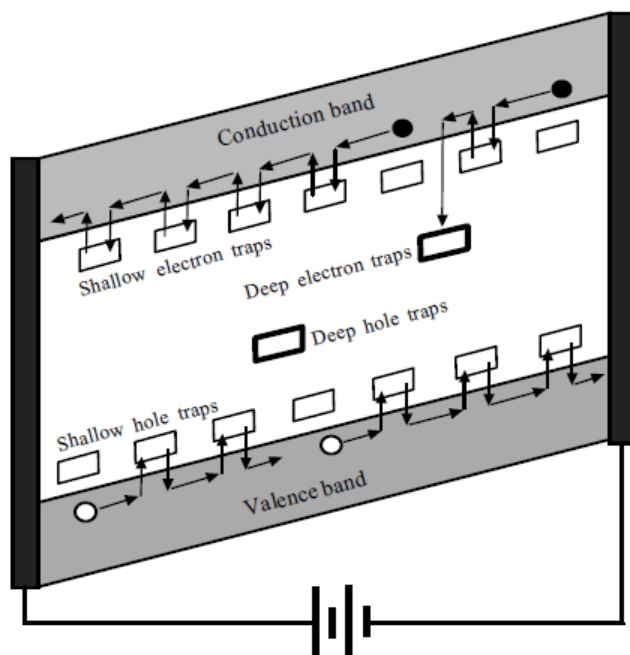


**Figure 3.6** Diagrammatic representation of electron and hole drift, with the microscopic mobilities in the transport bands reduced by short lived trapping and release events involving shallow traps. Carriers trapped by deep traps are essentially lost during the time scale of interest. The application of the electric field tilts the bands to demonstrate increased potential energy for electrons at the negative terminal of the source; after [63].

Work prior to the Abkowitz model suggested that a model with three levels of traps for each carrier is needed to correctly explain experimental results. In 1967, Blakney and Grunwald analyzed the shape of TOF transient photocurrents for electrons and found evidence for three electron trap levels: two near those later proposed by Abkowitz plus a peak 0.4 – 0.48 eV below  $E_c$  [153]. In 1969, Yasar reported that transient polarization hole currents are controlled by two levels of traps: 0.48 and 0.8 eV above  $E_v$  [154]. However, in 1977 Noolandi found that three levels were needed to fit hole TOF experiments [155].

In the past 20 years, two new models for the DOS in a-Se have been put forth, the first of which emerged late last century. Adriaenssens' group, after much work with post transit photocurrent analysis, settled on the distribution shown in Fig. 3.7 [156,157]. In this model, there are peaks of hole traps 0.4 eV above  $E_v$  and electron traps 0.52 eV below  $E_c$ , but carrier drift is controlled by energetically distributed shallow localized states tailing from the transport

bands. If this is the case, then the reduction of microscopic drift mobility described in Eq. 3.1 becomes

$$\mu \approx \mu_0 \left( \frac{\Delta E}{kT} \right) \exp \left( -\frac{\Delta E}{kT} \right) \quad (3.5)$$

where  $\Delta E$  is the width of the tail from the transport band [158].

An interpretation using Eq. 3.5 and Fig. 3.7, implying electron drift in the tail states, gives a mobility with activation energy equal to the width of the decaying tail states,  $\sim 0.4$  eV. However, this is experimentally measured as 0.35 eV [65]. Adriaenssens' group explained the differences with the Abkowitz model by suggesting that the experimental results used to form the Abkowitz model had been misinterpreted [159], but due to the aforementioned inconsistency of the model and the experimental support for the Abkowitz model, the Adriaenssens model is not as widely accepted in the scientific community [7].

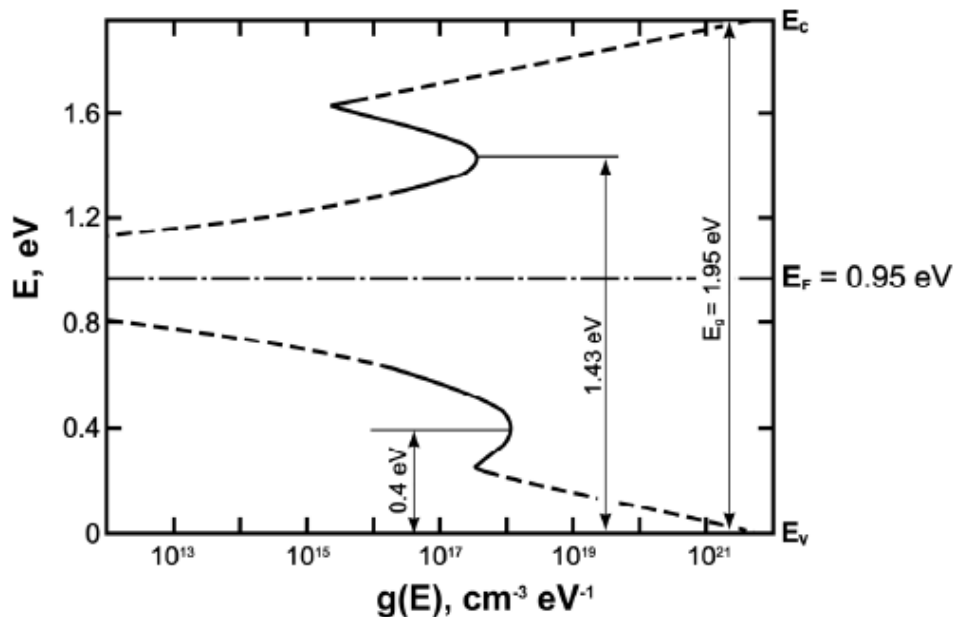


**Figure 3.7** The density of electronic states in a-Se as proposed by Adriaenssens *et al.* [7,156,157]; after [7]. The solid lines represent data from the energy range that is accessible by the post transit time-of-flight experiments used. There are single peaks at 0.4 eV above  $E_v$  and 0.52 eV below  $E_c$ .

Recent work by Koughia *et al.* [160-162] has attempted to construct the effective DOS of a-Se by comparing the measured electron and hole transient TOF photocurrents with the theoretically calculated photocurrent for a given DOS, using an approximate numerical inversion of the Laplace transform. This was based on the original assumption that the DOS is a nearly continuous function; a sum of predefined functions. They originally assumed a sum of spline functions which was later replaced with the sum of an exponential and several Gaussians. Their results were supported by Monte Carlo simulations which simulated photocurrents for the given DOS. As seen in Fig. 3.8, this work suggests that there is a peak at 0.3 eV and a shoulder at 0.45 – 0.5 eV below  $E_c$  and concentrations of deep states more than 0.65 eV below  $E_c$  and 0.55 eV above  $E_v$ , the exact distribution of which could not be resolved from these methods. The more controversial result is the featureless, monotonically decreasing distribution of shallow localized states near  $E_v$  without the previously accepted peak at 0.25 eV above  $E_v$ . The proposed DOS correctly predicts the dependence of carrier mobility on temperature at different electric fields. While the smooth decay of states near the valence band edge is in agreement with the DOS proposed by Naito *et al.* [163], it bears little resemblance to the Abkowitz model, nor the Adriaenssens model, near  $E_v$  and implies a wider tail than has been observed experimentally [144,145]. Furthermore, the methods used in this work have been criticized as being unreliable due to the difficulty of gathering data over a time scale of as much as 15 orders of magnitude and the fact that one must start with a predefined general form for the DOS [7]. In essence, if you look hard enough for something, you will probably find it.

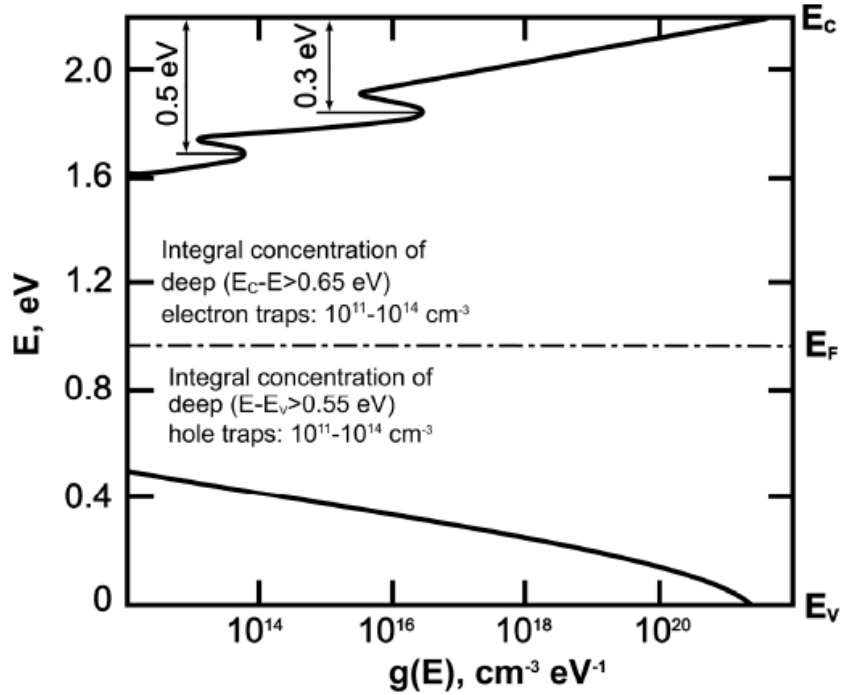


**Figure 3.8** The density of electronic states in a-Se as proposed by Koughia *et al.* [7,160-162]; after [7]. There are two peaks of shallow states at 0.3 eV and 0.5 eV below  $E_c$  while there is a featureless decay in state concentration near  $E_v$ . The exact location of deep states could not be resolved with the method used.

Clearly, there is still much contention about the true DOS of a-Se. Furthermore, while it is known that both the mobility of electrons and holes in a-Se are thermally activated [65], the nature of the microscopic conduction process in a-Se has not been conclusively established. It could be due to extended state transport, as discussed above, to small polaron hopping [164] or hopping in the localized tail states [165]. This last option would involve holes hopping in a region  $\Delta E$  above  $E_v$  with interruptions due to trapping at a level  $E_t$  above  $E_v$ . Observed mobility activation energy would be  $E_t - \Delta E + W_{hop}$  where  $W_{hop}$  is the activation energy for hopping in the tail states [65]. At low temperatures, this energy should decrease to  $W'_{hop}$ , corresponding to hopping at  $E_t$ . This has not been observed experimentally for a-Se down to 124 K [166]. Further, it has been argued that the lack of pressure dependence in the thermally activated drift mobility down to  $\sim 230$  K does not represent a purely hopping transport process [118,167].

A good understanding of the DOS is crucial to improvements in photoconductor performance as carrier drift mobility is controlled by shallow localized states in the mobility gap

and carrier lifetime is determined by the concentration of deep localized states and together these two properties determine the carrier range in the photoconductor. Despite the continued controversy, much research has been based on the idea that the valence and conduction bands have quickly decaying tails and the bandgap contains narrow peaks of localized states with relatively low concentrations (when compared to other photoconductors). Modeling of the dark current, MTF and sensitivity of a-Se FPXIs has yielded positive results by assuming that each peak can essentially be treated as a single discrete state [2,57,59,63].

### 3.3.2.3 Structural Defects in Amorphous Selenium

While there still exists speculation as to the true density of states in the bandgap of a-Se, it is understood that there is a large concentration of deep states near the Fermi level. These deep states are due to equilibrium defects which cannot be removed through means of quality control [168,169]. Several studies have attempted to unveil the true nature of structural defects in a-Se, but much like the work aimed at uncovering the structure of a-Se, some results contradict others.

Based on Anderson's idea of negative  $U$  defects [170], that is, defects with a negative correlation energy, Street and Mott [171] proposed the following exothermic reaction for chalcogens:



in which the homolytic breaking of bonds forms pairs of charged defects.

Work by Kastner, Adler, Fritzsche and Feltz [134,172-175] has concluded that the lowest energy defect in chalcogens, and hence in a-Se, is a pair of over- and under-coordinated atoms: triply bonded  $Se_3^+$  and singly bonded  $Se_1^-$  centers (in the case of Se), as explained diagrammatically in Fig. 3.9. If we take the energy of the nonbonding (NB) orbital to be zero, then the energy of an electron in a bonding (B) orbital is  $-E_b$ . Anti-bonding (AB) orbitals are pushed up in energy more than B orbitals are pushed down, so the energy of an AB orbital is  $E_b + \Delta$ , where  $\Delta > 0$ . The correlation energy ( $U$ ) of placing an electron in an antibonding orbital is

smaller than for a lone pair (LP) orbital ( $U_{AB} < U_{LP}$ ).  $E_b$  is much larger than  $\Delta$ ,  $U_{AB}$  and  $U_{LP}$ . While the energy of a normally bonded Se atom is  $-2E_b$ , a dangling bond,  $Se_1^0$ , has an energy of  $-E_b$ . The lowest energy neutral defect is a neutral, triply-bonded Se atom,  $Se_3^0$ . However, this defect is unstable [172], and the following reaction takes place:



with a reduction in total energy from  $(-4E_b + 2\Delta)$  to  $(-4E_b + U_{LP})$  where  $U_{LP}$  is less than  $2\Delta$ .

The resulting set of charged defects is called a “valence alternation pair” or VAP. If they are in close physical proximity, they are called an “intimate valence alternation pair” or IVAP, as seen in Fig. 3.10. This set of traps appears overall charge neutral but can still trap either a hole or electron [118]. In support of this theory, it has been shown through TOF and xerographic cycled-up residual measurements that the deep hole trap capture radius is 0.2 – 0.3 nm [176], characteristic of a neutral trap [65]. These defects are either doubly occupied or unoccupied which means they carry no net electron spin. This accounts for the lack of a measurable electron spin resonance (ESR) signal in a-Se [177,178]. Many of the photoelectric properties of a-Se can be at least qualitatively explained by the IVAP model. For example, it has been used to interpret the linear dependence of the steady-state photoconductivity of a-Se on the incident light intensity [179] and some molecular-dynamic simulations [180] support this model as well.

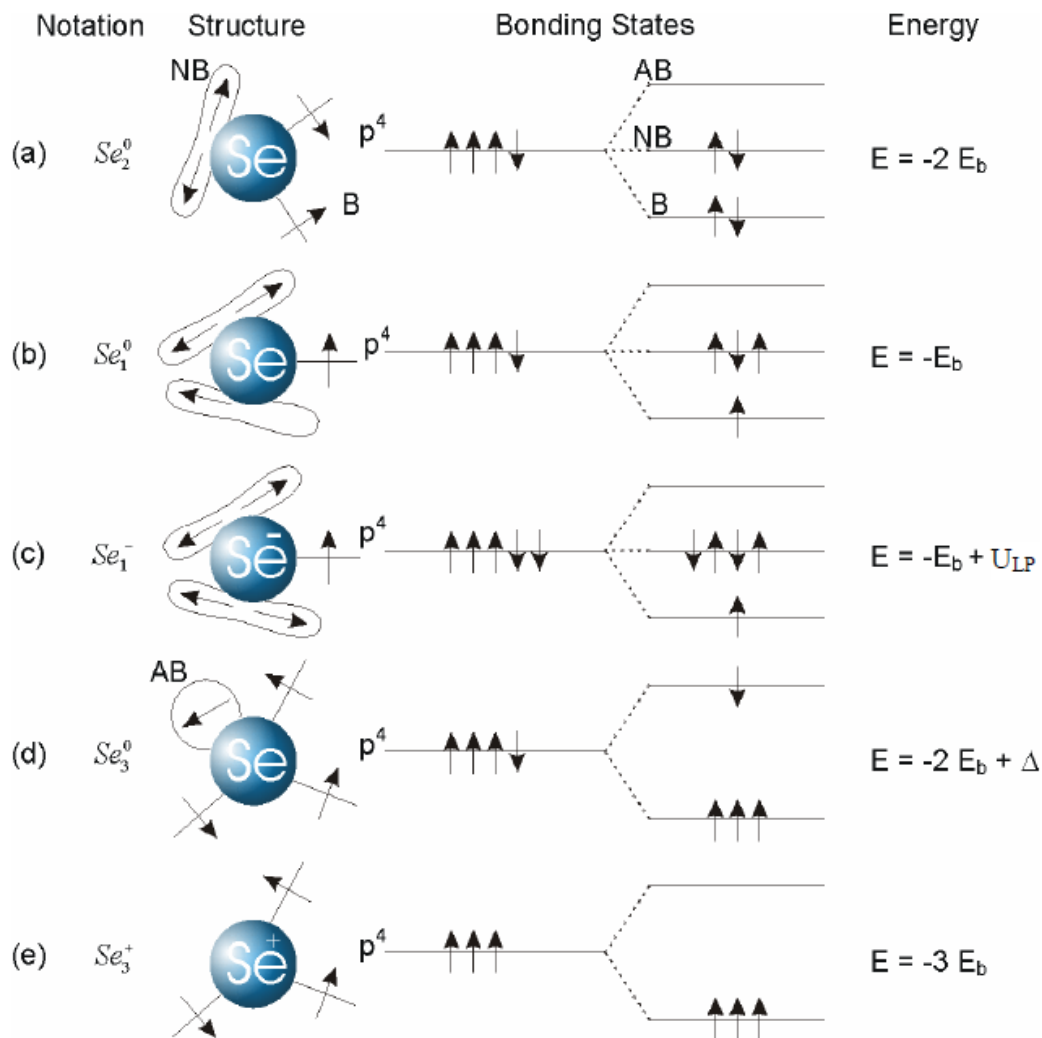


**Figure 3.9 Structure and energy of simple bonding configurations for selenium atoms. Straight lines represent bonding (B) orbitals, lobes represent lone-pair (NB) orbitals, and circles represent anti-bonding (AB) orbitals. The energy of a lone-pair is taken as zero; after [63]. (a) A normally bonded a-Se atom,  $Se_2^0$ , (b) A neutral under-coordinated Se atom,  $Se_1^0$ , (c) A negatively charged under-coordinated Se atom,  $Se_1^-$ , (d) The lowest energy neutral defect in a-Se, an  $Se_3^0$  atom, (e) A positively charged over-coordinated Se atom,  $Se_3^+$ .**

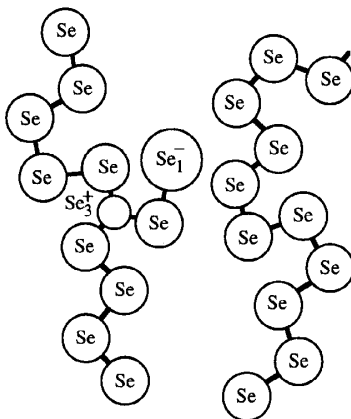


**Figure 3.10 Schematic representation of a possible atomic structure of a-Se, showing over- and under-coordinated defects; after [118].**

Arguments have been made that VAPs cannot be the dominant type of defect in a-Se, as the average coordination number in a-Se is  $\sim 2.2$  [181] and the coordination number of a VAP is exactly 2. Based on calculations by Vanderbilt and Joannopoulos [182] which show that VAPs are not energetically favourable, Stuedel [183] has suggested a model containing hypervalent defects, namely  $Se_4^0$  and  $Se_3^d - Se_1^d$  (where the bond between the centers is a double bond). There is some evidence for the  $Se_4^0$  defect in the IR spectra of red a-Se [184].

Molecular-dynamic simulations have offered models which contain a mixture of isolated  $Se_3$  defects, paired  $Se_3$  defects ( $Se_3 - Se_3$ ), VAPs, isolated  $Se_1$  defects and  $Se_4$  defects or some subset of these [180,185]. However, these types of simulations have been criticized as being unreliable as, due to their complex nature, they cannot currently be carried out on hypothetical systems containing more than  $\sim 4000$  atoms (due to the limit of computational power). Indeed, many of the aforementioned works considered systems of only 64 or 216 atoms and one must be concerned about the effects of such scaling when even a single chain of Se can contain  $10^5$  atoms [7].

Much like the story of the structure of a-Se and its DOS, the tale of the structural defects in a-Se has no conclusive ending yet. It should be mentioned that further complicating the situation is the fact that defects other than the ones mentioned above can exist in a-Se. These defects can be due to impurities of different sizes and valencies and to nano- and micro-crystals

of one of the many crystalline modifications of Se, which are nearly impossible to avoid in the preparation of a-Se films [186]. Clearly, much has yet to be discovered about the true nature of a-Se.

### 3.3.2.4 Amorphous Selenium as an X-ray Photoconductor

While the discussion thus far in this chapter has been focused on pure a-Se, pure a-Se has a tendency to crystallize over time, altering its electronic properties. The photoconductor used in flat panel detectors is called “stabilized a-Se”. It is a-Se alloyed with a small amount (0.2 – 0.5%) As and doped with 10 – 40 ppm (parts per million) Cl. Stabilized a-Se has similar properties to pure a-Se and its important properties are listed in Table 3.2.

**Table 3.2 Properties of stabilized a-Se (a-Se:0.2-0.5%As + 10-40 ppm Cl) films at room temperature (data taken from [65]).**

Property	Typical Range	Schubweg at 5 V $\mu\text{m}^{-1}$	Comment
Hole mobility $\mu_h$	0.12-0.14 $\text{cm}^2 \text{V}^{-1} \text{s}^{-1}$		Well reproducible. Probably shallow trap controlled.
Electron mobility $\mu_e$	0.003-0.006 $\text{cm}^2 \text{V}^{-1} \text{s}^{-1}$		Decreases rapidly with As addition. Probably shallow trap controlled.
Hole lifetime $\tau_h$	20-200 $\mu\text{s}$	1.2 – 12 mm	Depends on the substrate temperature.
Electron lifetime $\tau_e$	200-1000 $\mu\text{s}$	0.3 – 1.5 mm	Sensitive to small quantity of impurities.
Hole range $\mu_h\tau_h$	2- 20 $\times 10^{-6} \text{cm}^2 \text{V}^{-1}$		Substantially higher than $\text{PbI}_2$ .
Electron range $\mu_e\tau_e$	1- 6 $\times 10^{-6} \text{cm}^2 \text{V}^{-1}$		Somewhat higher than $\text{PbI}_2$ .

The success of stabilized a-Se as an x-ray photoconductor in commercialized FPXIs is largely due to the fact that it can be coated over large areas by straightforward thermal evaporation in a conventional vacuum coater, as will be discussed in Section 4.2.1. However, evaporating a Se-As alloy such as stabilized a-Se can result in fractionation of the film where condensed layers have different compositions [65]. Fractionation can be contributed to by non-uniform temperatures in the boat containing the source material, the material’s finite thermal

conductivity and limited diffusion in the source material [65]. During evaporation, the initial vapour is Se-rich and as it leaves the boat, the surface region of the source material becomes rich in As, leaving a different composition of material to be evaporated [187]. If the source material is evaporated to completion, the surface region of the film will have a higher As concentration than the bulk of the film. It has been found that if the beads used as the source material are surface crystallized by tumbling in a rotary mixer, the fractionation effects are greatly reduced [188].

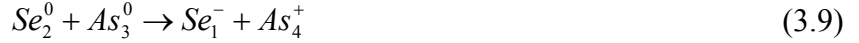
### 3.3.2.4.1 Effects of Alloying with As

As has a valency of three and therefore the As atoms are triply bonded, linking neighbouring Se chains. This increases viscosity and prevents crystallization of films. Extensive work by Belev [7,189,190] studying the carrier transport of several alloys of stabilized a-Se films has confirmed that the addition of As decreases the hole lifetime and, hence, range. Conversely, the addition of As increases the lifetime of electrons. It also decreases the mobility of electrons, but as the As content increases, the electron lifetime increases more than the mobility decreases and thus the electron range shows an overall increase with the addition of As. A summary of these effects can be seen in Table 3.3.

The exact way in which the addition of As causes these changes is still speculative, but one explanation can be given in terms of a change in the balance of the charged over- and under-coordinated defects ( $Se_3^+$  and  $Se_1^-$ ) involved in VAP theory [7]. The experimentally observed changes in carrier transport can be partially explained by the following reaction:



where deep electrons traps ( $Se_3^+$ ) are sacrificed for shallow electron traps ( $As_4^+$ ), predicting an increase in electron lifetime and a decrease in electron mobility. This second reaction completes the explanation:



where a normally bonded Se atom becomes a deep hole trap ( $Se_1^-$ ) predicting the observed decrease in hole lifetime. Eq. 3.9 also predicts the creation of shallow electron traps ( $As_4^+$ ), as does Eq. 3.8. Since both reactions involve the creation of shallow electron traps and only the first involves the loss of deep electron traps, one would assume from this theory that the electron mobility would decrease more than the electron lifetime increases, resulting in an overall decrease in electron range. This is the opposite of what is observed experimentally [7]. Another inconsistency in this theory is that the electronegativity of As is close to that of Se, meaning that both  $As_2^-$  and  $As_4^+$  defects would be created. Formation of  $As_2^-$  defects should require less energy than  $As_4^+$  defects, as  $As_2^-$  defects fit nicely into a Se chain structure while  $As_4^+$  defects need to form 4 bonds, causing a greater lattice distortion.  $As_2^-$  defects would act as hole traps and thus the exact role of As is not completely clear. Belev's work has also shown that charge transport in stabilized a-Se films also depends on the properties of the starting a-Se material and the addition of As can actually cause a decrease in electron range in some alloys [7]. It is obvious that the As atoms must be altering the structure of the a-Se in ways other than, or in addition to, the defect formation described above.

### 3.3.2.4.2 Effects of Doping with Cl

While the addition of small amounts of Cl to pure a-Se can have very different effects [7], Cl is added to stabilized a-Se to restore the hole transport. Cl is added in very low levels of ppm so it is difficult to detect and determine the doping profile throughout a thick film. However, interrupted field time-of-flight (IFTOF) measurements have suggested that the Cl doping profile is approximately uniform [191]. Work by Belev [7,192] has shown that the addition of Cl increases the hole lifetime and range very strongly and it only takes the addition of around 20 ppm Cl to compensate for the addition of 0.2% As. Adding Cl has also been shown to decrease electron lifetime. These effects are summarized in Table 3.3.

As for As, an explanation of the effects of Cl addition has been attempted using the framework of VAP theory. Cl is highly electronegative, so the following two reactions are probable:



The first reaction shows the creation of deep electrons traps ( $Se_3^+$ ) and hence a decrease in electron lifetime, as observed. Equation 3.11 predicts the loss of deep hole traps ( $Se_1^-$ ) and the observed increase in hole lifetime. Of course, this theory only works if  $Cl_0^-$  does not act as a shallow or deep carrier trap.

### 3.3.2.4.3 Effects of Doping with O

Belev has also done in depth work measuring the effect of oxygen doping [7,192], introduced as  $SeO_2$ , in pure a-Se films, as O is a highly probable contaminant in a-Se alloys. Previous work had shown that O, in concentrations of less than 1800 ppm has no effect on carrier mobilities, but both electron and hole lifetimes decrease when the O concentration is greater than 100 ppm [193]. The work by Belev found that O levels as low as 47 ppm eliminate electron transport almost completely, as the electron lifetime is reduced by around 150 times. However, it was found that the same level of O actually increased hole lifetime by around 26 times, while the hole mobility was decreased. Even 7 ppm O was found to change both carrier lifetimes, while the mobilities were unaffected.

To explain these results, Belev [7] has used a treatment based on VAP theory with the more highly electronegative O atoms competing with chain ending Se atoms ( $Se_1^0$ ) for electrons from  $Se_3^0$  defects. This explanation shows that above a certain threshold of O concentration, the concentration of deep electron traps ( $Se_3^+$ ) increases while the concentration of deep hole traps

( $Se_1^-$ ) decreases, though not necessarily in the same proportion as observed experimentally. Other explanations include the formation of other types of defects or nano- and micro-crystals of Se [7].

Belev's results [7] also showed that ageing of O doped a-Se samples in the dark for several months resulted in improved electron transport, but deteriorated hole transport. Ageing of both pure and stabilized a-Se films usually results in the transport of both types of carriers improving [194].

Again, it must be concluded that what is happening on the atomic level in a-Se is simply not understood at present. Another important, but generally unexplained effect is that the addition of a few ppm of an alkali metal, such as Na, to stabilized a-Se increases the electron range, but greatly reduces hole transport making a-Se:Na behave as if it were *n*-type [13]. It should be noted that although terminologies such as *n*- and *p*-type are convenient, a-Se cannot actually be doped in the same way that crystalline semiconductors are doped, as the Fermi level in a-Se is pinned relatively close to the middle of the bandgap due to the large concentration of localized states near midgap [13]. The exact method by which these impurities control the charge transport properties remains unsolved, but their use to do so has been one of the key factors in the success of a-Se as a photoconductor [195].

**Table 3.3 The influence of As alloying and Cl and O doping on charge transport in vacuum deposited a-Se films (summarized from [7]).**

Additive	Effects on Hole Transport			Effects on Electron Transport		
	Mobility	Lifetime	Mobility-lifetime product	Mobility	Lifetime	Mobility-lifetime product
<b>As</b>	no or very small change	decrease	decrease	decrease	increase	increase
<b>Cl</b>	no or very small change	strong increase	strong increase	no or very small change	strong decrease	strong decrease
<b>O</b>	decrease	strong increase	increase	no or very small change	strong decrease	strong decrease

### 3.4 Polycrystalline Photoconductor Candidates

Several polycrystalline photoconductors have shown promise for use as the conversion layer in an FPXI. Several of these are heavy metal compounds which attenuate x-rays much more efficiently than a-Se and have a lower  $W_{\pm}$ . These important photoconductors will be discussed in this section and their important photoconductive properties are summarized in Table 3.4, along with those of a-Se, for ease of comparison.

**Table 3.4** Some typical or expected properties of selected x-ray photoconductors for large area applications. PVD is physical vapor deposition; SP is screen printed.  $\delta$  is the attenuation depth at the shown photon energy, either 20 keV or 60 keV.  $\mu\tau$  represents the carrier range. From various references and combined selectively, including [28,29,196] and those listed in the table.

Photoconductor State Preparation	$\delta$ at 20 keV $\delta$ at 60 keV	$E_g$ eV	$W_{\pm}$ eV	Electron $\mu_e\tau_e$ (cm <sup>2</sup> /V)	Hole $\mu_h\tau_h$ (cm <sup>2</sup> /V)
Stabilized a-Se Amorphous Vacuum deposition [13]	49 $\mu\text{m}$ 998 $\mu\text{m}$	2.2	45 at 10V/ $\mu\text{m}$ 20 at 30V/ $\mu\text{m}$	$3 \times 10^{-7} - 10^{-5}$	$10^{-6} - 6 \times 10^{-5}$
HgI <sub>2</sub> Polycrystalline PVD [197]	32 $\mu\text{m}$ 252 $\mu\text{m}$	2.1	5	$10^{-5} - 10^{-3}$	$10^{-6} - 10^{-5}$
HgI <sub>2</sub> Polycrystalline SP [122,197-199]	32 $\mu\text{m}$ 252 $\mu\text{m}$	2.1	5	$10^{-6} - 10^{-5}$	$\sim 10^{-7}$
Cd <sub>0.95</sub> Zn <sub>0.05</sub> Te Polycrystalline Vacuum deposition (sublimation)	80 $\mu\text{m}$ 250 $\mu\text{m}$	1.7	5	$\sim 2 \times 10^{-4}$	$\sim 3 \times 10^{-6}$
CdTe Close-space-sublimation [66,200,201]	75 $\mu\text{m}$ 247 $\mu\text{m}$	1.45	4.43	Varies widely	Varies widely
PbI <sub>2</sub> , Polycrystalline Normally PVD [123,202]	28 $\mu\text{m}$ 259 $\mu\text{m}$	2.3	5	$7 \times 10^{-8}$	$\sim 2 \times 10^{-6}$ [203]
PbO, Polycrystalline Vacuum deposition	12 $\mu\text{m}$ 218 $\mu\text{m}$	1.9	8–20	$5 \times 10^{-7}$	small
TlBr Polycrystalline Vacuum deposition [204,205]	18 $\mu\text{m}$ 317 $\mu\text{m}$	2.7	6.5	$3 \times 10^{-6}$	$1.5-3 \times 10^{-6}$

### 3.4.1 Polycrystalline Mercuric Iodide (Poly-HgI<sub>2</sub>)

One of the more developed polycrystalline x-ray photoconductors is HgI<sub>2</sub>. It has a bandgap of 2.1 eV,  $W_{\pm}$  of roughly 5 eV, a density of 6.3 g/cm<sup>3</sup> [64] and resistivity of  $4 \times 10^{13} \Omega \text{ cm}$  [198]. Layers of HgI<sub>2</sub> can be deposited by physical vapour deposition (PVD) or screen printing (SP) from a slurry of HgI<sub>2</sub> crystals using a wet particle-in-binder process. FPXIs  $20 \times 25 \text{ cm}^2$  have been demonstrated through PVD and  $5 \times 5 \text{ cm}^2$  with SP [122]. The thickness of HgI<sub>2</sub> layers used varies from 100 – 500  $\mu\text{m}$  with grain sizes of 20 – 60  $\mu\text{m}$ . In an FPXI, a 1  $\mu\text{m}$  thick layer of insulating polymer is deposited between the HgI<sub>2</sub> layer and the pixellated electrode to reduce dark current and prevent the HgI<sub>2</sub> from reacting with the metal [122]. HgI<sub>2</sub> is very reactive and the photoconductive layer must be entirely encapsulated with a polymer layer to prevent reaction with the surrounding air. Recently demonstrated PVD HgI<sub>2</sub> FPXIs have shown a 10 – 70% decrease in x-ray sensitivity over the course of a few years, possibly due to insufficient encapsulation. This was not noticed in screen printed detectors used in the same study [120].

The dark current in HgI<sub>2</sub> layers increases super-linearly with the applied field. In PVD layers, the dark current depends strongly on temperature and can go from 2 pA/mm<sup>2</sup> at 10 °C to 180 pA/mm<sup>2</sup> at 35 °C at a field of 0.95 V/ $\mu\text{m}$  [206]. The dark current in screen printed layers is an order of magnitude lower, but the sensitivity is 2 – 4 times less.

Electrons are much more mobile than holes in HgI<sub>2</sub> and as a result, the top electrode is negatively biased.  $\mu_e \tau_e$  is  $10^{-6} - 10^{-5} \text{ cm}^2/\text{V}$  in screen printed films [122,207] and  $10^{-5} - 10^{-4} \text{ cm}^2/\text{V}$  in PVD films which is close to that of single crystal HgI<sub>2</sub>. This is likely due to the fact that the film grows upwards from the substrate in columns, allowing electrons to drift without crossing grain boundaries [208,209].

The lowest reported image lag is  $\sim 7\%$  first frame, 0.8% after 1 s and 0.1% after 3 s, operating at 15 frames/s. The lowest standard deviation in pixel-to-pixel sensitivity variation is

10% [206]. HgI<sub>2</sub> FPXIs have good resolution with a pre-sampling MTF almost equal to the theoretical sinc function resulting from the pixel aperture [64].

A recent advancement has been made where 50 – 250 μm thick films have been coated onto 400 × 400 pixel CMOS readout chips with a 30 μm pixel pitch [210]. The estimated MTF at 5 lp/mm is 0.6 and at an applied bias of 0.12 V/μm the sensitivity was 6200 pC cm<sup>-2</sup> mR<sup>-1</sup> and the dark current was 27 pA/mm<sup>2</sup>. These detectors were successfully used in small animal CT scans with an absorbed dose estimated to be about one order of magnitude less than would have been achieved with a commercially available phosphor coated readout.

### 3.4.2 Polycrystalline Lead Iodide (Poly – PbI<sub>2</sub>)

PbI<sub>2</sub> has a bandgap of 2.3 eV,  $W_{\pm}$  of 5 eV and a resistivity of 10<sup>11</sup> – 10<sup>12</sup> Ω cm [64]. PbI<sub>2</sub> films are usually created by PVD at temperatures of 200 – 230 °C. Usable layers are 60 – 250 μm thick and a detector with an area of 20 × 25 cm<sup>2</sup> has been demonstrated [211]. The grains in the films are hexagonal platelets less than 10 μm in size and this produces a layer with a density of 3 – 5 g/cm<sup>3</sup>, less dense than crystalline PbI<sub>2</sub> (6.2 g/cm<sup>3</sup>).

The dark current in PbI<sub>2</sub> increases sub-linearly with bias [211] and values as low as 10 pA/mm<sup>2</sup> have been reported [122], though are often higher than in HgI<sub>2</sub> detectors. The pixel-to-pixel sensitivity variation in PbI<sub>2</sub> detectors is lower than in HgI<sub>2</sub> detectors, but the overall sensitivity and resolution are lower [64]. PbI<sub>2</sub> detectors suffer from poor image lag characteristics (75% first frame and 15% after 3 s at 15 frames/s [211]). Holes are much more mobile than electrons in PbI<sub>2</sub> with a  $\mu_h\tau_h$  value of 1.8 × 10<sup>-6</sup> cm<sup>2</sup>/V [211].

PbI<sub>2</sub> can also be deposited through screen printing. Recently, new PbI<sub>2</sub> detectors have been developed where a reverse biased *p-n* junction is created between laminate layers of either BiI<sub>3</sub> and HgI<sub>2</sub> or PbO and PbI<sub>2</sub> [212]. 2 × 2 cm<sup>2</sup> prototypes were created using screen printing of PbI<sub>2</sub> and an impressively low dark current of 2 pA/mm<sup>2</sup> was measured at an applied field of 2 V/μm. This was decreased by a factor of 4 from single layer PbI<sub>2</sub> films. However, the laminate structure did show slightly reduced sensitivity in comparison to the single layer.

Very recently, a “sedimentation” method similar to screen printing has been used to create 200  $\mu\text{m}$  thick prototype films with an area of  $2 \times 2 \text{ cm}^2$  [123]. These films demonstrated a dark current of  $2.2 \text{ pA/mm}^2$  and a sensitivity of  $480 \text{ pC cm}^{-2} \text{ mR}^{-1}$  at  $1 \text{ V}/\mu\text{m}$ . This was only a slight improvement over previous screen printed films, but films made with the sedimentation method had excellent property linearity and a more uniform surface.

### 3.4.3 Polycrystalline Cadmium Zinc Telluride (Poly - $\text{Cd}_{0.95}\text{Zn}_{0.05}\text{Te}$ )

Polycrystalline CdZnTe (or CZT, as it is often called for short) films are initially coated onto an ITO coated alumina substrate by close-space-sublimation and subsequently bonded to each pixel of an AMA by resin bumps. CZT has a bandgap of 1.7 eV,  $W_{\pm}$  of 5 eV, a density of  $5.8 \text{ g/cm}^3$  and a resistivity of  $10^{11} \Omega \text{ cm}$  when comprised of 5% Zn, as is common ( $\text{Cd}_{0.95}\text{Zn}_{0.05}\text{Te}$ ). The introduction of Zn into the CdTe lattice increases the bandgap and hence the resistivity. It has been shown that CZT layers produce a dark current which increases almost linearly with the applied field and is roughly  $70 \text{ pA/mm}^2$  at  $0.4 \text{ V}/\mu\text{m}$  [124]. It has also been shown that continuing to increase the Zn concentration of the material decreases the dark current, as an 8% Zn film ( $\text{Cd}_{0.92}\text{Zn}_{0.08}\text{Te}$ ) exhibits a dark current of  $40 \text{ pA/mm}^2$  at  $0.4 \text{ V}/\mu\text{m}$  [213]. Electrons are more mobile than holes in polycrystalline CZT films, but  $\mu_e\tau_e$  is considerably less than in single CZT crystals [64].

FPXIs utilizing CZT as the photoconductive layer have been demonstrated [214] with a 200 – 500  $\mu\text{m}$  thick film covering a surface area of  $7.7 \times 7.7 \text{ cm}^2$ . CZT detectors have very high x-ray sensitivity, though not as high as CdTe [64]. The best reported values for the standard deviation of pixel-to-pixel sensitivity is 20% and image lag is quite high at 70% first frame,  $\sim$  20% after 3 frames and 10% at 1 s at 30 frames/s [213]. This could be due to large, non-uniform grain sizes but doping with Cl can make a finer, more uniform grain, potentially increasing performance. Currently, CZT based detectors have good resolution, though far from that theoretically possible [124].

### 3.4.4 Polycrystalline Cadmium Telluride (Poly-CdTe)

Though polycrystalline CdZnTe has received greater consideration as a potential photoconductor for FPXIs due to its larger bandgap and higher resistivity, much work has recently focused on developing CdTe as a candidate. CdTe has been used as a single crystal detector for x- and  $\gamma$ -ray detection for a long time and, due to developments in the photovoltaic cell industry, can be grown as a polycrystalline film in areas bigger than 1 m<sup>2</sup> by CSS [215]. Unlike HgI<sub>2</sub>, CdTe films are very stable in open air with little change in electrical characteristics over a five year period [200]. CdTe has a density of 6.20 g/cm<sup>3</sup> and a relatively small bandgap of 1.45 eV [216] leading to a low  $W_{\pm}$  of 4.43 eV [201]. Wide ranging values of resistivity have been reported by different sources for CdTe films, varying from  $2 \times 10^5$  to  $4 \times 10^{10}$   $\Omega$  cm [200,215].

Advancements in photovoltaic CdTe technology have shown that films can be deposited by chemical bath deposition and subsequently annealed [216]. The optimum temperature for deposition by this method is 60 °C and low (room temperature) annealing temperatures provide the smallest grain sizes (21 nm) making it a good option for creating high density films. Unrelated recent work has shown that using a nano-particle (100 – 500 nm) CdTe powder for CSS can result in a 1.7 times reduction in deposition time to 0.94  $\mu$ m/min [217].

Work more applicable to FPXIs has involved the reduction of dark current by the deposition of Schottky contacts on a CdTe layer used in x-ray imaging in the 10 – 100 keV range [218]. However, due to the low resistivity of CdTe, only a dark current of 250 pA/mm<sup>2</sup> was achieved when the Schottky diode structure created between an Al contact and *p*-type CdTe was reversed biased at 1 V.

CdTe layers used in photovoltaic cells have been modeled as detectors for portal imaging where very high energy treatment photons (6 MeV) are converted into lower energy primary electrons (0.5 – 1.5 MeV) by a metal layer so that the charged particle's energy can be absorbed by a film of CdTe [219-221]. A prototype detector of this sort produced from photovoltaic films

exhibited very high dark currents of 80 pA/mm<sup>2</sup> at 0.01 V/μm, but experienced a 3 order of magnitude increase in resistance under irradiation due to polarization [219].

A prototype CdTe FPXI has been developed in which the CdTe layer was deposited directly onto a Medipix2 readout chip by PVD at 375 °C at a growth rate of 10 μm/hour producing large grain sizes of 10 μm [222]. While it was shown that the readout chip still worked after deposition, this method would not be compatible with an a-Si:H AMA. This detector was used to obtain x-ray images at 60 kVp with an exposure time of 100 s using a 30 μm thick film biased at -24 V [223]. Schottky contacts were used to reduce the dark current, though only values as low as ~ 400 pA/mm<sup>2</sup> were attained at fields of 0.67 V/μm. While very much in the early stages of development, images obtained showed a spatial resolution of 5 lp/mm (though the MTF at this frequency was not reported). Using alpha-particle measurements and the Hecht relation,  $\mu_h\tau_h$  values of  $\sim 2 \times 10^{-7}$  cm<sup>2</sup>/V were determined.

### 3.4.5 Polycrystalline Lead Oxide (Poly – PbO)

Polycrystalline PbO used in FPXIs has a bandgap of 1.9 eV,  $W_{\pm}$  of 8 eV, a resistivity of  $(7 - 10) \times 10^{12}$  Ω cm and a density of 9.6 g/cm<sup>3</sup> [125], although films deposited by PVD at 100 °C have a density of ~ 50% that of single crystals [224]. PbO has the benefit of having no heavy element k-edges in the typical diagnostic range up to 88 keV meaning no noise from k-fluorescence. However, PbO reacts with water and CO<sub>2</sub> and needs to be encapsulated like HgI<sub>2</sub> [224].

300 μm thick detectors with an area of 18 × 20 cm<sup>2</sup> have been demonstrated [125].  $\mu_e\tau_e$  values in these detectors were  $5 \times 10^{-7}$  cm<sup>2</sup>/V and they exhibited good resolution. However the image lag was 3 – 8% after 1 s and the dark current was quite high (40 pA/mm<sup>2</sup> at 3 V/μm).

PbO films for direct conversion detectors are most often deposited through evaporation techniques, as discussed above, as screen printed films tend to have lower mass density and are less stable. Yet recently, screen printed films of PbO 2.5 × 2.5 cm<sup>2</sup> and 150 μm thick were created using 200 – 500 nm synthesized PbO nano-particles [126]. This resulted in a higher

density film due to the higher packing factor of smaller particles. The films were annealed at various temperatures and films annealed at 500 °C had a dark current of only 20 pA/mm<sup>2</sup>, a sensitivity of 2400 pC cm<sup>-2</sup> mR<sup>-1</sup> and an SNR of 36 at 3 V/um. This was a significant improvement over films annealed at 100 °C which had dark current values of 40 pA/mm<sup>2</sup>, a sensitivity of 300 pC cm<sup>-2</sup> mR<sup>-1</sup> and an SNR of 3. Unfortunately, significant improvement in performance of the films only occurred at annealing temperatures above 300 °C, too high to allow for direct deposition onto an a-Si:H AMA.

It is also possible that the dark current in PbO detectors could be reduced by using a *p-i-n* photodiode like structure in the photoconductive layer as has been done in commercialized a-Se detectors. It is known that *n*- and *p*-type PbO can be created through the control of the oxygen pressure during sample preparation [225] and through doping with acceptor and donor impurities [226].

Recently, Kabir has modeled PbO detectors and has determined that although carrier ranges in PbO are worse than in CZT and HgI<sub>2</sub>, the resolution is excellent; a presampling MTF of 0.49 at 1 V/μm at  $f_{ny}$  was simulated and compared to that of the pixel aperture (0.64 at  $f_{ny} = 2.72$  lp/mm) [101]. It was determined that a nearly ideal MTF can be achieved by increasing the field to reduce trapping of photogenerated charge carriers (this can also be achieved by improving the carrier ranges through material development). The  $DQE(f)$  can also be greatly enhanced by increasing the applied field or the carrier  $\mu\tau$  products, but one has to wonder how these increases would affect the dark current.

### 3.4.6 Polycrystalline Thallium Bromide (Poly-TlBr)

Polycrystalline TlBr has been used as a direct conversion, 300 μm thick layer, ~ 23 cm in diameter in an x-ray sensitive electron-beam image tube called XEBIT [227]. This shows TlBr has potential as an x-ray photoconductor, but not much effort has gone into developing it as such. TlBr has a bandgap of 2.7 eV,  $W_{\pm}$  of 6.5 eV and a relatively low resistivity of  $5 \times 10^9 \Omega$  cm, leading to high dark currents [64]. However, the dark current, which is due mainly to ionic conductivity, decreases by an order of magnitude with every 19 °C decrease in temperature [64].

Both holes and electrons are fairly mobile in TlBr as  $\mu_e\tau_e$  is roughly  $3 \times 10^{-6} \text{ cm}^2/\text{V}$  [205] and  $\mu_h\tau_h$  is around  $1.5 \times 10^{-6} \text{ cm}^2/\text{V}$  [227].

### 3.4.7 Polycrystalline Bismuth Tri-Iodide (Poly-BiI<sub>3</sub>)

Polycrystalline BiI<sub>3</sub> films 130  $\mu\text{m}$  thick with a grain size of 20 – 50  $\mu\text{m}$  have been deposited by PVD at 150 °C [228]. The resistivity of these films was measured at  $6 \times 10^{12} \Omega \text{ cm}$  with a dark current of 6 pA/mm<sup>2</sup> at 0.4 V/ $\mu\text{m}$ . It was discovered that film deposition at 165 °C caused the BiI<sub>3</sub> crystals to change orientation to have their (0 0 l) planes parallel to the substrate, allowing for maximum radiation absorption [229]. These “oriented” films had a very high resistivity ( $3 \times 10^{15} \Omega \text{ cm}$ ) for a material with a bandgap of 1.7 eV. This led to extremely low values of dark current of  $\sim 0.16 \text{ pA/mm}^2$  at an applied field of  $\sim 5 \text{ V}/\mu\text{m}$ . However, charge transport properties were very poor leading to low x-ray sensitivity. The same group has more recently deposited BiI<sub>3</sub> films with a resistivity of  $1.4 \times 10^{13} \Omega \text{ cm}$  and observed dark current values of 9.7 pA/mm<sup>2</sup> at fields as high as 5.6 V/ $\mu\text{m}$  with a linear relationship between dark current and applied field [128]. The measured x-ray sensitivity was more acceptable, though still very low, at 23 pC cm<sup>-2</sup> mR<sup>-1</sup> at 0.8 V/ $\mu\text{m}$ . This low value of dark current is promising and it has also been shown that a blocking contact of BiO can be used to increase the bulk resistivity of the films by 2 orders of magnitude [230].  $\mu_e\tau_e$  in BiI<sub>3</sub> has been estimated to be  $\sim 3 \times 10^{-7} \text{ cm}^2/\text{V}$  [128].

### 3.4.8 Polycrystalline Lead Bromide (Poly-PbBr<sub>2</sub>) and Mercuric Bromide (Poly-HgBr<sub>2</sub>)

Fornaro *et al.* have grown films of PbBr<sub>2</sub> and HgBr<sub>2</sub> by PVD [127]. Layers of PbBr<sub>2</sub> with an area of  $2.5 \times 2.5 \text{ cm}^2$ , thickness of 40 – 60  $\mu\text{m}$  and grain sizes of 2 – 10  $\mu\text{m}$  demonstrated dark currents of less than 10 pA/mm<sup>2</sup> below 5 V/ $\mu\text{m}$  and an SNR of 14 at 7.5 V/ $\mu\text{m}$ . HgBr<sub>2</sub> layers with the same area, but thickness of 300  $\mu\text{m}$  and grain sizes of 20 – 50  $\mu\text{m}$  demonstrated dark currents of less than 10 pA/mm<sup>2</sup> below 0.2 V/ $\mu\text{m}$  and an SNR of 0.31 at 0.2 V/ $\mu\text{m}$ .

### 3.5 Conclusion

The sections of this chapter dealing with selenium generally end with a certain lack of conclusiveness. While a-Se based detectors have experienced commercial success, especially in the field of mammography, the lack of a full understanding of its properties would seem to slow the improvement of such detectors. This is the reason that so much effort has been put into developing other photoconductors, especially for use in general radiography, as described in the last section. Obviously, improvements in the fundamental understanding of these materials will lead to generations of better FPXIs, but in closing it is interesting to see a comparison of x-ray images acquired with a commercialized a-Se detector and prototype detectors based on different polycrystalline photoconductors, as presented in Fig. 3.11.

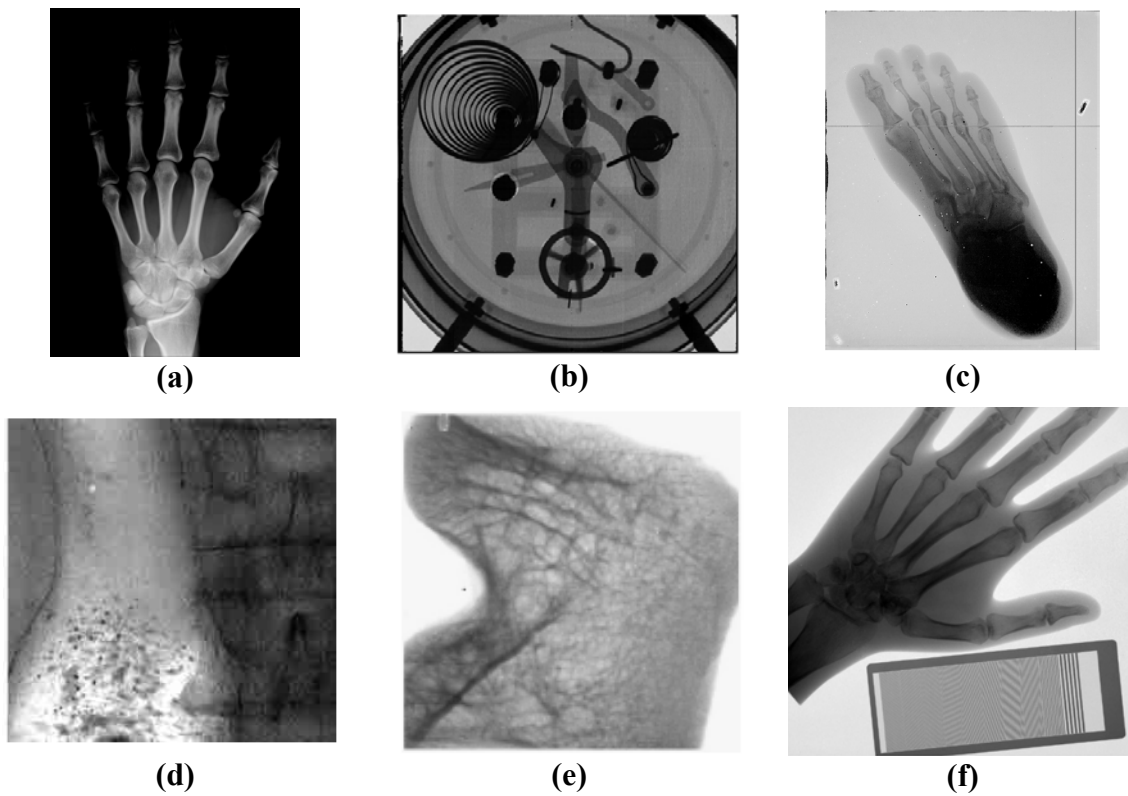


**Figure 3.11 Comparison of x-ray images obtained with direct conversion detectors utilizing different photoconductive layers: (a) Hand phantom with a-Se, after [231], (b) Alarm clock with HgI<sub>2</sub>, after [211], (c) Foot phantom with PbI<sub>2</sub>, after [211], (d) Gastrointestinal phantom with CZT, after [124], (e) Chicken bone with CdTe, after [215], (f) Hand phantom and Huettner phantom with PbO, after [125].**

# **4. EXPERIMENTAL STUDY OF DARK CURRENT IN AMORPHOUS SELENIUM FILMS**

## **4.1 Introduction**

There has been recent effort to characterize and explain the dark current transients in metal/a-Se/metal devices [7,41,55-57], as detailed in Section 2.6. Yet, the understanding is far from complete and this includes the understanding of the true origin of the dark current in these devices. An in-depth experimental study of the dark current in stabilized a-Se films will be presented in this chapter and this work has been carried out with five different sets of a-Se samples. Three of these sample sets, sample sets A, C and E, were created in Anrad's laboratories in Quebec, while sample sets B and D were created in the Electronic Materials Research Group laboratories at the U of S in the manner described in Section 4.2.1.1. Dark current transients produced by these samples have been analyzed as a function of time, applied field, sample structure, thickness and contact metal to determine the true source of the dark current in the samples.

## **4.2 Experimental Techniques**

This section describes the characteristics of the experimental sample sets used and the system which was used to measure the dark current transients.

### **4.2.1 Sample Sets**

Five separate sets of samples have been used to obtain the experimental data presented in this chapter. Sample set A was the first set created and results from that set are heavily featured in Sections 4.3.1, 4.3.2 and 4.3.4 to 4.3.7. While some of these sections also contain results from sample sets B, C and D, the majority of the data from these sets is discussed in Sections 4.3.3, 4.3.8 and 4.3.9. Sample set E contains a mixture of various samples, the measurements on which

were performed in Anrad's laboratories. The results of this work are presented in Section 4.3.10. A clear distinction will be made as to which sample sets were used to obtain the various results.

#### 4.2.1.1 Sample Preparation

The samples in sets B and D were created in the U of S Electronic Materials Research Group lab. The substrates used were 6.4 cm by 6.4 cm squares of glass coated with a thin layer of ITO. Before deposition, these substrates were cleaned with detergent and alcohol in an ultrasonic bath, rinsed several times with distilled water and blown dry with compressed, filtered air.

The deposition of the photoconductive layers is done in a vacuum coater based on the NORTON NRC 3117 and is shown schematically in Fig. 4.1. Once the vacuum chamber has been pumped down to a pressure below  $3 \times 10^{-6}$  Torr, the substrate heater is turned on, raising the substrate temperature above the glass transition temperature to 60 °C for Se, 70 °C for As<sub>2</sub>Se<sub>3</sub>. The boat, which is loaded with pellets of vitreous material quenched from the melt, is heated to 250 °C for Se or 400 °C for As<sub>2</sub>Se<sub>3</sub>, above the material melting temperature, by running electrical current through the boat. Both the boat and the substrate temperature are controlled through the use of a thermocouple feedback system. Once the evaporation rate from the boat reaches a constant level (as measured by a digital crystal rate monitor), the shutter is opened, allowing the vapour to be deposited on the substrate over an area of 5.1 cm by 5.1 cm. The rate of deposition is roughly 1 μm/min. The thickness of the first deposited layer, the *p*-layer, was measured with a Perkin Elmer Lambda 900 photospectrometer. The thickness of the remaining layers was measured with a digital micrometer.

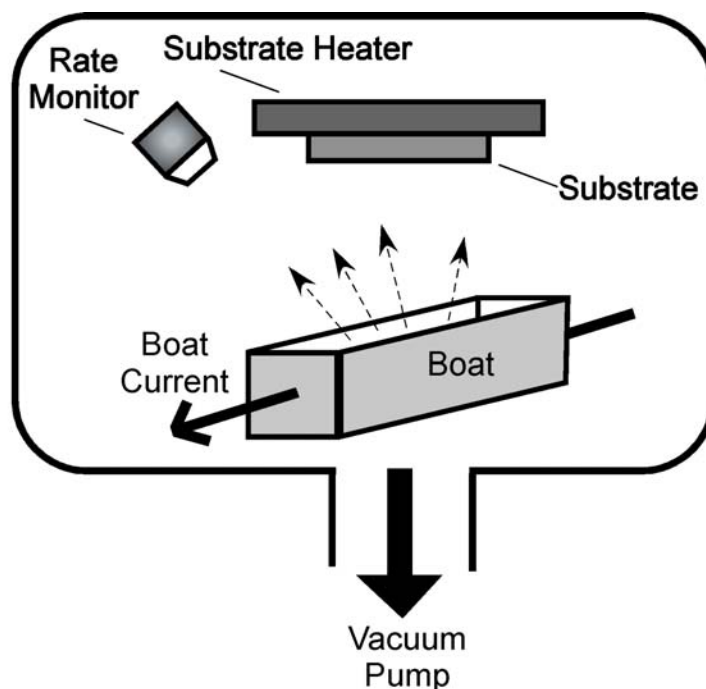


**Figure 4.1 Schematic of the vacuum deposition system used to create sample sets B and D.**

The samples were rested for several days before the top contacts were added. Top contacts were also deposited on the samples of set C in the U of S labs. The top contacts were deposited using a machined metal mask. The Cr and Al contacts were deposited through evaporation while the Au and Pt contacts were sputtered. High voltage leads have been connected to each contact using a two part, silver conductive epoxy.

The samples of sample set A, C and E, created and supplied by Anrad, were created in a similar manner to that described above.

#### **4.2.1.2 Sample Set A**

The implementation of the *n-i-p* photodiode-like structure in commercial FPXIs was based on the assumption that the dark current is dominated by the injection of carriers from the contacts. However, the actual effectiveness of each blocking layer and its position in the structure has never been systematically evaluated. To do this, a set of seven types of samples, *sample set A*, has been created. Sample set A contains mammographic-type ( $\sim 200 \mu\text{m}$  thick) samples with the seven different structures listed in Table 4.1, found at the end of Section 4.2.1.

The substrate electrode is glass coated with a conductive layer of ITO while the top electrode is Cr and has an area of  $21 \text{ cm}^2$ . A photograph of a sample from set A can be seen in Fig. 4.2, looking down on the top contact. All *i*-layers (intrinsic layers) consist of a non-chlorinated Se:0.2%As alloy with reported hole and electron schubwegs of 6 mm and 5 mm respectively at  $10 \text{ V}/\mu\text{m}$ . The *n*-layers are alkali-doped stabilized a-Se and are roughly  $6 \mu\text{m}$  thick and the *p*-layers are a-As<sub>2</sub>Se<sub>3</sub> and are roughly  $2 \mu\text{m}$  thick. By varying the *n-i-p* structure while holding all other parameters as constant as possible (layer thicknesses, contact area, *etc.*) the true effect of each layer and its position can be determined. This is done by measuring the dark current transients of these samples as a function of time and electric field (with the top electrode both negative and positive with respect to the substrate electrode for all samples) and comparing the transients of the different structures.



**Figure 4.2** A Photo of a sample from sample set A. The entire top surface of the sample is covered by a Cr contact.

#### 4.2.1.3 Sample Set B

While some success has been experienced in explaining the dark current transients in a-Se *n-i-p* structures using the Schottky injection model [57,59,109], as discussed in Section 2.6, little effort has been made to include the contribution of the bulk thermal generation of carriers, as has been shown to be necessary in the modeling of a-Si:H *p-i-n* structures [109]. One recent

simulation of a-Se sandwich structures has considered the contribution from generation in the bulk [106] and it has shown that this contribution is likely  $\sim 2$  orders of magnitude lower than the current injected by the contacts, even if blocking layers are used to reduce the injection current. If bulk thermal generation of carriers makes a significant contribution to the dark current in a-Se layers, the dark current should increase linearly with the thickness of the layer. There has been no systematic study of the effect of the thickness of the a-Se layer on the dark current levels measured. For this reason, *sample set B*, was created as described in Section 4.2.1.1 and is outlined in Table 4.1. This set of five samples employs an *n-i-p* structure with varying thickness of the *i*-layer from sample to sample. The substrate electrode is glass, coated with a conductive layer of ITO while the top surface contains four thin contacts, one each made of Cr, Al, Au and Pt, each having a surface area of roughly  $1.2 \text{ cm}^2$ . This can be seen in Fig. 4.3. All *i*-layers are a-Se alloyed with 0.3% As and doped with 2.5 ppm Cl. The *n*-layers are alkali-doped, stabilized a-Se and are roughly  $9 \text{ }\mu\text{m}$  thick and the *p*-layers are a-As<sub>2</sub>Se<sub>3</sub> and are roughly  $1 \text{ }\mu\text{m}$  thick. Dark current measurements as a function of time and applied field can be taken and compared between samples. If the dark current is due solely to the injection of carriers from the contacts, no difference in dark current levels should occur between samples while the same contact metal is used. The difference should appear between measurements on the same sample using different contacts and should have some relationship to the work function of the contact material. If bulk thermal generation does play a significant role, one would expect the dark current level to increase linearly with thickness, as the generation rate should depend on the volume of the a-Se layer, which depends linearly on the thickness.

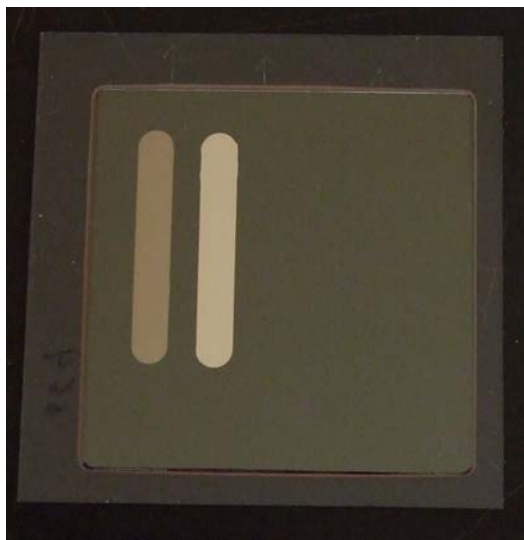


**Figure 4.3** A photo of a sample from set B after two of the top contacts were deposited. From left to right the contacts are Cr, Al, and Au and Pt would be deposited in a similar fashion. The exposed area outside the contacts is the *n*-layer of a-Se.

#### 4.2.1.4 Sample Set C

To further investigate the *i*-layer thickness dependence of the dark current in a-Se sandwich structures, *sample set C* was created. This set of 6 samples had an *n-i-p* structure with 2 different thicknesses of *i*-layer (3 samples of each thickness). The substrate electrode is glass coated with a conductive layer of ITO while the top surface contains two thin contacts, one of Al and one of Pt and each have a surface area of roughly 1.2 cm<sup>2</sup>. All *i*-layers are a-Se alloyed with 0.3% As and doped with 2.5 ppm Cl. The *n*-layers are alkali-doped stabilized a-Se and are roughly 6 μm thick and the *p*-layers are a-As<sub>2</sub>Se<sub>3</sub> and are roughly 6 μm thick. The properties of these samples are tabulated in Table 4.1.

#### 4.2.1.5 Sample Set D

The dark current level in a-Se *n-i-p* sandwich structures can depend strongly on the thickness of the *n*-layer [41] and this can be hard to control in a very exact manner between different sample production runs. For this reason, *sample set D* was created as described in Section 4.2.1.1, with two regions of different *i*-layer thickness on a single sample, as shown schematically in Fig. 4.4.

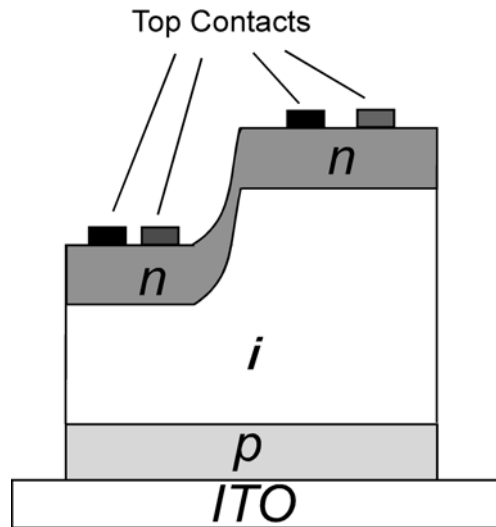


**Figure 4.4** Schematic representation of a sample from set D. The *i*-layer has two distinct regions of thickness while the *n*-layer thickness is as uniform as possible across the entire sample. Each thickness region has two top contacts allowing for two different metals in each region. Not to scale.

A slight modification was made to the deposition system to accommodate the creation of sample set D, which required the deposition of two different thicknesses of a-Se on the same substrate. A sensor was added to allow the shutter to be closed roughly halfway during deposition. In this way, half of the sample could be covered mid-evaporation, allowing the other half to grow thicker. The divide in thickness was along the diagonal of the sample and can be seen in Fig. 4.5. Contacts on these samples were designed to be smaller by necessity and are circular with an area of  $0.5 \text{ cm}^2$ . An example of these contacts is shown on a sample from set D in Fig. 4.5.

Two samples of this type were created: R687 and R689. The characteristics of these samples are summarized in Table 4.1. R687 contains an a-As<sub>2</sub>Se<sub>3</sub> *p*-layer, a 2% As, alkali-doped a-Se *n*-layer and an *i*-layer of pure a-Se while R689 has an a-As<sub>2</sub>Se<sub>3</sub> *p*-layer, a 8.8% As, alkali-doped a-Se *n*-layer and an *i*-layer of a-Se:0.3% As doped with 2.5 ppm Cl. One sample with a stabilized a-Se *i*-layer and one sample with a pure a-Se *i*-layer were created to determine if fractionation during evaporation of stabilized a-Se introduces an *i*-layer thickness dependence into the dark current transients.



**Figure 4.5** A photo of a sample from sample set D with round Al (light) and Pt (dark) contacts on each side. The reflection of light from the ridge dividing the thick and thin sides can be seen.

#### **4.2.1.6 Sample Set E**

*Sample Set E* consists of older samples which were used for various dark current and x-ray sensitivity measurements (presented in Chapter 6). There are 2 samples with chlorinated *i*-layers: a 500  $\mu\text{m}$  thick *i*-layer sample and a 1 mm thick *n-i-p* sample. These samples have reported hole and electron schubwegs at an applied field of 10  $\text{V}/\mu\text{m}$  of 23 mm and 2.9 mm, respectively. There are also 2 samples with non-chlorinated *i*-layers: a 500  $\mu\text{m}$  thick *i*-layer sample and a 1 mm thick *p-i-n* sample. These non-chlorinated samples have reported hole and electron schubwegs at an applied field of 10  $\text{V}/\mu\text{m}$  of 5.9 mm and 4.8 mm, respectively. The other parameters of these samples are summarized in Table 4.1.

**Table 4.1 Summary of characteristics for sample sets A, B, C, D, and E. The notation used to describe the sample structure uses the first letter to represent the top layer, or what would be the layer next to the radiation receiving electrode.**

Sample Set	Sample Number	Structure	<i>n</i> -layer Thickness (μm)	<i>i</i> -layer Thickness (μm)	<i>p</i> -layer Thickness (μm)
A	839 – 4, 6	<i>i</i> -layer	-	212	-
	846 – 4, 6	<i>i</i> - <i>p</i>	-	215	5
	847 – 2, 3	<i>n</i> - <i>i</i>	7	198	-
	845 – 2, 4, 6	<i>n</i> - <i>i</i> - <i>p</i>	6	209	5
	842 – 1, 3	<i>p</i> - <i>i</i>	-	223	2
	849 – 1, 5	<i>i</i> - <i>n</i>	6	192	-
	850 – 1, 2	<i>p</i> - <i>i</i> - <i>n</i>	6	193	2
B	US1	<i>n</i> - <i>i</i> - <i>p</i>	9	60	1
	US2	<i>n</i> - <i>i</i> - <i>p</i>	9	110	1
	US3	<i>n</i> - <i>i</i> - <i>p</i>	9	310	1
	US4	<i>n</i> - <i>i</i> - <i>p</i>	9	40	1
	US5	<i>n</i> - <i>i</i> - <i>p</i>	9	240	1
C	1452 – 1,2,3	<i>n</i> - <i>i</i> - <i>p</i>	6	196	6
	1452 – 4,5,6	<i>n</i> - <i>i</i> - <i>p</i>	6	74	6
D	R687	<i>n</i> - <i>i</i> - <i>p</i>	8	70 / 370	2
	R689	<i>n</i> - <i>i</i> - <i>p</i>	4	29 / 209	2
E	549-5	<i>i</i> -layer	-	500	-
	544-6	<i>i</i> -layer	-	500	-
	531-5	<i>n</i> - <i>i</i> - <i>p</i>	20	1000	5
	553-5	<i>p</i> - <i>i</i> - <i>n</i>	20	1000	5

#### 4.2.2 Dark Current Measurement Apparatus

While the dark current transients through the a-Se samples are complicated in nature, they are relatively easy to obtain. A schematic diagram of the measurement system is shown in Fig.

4.6. During measurements, the sample is placed in a light-proof chamber and rested, short-circuited in the dark for at least 12 hours before any measurements are taken and between all measurements to allow for sufficient release of trapped charge. A Stanford Research Systems PS350 Model High Voltage Power Supply is used to supply a bias voltage across the sample. It can provide stable DC voltages up to 5000 V, allowing for fields of up to 25 V/ $\mu\text{m}$  for mammographic samples. The resulting current is measured using a Keithley 6512 Model Programmable Electrometer which has a current range of 2 fA to 20 mA. Since the dark current transients have features of interest which can occur several hours after the application of the high voltage, the measurements are automated using a computer and communication over a GPIB connection. The maximum current allowed in the system is 0.5 mA, due to the internal current limiting resistance. Noise coupled capacitively from the power supply is on the order of 0.1 pA.

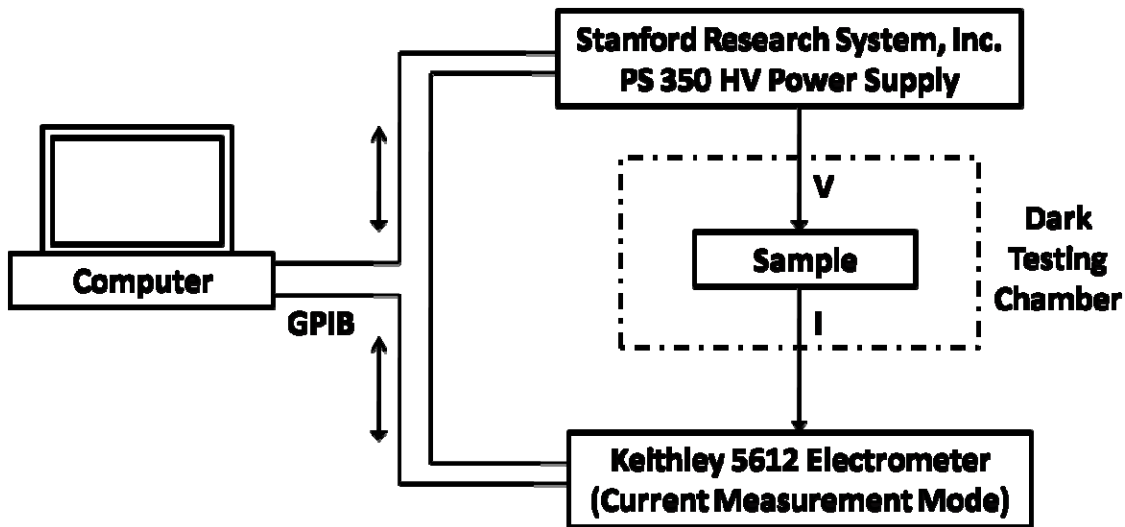
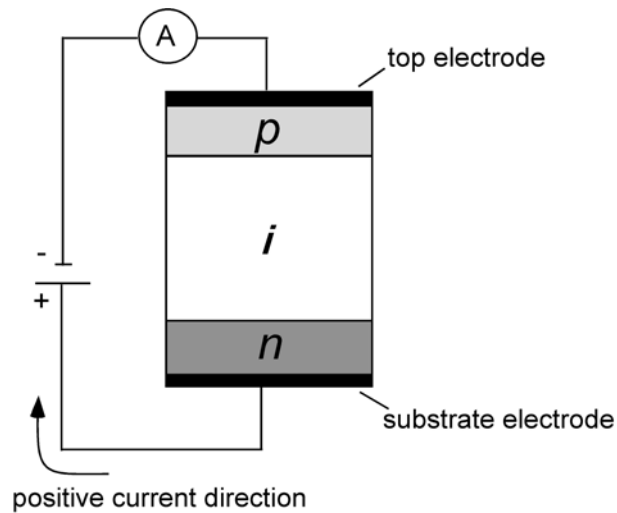


Figure 4.6 Schematic diagram of the dark current transient acquisition system.

It is important to clearly define a positive direction for current flow produced by these experiments. This is done in Fig. 4.7 where a *p-i-n* sample is shown (the *p* layer is next to the top contact, or what would be the radiation receiving electrode) with the top contact biased negatively with respect to the bottom contact. This is referred to as a *negative bias*. In this situation, electrons injected from the power supply will be trapped in the *p*-layer and injected holes will be trapped in the *n*-layer, as intended. For this reason, the term *reverse bias* will also be used to describe this situation. The term *forward bias* would refer to a *p-i-n* sample which is positively biased or an *n-i-p* sample which is negatively biased.

Regardless of the bias used, the positive direction of current will always be defined as flowing into the top contact, as shown in Fig. 4.7. As a result, a positive bias yields a positive current and a negative bias yields a negative current. This definition will be valid throughout the presented work unless only the magnitude of current is given, in which case that fact will be explicitly stated.



**Figure 4.7** Schematic representation of a *p-i-n* sample reverse (negatively) biased. Regardless of bias, positive current direction is defined as flowing into the top contact from the power supply.

## 4.3 Results

### 4.3.1 Dark Current as a Function of Time

It has been documented that the dark current flowing through a-Se sandwich structures decays in a non-exponential manner with time after the application of a voltage [7,13,55,56,119,232]. An example of typical transients is shown in Fig. 4.8 where the magnitude of the dark current density is shown for  $2 \times 10^4$  s after the application of the bias for an *i*-layer sample of sample set A at fields of -3, -5, -7 and -10 V/ $\mu\text{m}$ . A larger field results in a higher dark current.

One thing that is immediately obvious from Figure 4.8 is that even at a field magnitude of  $5 \text{ V}/\mu\text{m}$ , the dark current is well above the upper limit of the range deemed acceptable for detector operation ( $10 \text{ pA mm}^{-2}$ ), even after five hours of decay. At  $10 \text{ V}/\mu\text{m}$ , the dark current is orders of magnitude too high for detector operation.

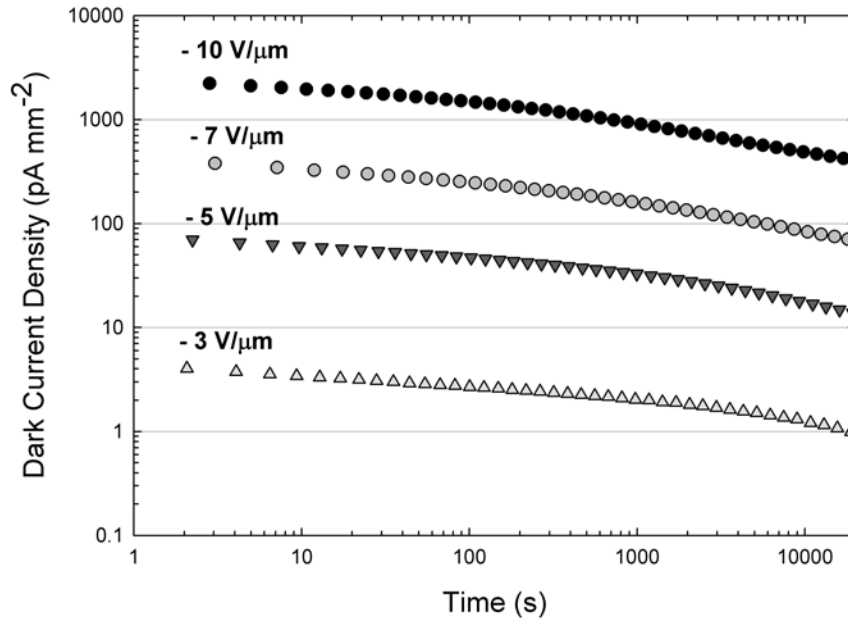


**Figure 4.8** Magnitude of typical dark current transients produced by a negatively biased *i*-layer sample at different fields. The dark current decays with time following the application of the bias in a non-exponential manner.

Recent models of the dark current in a-Se which only consider charge carrier injection [57,59] predict that once the rates of carrier trapping and release reach an equilibrium, the dark current will saturate and reach a steady-state. This is sometimes observed experimentally, as shown in Fig. 4.9 (a) for an *n-i-p* sample from set D. However, this result is more of an exception, as far more often than not, the dark current continues to decay almost indefinitely. This more typical result can be seen in Fig. 4.9 (b) where the dark current density in an *n-i-p* sample of set A continues to decay even after the bias has been applied for several hours.

Figure 4.9 (c) shows an interesting case where a sample of set C exhibits a typical decay when the applied field is  $5 \text{ V}/\mu\text{m}$ , but at  $10 \text{ V}/\mu\text{m}$  the transient reaches a plateau around 30 s after the application of the bias only to continue decreasing after roughly 200 s. This odd transient

type is actually typical of the samples in set C (and only the samples in set C), where the transient has a temporary plateau at fields above  $\sim 7 \text{ V}/\mu\text{m}$ .

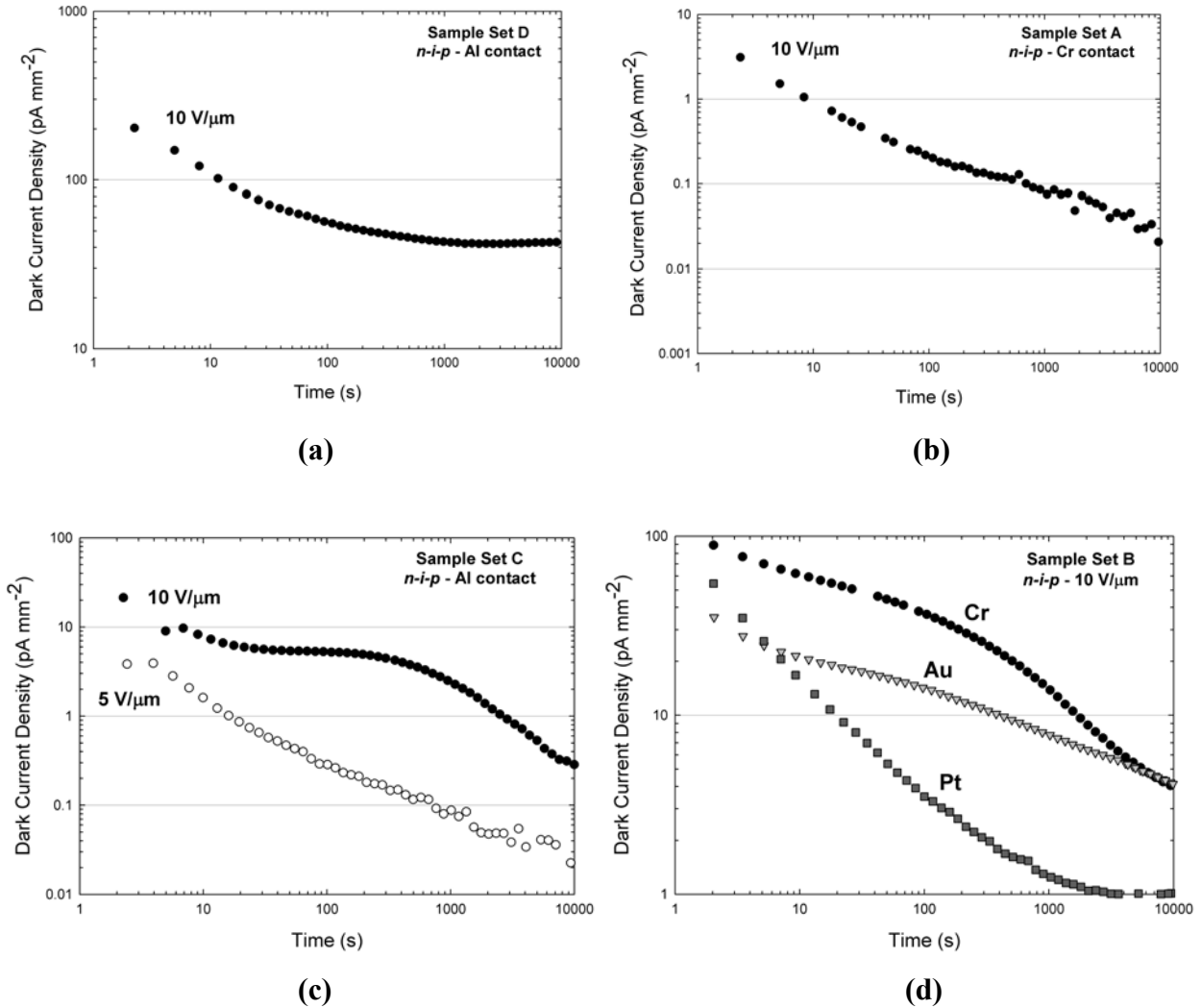


**Figure 4.9** Dark current density vs. time. (a) *n-i-p* sample from set D with an Al contact biased at  $10 \text{ V}/\mu\text{m}$ . The transient reaches a steady-state after  $\sim 1000 \text{ s}$ . (b) *n-i-p* sample from set A with a Cr contact biased at  $10 \text{ V}/\mu\text{m}$ . The transient seems to decay indefinitely. (c) *n-i-p* sample from set C with an Al contact biased at both  $10$  and  $5 \text{ V}/\mu\text{m}$ . At higher fields, most of the samples of set C display a temporary plateau before continuing to decay. (d) *n-i-p* sample from set B biased at  $10 \text{ V}/\mu\text{m}$ . Three different contacts of Cr, Al and Pt give quite differently shaped transients.

Furthermore, the shape of the transient often differs with the metal used to form the top contact to a sample. Fig. 4.9 (d) shows transients measured at  $10 \text{ V}/\mu\text{m}$  on a sample from set B, using three different contacts, each of a different metal. It can be seen that the shape of the decay

curve is different for each contact, suggesting that carrier injection plays a large role in determining the dark current transients in a-Se sandwich structures.

### 4.3.2 Dark Rest Tests

The dark current transients presented in this chapter were obtained by resting the sample for 12 hours between all measurements. This is very important as the sample can take a long time to relax and release all trapped charge. In a-Se, electrons have been shown to have a release time that is on the order of thousands of seconds [140]. Figure 4.10 shows the results of a dark rest experiment. Figure 4.10 (a) shows a transient from an *i*-layer sample from set A with an applied voltage of 3 V/ $\mu\text{m}$  after 24 hours of resting in the dark, short-circuited. The other two transients are from the same sample given only 1 or 2 hours of dark rest after having a field applied. The two latter transients agree well with each other, but differ by as much as 35% with the well rested sample. Figure 4.10 (b) shows a similar transient measured on the same sample after resting it for 5 days. It was then rested for 12 hours and another transient was measured. It can be seen that a rest period of 12 hours provides adequate time for the sample to release trapped charge and generate a transient very similar to a well rested sample, differing by at most 10%. For this reason, a 12 hour rest period between applications of voltage was deemed acceptable and used in all measurements.

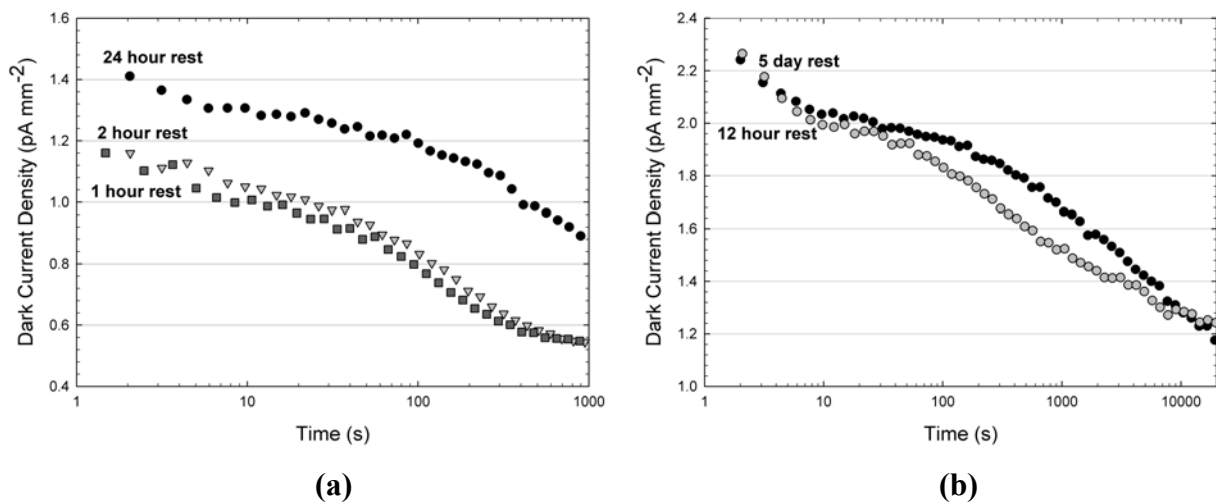


**Figure 4.10** Dark current transients produced by an *i*-layer sample of set A biased at 3 V/ $\mu\text{m}$ , after different rest periods, illustrating the need for adequate dark rest between measurements. A rest period of 12 hours produces transients which differ by at most 10% from very well rested samples.

### 4.3.3 Contact Formation Process

Though not a primary focus of this research, attention was paid to the existence of a “contact formation process” in the samples of sets B, C and D, as electric potentials were applied to them for the first time in this work. Several authors have referred to this contact formation process to describe a change in the behaviour of the metal/a-Se contact following the application of a sufficiently high bias [114] or with thermal annealing [233,234], following which the properties of the contacts are stable. This has been studied in detail by Belev [7] and it was proposed that the main cause was a decrease in conduction at low fields due to crystallization or diffusion of contact metal into the a-Se. For this reason, all contacts on all samples of set B were initially biased at 10 V/ $\mu\text{m}$  for  $1 \times 10^4$  s, rested for 12 hours and then biased at 10 V/ $\mu\text{m}$  again to invoke this effect. In all cases, the second transient was lower but the magnitude of the effect seemed to depend on the metal of the contact. The effect was smaller in Au and Cr contacts, the decrease being less than 3 times in all samples. The effect was much more pronounced in Al and Pt contacts, giving changes of around an order of magnitude or more. An example can be seen in Fig. 4.11 where the first transient for the Al contact on sample US3 starts about 10 times higher than the second transient, measured 12 hours later. The transients begin to look similar after about 1000 s. Subsequent transients agree with the second transient.

The samples of sets C and D also displayed this behaviour, to varying degrees. While this work cannot offer a new explanation of the reason for this effect, it is noteworthy that it is occurring. It should be mentioned that none of the transients reported outside of this section were the very first transients measured on any given sample. That is to say, a contact formation transient was measured on each contact of each new sample before reportable data was collected.

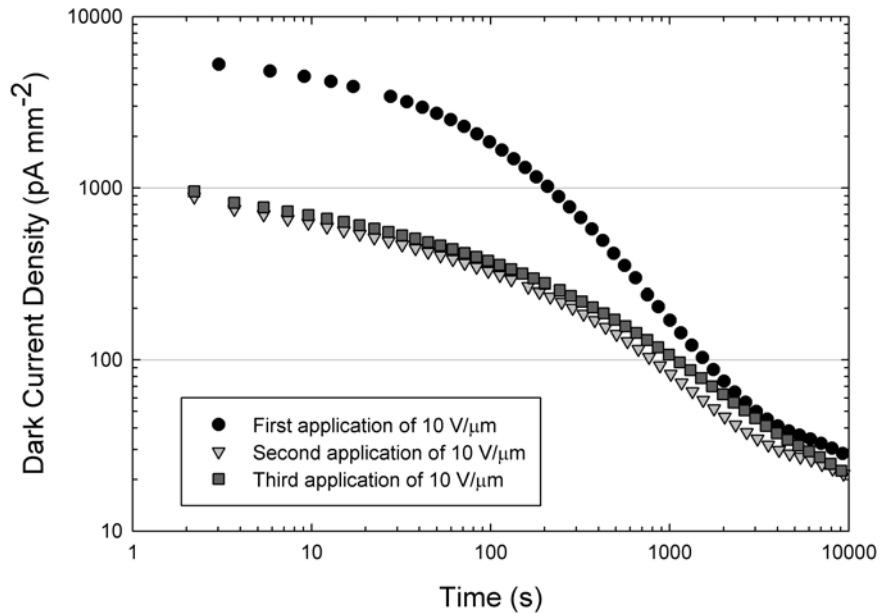


**Figure 4.11** Typical evidence of a contact formation process during the first application of a high voltage bias to the Al contact of a sample from set B. For all samples, the second transient in the test was lower than the first with subsequent transients being similar to the second. All transients represent data from a sample which was rested for 12 hours before the voltage was applied.

#### 4.3.4 Dark Current as a Function of Sample Structure

Figure 4.12 shows a comparison of the dark current transients from all 7 types of structures in sample set A with an applied field magnitude of  $10 \text{ V}/\mu\text{m}$  with a polarity which results in the multilayer structure being reverse biased, *i.e.*  $+10 \text{ V}/\mu\text{m}$  for an  $n-i-p$  structure and  $-10 \text{ V}/\mu\text{m}$  for a  $p-i-n$  structure. Figure 4.12 (a) shows the set of curves for the  $n-i-p$  family of samples and (b) shows the  $p-i-n$  family and these results are typical for all applied fields. Both families show clearly that the addition of only the thin  $p$ -layer has very little effect on the dark current transient. This supports the hypothesis that the dark current in metal/a-Se/ITO structures is due almost entirely to hole conduction. It may be that the roughly  $2 \mu\text{m}$  thick  $p$ -layers are not thick enough to effectively trap injected electrons, but if electron injection were playing a significant role, one would expect at least some decrease in the dark current between the  $i$ -layer and  $p-i$  and  $i-p$  samples. In further support of this theory, the addition of a roughly  $6 \mu\text{m}$  thick  $n$ -layer, to block the injection of holes, reduces the dark current level by over three orders of magnitude in the case of Fig. 4.12 (b). The increase in structural complexity from an  $i-n$  or  $n-i$

sample to a  $p-i-n$  or  $n-i-p$  does show continued reduction in the dark current. This is likely due to the fact that the  $p$ -layer in an  $n-i-p$  sample will trap electrons injected from the negative contact while in an  $n-i$  sample the electrons will be injected into the  $i$ -layer and can drift to the  $n$ -layer where they will recombine with the many trapped holes there. This will reduce the positive space charge build up near the positive contact, allowing more holes to be injected and leading to a higher current than in the  $n-i-p$  sample.

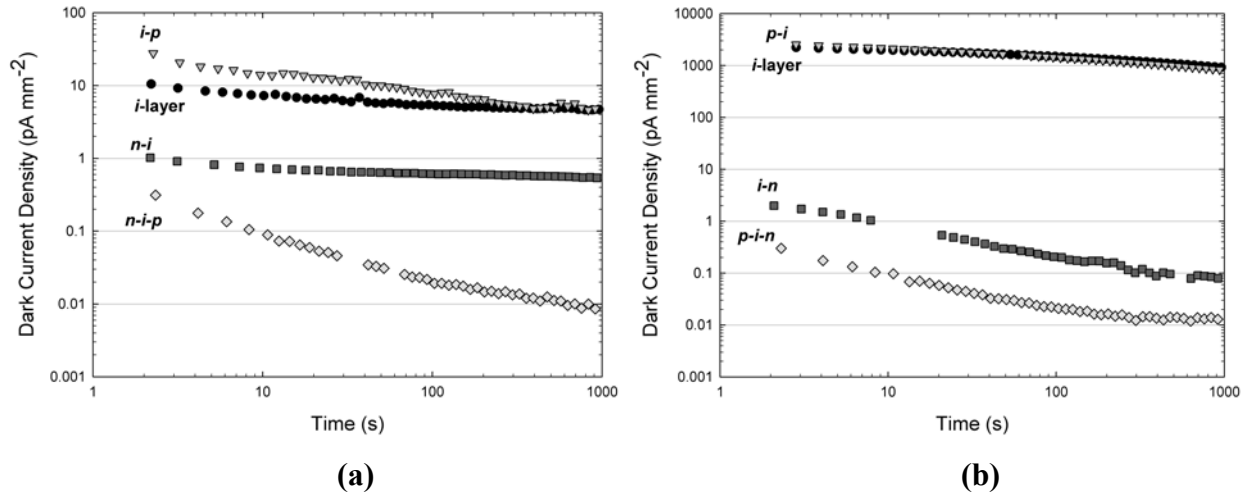


**Figure 4.12 Typical dark current transients (magnitude shown) for all seven sample structures in set A. The  $n-i-p$  family of samples in (a) are all positively biased at  $10 \text{ V}/\mu\text{m}$ , while the  $p-i-n$  family of samples in (b) are all negatively biased at  $-10 \text{ V}/\mu\text{m}$ .**

Figure 4.13 gives a clear comparison of the dark current magnitude in sample set A at  $10 \text{ V}/\mu\text{m}$ , 300 s after the application of the bias and shows the calculated acceptable level of  $1 - 10 \text{ pA}/\text{mm}^2$  [15] for flat panel detector operation.

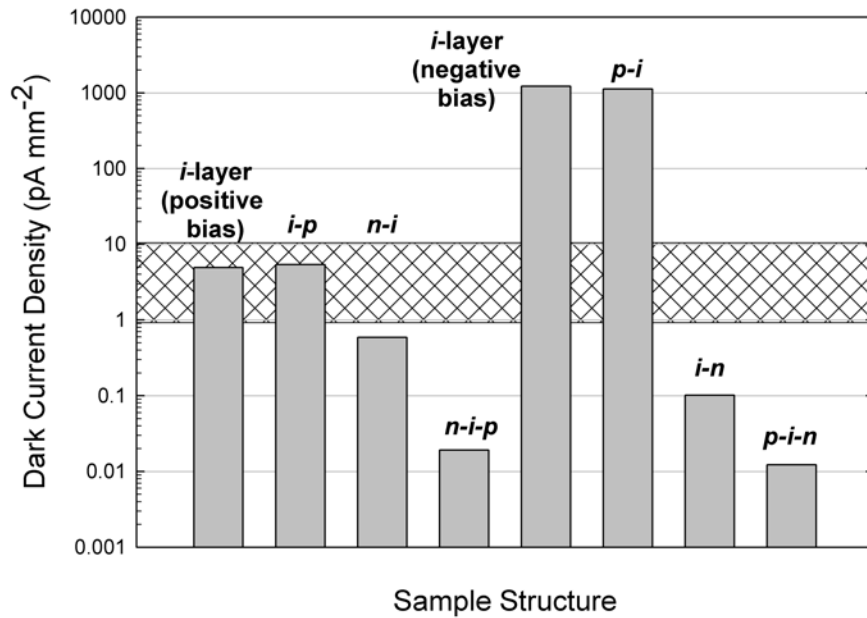


**Figure 4.13 Comparison of the magnitude of the dark current level 300 s after the application of the 10 V/ $\mu\text{m}$  reverse bias for all seven sample structures of set A. The level of dark current deemed acceptable for detector operation [15] is given by the hashed area. Only samples which contain an *n*-layer produce a dark current level below the acceptable range.**

An interesting result that is immediately noticeable in both Figs. 4.12 and 4.13 is that the current level in the simple *i*-layer sample is over two orders of magnitude higher when it is negatively biased than when it is positively biased. This result is reproducible and has been noticed in previous works [7]. This lack of symmetry is counterintuitive, as both Cr and ITO have similar work functions of around 4.5 eV [55,235], but can be partially attributed to a non-uniform distribution of carrier traps throughout the *i*-layer due to fractionation during the deposition of the layer [41] and the formation of different surface layers between the a-Se and each electrode during fabrication [236]. ITO is known to be an efficient injector of holes into semiconductors [237] and this may explain why the current is higher when the sample is negatively biased.

This asymmetry is even more pronounced, but expected, in the other samples of set A. As an example, the dark current transient of a *p*-*i*-*n* sample when forward biased is shown in Fig. 4.14. In this case, the *n*-layer is blocking the injection of electrons and the *p*-layer is blocking the injection of holes. The current at even +3 V/ $\mu\text{m}$  is considerably higher than that at -10 V/ $\mu\text{m}$  as

the blocking layers are not being used as intended when the sample is positively biased. What is especially interesting is the appearance of a “hump” in the forward biased transients between 10 and 100 s. This feature is typical in forward biased transients for all multilayer samples of set A at all fields and seems to occur earlier at higher fields. While the exact origin of this hump is unclear, it may be due to a complex interplay of space charge regions creating a constantly shifting electric field distribution across the sample. Initially injected carriers will drift to the opposite side of the sample where they will be trapped in the blocking layer rather than being collected by the opposite electrode. This will increase the field at both contacts, causing the current to increase. Eventually, as carriers are injected, they recombine with trapped, oppositely charged carriers in the blocking layer they are injected into (*i.e.* the *p*-layer is so full of trapped electrons that injected holes have a very high rate of recombination there). This reduces the field at both contacts, decreasing the current. A similar conclusion was reached by Majid and Johanson [238] when they recently measured the noise in the dark current of forward biased, multilayer a-Se samples. Of course, this explanation would predict that the process would be periodic and so another hump should appear after a certain amount of time. This has not been observed in the  $1 \times 10^5$  s following the application of the bias. However, some combination of this process with the release of large quantities of holes trapped during the initial rush of current could be responsible for the behaviour and explain the forward shift in time of the hump with increasing applied field.

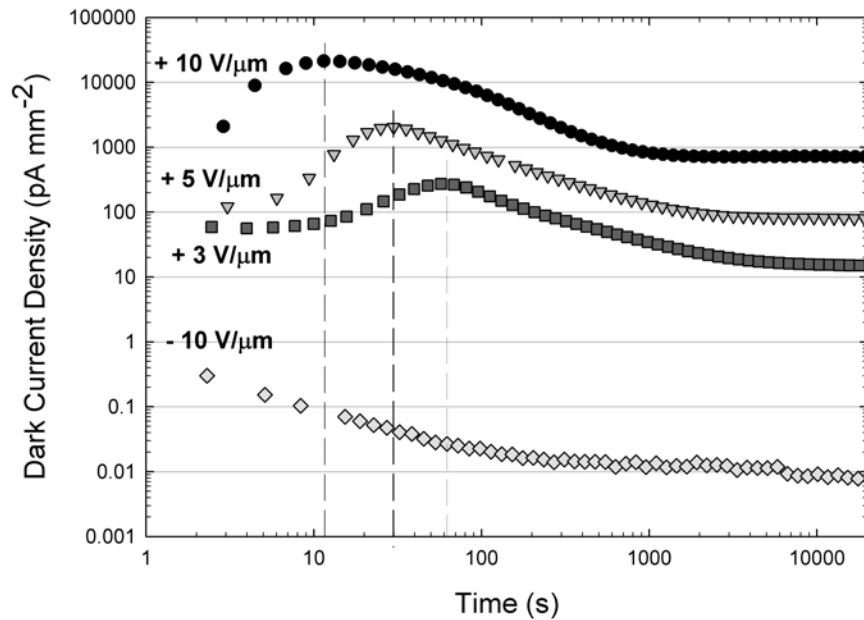


**Figure 4.14** Magnitude of dark current density for a *p-i-n* sample of set A forward biased at 3 different fields and negatively biased at  $-10 \text{ V}/\mu\text{m}$ . Forward biasing a multilayer sample results in much higher dark current and the appearance of a characteristic “hump” which appears at earlier times at higher forward fields.

#### 4.3.5 Dark Current as a Function of Applied Field

By taking the dark current values at one time for different applied fields, one can obtain the  $J$ - $F$  characteristics for each sample. Shown in Fig. 4.15 are the  $J$ - $F$  plots for several samples of set A with a power law fit giving  $J(F) \propto F^n$ . The exponent for each of the structures can be seen in Table 4.2. As expected, the *p*-layer does little to decrease the field dependence of the dark current, but the *n*-layer reduces it significantly. The relationship is not consistently ohmic ( $I \propto V$ ) nor does it imply space charge limited conduction for one carrier injection ( $I \propto V^2$ ) or two carrier injection ( $I \propto V^3$ ). The relationship is actually sub-ohmic for *n-i-p* and *p-i-n* structures, showing the effectiveness of the three-layer structure in reducing the dark current.

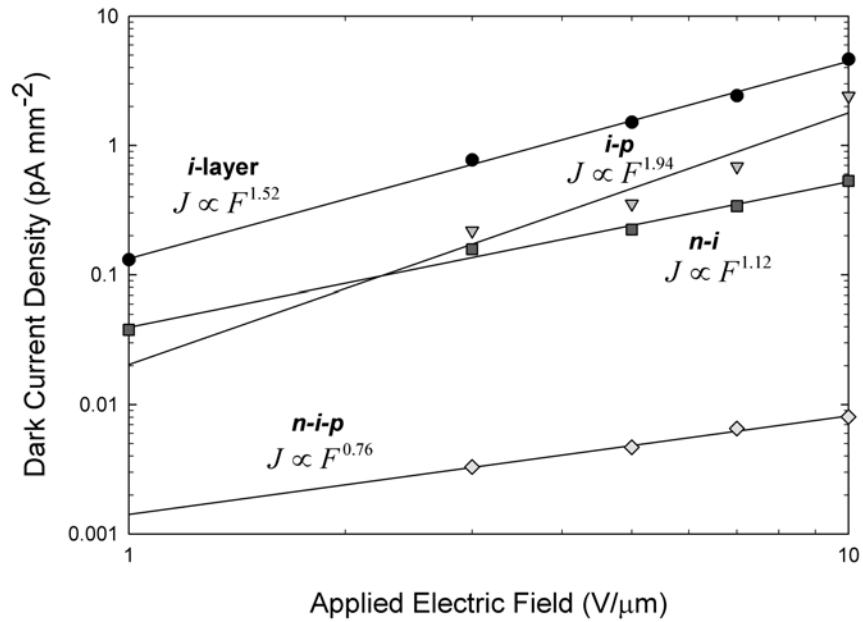


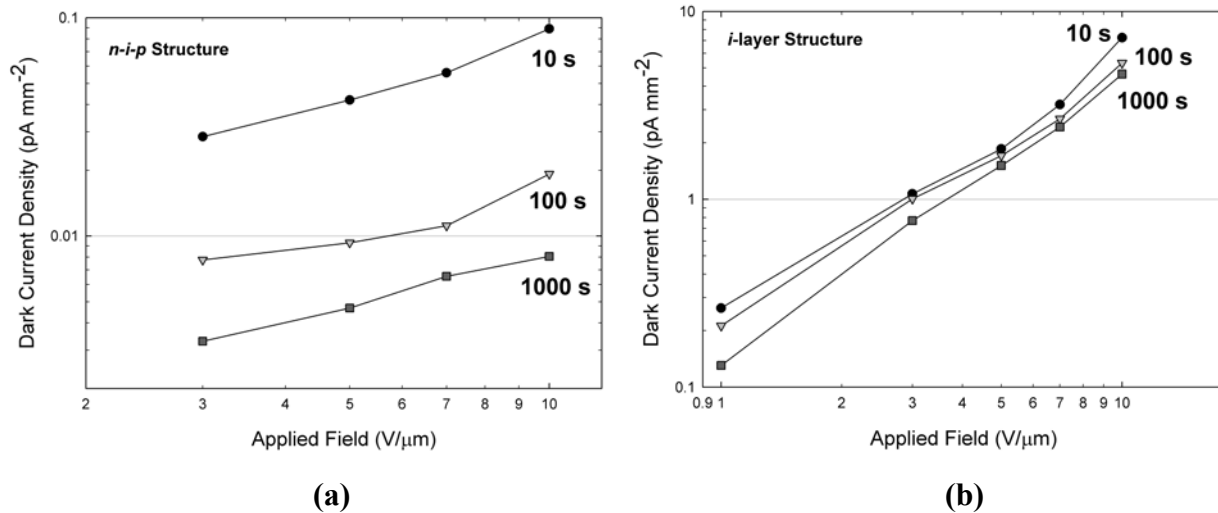
Figure 4.15  $J$ - $F$  characteristics for the positively biased  $n$ - $i$ - $p$  family of sample set A, 1000 s after the application of the bias. A good fit is given for each sample by a power law expression,  $J(F) \propto F^n$ , in which the value of  $n$  varies between samples and is tabulated in Table 4.2.

Table 4.2 Values of  $n$  in the relation  $J(F) \propto F^n$  for all sample structures and corresponding  $R^2$  (confidence in the fit of the power law). Applied voltages are positive for  $i$ - $p$ ,  $n$ - $i$  and  $n$ - $i$ - $p$  samples, negative for  $p$ - $i$ ,  $i$ - $n$  and  $p$ - $i$ - $n$  samples and both for  $i$ -layer samples. Current values are taken 1000 s after the application of the bias.

Sample Structure	Typical $n$	$R^2$
$i$ -layer (positive bias)	1.52	0.9982
$i$ - $p$	1.94	0.9105
$n$ - $i$	1.12	0.9925
$n$ - $i$ - $p$	0.76	0.9925
$i$ -layer (negative bias)	5.80	0.9945
$p$ - $i$	5.03	0.9992
$i$ - $n$	3.29	0.9920
$p$ - $i$ - $n$	0.77	0.8786

It can be seen in Fig. 4.16 that the relationship between the dark current and the applied field changes with time after the application of the field. This is especially true in multilayer

samples where the blocking layers cause a large decay in the dark current with time. The  $J$ - $F$  curves for an  $n$ - $i$ - $p$  sample of set A are shown in Fig. 4.16 (a) at 10, 100 and 1000 s after the application of the bias. As can be predicted from the time dependence of the dark current, the values are lower at longer times, but it is also clear that the field dependence decreases with time. The exponent in the power law fit decreases from 0.93 at 10 s to 0.76 at 1000 s, emphasizing this decrease in field dependence. It seems as time goes on after the application of the field, more and more injected charge is trapped in the blocking layers. A greater amount of charge is injected and trapped at higher fields, so the internal field built up inside the sample will be larger at higher applied fields. This is supported by the fact that the field dependence does not decrease nearly as much with time in a simple  $i$ -layer sample as it does in the  $n$ - $i$ - $p$  sample, as shown in Fig. 4.16 (b).



**Figure 4.16**  $J$ - $F$  characteristics at 10, 100 and 1000 s after the application of the field for (a) an  $n$ - $i$ - $p$  sample from set A and (b) an  $i$ -layer sample from set A. The field dependence of the dark current in the  $n$ - $i$ - $p$  sample decreases substantially with time following the application of the bias. This decrease is not nearly as substantial in the  $i$ -layer sample. The point connecting lines are only a guide for the eye.

It is noteworthy that even only 10 s after the application of the field across the  $n$ - $i$ - $p$  sample the power law fit still gives a sub-ohmic field dependence. This was not the case with  $n$ - $i$ - $p$  samples from the other sample sets, as most of them had  $J$ - $F$  characteristics which depended on  $F^n$  with  $n$  varying between 2 and 7 depending on the contact metal and efficiency of the  $n$ -layer in trapping injected holes. Even samples in the same set gave widely varying numbers.

A deeper investigation of the  $J$ - $F$  characteristics of sample set C was undertaken, where the dark current transients were measured for 100 s with three hour rests in between, at a range of applied fields which spanned over two orders of magnitude.  $J$ - $F$  curves for both the Pt and Al contacts on an  $n$ - $i$ - $p$  sample from set C with a 74  $\mu\text{m}$  thick  $i$ -layer are shown in Fig. 4.17. The values shown were recorded a very short time, roughly 2 s, after the application of the field (this was the earliest reliable measurement available). During such a short time, the space charge due to trapping of injected carriers in the blocking layers is still quite small and the  $J$ - $F$  curves are described quite closely by the relation for carrier emission over a Schottky barrier given by the combination of Eqs. 2.26 and 2.27. Values assumed for the fit were:  $\mu_h = 0.12 \text{ cm}^2/\text{V s}$ ,  $\mu_e = 0.003 \text{ cm}^2/\text{V s}$ ,  $N_v = N_c = 1 \times 10^{19} \text{ cm}^{-3}$ ,  $\phi_e = 0.85 \text{ eV}$  and  $\phi_h = 0.83 \text{ eV}$  for Pt and 0.84 eV for Al. It is expected that the barrier to injection for holes would be lower for the Pt contact, as Pt has a larger work function than Al. It can be seen in Fig. 4.17 that the Schottky relation gives a better fit for the Pt contact but Al also gives a reasonable approximation at most fields.

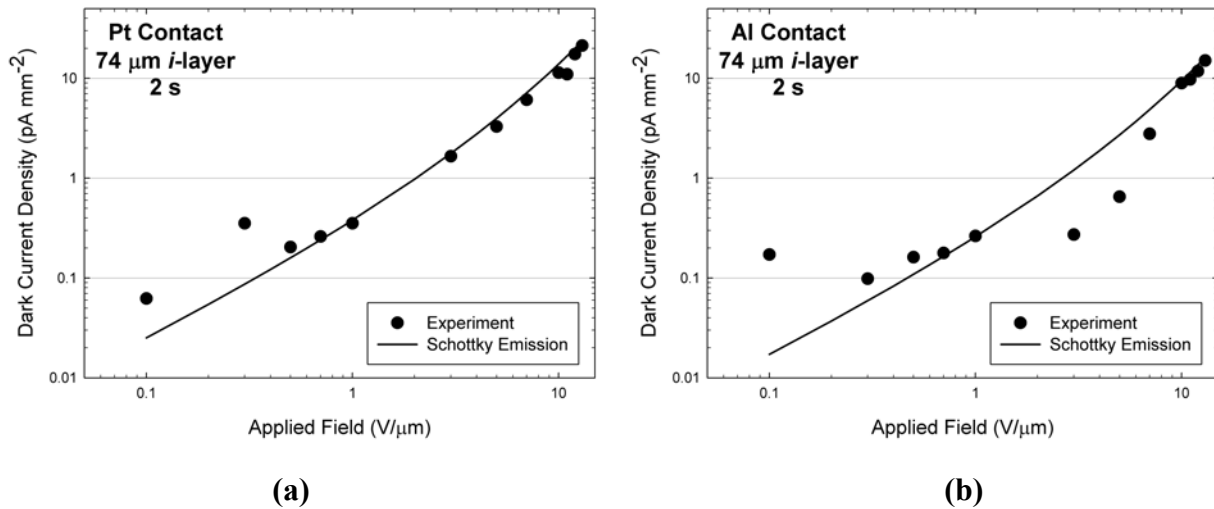


**Figure 4.17** Dark current density as a function of applied field for (a) the Pt contact and (b) the Al contact on an  $n$ - $i$ - $p$  sample from set C with a 74  $\mu\text{m}$   $i$ -layer, 2 s after the application of the field. Also shown in each plot is a fit for injection of carriers over a Schottky barrier. An electron barrier of 0.85 eV is assumed in both cases, while a hole barrier of 0.83 eV is assumed for the Pt contact and 0.84 eV is assumed for the Al contact. The Schottky injection model gives a reasonable fit, more so for the Pt contact.

Figure 4.18 shows plots similar to those in Fig. 4.17, but taken 100 s after the application of the field using the same sample. It can be seen that two distinct regions of field dependence emerge once the electric field has been applied for some time, a result unique to sample set C. For both the Pt and Al contacts, there is a sub-ohmic region below 1 V/ $\mu\text{m}$  while above that point, the current is proportional to roughly the square of the applied field. A similar change in  $I$ - $V$  characteristics with time was seen by Tabak and Scharfe while studying single  $i$ -layer samples of a-Se [239]. They noted that the samples exhibited SCLC-like  $I$ - $V$  characteristics once the samples had accumulated a charge equal to  $CV$  (the product of the sample capacitance and the voltage applied across the sample) and the field at the positive contact was reduced to zero. However, this transition required the illumination of the sample with strongly absorbed light to generate the required amount of charge and, even then, some samples displayed a more exponential-like current decay, non-indicative of a transition to SCLC.

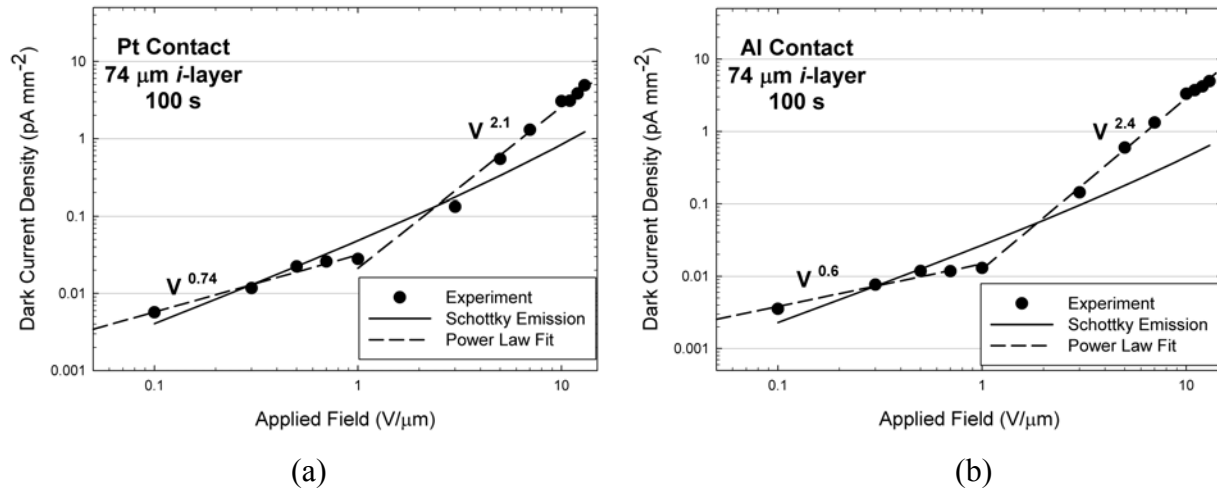


**Figure 4.18** Dark current density as a function of applied field for (a) the Pt contact and (b) the Al contact on an  $n$ - $i$ - $p$  sample from set C with a  $74\ \mu\text{m}$   $i$ -layer, 100 s after the application of the field. Also shown in each plot is a fit for injection of carriers over a Schottky barrier with the field reduced to 18% for the Pt contact and 15% for the Al contact due to trapping of charge carriers in the blocking layers. An electron barrier of 0.85 eV is assumed in both cases, while a hole barrier of 0.83 eV is assumed for the Pt contact and 0.84 eV is assumed for the Al contact. Best fit power law plots are shown for both the high and low field regions for each contact.

The same Schottky emission relation used in Fig. 4.17 is also plotted in Fig. 4.18 with the fields used in the calculation of each point reduced due to the trapping of the charge that is injected. It can be seen that for both the case of the Pt and Al contacts, the Schottky emission

relation gives a much closer fit in the low field region than in the high field region. It seems the Schottky relation underestimates the field dependence at high fields and this was also found to be true in the modeling results of Mahmood and Kabir [57] where a fitting factor,  $\gamma$ , was used to increase the value of the Schottky coefficient needed to match experimental results as the applied field increased.

As discussed in Section 2.6.1, if the dominant process contributing to the dark current is either carrier emission from the contacts over a Schottky barrier or Poole-Frenkel assisted bulk thermal generation of carriers in the bulk, the field dependence will be of the form:

$$J = C \exp\left(-\frac{\varphi - \beta\sqrt{F}}{kT}\right) \quad (4.1)$$

where  $C$  is a constant,  $\varphi$  is the barrier to emission and  $\beta$  will be the Schottky coefficient or the Poole-Frenkel coefficient, depending on the dominant mechanism. Which mechanism is dominant should be distinguishable in a plot of the natural log of the dark current density vs. the square root of the applied field. This is shown in Fig. 4.19 for an  $n-i-p$  sample and  $p-i-n$  sample, both from set A. The slope for each process is given by  $\beta/kT$  and has a value of  $6 \times 10^{-4} \text{ (m/V)}^{1/2}$  for Schottky injection,  $1.2 \times 10^{-3} \text{ (m/V)}^{1/2}$  for Poole-Frenkel emission and  $7 \times 10^{-4} \text{ (m/V)}^{1/2}$  for Hartke's three dimensional treatment of Poole-Frenkel emission [111]. It can be seen that both three layer structures give a best fit linear dependence that is very close to that expected for injection over a Schottky barrier. This result supports the idea that the dark current in a-Se sandwich structures is dominated by carrier injection from the contacts.

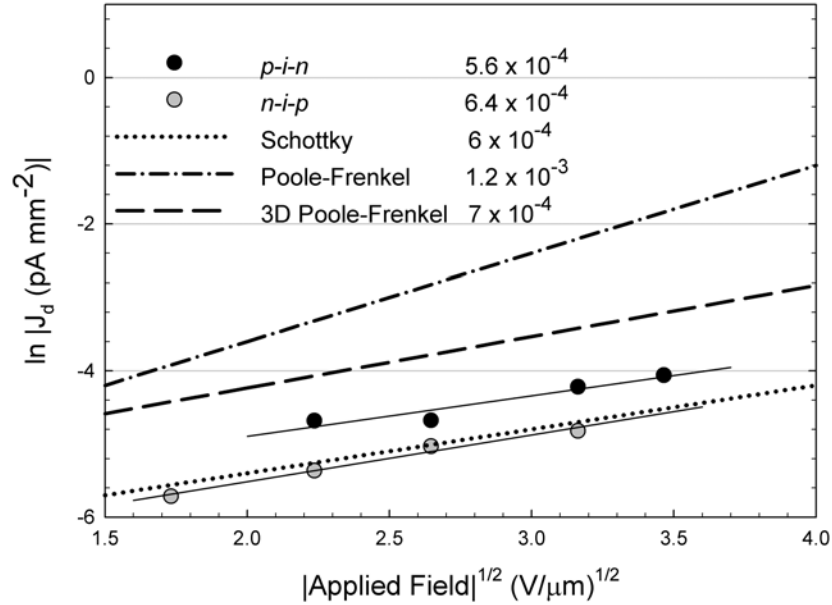


**Figure 4.19** Plot of the natural log of the magnitude of the dark current vs. the square root of the magnitude of the applied field for an *n-i-p* and *p-i-n* sample from set A. The plots give slopes very similar to that expected for Schottky injection. Both one and three dimensional Poole-Frenkel treatments give slopes higher than the data.

While this particular result is encouraging, three layer samples from the other sample sets produced plots with much higher slopes than predicted by any of the theories discussed, ranging from  $2.5 \times 10^{-3} \text{ (m/V)}^{1/2}$  for sample set C up to  $\sim 5 \times 10^{-3} \text{ (m/V)}^{1/2}$  for sample set D. Furthermore, single and two layer samples from set A gave slopes more typical of Poole-Frenkel assisted bulk thermal generation. It is hard to speculate what this wide range of results might mean, but it is likely that these high slopes are simply due to the higher field dependence exhibited by these other samples. It is likely that both Schottky injection and Poole-Frenkel assisted generation are occurring simultaneously, perhaps in conjunction with other processes, rendering the root field dependence analysis difficult to interpret.

#### 4.3.6 Space Charge Measurements

If the observed dark current transients are due to the trapping of injected charge carriers in the blocking layers, one should be able to find evidence of this space charge build up which, for a reverse biased, three layer structure, should be similar to the charge on the plates of a parallel

plate capacitor. Theoretical work by Simmons and Taylor [240] predicts that when the voltage applied to a defective insulator with a moderate dielectric relaxation time (corresponding to deep trap states with a depth between 0.5 and 1 eV) is increased or decreased in a step-wise manner, the resulting current will behave as shown in Fig. 4.20. The resulting current spike from a step up in voltage will be limited to the level of the original current spike and a step down in voltage will result in a current spike in the negative direction if the trapped space charge in the sample is great enough. Stabilized a-Se fits their definition of a “defective insulator” and so similar behaviour could be expected from the samples of set A.

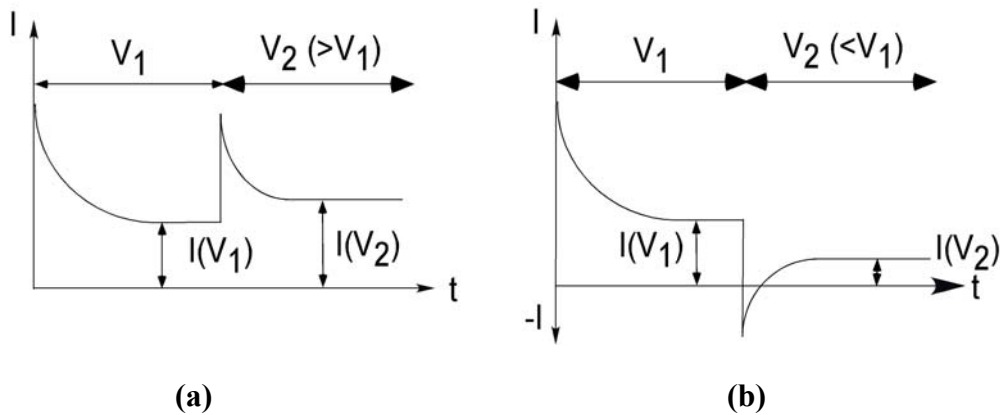


**Figure 4.20** Expected  $I$ - $t$  characteristics for samples in set A if large quantities of space charge due to trapped injected carriers control the dark current transients; redrawn from [240]. (a) gives the expected behaviour for a step up in voltage and (b) for a step down.

#### 4.3.6.1 Control Experiment

There is nothing in the schematic diagram included with the user manual of the Stanford Research Systems power supply used for these measurements which would indicate an impedance to an output transient in which the current flows in a direction opposite to that implied by the polarity of the output voltage, as suggested in Fig. 4.20. However a control experiment was performed to test this and to be certain that any results in which this occurs are not an artifact of the measurement system. This test is shown schematically in Fig. 4.21 (a) where the switch and two voltage sources represent a step change in voltage supplied by the Stanford power supply and the RC circuit is built from discrete components between the leads used for dark current

measurements. The values used are  $R_{int} = 10 \text{ M}$ ,  $R = 22 \text{ M}$ , and  $C = 1 \text{ } \mu\text{F}$  resulting in an expected time constant,  $\tau$ , of roughly 32 s. The expected waveforms are shown in Fig. 4.21 (b). After the capacitor charges to  $V_A$ , the input voltage is switched to  $V_B$ , resulting in a negative current as the voltage across the capacitor decreases to  $V_B$ . The area under the current graph of Fig. 4.21 (b) gives the charge accumulated as:

$$Q_A = \int_0^{\infty} \frac{V_A}{R_{tot}} e^{-\frac{t}{R_{tot}C}} dt = V_A C [1 - 0] = CV_A \quad (4.2)$$

The switch between  $V_A$  and  $V_B$  occurs at  $t = 100 \text{ s}$  with  $V_A = 40 \text{ V}$  and  $V_B = 20 \text{ V}$ . Table 4.3 gives the expected values for this control experiment and the observed values. The agreement is quite close and, most importantly, a current transient of the type shown in Fig. 4.21 (b) is observed, meaning that this system is capable of the proposed discharge and step measurements.

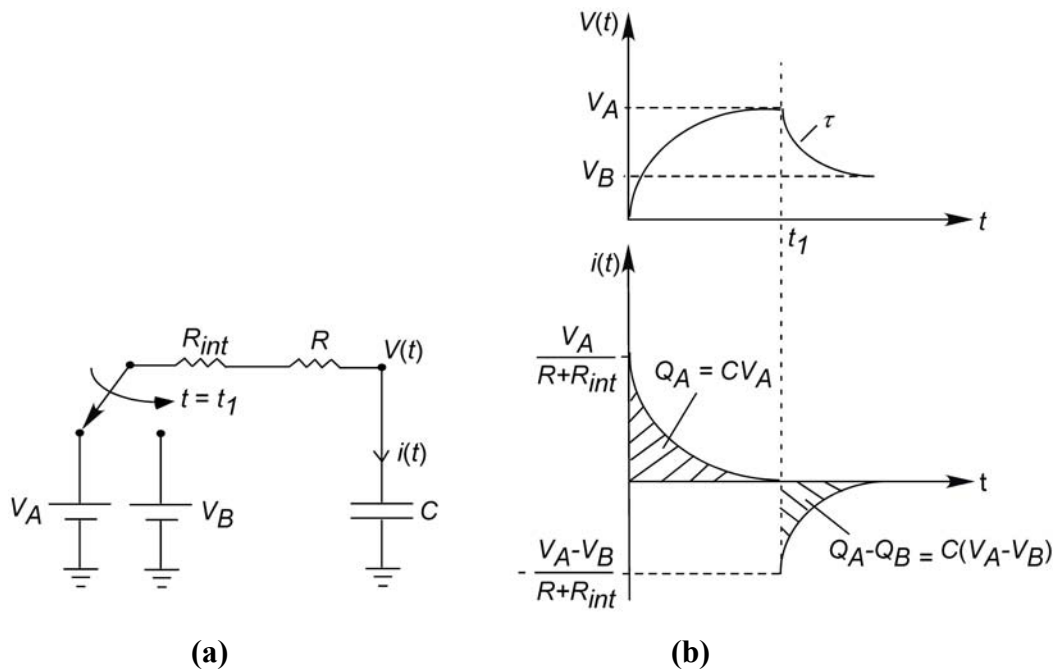


**Figure 4.21 (a)** Schematic representation of a current reversal control experiment. At  $t_1$  the applied voltage is switched from  $V_A$  to the lower voltage,  $V_B$ . **(b)** Expected transients for the voltage across the capacitor,  $V(t)$ , and current through the RC circuit,  $i(t)$ .

**Table 4.3 Results for the control experiment described by Fig. 4.21. Observed charges were calculated using Matlab to numerically integrate the measured current transients, setting initial values to zero.**

Parameter	Expected	Observed
$i_1$	1.25 $\mu\text{A}$	1.07 $\mu\text{A}$
$i_2$	0.625 $\mu\text{A}$	0.57 $\mu\text{A}$
$\tau$	32 s	35 s
$Q_A$	$4 \times 10^{-5}$ C	$3.3 \times 10^{-5}$ C
$Q_A-Q_B$	$2 \times 10^{-5}$ C	$1.7 \times 10^{-5}$ C

It should be noted that the electrometer is only capable of measuring data points roughly 2 s after a change in the applied bias. This means that none of the measurements in Section 4.3.6.2 or 4.3.6.3 are related to the response time of the power supply or transients due to the RC time constant of the sample, which will be roughly 6 ms in this system.

#### 4.3.6.2 Voltage Step Measurements

Figure 4.22 shows voltage step measurements for a *p-i-n* sample of set A. At  $t = 0$ , a field of  $-0.625$  V/ $\mu\text{m}$  is applied across the sample, resulting in a typical dark current transient for 1000 s, decreasing by an order of magnitude, reaching a plateau at around  $2 \times 10^{-3}$  pA mm<sup>-2</sup>. At  $t = 1000$  s, the applied field is doubled to  $-1.25$  V/ $\mu\text{m}$ , yet the initial peak of the current transient is no larger than that for an applied field of  $-0.625$  V/ $\mu\text{m}$ . It could be that the trapping of charge carriers injected during the first 1000 s has created a large enough opposing electric field within the sample to make it appear as if only half of the applied voltage is present. This effect is not reproduced at  $t = 2000$ , 3000 or 4000 s as the change represented by doubling the applied field is too great to be absorbed by the space charge regions in the sample. However, if smaller steps are taken, for example, increasing the field by 1.5 times, the effect is more pronounced, with the second and third peaks being below the first. The results of reducing the applied field by a factor of two at each step (starting at  $t = 5000$  s in Fig. 4.22) gives a very strong case for the presence of space charge in the sample, as the decrease in the field actually leads to a reversal of the current direction for a short time.

This shows good agreement with Simmons and Taylor's predicted result for defective insulators with deep trap states with a depth between 0.5 and 1 eV [240]. It is likely that the basic features of these transients are due to the release of trapped holes. However, trapped electrons, which have much longer release times than holes in a-Se, might be responsible for subtle features. An example of this can be seen in the last two transients in Fig. 4.22 (starting at  $t = 7000$  and  $8000$  s) which saturate at quasi-steady-state currents in the opposite direction to what would be expected for a negative bias. This could be due to space charge within the sample due to trapped electrons which simply will not be released for a very long time.

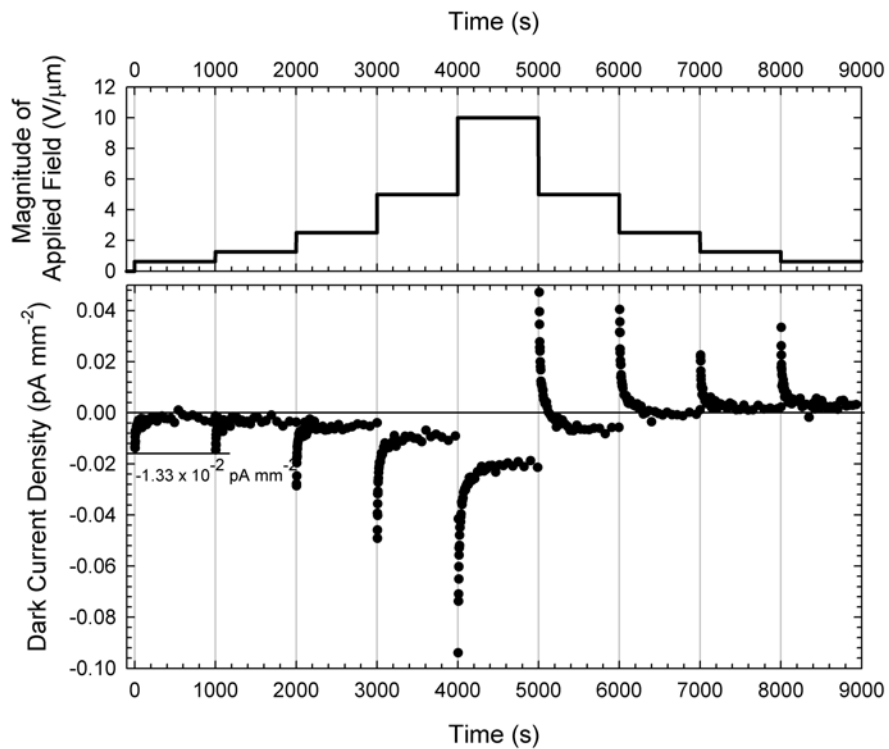


**Figure 4.22** Dark current density transients through a *p-i-n* sample from sample set A in response to step-wise changes in the applied field. The transient at  $t = 1000$  s has a peak value equal to the transient before it where the applied field was two times less. Steps down in voltage result in current spikes in the opposite direction. This could be evidence of space charge build up within the sample.

Of course, the prerequisite for this behaviour is that a large amount of injected charge must be trapped by the sample. As can be seen from Fig. 4.23, a similar experiment carried out on a simple *i*-layer sample did not result in the second peak being lower than the first for increasing steps and only the last 2 transients (at  $t = 7000$  and  $8000$  s), where the applied field

was quite low, gave rise to a relatively small initial current spike in the positive direction. Both the *p-i* and *i-n* samples showed results indicating an amount of stored charge greater than that for the *i-layer* sample but well below that of the *p-i-n* sample. This suggests that either much more charge is trapped in the blocking layers than in the *i-layer* or the location of the charge trapped in the samples with one or both blocking layers is more conducive to creating a potential in opposition to that applied. A summary of typical results for all sample types is given in Table 4.4. The “First 2 peaks even when doubling applied voltage?” column refers to the result shown in Fig. 4.22 for a *p-i-n* sample where the current peak resulting from a step up in voltage is even with the peak before it. This only occurred in the *p-i-n* samples and if this result is an indication of strong trapping of injected charge by the blocking layers, one would expect to see the same result in the *n-i-p* samples. This was not the case, and the reason for this will be discussed more in the following sections. The “Number of peaks reversed when halving applied voltage” column refers to the number of steps down in voltage which resulted in a current spike in the opposite direction (a maximum of four is possible in these measurements). The more times this occurred, the stronger the opposing field created by the charge carriers trapped in the sample.

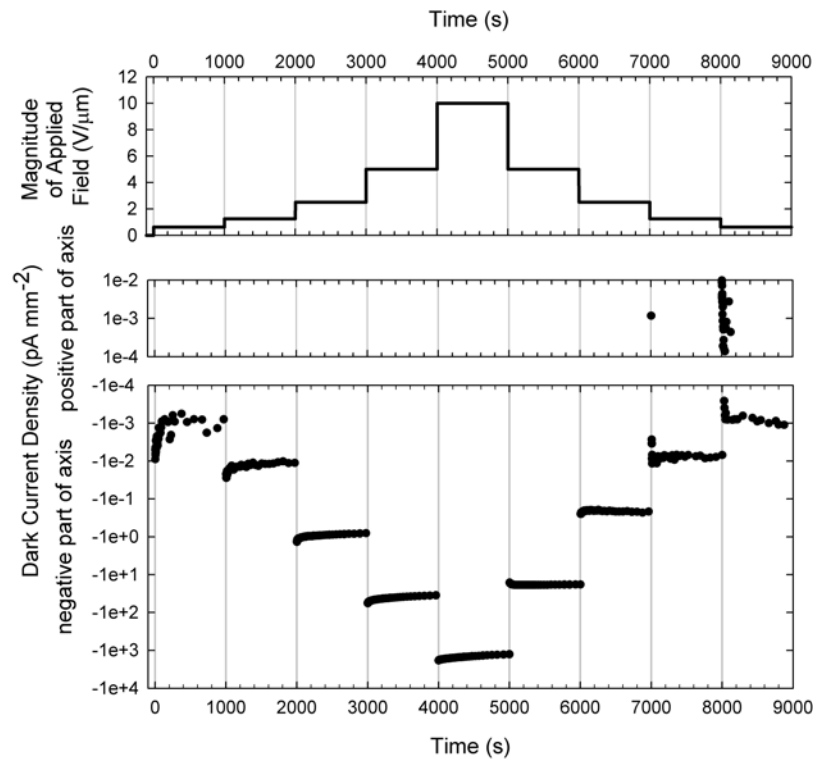


**Figure 4.23** Dark current density transients through an *i-layer* sample from set A in response to step-wise changes in the applied field. The current scale is logarithmic to account for the large

range of currents produced, as the *i*-layer samples have a much greater field dependence than multilayer samples.

**Table 4.4 Results for voltage step measurements on sample set A. The *p-i-n* samples display behaviour which is most indicative of large amounts of trapped charge carriers within the sample.**

Sample structure	Applied field (V/ $\mu\text{m}$ )	First 2 peaks even when doubling applied voltage?	Number of peaks reversed when halving applied voltage
<i>i</i> -layer	-10	No	0
<i>i</i> -layer	10	No	0
<i>p-i</i>	-10	No, but close	2
<i>i-p</i>	10	No, but close	2
<i>i-n</i>	-10	No, but close	4
<i>n-i</i>	10	No	4
<i>p-i-n</i>	-10	Yes	4
<i>n-i-p</i>	10	No	4

#### 4.3.6.3 Discharge Measurements

A further investigation of the space charge built up in the a-Se layer during the flow of dark current is performed by simple discharge measurements. This is done by short-circuiting the sample through a current-limiting resistance immediately after the bias has been applied for 1000 s and measuring the resulting current. It can be seen in Fig. 4.24 that the current through a *p-i-n* sample from set A after the bias is removed is on the same order of magnitude as that which occurred when the bias was applied, just in the opposite direction. It seems that the injected electrons have been trapped in the *p*-layer and the injected holes have been trapped in the *n*-layer, similar to the way stored charge builds up on the plates of a capacitor, creating an internal electric field in opposition to that applied. It is interesting that this is not the case for samples of all structures. While the discharge current will be in the opposite direction to that of when the bias was applied in samples that do not have both or either of the blocking layers, it is often of a much lower level than the preceding dark current. This can be seen in Fig. 4.25 for the *p-i-n* family of samples. Figure 4.25 (a) shows the magnitude of the dark current transients measured when -10 V/ $\mu\text{m}$  was applied across each sample for 1000 s while (b) shows the magnitude of the

corresponding discharge transients. The discharge transients of the different structures are all within one order of magnitude of each other while the original dark current transients are as much as four orders of magnitude apart, as in the case of the *i*-layer and *p-i-n* samples. A comparison of Fig. 4.25 (a) and (b) shows that only the *p-i-n* sample produces a discharge current on the same order of magnitude as the dark current, not because the discharge transient is any higher, but because the dark current transient is that much lower.

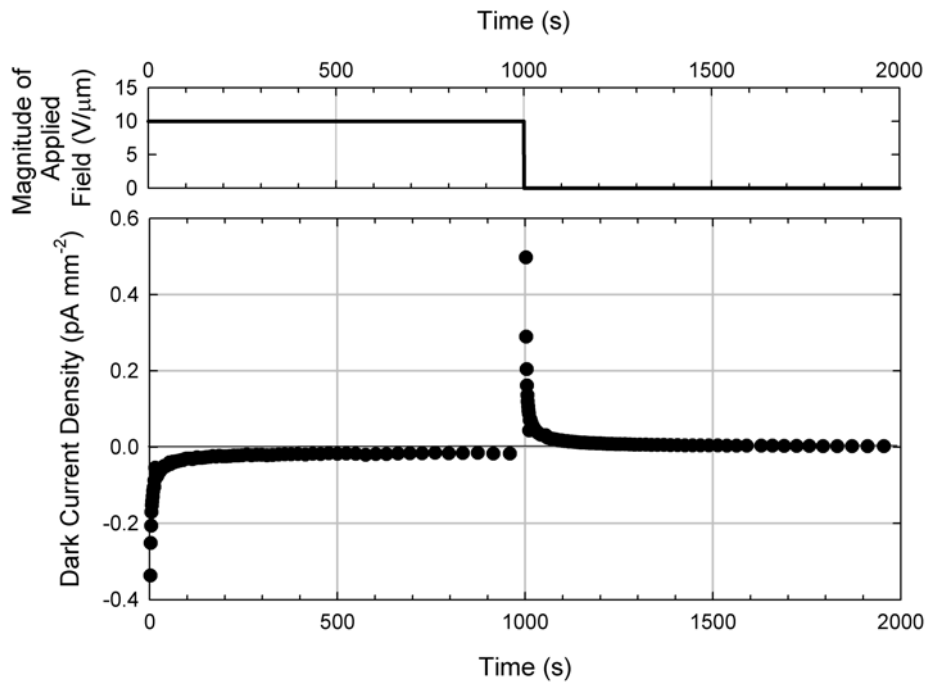


**Figure 4.24** Dark and discharge current density transients produced by applying  $-10 \text{ V}/\mu\text{m}$  across a *p-i-n* sample from set A for 1000 s followed by short-circuiting the sample through a resistor and measuring the discharge current for 2 hours (1000 s of discharge shown).

This analysis can be taken a step further by integrating the discharge currents to determine the amount of charge released. This was done as a numerical integration using Matlab by setting the initial value of the dark current at to 0. “Baseline” measurements were taken for each sample in which the sample was given at least 12 hours of dark rest, followed by monitoring the signal coming from the sample without an external field applied for another 12 hours. The measured signal was typically noisy and somewhere between 0.1 and 0.01 pA. While a noise signal this small makes very little difference in typical dark current transient measurements, discharge measurements can continue to decay for up to 12 hours after the removal of the bias, giving a

continued decay below the “baseline” value. While the fairly smooth nature of these transients seems to suggest that the data is useful, once the level of the dark current falls below the baseline, the values are no longer dependable. As a result, the discharge transients were only integrated up to the time when the current level fell below the baseline value measured for each sample. For all samples, this occurred sometime after the 2 hour mark and so a total integration time of 2 hours was used for all samples.

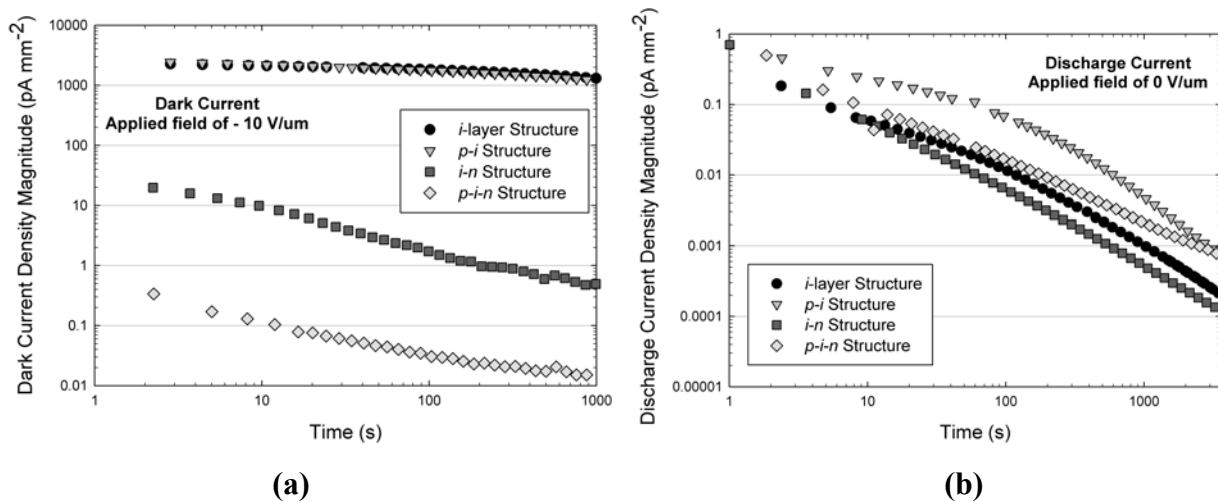


**Figure 4.25** Magnitudes of (a) the dark current density and (b) the discharge current density transients for the *p-i-n* family of sample set A. The dark current depends strongly on the sample structure but the corresponding discharge current does not.

Figure 4.26 (a) shows the charge released over the 2 hour integration time for the *p-i-n* family of samples after they were each negatively biased at three different fields. It can be seen that the *p-i* sample releases the most charge of all the samples at all fields and the *i-layer* and *i-n* samples consistently release very similar amounts of charge. This is unexpected, as the *i-layer* and *p-i* samples produce similar levels of dark current and it is the *i-n* sample which produces a much lower level of dark current. The greater amount of stored charge in the *p-i* sample may simply be due to the fact that that particular sample is roughly 225  $\mu\text{m}$  thick while the rest of the samples in the family are closer to 200  $\mu\text{m}$ , but it is strange that the amount of stored charge does not correspond directly the reduction in the dark current level. Figure 4.26 (b) shows the same comparison for the positively biased *n-i-p* family of samples. In this case, there is a more consistent increase in the amount of charge released as the complexity of the samples grows from

single to multilayer samples. However, the values of charge released are not very different between the different structures, especially at lower fields. Furthermore, the *n-i-p* sample, which one would expect would store the most charge, as it is the most effective at reducing the dark current level, stored less than either the *n-i* or *i-p* samples. This can be attributed to the fact that this particular sample was no longer effective at reducing the dark current levels at the time of these measurements. The dark current in these measurements was roughly three orders of magnitude larger than that in the previous measurements discussed in Section 4.3.4. This large increase in dark current values over extended periods of time is consistent with all *n-i-p* samples of set A and this result will be discussed in detail in Section 4.3.7.

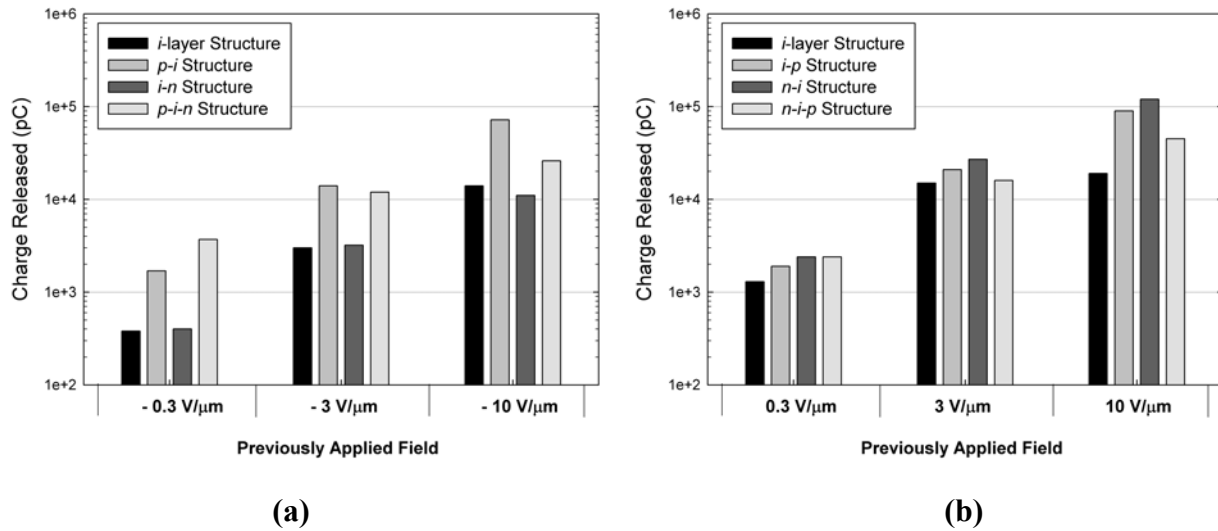


**Figure 4.26** Measured released charge as a function of sample structure and applied bias for (a) the *p-i-n* family and (b) the *n-i-p* family of sample set A. The values were obtained by using Matlab to numerically integrate the discharge currents over 2 hours, setting the initial current value to 0. The *p-i* sample releases a larger amount of trapped charge than the other samples of the *p-i-n* family while the samples of the *n-i-p* family release an amount of trapped charge that is fairly consistent between samples. All samples store more charge at higher applied fields.

It can be seen in Fig. 4.26 that the level of charge stored in each sample increases with the value of the field applied while the space charge built up. This is similar to the case of a parallel plate capacitor, where the charge stored on the capacitor is equivalent to the product of the applied voltage,  $V$ , and the capacitance,  $C$ . The capacitance of the samples of set A can be calculated by assuming the electrodes are the plates of the capacitor and the a-Se layers are the dielectric. Then  $C_{Se} = \epsilon_0 \epsilon_r (A/L)$  where  $\epsilon_0 = 8.854 \times 10^{-12}$  F/m [105],  $\epsilon_r = 6.7$  [59] and  $A = 21$  cm<sup>2</sup>

and  $L = 200 \mu\text{m}$  (nominally) for samples of set A. This gives a calculated value of 0.62 nF. Measurements of the capacitance of the samples of set A with a GenRad 1658 RLC Digibridge gave values very close to that calculated. At an applied field of  $10 \text{ V}/\mu\text{m}$  (2000 V), the charge stored on a 0.62 nF capacitor would be  $1.24 \mu\text{C}$ . From Fig. 4.26 (b), it can be seen that the highest released charge value is from the *n-i* sample, but even this is only  $\sim 0.1 \mu\text{C}$ . For all samples, it seems that the charge trapped in the sample is one to two orders of magnitude less than the charge present on the electrodes. That is to say, the *observed charge released* is much less than the charge present on the electrodes. It is possible that much longer integration times could increase the measured released charge, but accurate measurements of discharge currents at the low levels reached at these long integration times was not possible with the measurement system used.

The idea that the stored charge seems to depend upon the applied bias, but be relatively independent of the level of dark current which is produced by that bias, is supported by an observation made during measurement of the contact formation process on samples of set C. Transients measured during the application of a positive bias for the first time can be seen in Fig. 4.27 (a). As discussed in Section 4.3.3, the first transient measured after the deposition of the sample and corresponding contact is not reproducible and the second run at  $10 \text{ V}/\mu\text{m}$  yields a lower current level. However, when one compares these two applications of the same voltage which resulted in very different dark currents, the discharge transients are exactly the same. This can be seen in Fig. 4.27 (b). It should be noted that the discharge transient measured after a  $5 \text{ V}/\mu\text{m}$  transient was recorded is lower than that for the  $10 \text{ V}/\mu\text{m}$  discharge transient, and these results are consistent across all samples of set C.

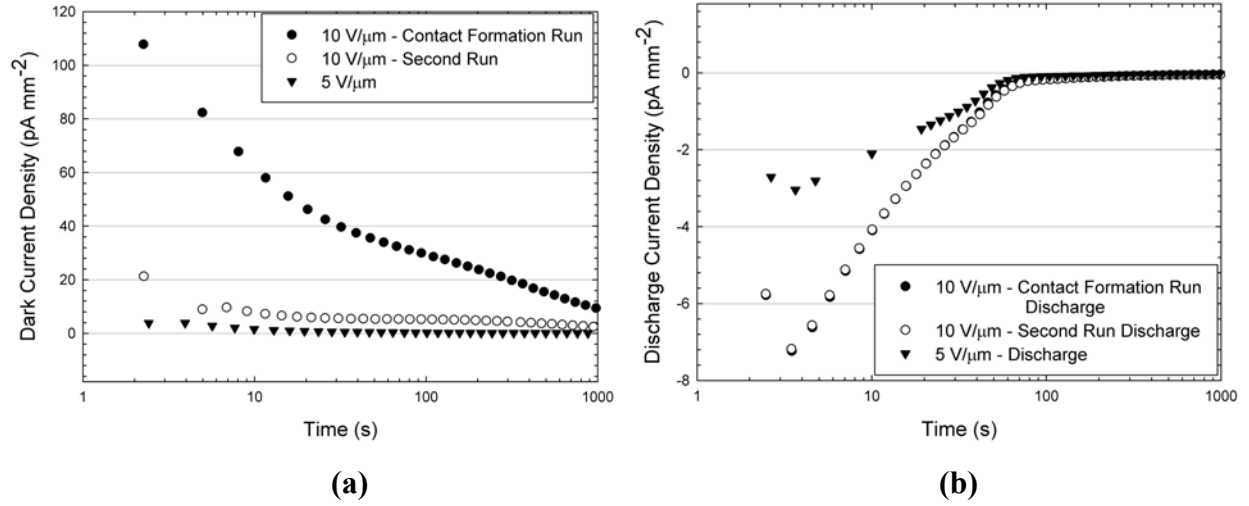


**Figure 4.27** Discharge measurements recorded during the observation of the contact formation process on the Al contact of an *n-i-p* sample from set C. (a) Transients measured during the application of the bias, (b) discharge transients measured by short-circuiting the sample after the application of the bias for 1000 s. Very different dark current levels at the same applied field result in identical discharge transients.

While the presence of the discharge current is evidence of appreciable space charge build up within the a-Se layers, the amount of charge stored in a structure does not seem to correspond to the efficiency of the structure in reducing the level of the dark current. Multilayer samples exhibit dark current levels orders of magnitude lower than single layer samples, yet they do not seem to store that much more charge. Perhaps then it is not how much charge a sample stores, but *where* it is stored. Figure 4.28 depicts four samples with an (a) *i*-layer structure, (b) *i-p* structure, (c) *n-i* structure and (d) *n-i-p* structure. If the trapped carrier concentration in each layer is assumed to be uniform over the layer, the fields at the positive and negative contacts,  $F_1$  and  $F_2$ , can be determined by solving Poisson's equation with the boundary condition that the integral of the electric field distribution must equal the applied voltage. This gives the following relations:

$$F_1 = F_0 - \frac{e}{\epsilon_r \epsilon_0} \left[ \left( L_n - \frac{L_n^2}{2L} \right) p_m + \left( \frac{L_n^2 - L_p^2}{2L} - L_n + \frac{L}{2} \right) (p_{ii} - n_{ii}) - \frac{L_p^2}{2L} n_{tp} \right] \quad (4.3)$$

$$F_2 = F_0 - \frac{e}{\epsilon_r \epsilon_0} \left[ -\frac{L_n^2}{2L} p_m + \left( \frac{L_n^2 - L_p^2}{2L} + L_p - \frac{L}{2} \right) (p_{ii} - n_{ii}) + \left( L_p - \frac{L_p^2}{2L} \right) n_{tp} \right] \quad (4.4)$$

where  $F_0$  is the nominal applied field,  $p_m$  is the concentration of holes trapped in the  $n$ -layer,  $n_{tp}$  is the concentration of trapped electrons in the  $p$ -layer,  $p_{ii}$  and  $n_{ii}$  are the concentration of holes and electrons trapped in the  $i$ -layer, respectively,  $L$  is the total thickness of the sample,  $L_n$  is the thickness of the  $n$ -layer and  $L_p$  is the thickness of the  $p$ -layer. A total thickness of 200  $\mu\text{m}$  is assumed for all samples, while a 5  $\mu\text{m}$   $n$ -layer and a 2  $\mu\text{m}$   $p$ -layer are assumed. This means that in the  $n$ - $i$ - $p$  sample of Fig. 4.28 (d), the  $i$ -layer is 193  $\mu\text{m}$  thick.

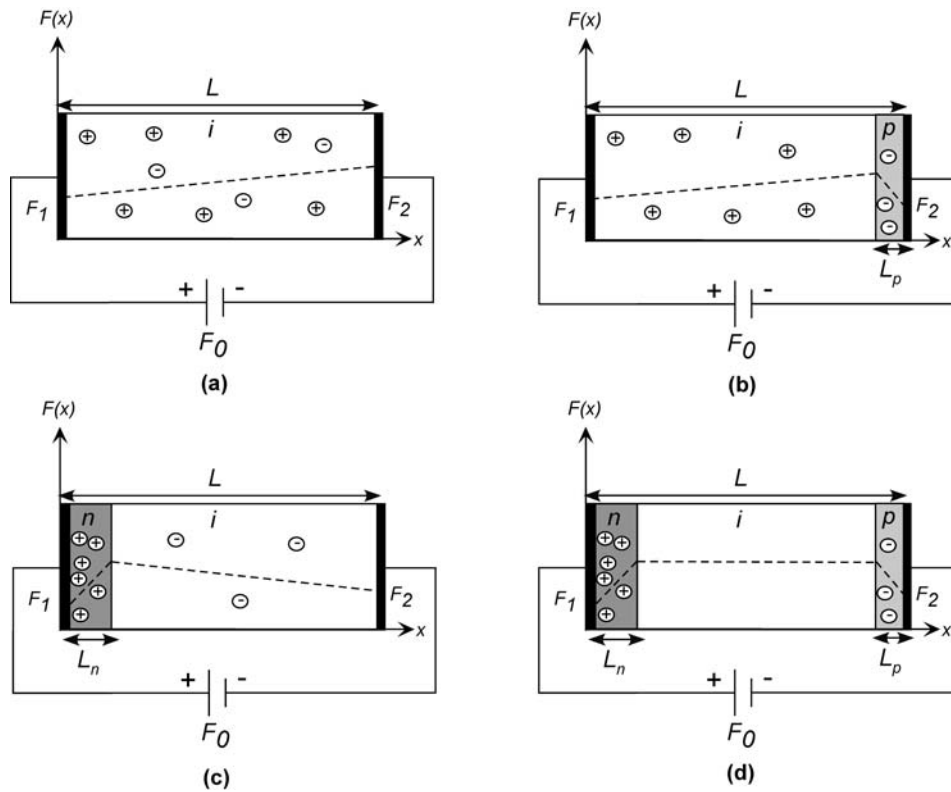


**Figure 4.28** Schematic illustration of (a) an  $i$ -layer sample with holes and electrons uniformly trapped throughout, (b) an  $i$ - $p$  sample with holes trapped in the  $i$ -layer and electrons trapped in the  $p$ -layer, (c) an  $n$ - $i$  sample with holes trapped in the  $n$ -layer and electrons trapped in the  $i$ -layer and (d) an  $n$ - $i$ - $p$  sample with holes trapped in the  $n$ -layer and electrons trapped in the  $p$ -layer. The same amount of charge is stored in each sample, but the location of the charge has a varying effect on the electric field at the contacts.

In all cases in Fig. 4.28, there is an equal amount of charge stored, only in different locations. It is assumed that there are twice as many trapped holes as electrons, as an equal number of trapped carriers, trapped evenly throughout the sample (as in the case of the *i*-layer sample), would cancel each other out, causing no change in the electric field distribution or the dark current with time. Obviously, the results in Fig. 4.27 show that the dark current in *i*-layer samples decays with time. This assumption is merely to simplify the proposed model. In reality it may be unnecessary, as much of the charge which is trapped in an *i*-layer sample may be trapped close to the electrodes. a-Se films can have deep trap concentrations which are several orders of magnitude higher near the surfaces than in the bulk [186], as often a layer of polycrystalline Se will form next to the substrate either during or after deposition [236,241].

Total concentrations of trapped carriers are assumed to be  $2 \times 10^{12} \text{ cm}^{-3}$  for holes and  $1 \times 10^{12} \text{ cm}^{-3}$  for electrons. For the *i*-layer shown in Fig. 4.28 (a),  $L_n$  and  $L_p$  are 0, and if an applied field value of  $10 \text{ V}/\mu\text{m}$  is assumed, Eqs. 4.3 and 4.4 give values of  $F_1 = 9.74 \text{ V}/\mu\text{m}$  and  $F_2 = 10.27 \text{ V}/\mu\text{m}$ , leading to a reduction in the dark current if it is dominated by hole injection. Considering the *i-p* structure shown in Fig. 4.28 (b), it is assumed that all of the trapped electrons in the previously considered *i*-layer are now trapped in the *p*-layer and all of the holes are trapped in the now smaller *i*-layer. This leads to further reduced field values at both contacts. The results of the calculations are tabulated for all four structures of Fig. 4.28 in Table 4.5. It can be seen that for the same amount of trapped charge, the field at the contacts is reduced more when the charge is trapped next to the contacts, as would be the case in samples with blocking layers. In the case of carrier injection from the contacts over a Schottky barrier, the dark current will depend exponentially on the square root of the field at the contacts (Eqs. 2.26 and 2.27), so that a small change in the field will have a large impact on the dark current level. Therefore, samples with blocking layers trap charge carriers in a way that is efficient in reducing the dark current and absorbing sudden changes in the applied field (as shown in the previous sub-section) without necessarily trapping much more charge than *i*-layer samples. These results also support the assumption used by Kabir and Mahmood [57,59,106] in the modeling of the dark current through a-Se *n-i-p* structures: that injected holes are deeply trapped in the *n*-layer while injected electrons are deeply trapped in the *p*-layer and interaction between injected carriers and the *i*-layer is likely negligible.

**Table 4.5** Electric field at the positive ( $F_1$ ) and negative ( $F_2$ ) contacts of the samples shown in Fig. 4.28, calculated using Eqs. 4.3 and 4.4 with assumed values of  $L = 200 \mu\text{m}$ ,  $L_p = 2 \mu\text{m}$ ,  $L_n = 5 \mu\text{m}$ , a total trapped hole concentration of  $2 \times 10^{12} \text{ cm}^{-3}$  and a total trapped electron concentration of  $1 \times 10^{12} \text{ cm}^{-3}$ .

Sample Structure	$F_1$ (V/ $\mu\text{m}$ )	$F_2$ (V/ $\mu\text{m}$ )
<i>i</i> -layer	9.74	10.27
<i>i</i> - <i>p</i>	9.48	9.97
<i>n</i> - <i>i</i>	9.19	9.74
<i>n</i> - <i>i</i> - <i>p</i>	8.93	9.47

It is interesting to note that for a *p-i-n* sample under forward bias, at fields above roughly 1 V/ $\mu\text{m}$ , the direction of the discharge current changes to be the same as the current during voltage application, as shown in Fig. 4.29. At fields above 1 V/ $\mu\text{m}$  the electrons can drift through the *n*-layer which they are being injected into and drift to the *p*-layer where they are trapped. The same will be true for holes drifting through the *p*-layer and into the *n*-layer, creating an internal electric field with a polarity opposite to that created by fields below 1 V/ $\mu\text{m}$ . This is shown schematically in Fig. 4.30.

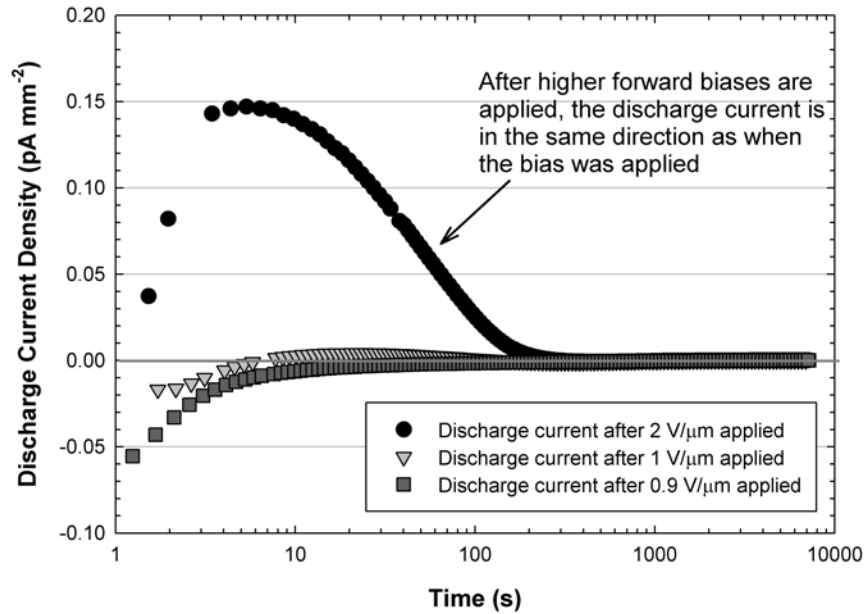


**Figure 4.29** Discharge currents for a *p-i-n* sample of set A after being forward biased at different voltages. At fields above 1 V/ $\mu\text{m}$ , the discharge current is in the same direction as the current when the bias was applied.

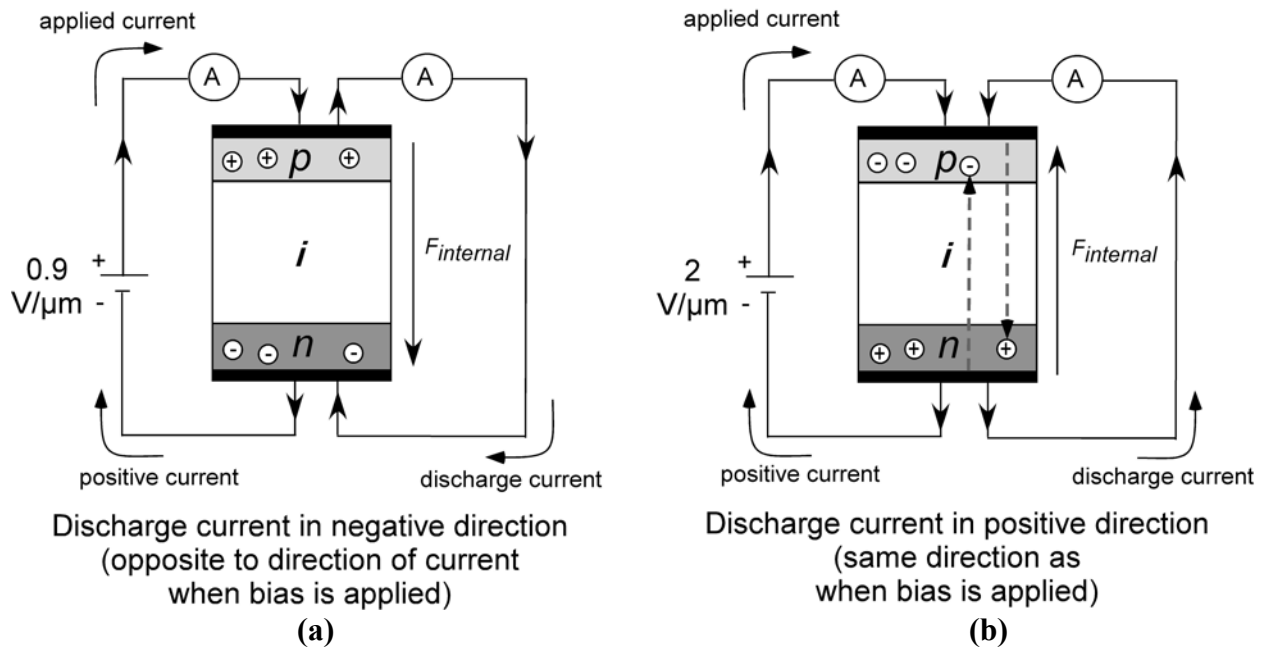


**Figure 4.30** Explanation of reversal of discharge current direction in a  $p-i-n$  sample when forward biased above a certain value. (a) Below an applied field of  $1 \text{ V}/\mu\text{m}$ , injected holes are trapped in the  $p$ -layer and injected electrons are trapped in the  $n$ -layer, creating an internal field in opposition to that applied. (b) Above  $1 \text{ V}/\mu\text{m}$ , injected holes drift through the  $p$ - and  $i$ -layer and are trapped in the  $n$ -layer and injected electrons drift through the  $n$ - and  $i$ -layer and are trapped in the  $p$ -layer, creating an internal field supporting that applied.

The fact that the discharge current is of the same order of magnitude as the current which flows when the bias is applied in three layer samples with effective blocking layers provides a simple method of checking the functionality of the blocking layers in other samples. Since all samples are rested in the dark for 12 hours between the recording of transients, it is a simple matter to record the discharge data during this time. In this way, if an irregular transient is recorded, the discharge data following that transient can be analyzed to determine if a blocking layer has broken down for some reason. This method of analysis is used throughout the rest of this chapter, in addition to a comparison of the general dark current level produced by a sample with the original measurements on the samples of set A presented in Section 4.3.4.

### 4.3.7 Long Term Reproducibility

Roughly one year passed between the start of dark current measurements on sample set A and the completion of the discharge and voltage-step measurements. It should be noted that many of the samples displayed quite different dark current levels when compared to transients measured one year earlier. Only two samples, one *p-i* and one *p-i-n*, displayed no change with one year of ageing. Most other samples experienced an increase of around one order of magnitude in the dark current measured immediately after the application of the bias followed by a faster decrease until the levels were similar, as in the case of an *i*-layer sample, as seen in Fig. 4.31 (a). Another year of ageing saw a further increase in dark current, though not nearly as significantly as during the first year. This difference could be due to small amounts of crystallization of the a-Se layers over time.

A notable exception occurs in samples with an *n-i-p* structure. As shown in Fig. 4.31 (b), the current levels have increased by three orders of magnitude in one year's time in an *n-i-p* sample and almost another order of magnitude during the second year. This change is consistent in two sister samples as well. It seems that the *n-i-p* samples experience a very large increase in dark current levels over long periods of time. Discharge and voltage-step measurements on these samples show much less evidence of charge carrier trapping in the blocking layers than similarly aged *p-i-n* samples (as seen in Table 4.4 and Fig. 4.26) suggesting a breakdown in the carrier trapping abilities of the blocking layers. The large increase in current suggests that the problem could lie in the crystallization of the *n*-layer. Even very small areas of crystallization in the *n*-layer could result in columns of crystalline Se which injected holes could use to bypass the *n*-layer, generating a large increase in the dark current. Because of the small effect of the *p*-layer shown in Section 4.3.4, it is unlikely that a breakdown in only the *p*-layer would cause such an increase in the dark current.

This theory is further supported by the transients in Fig. 4.31 (c) produced by the same *n-i-p* sample when negatively biased so that holes are injected from the bottom (ITO) contact into the *p*-layer. There was almost no change over 2 years when the sample is forward biased in this

way. It does seem that a breakdown in the hole trapping ability of the *n*-layers over time is the reason for the greatly increased dark current in some samples.

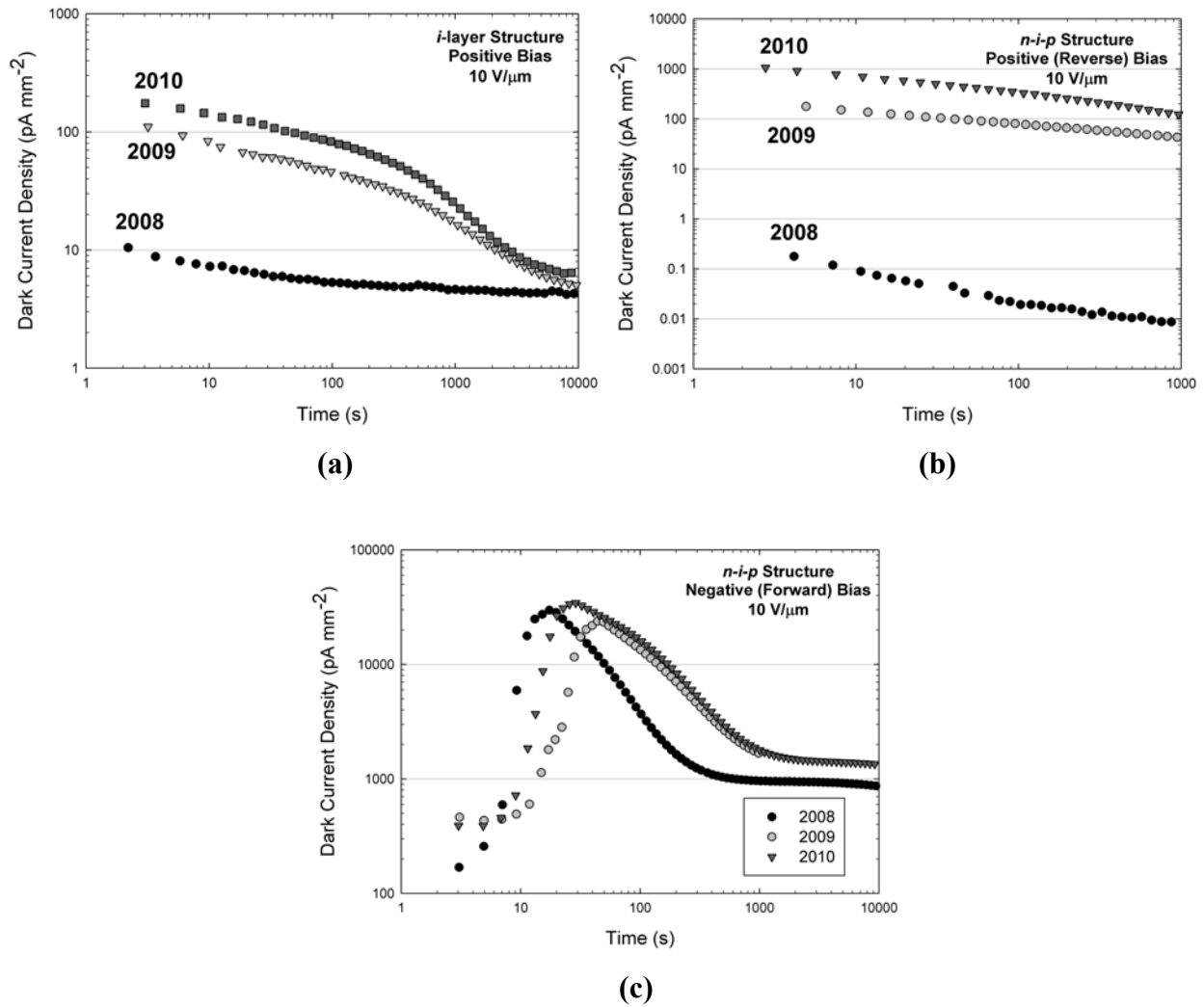


**Figure 4.31** Change in dark current transients with roughly one and two years of ageing of sample set A. (a) an *i*-layer sample biased at 10 V/μm, (b) an *n-i-p* sample, biased at 10 V/μm and (c) the same *n-i-p* sample biased at -10 V/μm (current magnitudes shown). Over two years, the dark current increased by roughly one order of magnitude in the *i*-layer sample. In the *n-i-p* sample, the dark current increased by roughly four orders of magnitude when reverse biased, but remained fairly consistent when forward biased.

#### 4.3.8 Dark Current as a Function of *i*-layer Thickness

If thermal generation of charge carriers in the bulk of the a-Se is making any significant contribution to the overall dark current density in a-Se multilayer sandwich structures, then there

should exist some dependence of the dark current on the thickness of the structure. As discussed in Section 2.6.1.3, if current due to bulk thermal generation is not negligibly low, the measured dark current should increase linearly with the thickness of the  $i$ -layer of the sample.

#### 4.3.8.1 Results From Sample Set B

The first attempt at an  $n-i-p$  sample set with varying thickness of  $i$ -layers with consistent thickness of blocking layers was made with sample set B, the properties of which are discussed in Section 4.2.1.3. A plot of dark current density vs.  $i$ -layer thickness for the Pt contacts on all five samples of set B, biased at 10 V/ $\mu\text{m}$ , is shown in Fig. 4.32. Data are plotted for both 100 s and 1000 s after the application of the bias. It can be seen that there is a significant increase in the dark current level as the thickness of the  $i$ -layer increases. Best fit lines are given for both times by the solid lines, showing that the thickness dependence decreases with time after the application of the bias. The points marked with an “x” represent the data from sample US5 (240  $\mu\text{m}$   $i$ -layer). This sample gave dark current values which were uncharacteristically low for sample set B, especially in the case of the Pt and Cr contacts. As a result, all data points produced by this sample are considered outliers and are denoted by an “x” and a “?”. Ignoring the point from sample US5, the Pt contacts give a remarkably linear relationship between dark current and  $i$ -layer thickness, the slope of the relation depending on the time passed from the application of the bias. This type of linear relationship is what would be expected in the case of bulk thermal generation dominated dark current.

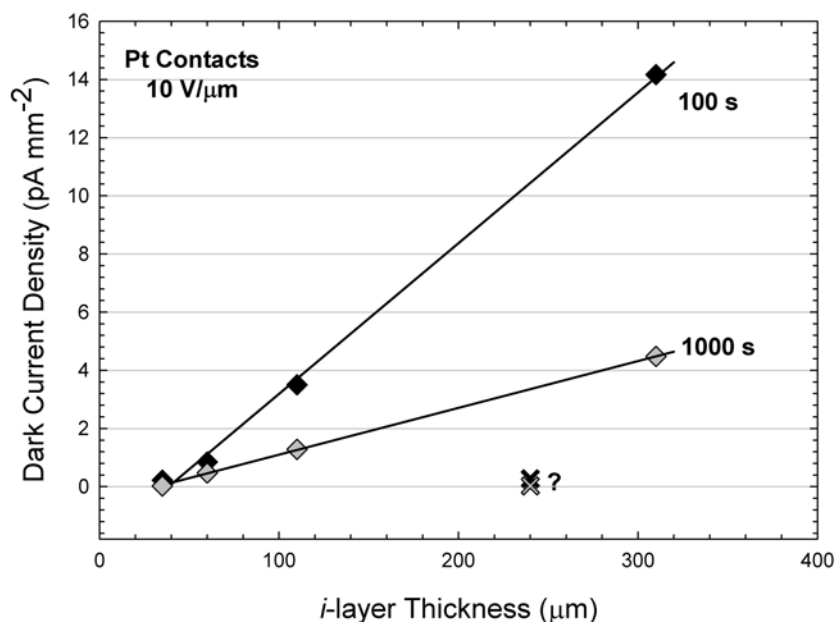


**Figure 4.32** Dark current density as a function of *i*-layer thickness for the Pt contacts on samples of set B, 100 s and 1000 s after the application of the 10 V/μm bias. The solid lines give the best linear fit at both times. The points marked with an “x” represent the uncharacteristically low points from sample US5 (240 μm *i*-layer), which are considered outliers.

Though the other contacts show a strong *i*-layer thickness dependence, it does not fit so neatly into the bulk thermal generation theory. Figure 4.33 shows the dark current density vs. *i*-layer thickness for the Al, Cr and Au contacts. Figure 4.33 (a) shows the thickness dependence for Al and although the current generally increases with increasing thickness, it is much more than would be expected in the case of bulk thermal generation. The dark current increases by over 3 orders of magnitude between the thinnest and thickest samples (a change in thickness of only ~ 7 times).

Figure 4.33 (b) shows the thickness dependence for the Cr contacts and, like the Al contacts, the dark current increases several orders of magnitude as the thickness of the samples increases. The solid line shows a very close power law fit to the Cr data if the relatively low point from US5 (240 μm *i*-layer) is omitted. This fit gives a current dependence which is proportional to the thickness to the power of 3.3, hardly a linear relationship.

Further complicating the situation, the dark current vs. *i*-layer thickness data for Au contacts is plotted in Fig. 4.33 (c). For the thinnest samples, the Au contacts show a large increase in current with thickness (almost 2 orders of magnitude) but the thickest samples actually show a decrease in current with continued increase in thickness.

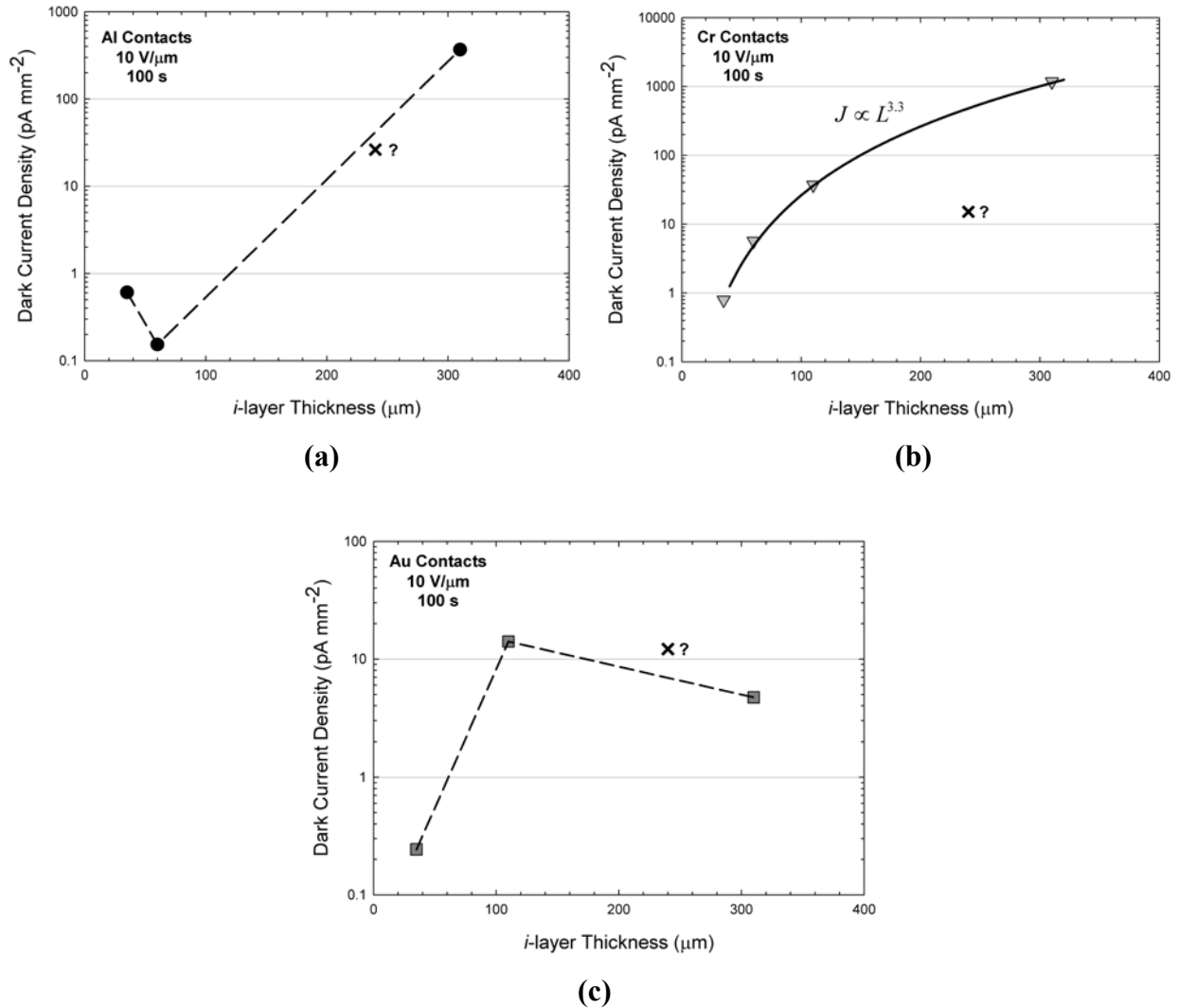


**Figure 4.33** Dark current density as a function of *i*-layer thickness for sample set B at 10 V/μm, 100 s after the application of the bias for (a) Al contacts, (b) Cr contacts and (c) Au contacts. The points marked with an “x” represent the uncharacteristically low points from sample US5 (240 μm *i*-layer). The dashed lines are only a guide for the eye. The solid line in (b) is a power law fit to the Cr data, omitting the outlying point at 240 μm.

While the profound thickness dependence described thus far is very interesting in that it has not been reported before for a-Se sandwich structures, none of the data, other than that

reported for the Pt contacts, supports the theory of bulk thermal generation dominated dark current. Another interesting plot of Pt data can be seen in Fig. 4.34 where the thickness dependence of the current is plotted for applied fields of 10 and 5 V/ $\mu\text{m}$ . While there is a linear increase in current with thickness at 10 V/ $\mu\text{m}$ , this effect disappears at 5 V/ $\mu\text{m}$ . This result is also seen in the other contact metals where the dark current is almost independent of thickness at low fields (e.g. 1 V/ $\mu\text{m}$ ).

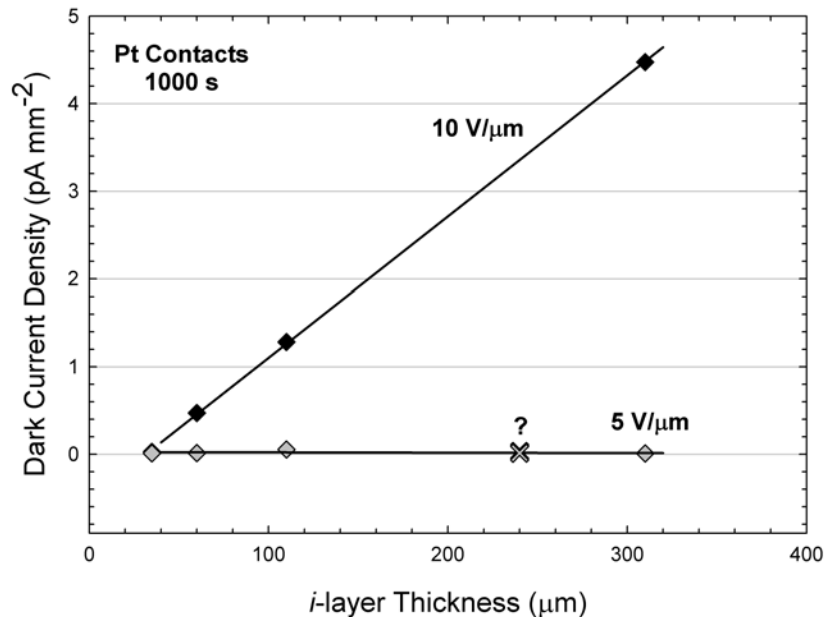


**Figure 4.34** Dark current density as a function of  $i$ -layer thickness for Pt contacts on samples of set B, 1000 s after the application of the 10 or 5 V/ $\mu\text{m}$  bias. The points marked with an “x” represent the uncharacteristically low points from sample US5 (240  $\mu\text{m}$   $i$ -layer). The solid lines give the best linear fit at both applied fields.

It is difficult to explain the behaviour of the samples of set B until one compares the data to that of samples from set A. This is done in Fig. 4.35, where the dark current levels produced by the Pt and Cr contacts on sample US2 (110  $\mu\text{m}$   $i$ -layer), 1000 s after the application of 10 V/ $\mu\text{m}$  are compared to similar data from  $i$ -layer,  $i$ - $p$ ,  $n$ - $i$ , and  $n$ - $i$ - $p$  samples from sample set A (nominally 200  $\mu\text{m}$  thick). It can be seen that the current levels produced by sample US2 are closer to that of the  $i$ -layer and  $i$ - $p$  samples than the  $n$ - $i$ - $p$  sample. The dark current from the Cr contact on US2 is even higher than the  $i$ -layer sample of set A. It seems the samples of set B behave as if they do not even have an  $n$ -layer. This is confirmed by the fact that the discharge transients for sample US2 range from 1 order of magnitude lower than the preceding dark current

level for the Pt contact to 3 orders of magnitude lower for the Cr contact. The *p-i-n* samples of set A showed that properly functioning blocking layers produce a discharge current on the same order of magnitude as the preceding dark current transient.

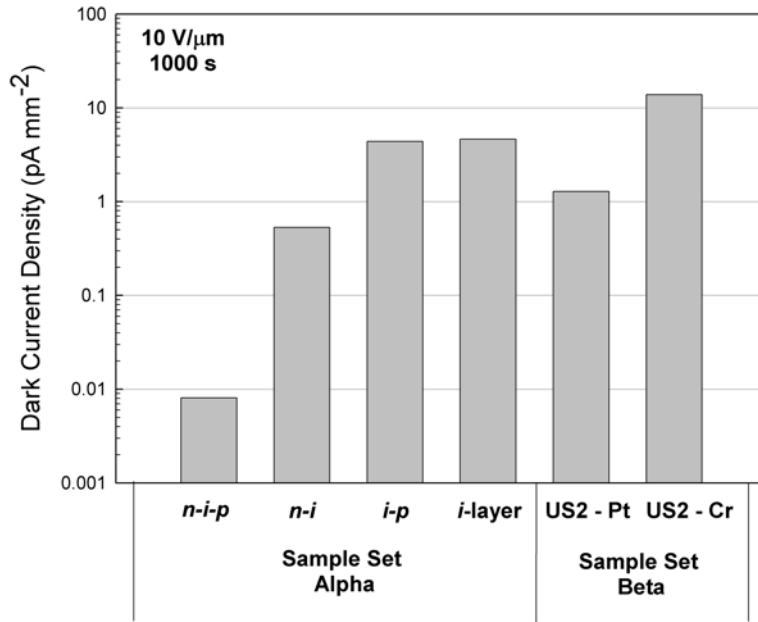


**Figure 4.35** A comparison of dark current density values for *n-i-p* family samples of set A (nominally 200  $\mu\text{m}$  thick) and Pt and Cr contacts on sample US2 (110  $\mu\text{m}$  *i-layer*) of sample set B, 1000 s after the application of the positive bias of 10 V/ $\mu\text{m}$ .

Further evidence for the failure of the *n*-layers in sample set B at high fields is shown in Fig. 4.36 which shows the *J-F* curve for the Pt contact of US2. There are two distinct regions of field dependence. Below 5 V/ $\mu\text{m}$ , the relationship is just above linear, but above 5 V/ $\mu\text{m}$  the dark current is proportional to the field to the power of  $\sim 3.5$ . Similar results have been produced by Al and Au contacts on other samples, where there is a region of greater field dependence at high fields. Three layer samples of set A with properly functioning blocking layers displayed a sub-linear field dependence even at high fields.

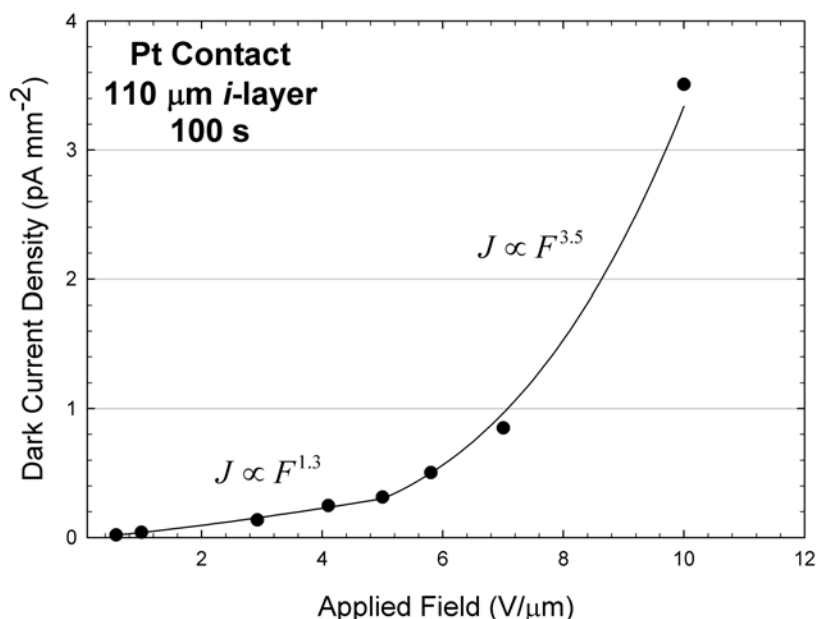


**Figure 4.36**  $J$ - $F$  curve for the Pt contact on sample US2 of sample set B, 100 s after the application of the bias. There are two regions of different field dependence. The transition between the two occurs at  $\sim 5$  V/ $\mu\text{m}$ .

The above arguments give strong evidence for the failure of the  $n$ -layer to block injected holes at high fields. The  $n$ -layers in the samples of set B are  $9 \mu\text{m}$  thick, 50% thicker than those in sample set A. Therefore, it is likely that this phenomenon is due to the use of an a-Se alloy with poor hole trapping properties being used for deposition of the  $n$ -layers in set B.

While all this explains the fact that the samples of set B produce higher overall current levels than those of set A, it does not explain the strong  $i$ -layer thickness dependence exhibited by these samples at high fields. One possible explanation for this result comes from analyzing the electric field distribution across the  $n$ - $i$ - $p$  sample as the  $n$ -layer starts to “leak” (allowing injected holes to drift through) at high fields.

In the case of an  $n$ - $i$ - $p$  sample with properly functioning blocking layers, the field at both the positive and negative contacts will be reduced as injected holes are trapped in the  $n$ -layer and injected electrons are trapped in the  $p$ -layer, as shown in Fig. 4.37. This will be the case for samples of set B at low applied fields. Equations 4.3 and 4.4 can be used to calculate the field at the positive contact,  $F_1$ , and negative contact,  $F_2$ . All interactions in the  $i$ -layer are ignored, *i.e.*

no space charge is built up there due to trapping of injected carriers and  $p_{ti}$  and  $n_{ti}$  are 0. Given the fields at the contacts, one can calculate the current due to the injection of holes and electrons using Eqs. 2.26 and 2.27, giving the total current as:

$$J_{tot} = J_h + J_e = e\mu_h F_1 N_v \exp\left(-\frac{\phi_h - \beta_s \sqrt{F_1}}{kT}\right) + e\mu_e F_2 N_c \exp\left(-\frac{\phi_e - \beta_s \sqrt{F_2}}{kT}\right) \quad (4.5)$$

Using Eqs. 4.3 to 4.5 and the values in Table 4.6, plots of the field at the contacts and the corresponding currents as a function of sample thickness are shown in Fig. 4.38. The applied field was assumed to be 10 V/ $\mu\text{m}$  and  $p_{tm}$  and  $n_{tp}$  were both taken to be  $1 \times 10^{14} \text{ cm}^{-3}$ . The electric field at both contacts stays constant as the thickness of the sample increases over a practical range (40 – 400  $\mu\text{m}$ ) and so do the corresponding currents. It can be seen in Fig 4.38 (b) that the electron current is almost twice as large as the hole current due to the lower barrier to injection assumed for electrons. This scenario could describe the operation of the samples of set B at low fields, some time after the application of the field. A required condition for the successful application of the “leaky  $n$ -layer” model is that the barrier to electron injection at the negative contact be less than the barrier to hole injection at the positive contact. It can be seen in Table 4.6 that 0.9 eV was assumed for the barrier to hole injection while 0.8 eV was assumed for electron injection. In reality, this is a distinct possibility, as holes will be injected into alkali-doped a-Se with a bandgap of  $\sim 2.2$  eV [140] while electrons will be injected into a-As<sub>2</sub>Se<sub>3</sub> which has a bandgap of between 1.7 and 1.8 eV [242]. Despite the complications of interface states, it is reasonable to assume that a smaller bandgap will lead to a smaller barrier to carrier injection.

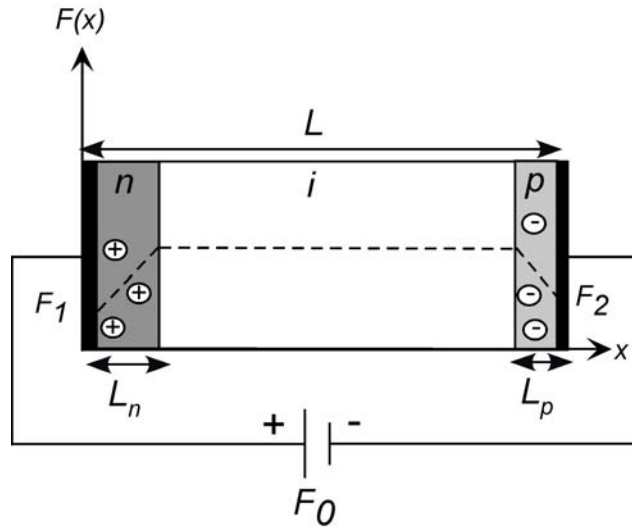
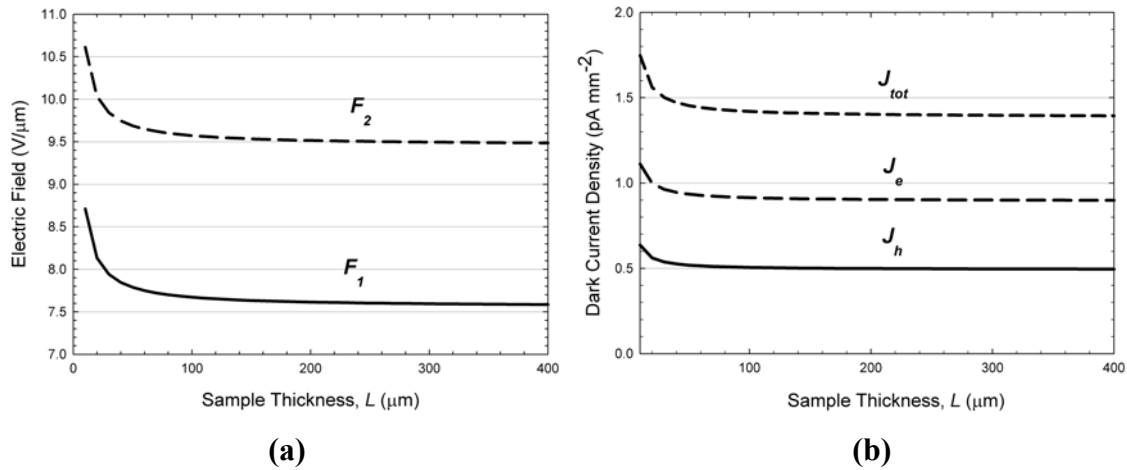


Figure 4.37 Schematic diagram of the electric field distribution across an  $n-i-p$  sample with properly functioning blocking layers.  $L$  is the total thickness of the sample,  $L_n$  is the thickness of the  $n$ -layer and  $L_p$  is the thickness of the  $p$ -layer.

Table 4.6 Material and structural properties assumed for calculations of the electric field at the contacts and the corresponding hole and electron injection currents in an  $n-i-p$  a-Se sandwich structure using Eqs. 4.3 – 4.5.

Property	Assumed Value	Property	Assumed Value
$\mu_h$	$0.12 \text{ cm}^2 \text{ V}^{-1} \text{ s}^{-1}$	$N_{vc}$	$1 \times 10^{19} \text{ cm}^{-3}$
$\mu_e$	$0.0035 \text{ cm}^2 \text{ V}^{-1} \text{ s}^{-1}$	$\epsilon_r$	6.7
$\varphi_h$	0.9 eV	$L_n$	9 $\mu\text{m}$
$\varphi_e$	0.8 eV	$L_p$	2 $\mu\text{m}$



**Figure 4.38 (a) Electric field at the positive ( $F_1$ ) and negative ( $F_2$ ) contacts and (b) the corresponding hole, electron and total injection current as a function of sample thickness for an  $n$ - $i$ - $p$  sample with working blocking layers, once the dark current has reached a steady-state. At practical thicknesses ( $> 100 \mu\text{m}$ ), the electric field at both contacts and the dark current are relatively independent of  $i$ -layer thickness.**

At high fields, if the  $n$ -layer starts to allow injected holes to drift through due to their increased schubweg at higher fields, the situation could begin to look as depicted in Fig. 4.39. Some holes will be trapped in the  $n$ -layer, but no more than in the  $i$ -layer, as holes will now be trapped in the  $i$ -layer as they drift towards the negative contact. The concentration of trapped holes in the  $i$ -layer,  $p_{ti}$ , is taken to be equal to  $p_{tn}$  which is now assumed to be  $1.5 \times 10^{13} \text{ cm}^{-3}$ . The fields calculated by Eqs. 4.3 and 4.4 and the corresponding injection currents, once again calculated with Eq. 4.5, are shown in Fig. 4.40. As the thickness of the sample increases, the space charge built up by the trapping of holes in the  $i$ -layer drives the field at the negative contact higher and higher until the total current is completely dominated by the injection of electrons. Figure 4.40 (b) shows that the electron and total current increase substantially with increasing sample thickness. While this increase is not several orders of magnitude, as observed experimentally with sample set B at high fields, this example does show a possible situation where a less than ideal  $n$ -layer can cause a dark current dependence on  $i$ -layer thickness. An additional increase in current could be due to a surge in Poole-Frenkel assisted thermal generation of carriers in the  $i$ -layer, near the  $p$ -layer, where the field grows very large.

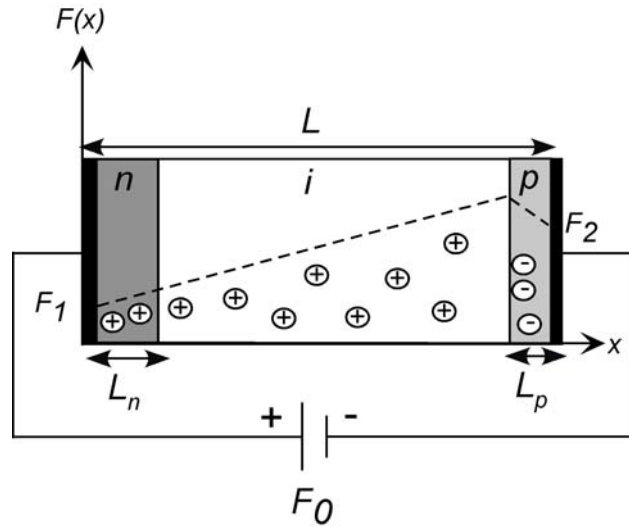


Figure 4.39 Schematic diagram of the electric field distribution across an  $n$ - $i$ - $p$  sample with a leaky  $n$ -layer.

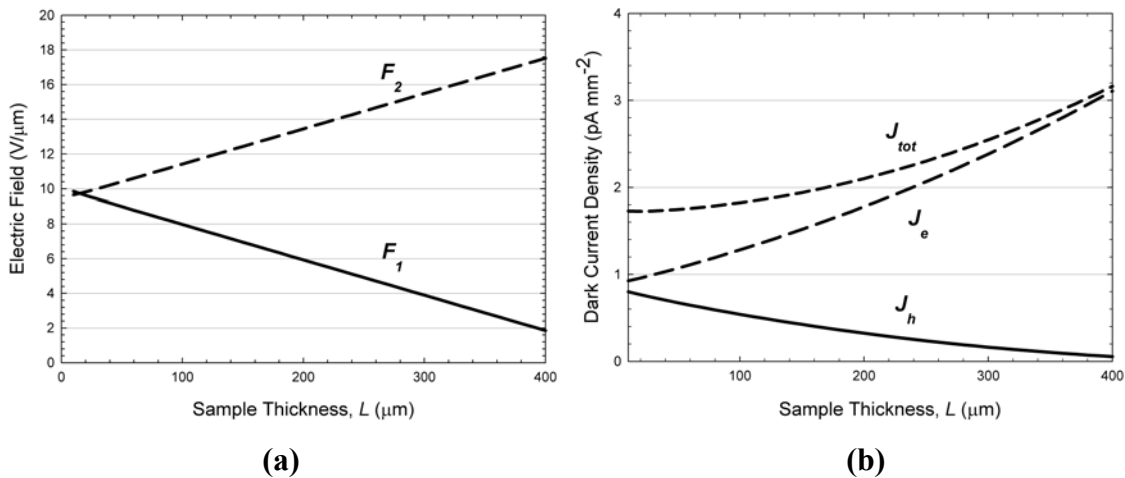
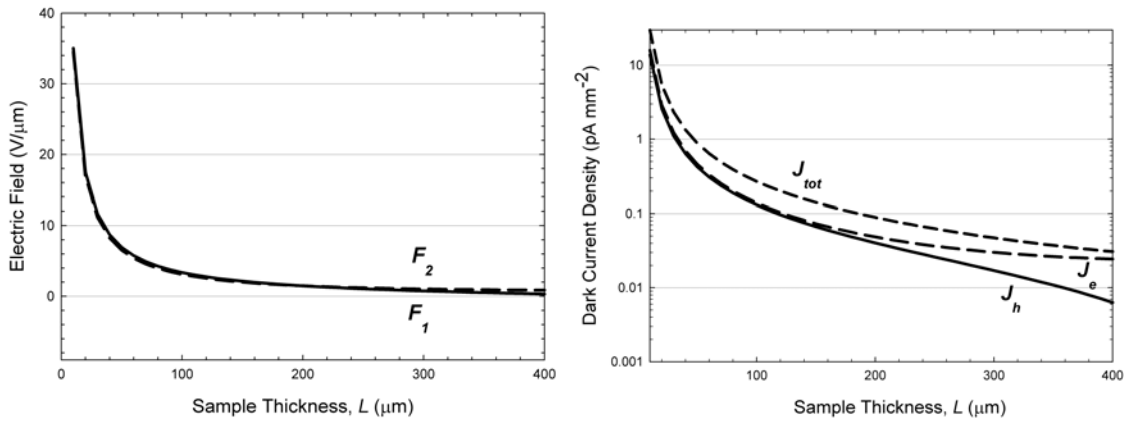


Figure 4.40 (a) Electric field at the positive ( $F_1$ ) and negative ( $F_2$ ) contacts and (b) the corresponding hole, electron and total injection current as a function of sample thickness for an  $n$ - $i$ - $p$  sample with a leaky  $n$ -layer, once the dark current has reached a steady state. The field at the positive contact decreases with increasing  $i$ -layer thickness, while the field at the negative contact increases. As a result, the electron current increases and so too does the total dark current.

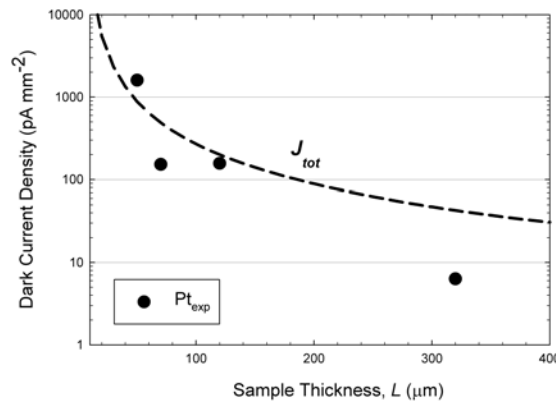
It is also interesting to look at what this “leaky  $n$ -layer” model predicts when the applied voltage is kept constant, allowing the field to change with the thickness. Fig. 4.41 shows the result of this calculation, assuming an applied voltage of 350 V and reduced values of  $p_{in}$  and  $p_{ii}$  of  $1 \times 10^{12} \text{ cm}^{-3}$ , due to the lower amount of charge injected at lower fields. Obviously, the field at both contacts now decreases with increasing thickness, and so too do both the hole and

electron current. While the actual levels of current produced by the model are too low to compare directly with experimental data, Fig. 4.41 (c) shows the total calculated current scaled up by 1000 times along with experimental data collected from sample set B using the Pt contacts and maintaining the applied voltage at 350 V. The model does agree with the observed decay in current with increasing sample thickness for a constant applied voltage.



(a)

(b)



(c)

**Figure 4.41 (a) Electric field at the positive ( $F_1$ ) and negative ( $F_2$ ) contacts and (b) the corresponding hole, electron and total injection current as a function of sample thickness for an  $n$ - $i$ - $p$  sample with a leaky  $n$ -layer when the applied voltage, not the applied field, is kept constant. (c) The total calculated current, scaled up by 1000 times, compared with experimental data for the Pt contacts of sample set B. When the applied voltage is kept constant, the leaky  $n$ -layer model predicts a decrease in dark current with increasing  $i$ -layer thickness that is similar to that observed experimentally.**

There are likely several processes contributing to the strong  $i$ -layer thickness dependence of the dark current in sample set B. However, it seems unlikely that the dominant contribution is

due to bulk thermal generation of charge carriers, due to a general lack of thickness dependence at low fields. The presented “leaky  $n$ -layer” model offers a possible explanation for the large currents observed at high fields, but an all encompassing explanation would probably include some combination of the leaky  $n$ -layer effect, an increase in bulk thermal generation near the  $p$ -layer and other possible factors.

#### **4.3.8.2 Results from Sample Sets C and D**

Due to the high and unreliable currents produced by sample set B, two additional sample sets were created to explore the  $i$ -layer thickness dependence of the dark current. Sample set C was comprised of 6  $n$ - $i$ - $p$  samples with consistently thick blocking layers, 3 with thin  $i$ -layers and 3 with thick  $i$ -layers. Sample set D consisted of two  $n$ - $i$ - $p$  samples with varying  $i$ -layer thicknesses on each sample. The detailed characteristics of each of these sample sets is outlined in Sections 4.2.1.4 and 4.2.1.5. Both sample sets produced dark current transients with levels more typical of those produced by the three layer samples of set A.

Transients produced by sample set C are shown in Fig. 4.42. Transients for four of the samples, two with a thin  $i$ -layer and two with an  $i$ -layer roughly 2.5 times thicker, biased at 5 V/ $\mu\text{m}$ , are shown. All four transients are essentially right on top of each other, showing excellent reproducibility between samples and absolutely no  $i$ -layer thickness dependence.

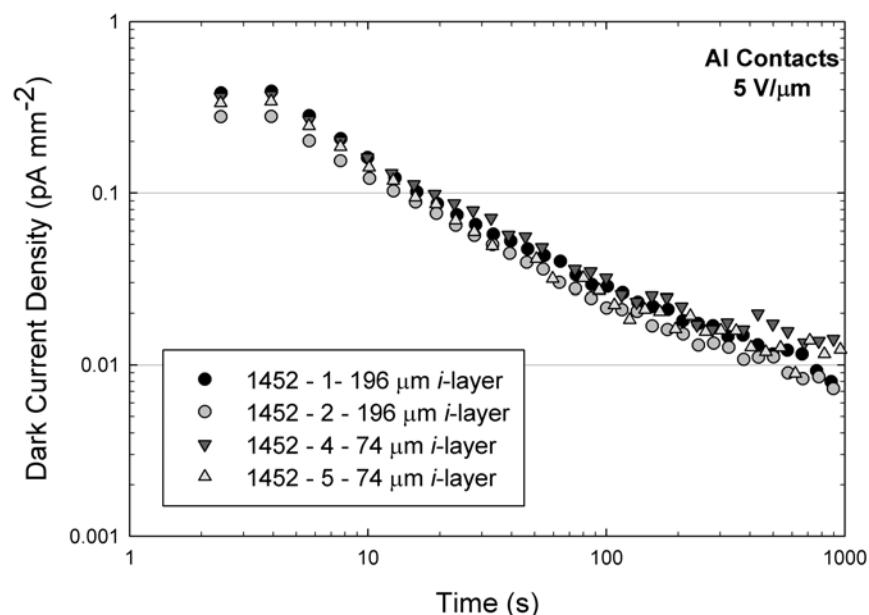


**Figure 4.42** Dark current density transients for four samples of set C with the Al contacts biased at 5 V/μm. Samples at both thicknesses give identical transients, showing a lack of *i*-layer thickness dependence.

Figure 4.43 shows similarly measured transients for the stabilized a-Se sample of set D, except that in this case, the Pt contacts were used and biased at 10 V/μm. The thicker sample does give a slightly higher dark current, ~ 2.2 times higher at 2 s and ~ 1.2 times higher at 1000 s after the application of the bias. However, the *i*-layer is more than 7 times thicker on the thick side than on the thin side. It should also be noted, as is clear in Fig. 4.44, the overall current levels produced by this sample were fairly high, similar to the case of sample set B. This is likely due to the relatively thin *n*-layers which were deposited on this sample and this will be discussed in greater detail below.

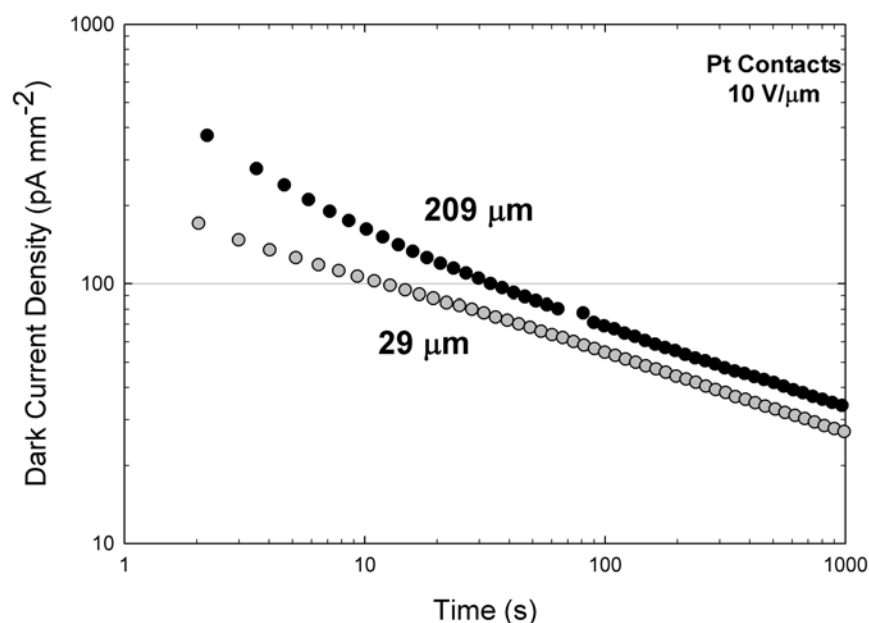


**Figure 4.43** Dark current density transients for the stabilized a-Se samples of set D with the Pt contacts biased at  $10 \text{ V}/\mu\text{m}$ . The 7 times thicker side gives currents slightly higher than the thin side, but the difference is not great enough to indicate the presence of a significant contribution from bulk thermal generation.

The lack of a predictable *i*-layer thickness dependence in sample sets C and D is summarized in Fig. 4.44. The dark current levels for four samples of set C, two of each thickness, and both samples of set D are compared 300 s after the application of the bias. Levels for biases of both  $10$  and  $5 \text{ V}/\mu\text{m}$  on both Al and Pt contacts are shown. It can be seen that there is very little increase in the dark current level for a given sample or sample set as the *i*-layer thickness is increased. In fact, it seems the dark current is just as likely to decrease as the *i*-layer thickness is increased, as is the case for the Pt contacts on the pure a-Se sample of set D (Fig. 4.44 (c) and (d)). The Pt contacts on samples of set C also gave higher currents in the thinner samples, particularly in sample 1452-5 which is shown as the second  $74 \mu\text{m}$  thick *i*-layer sample of set C in Fig. 4.44 (c) and (d). It is suspected that the *n*-layer on that particular sample may be slightly thinner than those of the rest of the set. Or it is possible that it is slightly leaky, as in the case of sample set B. The importance of the thickness of the hole trapping *n*-layer is shown clearly in the comparisons in Fig. 4.44. The pure a-Se sample of set D had the thickest *n*-layer ( $8 \mu\text{m}$ ) and had the lowest dark current while the stabilized a-Se sample had the thinnest *n*-layer ( $4 \mu\text{m}$ ) and consistently produced the highest dark currents. The samples of set C had  $6 \mu\text{m}$  *n*-layers

(nominally) and usually produced dark current levels in between those of the samples of set D. This is certainly the case for both contacts at high fields, such as 10 V/ $\mu\text{m}$ . In Fig. 4.44 (a) and (c), it can be seen that dark current levels increase roughly one order of magnitude for every increase of 2  $\mu\text{m}$  in  $n$ -layer thickness.

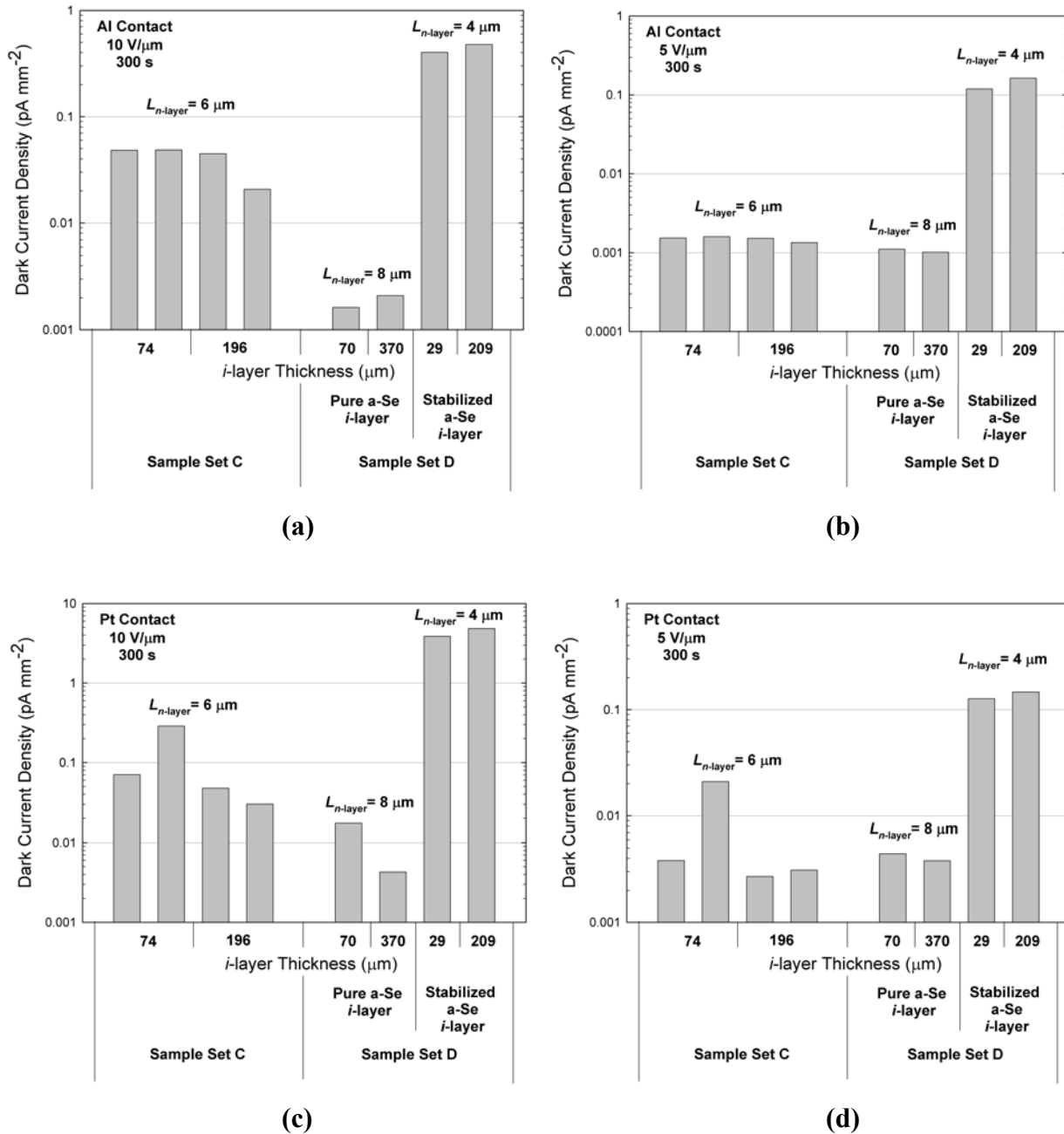


**Figure 4.44** A comparison of dark current levels 300 s after the application of the bias to samples of sets C and D. (a) Al contacts biased at 10 V/ $\mu\text{m}$ , (b) Al contacts biased at 5 V/ $\mu\text{m}$ , (c) Pt contacts

**biased at 10 V/ $\mu\text{m}$ , (d) Pt contacts biased at 5 V/ $\mu\text{m}$ . A change in *i*-layer thickness has no consistent effect on the dark current while an increase of 2  $\mu\text{m}$  in *n*-layer thickness decreases the dark current by roughly one order of magnitude at high applied fields.**

Sample set D was created not only to eliminate the variance of *n*-layer thickness between samples, but to observe the difference between *n-i-p* samples with pure and stabilized a-Se *i*-layers. It was thought that the effects of fractionation during deposition of stabilized a-Se *i*-layers might enhance the change in the dark current as the thickness of the *i*-layer is changed. However, it seems the variance in measured dark current values was actually greater in the pure a-Se sample than in the stabilized sample.

Given the possible “leaky *n*-layer” explanation for the behaviour of sample set B and the results produced by sample sets C and D, it would seem that there is no significant dependence of the dark current in multilayer a-Se sandwich structures on the thickness of the *i*-layer. There is, however, a strong dependence on the thickness of the hole trapping *n*-layer. This strongly suggests that carrier injection from the contacts is the dominant contributor to the dark current and bulk thermal generation, while likely present, is not directly observable and is a negligible source of dark current in a-Se sandwich structures used in FPXIs.

#### **4.3.9 Dark Current as a Function of Contact Metal**

All of the samples of sets B, C and D had at least two different contacts deposited on the top side of the sample to observe the effects of changing the contact metal while all else remains constant. As concluded in the previous section, bulk thermal generation in these a-Se sandwich structures is negligible, so if the dark current truly is dominated by carrier injection over a potential barrier from the contacts, the choice of contact metal should have a strong effect.

Sample sets C and D both had top contacts of Al and Pt on each sample. Figure 4.45 shows a comparison of the dark current level for the Al and Pt contacts on several samples 1000 s after the application of the bias of 10 V/ $\mu\text{m}$ . It can be seen that the Pt contact always gives a higher current than the Al contact and this is consistent on all samples of sets C and D, at all fields. The difference between the dark current levels varies between samples and with the time

which has elapsed since the bias was applied. The ratio of the dark current produced by the Pt contact to the Al contact,  $R_{Pt/Al}$ , is larger at earlier times. 2 s after the application of the bias,  $R_{Pt/Al}$  ranges from as little as 3 on one sample of set C to as much as 32 on a sample of set D. After 1000 s of applied bias,  $R_{Pt/Al}$  varies between 1.1 for a sample from set C to 8 for a sample from set D. Figure 4.46 shows the  $J$ - $F$  trends for both the Al and Pt contacts on a sample from set C. It can be seen that not only are the current values for the Pt contact higher, but the general field dependence is higher in the case of Pt with a power law fit exponent of 3.53 vs. 3.01 in the case of Al.

The variance in  $R_{Pt/Al}$  between samples is likely due to different surface states being produced between the  $n$ -layer and the contact during contact deposition, as the  $n$ -layers in sample set C are of a different composition than those in sample set D. However, the higher level of current in the case of Pt is predictable from the model of injection over a Schottky barrier. As explained in Section 2.6.1.1, the higher the work function of the contact metal, the lower the barrier to injection of holes. As the varying contact here is the positive contact, it is expected that the Pt contact, with  $\phi = 5.65$ , would give a higher current than the Al contact, with  $\phi = 4.25$ .

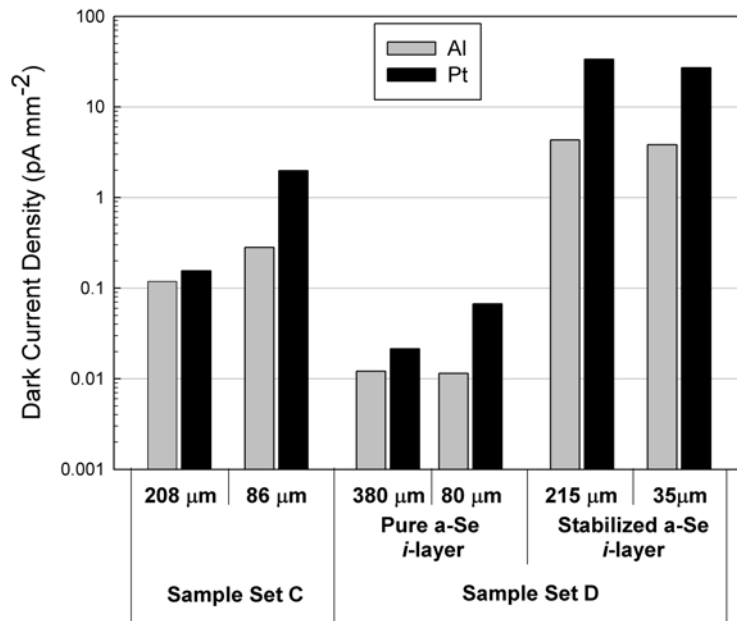


**Figure 4.45** Dark current density levels 1000 s after the application of the 10 V/μm bias for  $n$ - $i$ - $p$  samples of sets C and D. The comparison clearly shows that the Pt contacts invariably give higher levels of dark current than the Al contacts for each sample.

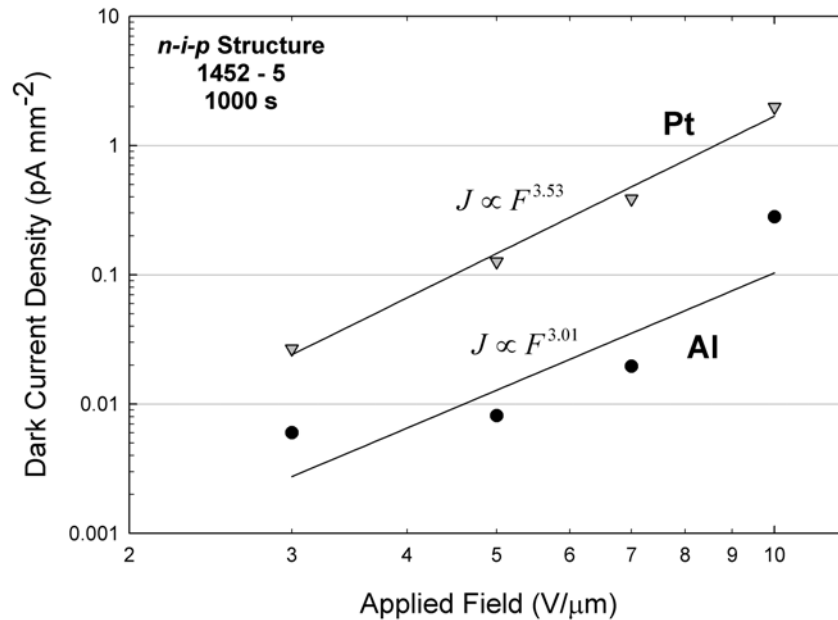


**Figure 4.46** Dark current density vs. applied field for an 86 μm thick sample of set C for both the Pt and Al contact, 1000 s after the application of the field. The solid lines give the power law fits. The Pt contact gives higher dark current levels and exhibits a stronger field dependence.

The results exhibited by sample set B are a little different than those for sets C and D. Dark current transients for each contact on each sample of set B are shown in Fig. 4.47. While samples in set B had four different metals deposited on each sample, not every contact on every sample produced meaningful results. Both the Au contact on US1 and the Al contact on US2 produced very high current levels which did not decay with time, indicative of a short across the sample, and these results are not shown. Further, the Cr contact on US3 produced a large, oddly shaped transient, as can be seen in Fig. 4.47 (c). Discharge measurements on that contact suggest that the *n*-layer below that contact was particularly poor at trapping injected holes and that could explain the anomalous transient.

As discussed previously, the dark current levels produced by the samples of set B are much larger than expected for *n-i-p* samples and one must be careful when interpreting the results. An examination of Fig. 4.47 reveals that the dark current does not follow a consistent dependence on the contact metal work function. On sample US1, Al gives the lowest transient, while Pt and Au are usually the lowest transients on the other samples. Samples US4 and US5

show much less variation between the metals and the trend with work function depends strongly on the time chosen to compare the levels.

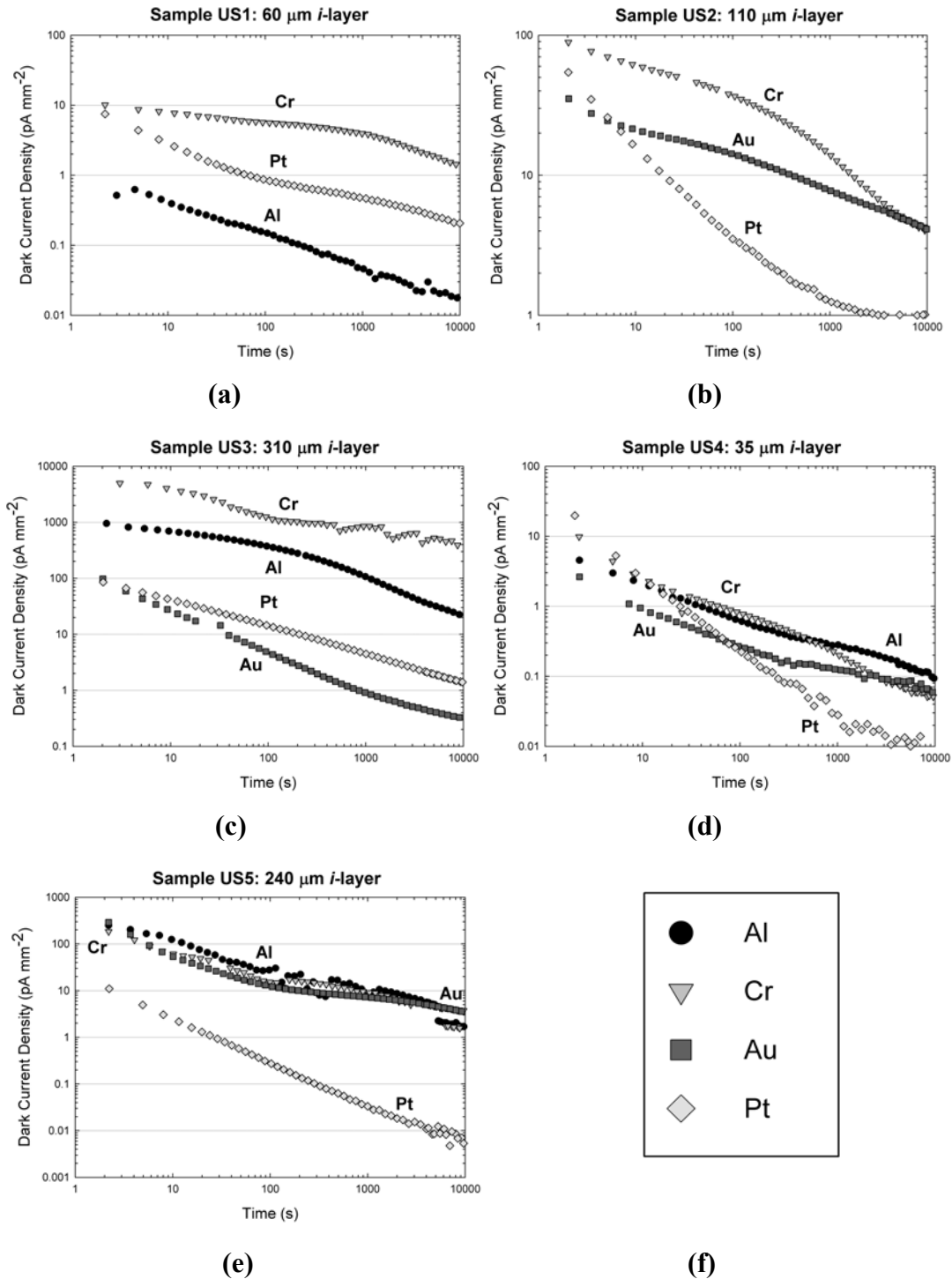
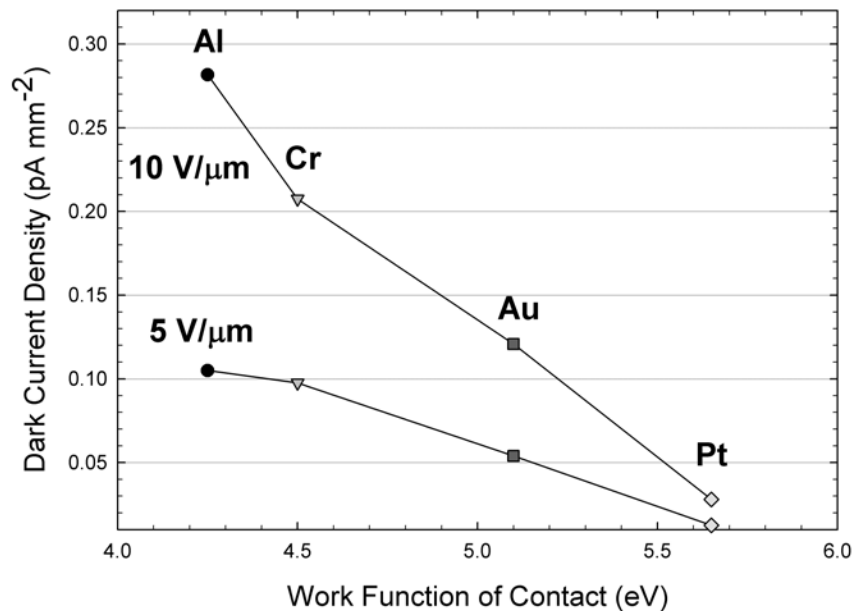


Figure 4.47 Dark current transients produced by samples of set B. All samples are *n-i-p* structures and were biased at 10 V/μm. (a) 60 μm *i*-layer sample with Cr, Al and Pt contacts, (b) 110 μm *i*-layer

**sample with Cr, Au and Pt contacts, (c) 310  $\mu\text{m}$  *i*-layer sample with Cr, Al, Au and Pt contacts, (d) 35  $\mu\text{m}$  *i*-layer sample with Cr, Al, Au and Pt contacts, (e) 240  $\mu\text{m}$  *i*-layer sample with Cr, Al, Au and Pt contacts, (f) legend. Cr consistently gives the highest level of dark current while Pt often results in the lowest.**

An interesting result is considered in Fig. 4.48, where the dark current level vs. contact metal work function is given for sample US4, 1000 s after the application of the bias, for two different applied fields. The dark current actually shows a monotonic decrease with increasing metal work function. This does not agree with the theory of injection over a Schottky barrier, as this is the positive contact and an increase in  $\phi$  should decrease the barrier to hole injection. Work by Belev [41] has shown a similar trend for contacts of this type, but in that case, the various metals were used as the negative contact. While the work function at the negative contact is constant across the measurements presented here, the dark current in sample set B could be dominated by electron conduction, as discussed in the previous section. While speculative, this offers at least a possible explanation for the anomaly. The results of these measurements on sample set B support the conclusions of Johanson *et al.* [55] that the injection of carriers from the contacts in a-Se sandwich structures does not clearly follow a neatly defined theory such as Schottky injection. While the results from sample sets C and D agree with the Schottky theory, they yield data for only two metals while the work published by Johanson studied fourteen metals. Hole injection over a Schottky barrier does not seem to completely describe the dark current trends for all the samples measured in this work.



**Figure 4.48** Dark current density as a function of positive contact work function for sample US4 of sample set B, 1000 s after the application of two different fields, 5 and 10 V/μm. The lines are only a guide for the eye. There is a general trend of decreasing dark current with increasing work function of positive contact metal.

#### 4.3.10 Dark Current Measurements on Sample Set E

Dark current transient measurements were also taken with sample set E in an industrial laboratory. The samples tested were of varying thicknesses and alloys. The system used to measure the transients consisted of a high voltage power supply capable of providing voltages above 10 kV, allowing for fields of 10 V/μm on even 1000 μm thick samples. Current values were captured using an oscilloscope connected to a computer using a data acquisition program. Since a different measurement system was used, no exact comparison can be drawn between the data presented here and the results of earlier sections, but this work provided some valuable data nonetheless. The important characteristics of the samples of set E, including reported *i*-layer schubwegs, are given in Table 4.7. The basic features of the samples such as the substrate and top electrode are the same as for sample set A. An important point to notice is that samples made from alloy 324 have a hole schubweg which is 4 times greater than that in samples made from alloy 325, as alloy 324 is chlorinated with 5 ppm and alloy 325 is not. The chlorinated alloy also has an electron schubweg which is a little more than half that of the non-chlorinated alloy.

**Table 4.7 Sample numbers and corresponding characteristics, including hole and electron schubwegs for samples of set E.**

<b>Sample Number</b>	<b>Alloy Number</b>	<b>Structure</b>	<b>Nominal Thickness (mm)</b>	<b>Hole Schubweg @ 10 V/<math>\mu\text{m}</math> (mm)</b>	<b>Electron Schubweg @ 10 V/<math>\mu\text{m}</math> (mm)</b>
549-5	325	<i>i</i> -layer	0.5	5.9	4.8
544-6	324	<i>i</i> -layer	0.5	23	2.9
531-5	324	<i>n-i-p</i>	1	23	2.9
553-5	325	<i>p-i-n</i>	1	5.9	4.8

Figure 4.49 shows that at the same applied field, a chlorinated *i*-layer sample gives a considerably higher current than a non-chlorinated *i*-layer sample, at least initially. At a point 100 s after the application of the bias, the chlorinated sample gives dark current which is roughly twice that of the non-chlorinated sample. This would indicate that the dark current at that time is dominated by the drift of holes, since the sample with better hole transport results in higher current. However, as more time passes, the transients converge and 10,000 s after the application of the bias, the difference is only a fraction of a  $\text{pA mm}^{-2}$ . The electron transport is comparable in both samples and this could mean that the current at later times has a stronger electron contribution, as suggested in previous sections. Neither of the transients produced by the *i*-layer samples reach a steady-state, similar to the behaviour of samples from all other sets.

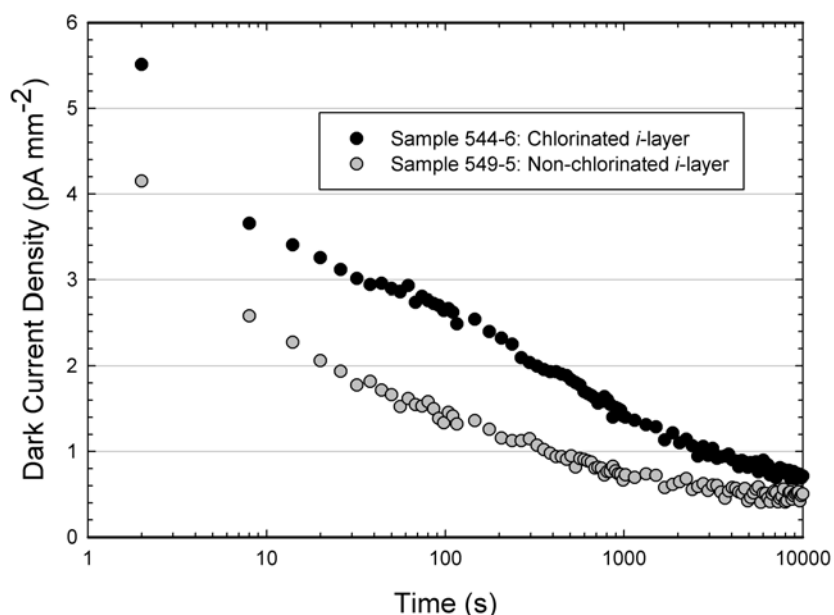


**Figure 4.49** Dark current density vs. time for non-chlorinated *i*-layer sample, 549-5, and chlorinated *i*-layer sample, 544-6, both biased at  $3 \text{ V}/\mu\text{m}$ . The chlorinated sample initially gives a higher dark current than the non-chlorinated sample but as time goes by the difference becomes much less. This potentially suggests that the dark current changes from being dominated by hole drift to electron drift as time passes after the application of the bias.

Figure 4.50 shows typical results for  $1000 \mu\text{m}$  thick samples. Both the *i*-layer sample and *n-i-p* sample used here are made of the same alloy and even though the *n-i-p* sample is twice as thick and biased at a much higher field, the pronounced effect of the blocking layers in reducing the dark current can be observed. While the *p-i-n* sample is made from a different alloy, its transient is shown here because a forward bias was used and the “hump” which appeared in the results of Section 4.3.4 can also be seen here. The appearance of this hump in measurements taken with a different measurement system than that used to acquire the data presented in Section 4.3.4 suggests that the hump is not an artifact of either of the current measurement systems.

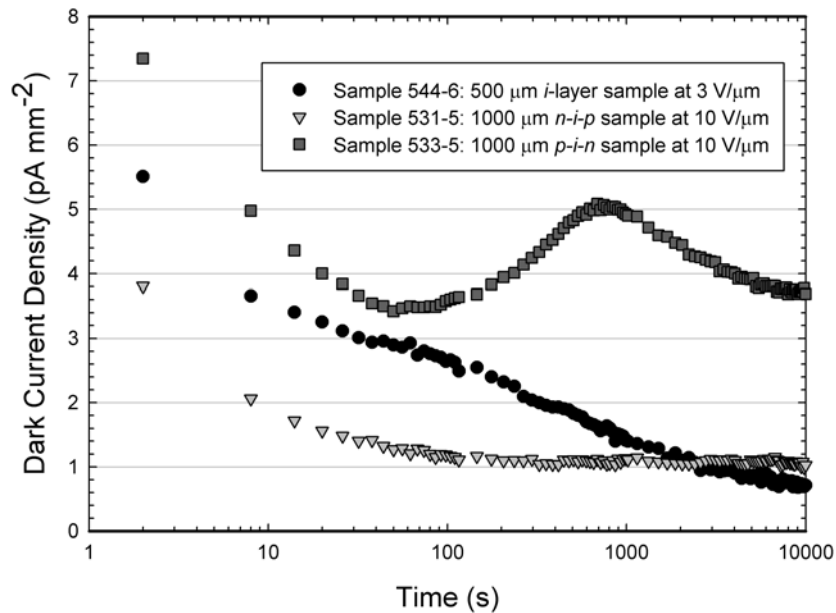


Figure 4.50 Dark current density vs. time for chlorinated *i*-layer sample, 544-6, chlorinated *n-i-p* sample, 531-5 and non-chlorinated *p-i-n* sample, 553-5. The *n-i-p* sample produces a transient which does not reach a steady-state after roughly 100 s. The dark current produced is lower than that produced by the *i*-layer sample until roughly 2000 s even though the *n-i-p* sample is biased at a much higher field. The forward biased *p-i-n* sample produces a transient with a hump at around 1000 s, similar to the transients produced by forward biased multilayer samples of other sample sets.

#### 4.4 Conclusion

The experimental analysis of the dark current in five separate sets of a-Se sandwich structure samples presented in this chapter has yielded some definitive conclusions. Results from the work with sample set A have shown that the *n*-type blocking layer, when deposited next to the positive contact, has a profound effect on reducing both the level of the dark current and its dependence on the applied field. The *p*-type blocking layer, when deposited next to the negative contact, has much less effect on the dark current, as the dark current has been shown to be dominated by the drift of holes in most cases. Sample set A has also been used to show that the instability of the hole trapping properties of the *n*-layer with time can result in increasing dark current levels, as with ageing, samples with blocking layers can start to behave as though they were single layer samples.

Much evidence from sample set A has been presented which shows that charge injected during the application of the bias is trapped and stored in the a-Se samples. The amount of charge stored tends to be slightly greater in samples with blocking layers, but the greater reduction of the dark current in these samples seems to be due to the location of the trapped charge and not necessarily the total concentration.

Work with sample sets C and D has shown little to no dependence of the dark current on the thickness of the *i*-layer of the sample. This suggests that the contribution of Poole-Frenkel enhanced bulk thermal generation of carriers in the *i*-layer is, in fact, negligible. The strong dependence of the dark current on the thickness of the *n*-layer and on the contact metal used as the positive contact give evidence that the dark current is dominated by the injection of holes from the positive contact and the model of injection over a Schottky barrier, while not being a perfect descriptor, can still be used.

The results presented from sample set B tell a different story, in that a strong *i*-layer thickness dependence was observed as well as a positive contact metal dependence that is not relatable to the Schottky emission model. However, an *n*-layer alloy with poor trapping properties seems to have been used to create these samples and the “leaky *n*-layer” model presented provides at least a possible explanation of these results which does not require a significant contribution from bulk thermal generation.

Given the reliability of the results from sample sets A, C and D, it is reasonable to conclude that the dark current in multilayer a-Se sandwich structures is due to carrier injection from the contacts, the primary contributor being hole injection from the positive contact, and this injection is reasonably well described by the model of injection over a Schottky barrier for the contact metals considered. However, it is possible that electron injection becomes a significant contributor to the dark current several minutes after the application of the bias. The contribution from the Poole-Frenkel enhanced bulk thermal generation of carriers is negligible.

# 5. MODELING OF DARK CURRENT TRANSIENTS IN AMORPHOUS SELENIUM FILMS

The previous chapter contained some steady-state modeling of the dark current produced by a-Se sandwich structures to explain features such as the  $J$ - $F$  characteristics of the samples. However, it is of interest to model the decay of the dark current with time. A computer model which can accurately and consistently predict the dark current transients could help to explain the exact origin of the transients and could be used to optimize the performance of practical detectors.

## 5.1 Monte Carlo Simulations

The initial goal of this work was to model the dark current flowing during detector operation to predict trapped carrier concentrations which build up between x-ray exposures due to the dark current and the effect this would have on the x-ray sensitivity of the detector. As a result, dark current transients were originally modeled with Monte Carlo simulations, so that the simulations could be performed in the framework of the Monte Carlo simulations of x-ray sensitivity described in Chapter 6. Furthermore, Monte Carlo simulations give a very direct connection to what is going on in real world principles while numerical calculations involving the solution of continuity equations are often difficult to solve and require special mathematical tools. It was assumed that the simplest case would be to model the typical dark current transients in  $i$ -layer samples, building in structural complexity to multilayer samples. It was also initially assumed that the dark current could be modeled as being due entirely to the injection of charge carriers from the contacts. The Monte Carlo simulations follow each charge carrier in the a-Se layer, pausing every  $\Delta t$  seconds to decide the fate of the carrier using randomly generated numbers. The equations and methods for pure Monte Carlo simulations are discussed in detail in Chapter 6 where all of the results presented on modeling of x-ray sensitivity are based on Monte Carlo simulations. As will be discussed in this chapter, it was found that other methods of simulating or calculating dark current were more suitable than pure Monte Carlo type simulations.

Initial results from Monte Carlo simulations can be seen in Fig. 5.1 where decent calibration has been achieved with experimental results produced by an *i*-layer sample by varying the concentration of deep hole traps,  $N_{th}$ , assumed in the simulation. This initial simulation, which was programmed in the C programming language to optimize computational speed, took more than 24 hours to run and as shown in Fig. 5.1, only 20 s of data was generated. As seen in Chapter 4, the dark current transients in these a-Se samples can change for tens, if not hundreds, of thousands of seconds following the application of the bias. Therefore, this pure style of Monte Carlo simulation is just not appropriate for this particular task. As a result, a modified Monte Carlo simulation technique was developed to model the dark current and it will be described in detail in the next section.

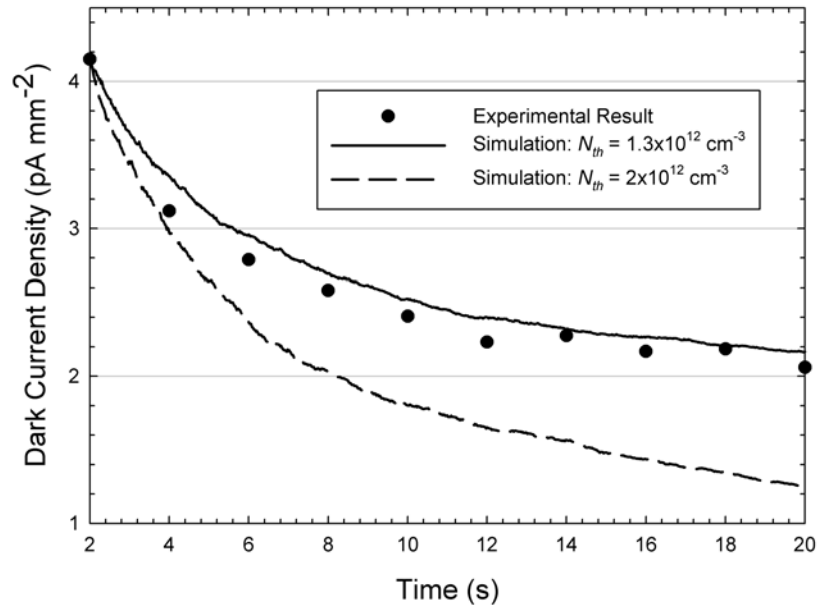


**Figure 5.1** Experimental results for the first 20 s of an *i*-layer dark current measurement along with two pure Monte Carlo simulation results using different values of deep hole trap concentration,  $N_{th}$ .

## 5.2 Modified Monte Carlo Simulations

A modified method of simulating the dark current transients in a-Se samples was developed where the basic principles of Monte Carlo simulations were used, but each charge carrier was no longer followed. Instead, the model considered a cloud of charge carriers, the

concentration of which was altered by interactions with the a-Se. Again, the basic assumption was made that the bulk thermal generation of carriers in the a-Se is negligible due to its large bandgap and the dark current is due mainly to the injection of charge carriers from the contacts. The sample was divided into dimensional slices and the injected concentration of carriers from each contact interacts with each slice as it drifts through the sample. Each slice was assigned values for deep trap concentration, number of presently trapped carriers and other important parameters. Phenomena that are considered as the carriers drift include: (a) the trapping of charge carriers in deep trap states, (b) the release of holes from deep trap states (electron release time is too long to be considered in the simulations), (c) recombination between drifting carriers and trapped carriers of opposite charge, (d) the reduction of the carrier trapping time,  $\tau$ , due to the filling of the finite number of deep trap states with time, and (e) the effect of areas of space charge due to (a), (b) and (c) on the electric field distribution across the sample and the corresponding effect of this on carrier drift.

### 5.2.1 Dimensional Slices

The sample was divided into dimensional slices as shown in Fig. 5.2. Splitting a 200  $\mu\text{m}$  sample into, for example, 1000 slices would give a dimension slice width,  $\Delta x$ , of 0.2  $\mu\text{m}$ . For each dimensional slice, important parameters were stored during the simulation. These included the deep carrier trap concentrations and the number of trapped carriers, as well as several values which were calculated each time step such as the electric field, the probability of a carrier being trapped or recombining with a trapped carrier of opposite charge and the charge carrier lifetime. In this way, different layers (*e.g.* *i*-layer, *n*-layer) could be distinguished just by changing the values for the slices which comprise it.

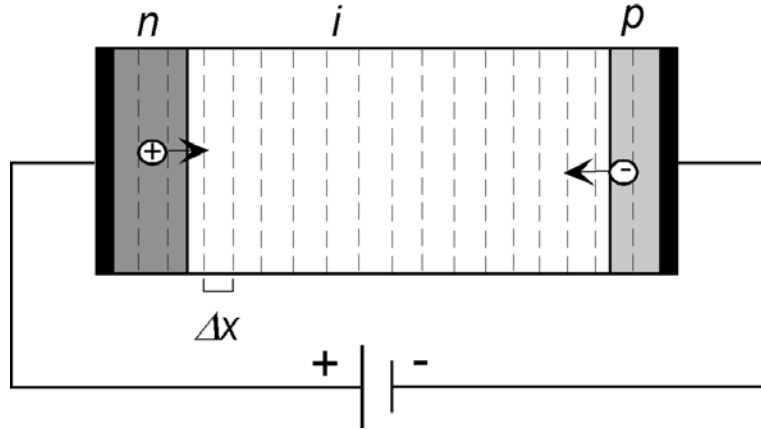


Figure 5.2 An illustration of an *n-i-p* sample divided into dimensional slices.

### 5.2.2 Time Steps

The simulation is calculated in time steps,  $\Delta t$ . In reality, time flows continuously, so the smaller the time steps used, the more closely the simulation should approximate reality. However, one is limited in how small the time steps can be by computational speed limitations. For pure Monte Carlo simulations,  $\Delta t$  should be the time it takes for a carrier to cross  $\Delta x$ . However, to improve the speed of the simulations,  $\Delta t$  was taken to be the transit time of the faster carrier (holes, in the case of a-Se) across the sample,  $t_h$ . In reality then, many interactions should take place in the time it takes for one calculation, so each trapped or recombined carrier represents many. Just how many is given by a multiplication factor,  $m_f$ , which is the ratio of  $t_h$  to the time it takes a hole to drift a distance  $\Delta x$ . Electron drift calculations are done every  $t_e/t_h$  time steps, as electrons drift much more slowly than holes in a-Se.

### 5.2.3 Charge Carrier Injection

The injected concentration of charge carriers from the contacts over a Schottky barrier can be modeled as [59]

$$p = N_v \exp \left\{ - \frac{\phi_h - \beta_s \sqrt{F_1(t)}}{kT} \right\} \quad (5.1)$$

for holes where  $p$  is the injected hole concentration,  $N_v$  is the effective density of states at the valence band edge ( $1 \times 10^{19} \text{ cm}^{-3}$  [140]),  $\phi_h$  is the effective barrier height,  $\beta_s$  is the Schottky coefficient ( $(e^3/4\pi\epsilon)^{1/2}$  [102]),  $\epsilon = \epsilon_0\epsilon_r$  is the permittivity of a-Se ( $\epsilon_0 = 8.85 \times 10^{-12} \text{ F/m}$  [105],  $\epsilon_r = 6.7$  [63]),  $k$  is the Boltzmann constant ( $8.61 \times 10^{-5} \text{ eV/K}$  [105]),  $T$  is the temperature in K and  $F_1(t)$  is the instantaneous electric field at the positive contact. Similarly,

$$n = N_c \exp\left\{-\frac{\phi_e - \beta_s \sqrt{F_2(t)}}{kT}\right\} \quad (5.2)$$

for electrons, now considering the conduction band and the barrier to electron injection and field at the negative contact. The corresponding current densities are given by:

$$J_h = pF_1(t)\mu_h e \quad (5.3)$$

$$J_e = nF_2(t)\mu_e e \quad (5.4)$$

for holes and electrons respectively.  $e$  is the elementary charge ( $1.602 \times 10^{-19} \text{ C}$  [105]) and  $\mu_h$  ( $0.12 \text{ cm}^2/\text{V s}$ ) and  $\mu_e$  ( $0.003 \text{ cm}^2/\text{V s}$ ) [65] are the effective hole and electron drift mobility, respectively. The total current is the sum of  $J_h$  and  $J_e$ .

#### 5.2.4 Carrier Trapping

Each time step, a new probability of trapping for both holes and electrons is calculated for each dimensional step. This probability is given by

$$prob\_trap_h = 1 - \exp\left\{-\frac{\Delta t(1 - p_t/N_{th})}{\tau_h}\right\} \quad (5.5)$$

for holes and

$$prob\_trap_e = 1 - \exp\left\{-\frac{\Delta t(1 - n_t / N_{te})}{\tau_e}\right\} \quad (5.6)$$

for electrons.  $p_t$  and  $n_t$  are the trapped hole and electron concentrations,  $N_{th}$  and  $N_{te}$  are the deep trap concentrations for holes and electrons and  $\tau_h$  and  $\tau_e$  are the lifetimes for holes and electrons, respectively, on that dimensional step. The carrier lifetime is the time it takes for a drifting carrier to be trapped and is given by

$$\tau_h = \frac{1}{C_{th}N_{th}\theta_h} \quad (5.7)$$

for holes and

$$\tau_e = \frac{1}{C_{te}N_{te}\theta_e} \quad (5.8)$$

for electrons, where  $C_t$  ( $1.22 \times 10^{-13}$  m<sup>3</sup>/s [150]) is the deep trapping capture coefficient and  $\theta$  is a ratio of  $\mu$  to  $\mu_0$  as discussed in Section 3.3.2.2 (0.4 for holes and 0.03 for electrons [150]). The effect of the traps filling with time is accounted for by the  $(1 - p_t/N_{th})$  term in the probability of trapping equations. Every time step, a concentration of holes,  $p$ , is injected from the positive contact. As they drift across the sample, they interact with each dimensional slice and for each slice  $prob\_trap_h \times p \times m_f$  holes are trapped while  $(1 - prob\_trap_h) \times p$  holes continue on to the next slice. A similar calculation is done for electrons, only using larger time steps and electron related values for parameters.

### 5.2.5 Carrier Recombination

As trapped carrier concentrations build up in each dimensional slice, it becomes more and more likely that drifting carriers of opposite charge will recombine with them. The trapped carrier concentration will quickly become much greater than the drifting carrier concentration so recombination between drifting carriers of opposite charge is negligible [63]. The process of

recombination between drifting and trapped carriers has been shown to be a Langevin governed process [243] and each time step, the probability of recombination was calculated for each dimension slice as follows:

$$prob\_recomb_h = 1 - \exp(-\Delta t C_{L_h} n_t) \quad (5.9)$$

for drifting holes recombining with trapped electrons and

$$prob\_recomb_e = 1 - \exp(-\Delta t C_{L_e} p_t) \quad (5.10)$$

for drifting electrons recombining with trapped holes. Clearly this probability depends on the concentration of trapped electrons for drifting holes and on the concentration of trapped holes for drifting electrons. The Langevin coefficients are given by

$$C_{L_h} = \frac{e\mu_h}{\epsilon_0 \epsilon_r} \quad (5.11)$$

for holes and

$$C_{L_e} = \frac{e\mu_e}{\epsilon_0 \epsilon_r} \quad (5.12)$$

for electrons [243]. As with trapping, each time step, for each dimensional slice, the concentration of drifting carriers is multiplied by this probability and the multiplication factor except that, in this case, that number of trapped carriers of the opposite charge are removed from the dimensional slice.

### 5.2.6 Carrier Release

The release time of electrons in a-Se is too long to be considered in simulations of this time scale [65]. However, hole release must be included. Each time holes are trapped, the

number of holes that are trapped is stored in a time array. The simulation time,  $T$ , is divided into steps,  $\Delta t_{trap}$ . For a simulation time of 1000 s and 10,000 hole release array steps, hole release is calculated every 0.1 s. Which step of the release array the trapped holes will be added to depends on the release time, as demonstrated in Fig. 5.3 (a). The release time is calculated as:

$$\tau_r = \frac{1}{\nu_0} \exp\left(\frac{E_t}{kT}\right) \quad (5.13)$$

where  $\nu_0$  is the attempt to escape frequency, a typical value of which is  $1 \times 10^{12} \text{ s}^{-1}$  [243].  $\nu_0$  is related to  $N_v$  and  $C_{th}$  by the principle of detailed balance,  $\nu_0 = N_v C_{th}$  [59].  $E_t$  is the energy depth of the trap and this can be determined for each calculation in a few ways. A single trap level can be used, giving a constant release time for all calculations, multiple levels can be used with a portion of the total concentration of deep traps at each level (this is done by Mahmood and Kabir [57]) or by using a Gaussian distribution of trap states about a mean level. Preliminary results have shown that for this type of simulation, the Gaussian distribution gives the smoothest transient. In this case, the trap depth is given by

$$E_T = E_{avg} \pm \sqrt{-2\sigma^2 \ln(r)} \quad (5.14)$$

where  $E_{avg}$  is the mean trap depth,  $\sigma^2$  is the variance of the distribution and  $r$  is a randomly generated number. It should be noted that a Gaussian distribution of trap states does not give a Gaussian distribution of release times. In this way, deeper trap depths lead to much longer release times and holes which are randomly assigned a longer release time when they are trapped will be added to a higher step in the release array.

Every so many time steps, a new step of the release array will be entered and the number of holes trapped there will be released. An example of this can be seen in Fig. 5.3 (b). Keeping track of which dimensional slices those holes were trapped on would take an immense amount of computer memory and so the number of holes to be released is distributed evenly over all dimensional steps being sure to check that no negative trapped hole concentrations are allowed.

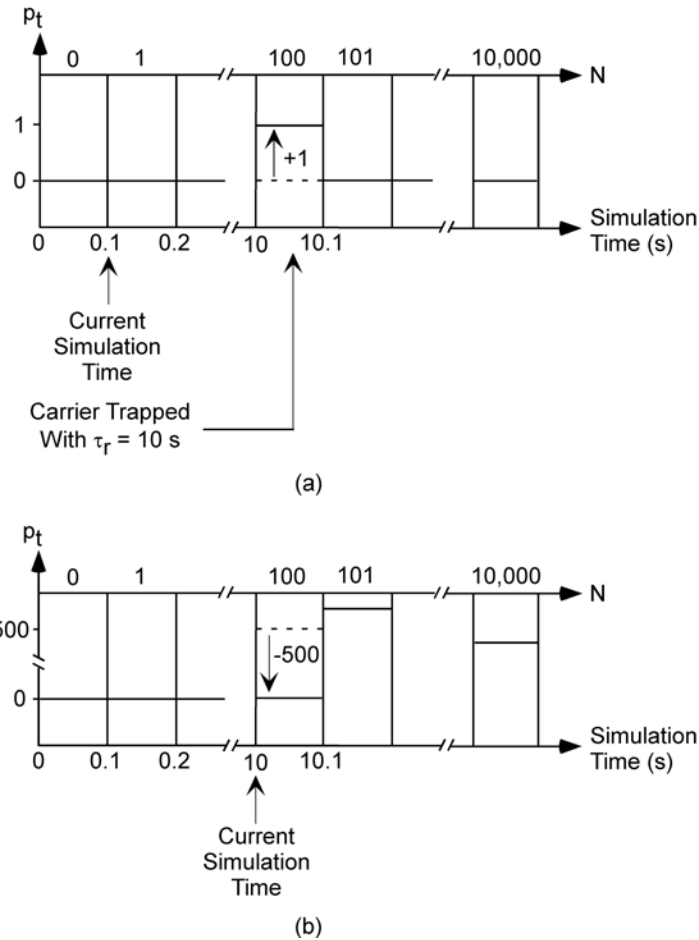


**Figure 5.3** Diagrammatic representation of the carrier release array. The bottom axis represents the time in the simulation while the top axis shows the corresponding steps in the release array. The vertical axis represents the trapped carrier concentration. (a) A carrier trapped 0.1 s into the simulation is randomly assigned a release time of 10 s. Therefore, one trapped carrier is added to step 100 of the release array, corresponding to 10 s of simulation time. (b) By 10 s of simulation time, 500 carriers have been trapped which have been assigned a release time between 10 and 10.1 s. At that point, the number of trapped carriers in step 100 of the release array is reduced to 0. A corresponding amount of trapped carriers are released from each step in the dimensional array.

### 5.2.7 Electric Field Distribution

It is assumed that at the beginning of the simulation, the electric field distribution across the sample will be uniform and equal to the applied field. As injected carriers are trapped, released and recombined, the space charge density within the sample will change and so too will the electric field distribution. This effect on the field is calculated by solving Poisson's equation:

$$\frac{dF(x)}{dx} = \frac{\rho(x)}{\epsilon_0 \epsilon_r} \quad (5.15)$$

with the boundary condition

$$\int_0^L F(x) dx = V \quad (5.16)$$

through numerical integration. Here  $\rho$  is the space charge density due to trapped carriers,  $L$  is the thickness of the sample and  $V$  is the applied voltage. This calculation is done every time step and the resulting field is stored for each dimensional step.

### 5.2.8 Random Number Generation

Monte Carlo simulations rely on probabilities to determine the outcome of different situations, but for this to happen, the program needs to be able to generate many “random” numbers. A sequence of “random” numbers contains terms which are unpredictable and pass certain statistical tests. Some programming languages, such as Matlab, contain functions which will generate random numbers. These simulations were originally coded in Matlab, but were exported to C to increase the simulation speed by roughly 30 times. C does not have a built in random number generator, but one can be coded easily enough. The code for a “subtract with borrow” random number generator which uses a computer’s date and time information as a seed value has been inherited from Yunus. It has been shown to provide an even distribution of numbers between zero and one [2] and has been used successfully in this work.

### 5.2.9 Results

Considerable time and effort have been spent trying to match modified Monte Carlo simulation results to the experimental results of the dark current measurements on sample set A presented in Section 4.3. While these simulations give the expected shape of transients, to match them exactly requires the fine tuning of several variable parameters including deep trap concentration, depth and variance, carrier drift mobility and lifetime and the height of the

Schottky barrier to injection. Small changes in any of these parameters can have a profound impact on the level and shape of the resulting transient. Figure 5.4 shows the first 300 s of the experimental dark current transient produced by an *i*-layer sample at 10 V/ $\mu\text{m}$  compared to a fairly well matched simulation result. The parameters used in this simulation which were not stated thus far were:  $L = 212 \mu\text{m}$ ,  $\varphi_h = 0.83 \text{ eV}$ ,  $\varphi_e = 0.9 \text{ eV}$ ,  $N_{th} = 5 \times 10^{13} \text{ cm}^{-3}$ ,  $N_{te} = 2 \times 10^{13} \text{ cm}^{-3}$ ,  $E_{avg} = 0.72 \text{ eV}$ ,  $\sigma^2 = 0.03 \text{ eV}$  and the sample was divided into 300 dimensional steps. Figure 5.5 shows the deeply trapped carrier concentration for holes and electrons across the sample and the resulting electric field distribution at  $t = 300 \text{ s}$ . The result is intuitively correct as there are more trapped holes near the positive contact and more trapped electrons near the negative contact and no abrupt changes across the sample as the *i*-layer sample is assumed to have uniform trap densities throughout.

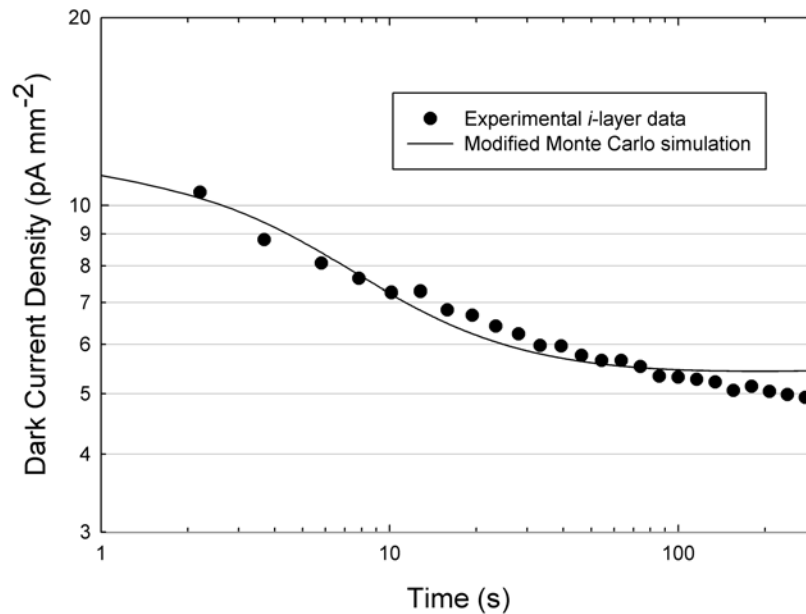


**Figure 5.4** Dark current density transient for an *i*-layer sample of set A biased at 10 V/ $\mu\text{m}$  compared with the result of a corresponding modified Monte Carlo simulation. The simulated transient appears to reach a steady state at roughly 100 s while the experimental transient does not.

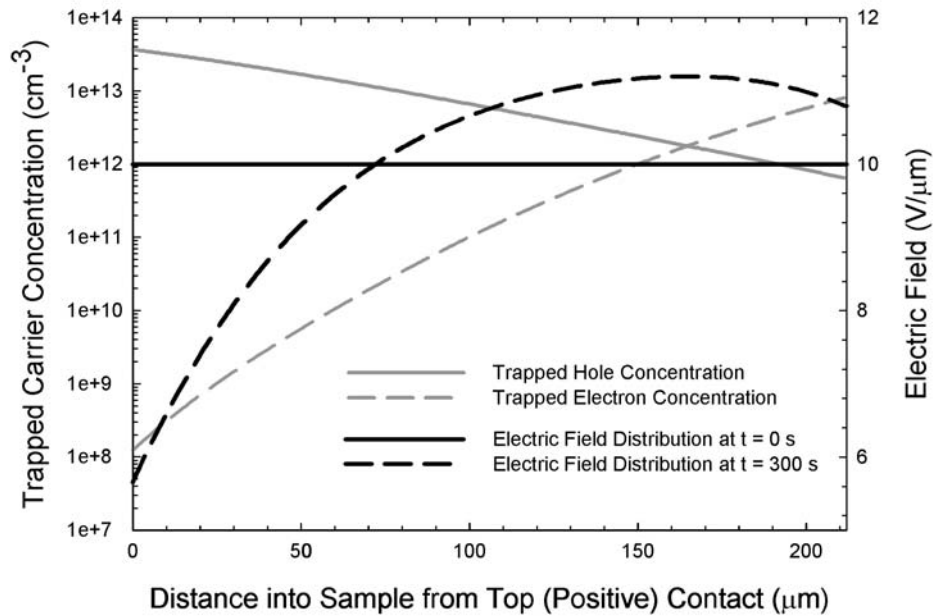


**Figure 5.5 Trapped hole and electron concentration distribution across the *i*-layer sample after 300 s of simulation. The resulting electric field distribution is also shown and compared to the original, uniform field.**

While this result is promising, by comparing the exact shapes of the dark current transients in Fig. 5.4, one can see that the simulation result reaches something of a steady-state around 100 s, while the experimental result really does not. Figure 5.6 shows experimental data for the same *i*-layer sample at 5 V/μm compared to a simulation using the same parameters as highlighted above, except for an applied field of 5 V/μm instead of 10 V/μm. The match is not nearly as close as in the 10 V/μm case. If these simulations were considering all of the important physical phenomena involved, one should be able to match the dark current transients at all applied fields without changing any other parameter.

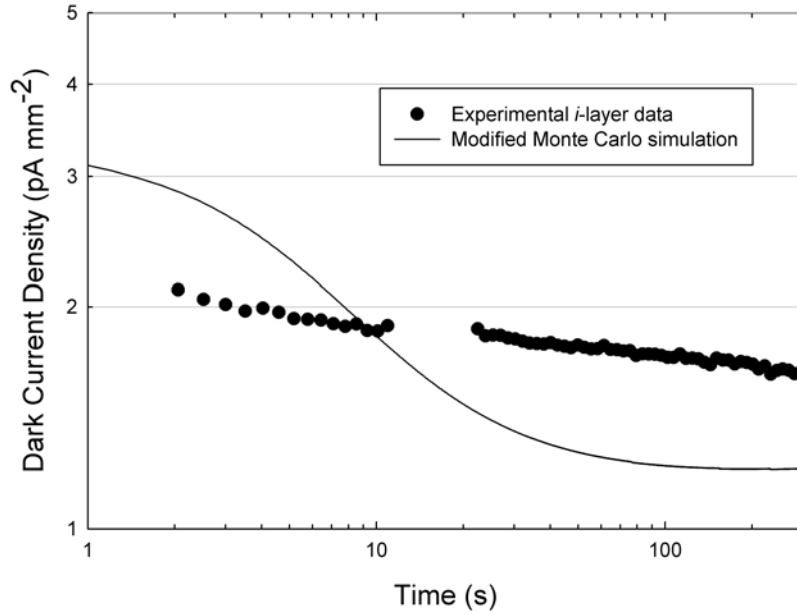


**Figure 5.6 Dark current density transient for an *i*-layer sample of set A biased at 5 V/ $\mu\text{m}$  compared with the result of a modified Monte Carlo simulation. The correlation is not nearly as good as for the transient produced at 10 V/ $\mu\text{m}$ .**

The effect of slight changes in certain parameters can be seen in Fig. 5.7 where the simulation result from Fig. 5.4 is shown along with a lower transient produced by increasing  $N_{th}$  from  $5 \times 10^{13} \text{ cm}^{-3}$  to  $6 \times 10^{13} \text{ cm}^{-3}$  and  $N_{te}$  from  $2 \times 10^{13} \text{ cm}^{-3}$  to  $3 \times 10^{13} \text{ cm}^{-3}$ . A higher transient is also shown where only  $E_{avg}$  was changed from 0.72 eV to 0.715 eV. The change in the transients is quite large given the small change in only one parameter.

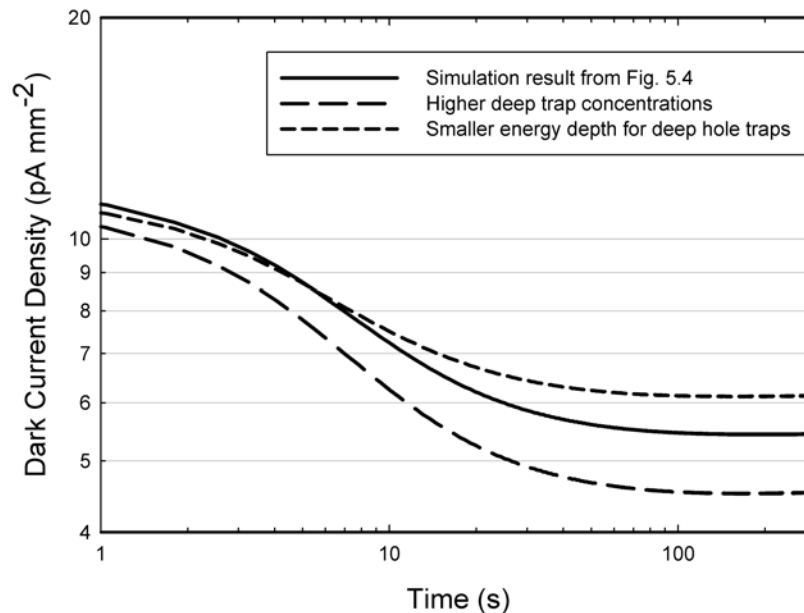


**Figure 5.7 Dark current density transients produced by modified Monte Carlo simulations. The simulation which produced the lowest curve has slightly higher values for deep trap concentrations than the simulation which produced the middle curve. The curve which ends at the highest level corresponds to a slightly lower energy depth for deep hole traps as compared to the middle curve. While these results are intuitive, the number of adjustable parameters makes it very difficult to match simulation results with experimental results through trial and error adjustment of those parameters.**

It is important to note that the generation of each 300 s worth of simulation data took roughly 16 hours of computational time. Given the number of parameters which must be fine tuned to obtain results which agree with experiment (this number increases as blocking layers are added), and the long simulation time, the likelihood of finding convincing matches using these techniques is low. Couple this with the fact that the exact shape and level of the dark current transients produced by a given sample can change with time and conditions and finding a good match with this model is beyond practical means. For these reasons, it was decided during the course of this work that point for point agreement with experimental data was an ill-posed problem, and a compromise was sought using faster simulation techniques with a model that describes basic trends of dark current with time and applied field. This model is described in the next section.

## 5.3 Numerical Calculations

While these simulations were being developed, Kabir and Mahmood published results of a similar nature [57,59]. They used numerical calculations to model the dark current transients in 1 mm thick *n-i-p* a-Se samples which reached a steady less than 1000 s after the application of the bias. They found good agreement at different applied fields by assuming that the dark current was due entirely to the injection of holes from the positive contact and the resulting transient was due only to trapping of those holes in the *n*-layer. Due to the success of this work, it was decided that this published work should be recreated in the C programming language and modified to see if its simplified nature could be applied to the modified Monte Carlo model described in Section 5.2.

### 5.3.1 Matching Similar Published Work

The work published by Mahmood and Kabir [57] uses equations similar to Eqs. 5.1 – 5.4 to govern the injection of charge carriers and current. However, they use an ideality factor,  $\gamma$ , in the exponential term, the need for which indicates that the required coefficient is somewhere between the Schottky coefficient and the Poole-Frenkel coefficient. Since only the trapping of holes in the *n*-layer is considered, the instantaneous electric field at both contacts can be calculated using the two following simplified equations (obtained by symbolically solving Eqs. 5.15 and 5.16):

$$F_1(t) = F_0 - \frac{e}{\varepsilon} \left( L_n - \frac{L_n^2}{2L} \right) p_t(t) \quad (5.17)$$

$$F_2(t) = F_0 + \frac{e}{\varepsilon} \frac{L_n^2}{2L} p_t(t) \quad (5.18)$$

The rate of change of the deeply trapped hole concentration is given by:

$$\frac{dp_t(t)}{dt} = C_{th} N_{th} \theta_h \left( 1 - \frac{p_t(t)}{N_{th}} \right) p(t) - \frac{p_t(t)}{\tau_{rh}} \quad (5.19)$$

which encompasses trapping, the trap filling effect and trap release. Here,  $N_{th}$  is the deep hole trap concentration in the  $n$ -layer. Equation 5.19 is used for two discrete trap levels, 0.76 eV and 0.81 eV from the valence band edge, to emulate a broadened energy state 0.05 eV wide. This simplified approach to modeling a-Se layers was adopted to see if the published results could be reproduced.

Though the work published by Mahmood and Kabir makes some large assumptions, the merit of their work is in the fact that they were able to match the dark current transients at three different fields by only slightly changing the parameters used between simulations. Their equations were used within the framework of the Monte Carlo simulations, using their published parameters, and their results were matched almost perfectly as shown in Fig. 5.8.

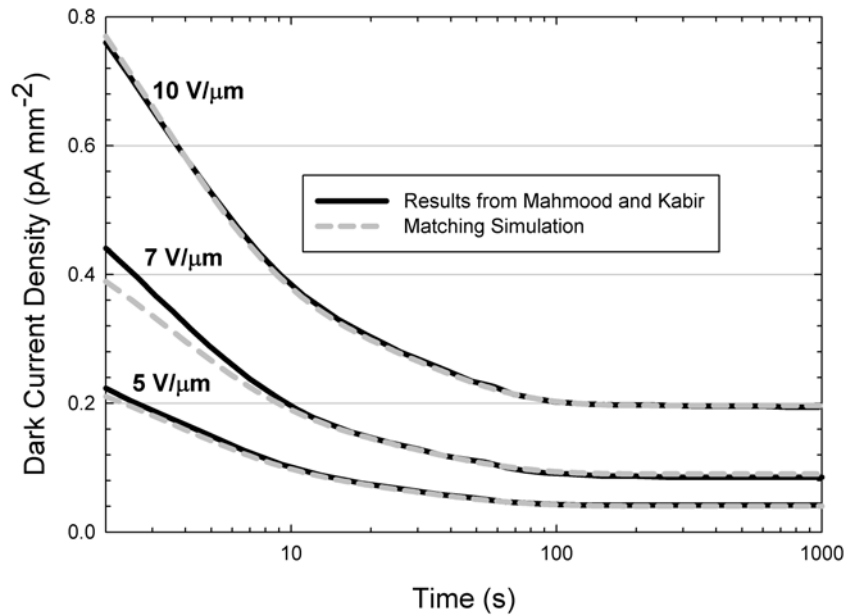


**Figure 5.8 Comparison of simulation results for a 1 mm thick  $n$ - $i$ - $p$  a-Se layer with published results (replotted from [57]). Using the same equations and parameters, the results were matched almost perfectly at fields of 10, 7 and 5 V/ $\mu$ m.**

### 5.3.2 Removing Simplifying Assumptions of Published Work

The assumptions made with this model, while allowing for fast computational time, reduce the usefulness of the result. For example, this model could not be used to describe the dark current transients in *i*-layer or two layer samples with structures such as *i-p*, as the interaction of injected charge carriers with the *i*-layer cannot be included. As a result, features of the Monte Carlo simulations were added back in to see if Mahmood and Kabir's simplifying assumptions would hold up in a more realistic simulation. First, the sample was divided into dimensional slices again, this time 1000 slices, and the field was once again calculated by numerical integration of Poisson's equation. While this increased the simulation time by roughly 40 times, there was no change in the resulting transients and they still matched the published work. It should be noted that even with the rigorous field calculations, the computational time to generate 300 s of data was still less than 30 minutes.

The published work makes the assumption that once holes are injected, they immediately occupy the entirety of the *n*-layer with a uniform concentration. This leads to uniform trapping in the *n*-layer, which is 20  $\mu\text{m}$  thick. It is more realistic to think that the holes are injected as an infinitesimally thin sheet right next to the contact, gradually filling the traps further and further from the contact, as shown in Fig. 5.9. With the sample divided into dimensional slices, this can now be approximated more closely. If the same number of holes are injected in each time step as in the published work ( $p \times A \times L_n$  where  $L_n$  is the thickness of the *n*-layer), the larger amount of charge stored near the contact drives the field at the contact to become negative, leading to a reversal of current direction after about 80 s. Nothing like this has ever been observed experimentally. Clearly, when handled in a more realistic fashion, Mahmood and Kabir's assumed value for  $N_{th}$  in the *n*-layer of  $9 \times 10^{15} \text{ cm}^{-3}$  is just too high. Decreasing this value to  $9 \times 10^{14} \text{ cm}^{-3}$  gives the result shown in Fig. 5.10. The shape of the transient changes in a way that makes matching experimental results impossible and it becomes evident that these techniques cannot be used to model the dark current transients in samples of different structures in sample set A.

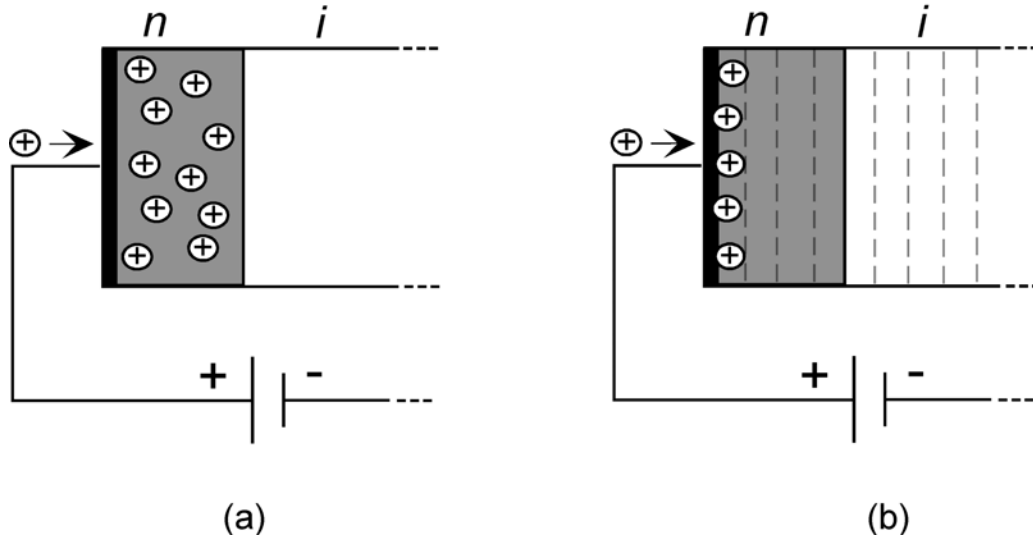


Figure 5.9 (a) Representation of published model [57] where injected holes immediately fill the entire  $n$ -layer. (b) With the theoretical sample divided into dimensional slices much thinner than the  $n$ -layer, injected holes now fill the slice closest to the positive contact. Holes which are not trapped in the first slice drift into neighbouring slices in subsequent time steps.

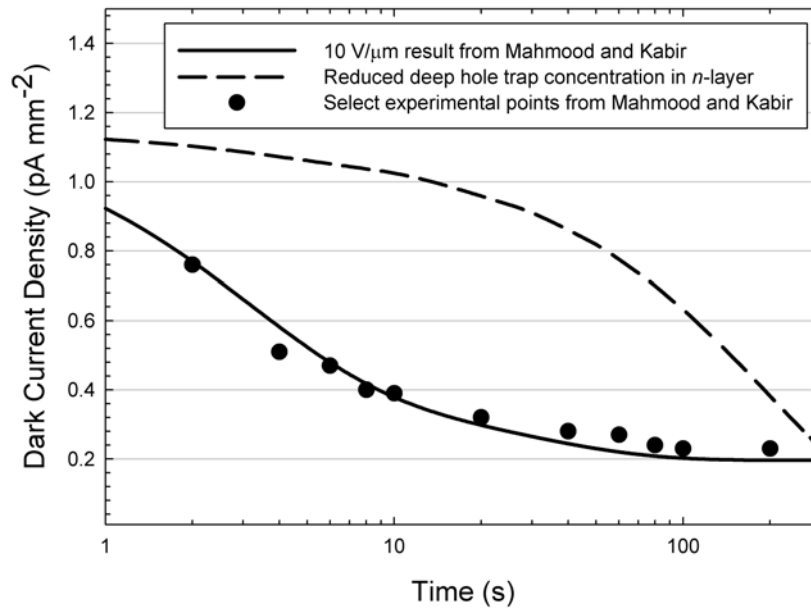
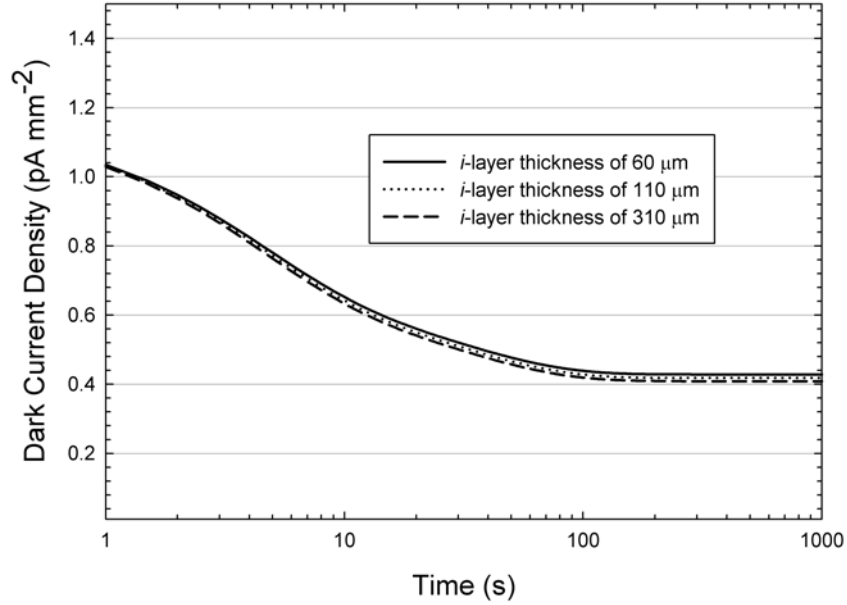


Figure 5.10 Dark current transients obtained by adding in Monte Carlo style features to the simulations of Mahmood and Kabir, compared with their results (bottom theoretical curve and experimental data selectively replotted from [57]). The top curve was obtained by reducing the deep hole trap concentration by an order of magnitude from that quoted in [57]. The shape of the decay is now unlike that of the experimental transient.

### 5.3.3 Matching Experimental Results with the Published Model

While the published results of Mahmood and Kabir's model work well for transients which reach a steady-state within 1000 s of the application of the bias, most of the dark current transients experimentally measured and presented in Chapter 4 did not reach a steady-state at all. Due to the large  $i$ -layer thickness dependence of the dark current in the samples of set B, it was thought that a contribution from bulk thermal generation would need to be included to model this much longer decay. A model was developed which included both a steady-state current due to thermal generation of holes and electrons in the bulk and a depletion current due to the generation of holes as the Fermi level in the a-Se shifted upwards after the application of the bias. However, for several reasons, this model was not developed. Very recently, Mahmood and Kabir published additional work with the above mentioned model which also included the steady-state bulk thermal generation current [106]. This work showed that the contribution from this current was at least 2 orders of magnitude below the injection current and was negligible. Initial simulations carried out in the U of S laboratories gave a similar conclusion. The depletion current, due to the generation of holes in the bandgap, was found to be appreciable, but only if very large concentrations of deep traps existed and the Fermi level moved significantly, two mutually exclusive conditions in that a large concentration of states near mid-gap will essentially prevent the Fermi level from moving much. Furthermore, these initial simulations of the depletion current and steady-state bulk thermal generation current were found to depend linearly on the  $i$ -layer thickness, something which was not observed in the measurements of sample sets C and D, both of which gave more reliable data than sample set B. For these reasons, the attempt at modeling the bulk contributions to the dark current was abandoned. It can be seen in Fig. 5.11 that the model put forth by Mahmood and Kabir has very little dependence on the thickness of the  $i$ -layer and the small change that is present is simply due to a factor of  $L$  in the simplified field calculations.



**Figure 5.11** Simulation results using the model of [57] to simulate the dark current density in three *n-i-p* structures with varying *i*-layer thicknesses of 60, 110 and 310  $\mu\text{m}$ . The change in thickness makes almost no difference, in agreement with the most reliable experimental results from Chapter 4.

It was decided that the simplified model of Mahmood and Kabir would be used to model the dark current transients produced by the Pt contact on sample 1452-1 of set C. This roughly 208  $\mu\text{m}$  thick *n-i-p* sample yielded transients that decayed seemingly indefinitely, certainly not reaching steady-state before the 1000 s mark. To match these results with the simplified model, the second deep hole trap level was assumed to be much deeper than in Mahmood and Kabir's work. To model such a long decay, it was also critical that the contribution due to electron injection and trapping in the *p*-layer be included and that this contribution become significant once the hole current has decayed. Equations 5.1 - 5.4 were used to govern the injection of holes and electrons and Eq. 5.19 was used to determine the trapping rates for each of the two deep hole states assumed to approximate a single state of broadened width, as was done by Mahmood and Kabir [57]. Equation 5.19, modified for electrons, was also used to calculate the trapping rates for deep electron traps, as

$$\frac{dn_t(t)}{dt} = C_{te} N_{te} \theta_e \left( 1 - \frac{n_t(t)}{N_{te}} \right) n(t) - \frac{n_t(t)}{\tau_{re}} \quad (5.20)$$

The release times for holes and electrons,  $\tau_{rh}$  and  $\tau_{re}$ , were calculated using Eq. 3.4. Finally, the electric field at the positive and negative contact,  $F_1$  and  $F_2$ , were calculated using the following equations which consider both the charge built up by holes trapped in the  $n$ -layer and by electrons trapped in the  $p$ -layer:

$$F_1 = F_0 - \frac{e}{\epsilon_r \epsilon_0} \left[ \left( L_n - \frac{L_n^2}{2L} \right) p_m - \frac{L_p^2}{2L} n_{tp} \right] \quad (5.21)$$

$$F_2 = F_0 - \frac{e}{\epsilon_r \epsilon_0} \left[ -\frac{L_n^2}{2L} p_m + \left( L_p - \frac{L_p^2}{2L} \right) n_{tp} \right] \quad (5.22)$$

The dark current was simulated for 2000 s for sample 1452-1 at four different applied fields. The assumed parameter values which remained constant between all simulations are shown in Table 5.1. The barrier to hole injection was taken to be 0.82 eV in all simulations while the barrier to electron injection was reduced from 0.86 eV at 3, 5, and 7 V/ $\mu\text{m}$  to 0.81 eV at 10 V/ $\mu\text{m}$  to account for the temporary plateau exhibited experimentally at that field. A value of  $4 \times 10^{14} \text{ cm}^{-3}$  was assumed for  $N_{te}$  for all simulations, but the concentration of deep hole traps had to be adjusted to get reasonable matches at all fields. These changes are tabulated in Table 5.2. The results of these simulations are shown in Fig. 5.12, compared against the experimental results.

**Table 5.1 Material properties assumed for the numerical calculations done to match dark current transients measured experimentally.**

Property	Assumed Value	Property	Assumed Value
$L$	208 $\mu\text{m}$	$\theta_h$	0.4
$L_n$	6 $\mu\text{m}$	$\theta_e$	0.03
$L_p$	6 $\mu\text{m}$	$C_{th}$	$1 \times 10^{-7} \text{ cm}^3 \text{ s}^{-1}$
$\mu_h$	$0.12 \text{ cm}^2 \text{ V}^{-1} \text{ s}^{-1}$	$C_{te}$	$1 \times 10^{-7} \text{ cm}^3 \text{ s}^{-1}$
$\mu_e$	$0.003 \text{ cm}^2 \text{ V}^{-1} \text{ s}^{-1}$	$E_{h1}$	0.78 eV
$N_v$	$1 \times 10^{19} \text{ cm}^{-3}$	$E_{h2}$	0.9 eV
$N_c$	$1 \times 10^{19} \text{ cm}^{-3}$	$E_e$	0.98 eV

**Table 5.2** Values of  $n$ -layer deep hole trap concentrations assumed for dark current simulations at different applied fields.

Field (V/ $\mu\text{m}$ )	$N_{th1}$ ( $\times 10^{14} \text{ cm}^{-3}$ )	$N_{th2}$ ( $\times 10^{14} \text{ cm}^{-3}$ )
10	35	3.2
7	30	2.2
5	20	1.7
3	15	0.75

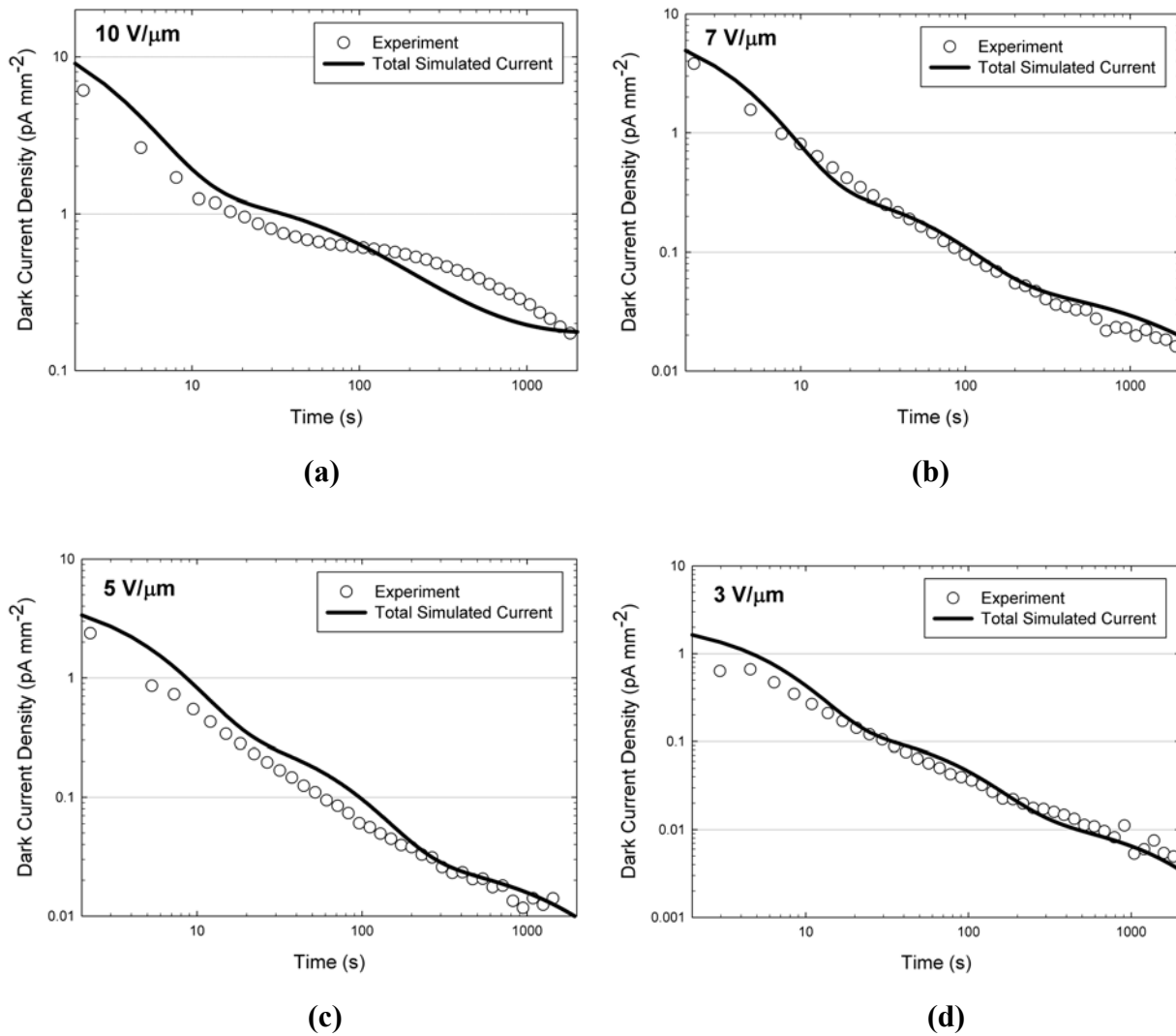


**Figure 5.12** Dark current density transients experimentally measured (circles) and calculated (lines) for the Pt contact on an  $n$ - $i$ - $p$  sample of set C for applied fields of (a) 10 V/ $\mu\text{m}$ , (b) 7 V/ $\mu\text{m}$ , (c) 5 V/ $\mu\text{m}$ , (d) 3 V/ $\mu\text{m}$ . The matching is quite good at all fields except at 10 V/ $\mu\text{m}$  where the plateau at

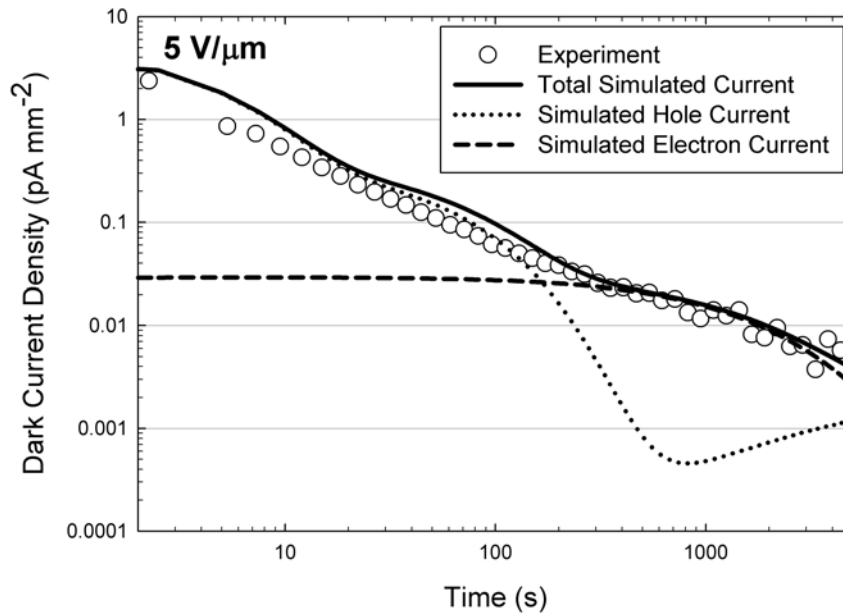
**100 s is not accurately predicted by the model. The “wavy” appearance of the theoretical curves is due to the fact that only 2 discrete deep hole trap states were assumed. A smoother transient could be produced by assuming many deep hole trap states to approximate a continuous distribution in energy.**

Figure 5.12 shows a fair match between the simulation results and the experimental results for the levels and the general decay with time of the dark current in the a-Se sample. The transients produced by the computer simulation appear a bit wavy and this is due to the fact that only 2 deep hole trap states are assumed. The downward “humps” appear when the rates of trapping and release from a given trap state become equal. Smoother transients could be produced by assuming many deep hole trap states, spread in energy. It was attempted to model the spread of states as a Gaussian distribution in energy. However, by only being able to adjust the mean, variance and peak value of the distribution, a reasonable match with experiment could not be attained. It seems that the concentrations would need to be adjusted individually and this could take a great amount of trial and error. One must remember that the goal is to model the general behaviour of these transients and not to generate a point for point match.

It should be noted that the final decaying portion of the transients is due mostly to electron current. This can be seen in Fig. 5.13 where the simulated hole, electron and total current are compared against the experimental transient for an applied field of 5 V/ $\mu\text{m}$ . By  $\sim 200$  s, the hole current has decayed to the point where the electron current becomes significant. The hole current continues to decay and the electron current becomes the dominant contributor. While it has been assumed that electron injection current is negligible in previous works [57], it would seem that it is necessary to describe very long transient decay times. This is not unreasonable, as discussed in Chapter 4, it is possible that electron injection current dominated the dark current in sample set B. It should also be mentioned that in experimental measurements, initially, the Pt contacts on sample set C gave a much higher current than the Al contacts, but after the voltage had been applied for some time, the difference became much smaller. This can be seen for the case of an applied bias of 10 V/ $\mu\text{m}$  in Fig. 5.14. One would expect a higher current in the case of the Pt contact if hole injection were dominant, as would be the case immediately after the bias is applied. But it is possible that with time the difference between the Pt and Al contact would be reduced if electron current were becoming significant, as in both cases electrons are injected from the ITO contact. Further, work by Belev *et al.* on *i-n* structures

with a cold deposited  $n$ -layer showed a strong dependence on the metal used for the negative contact, a good indication that there was a significant electron contribution to the dark current [41].

Figure 5.13 also shows that after about 700 s, the hole current begins to slowly increase. This is likely due to a combination of the release of holes trapped in the  $n$ -layer and an increase in the field at the positive contact due to large amounts of electrons trapped in the  $p$ -layer. This could happen in reality, but with time the increased injection of holes into the  $n$ -layer would likely cause this increase to plateau or possibly even begin decaying again. If the hole current has fallen low enough, these ripples would never be noticed in experiment.



**Figure 5.13** Dark current density transients experimentally measured (circles) and simulated (lines) for the Pt contact on an  $n$ - $i$ - $p$  sample of set C at  $5 \text{ V}/\mu\text{m}$ . The total simulated current is the sum of the simulated hole and electron currents. The electron current becomes dominant after roughly 200 s. The eventual increase in the hole current is due to an increasing field at the positive contact as the trapped carrier concentration distribution across the sample continues to change. This effect could be eliminated through the inclusion of several finely tuned deep hole trap states.

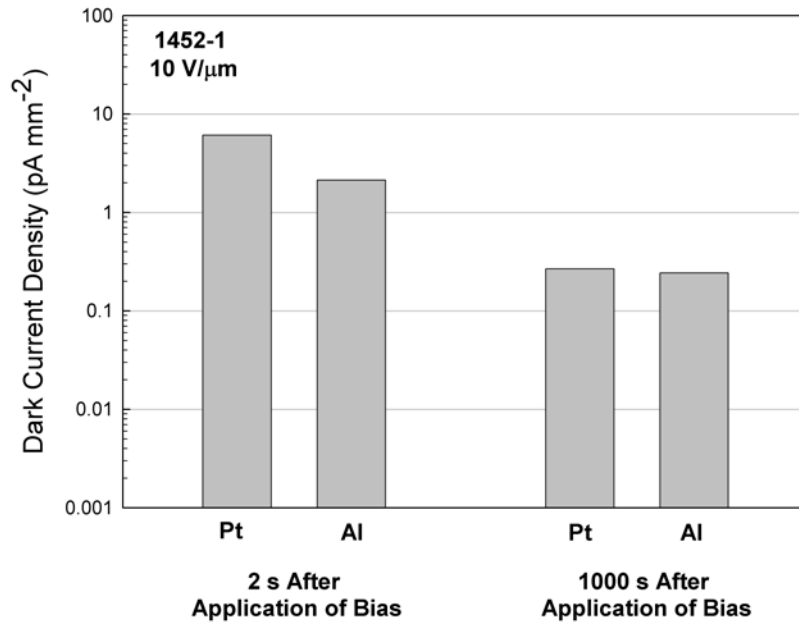


**Figure 5.14** Comparison of the dark current levels produced by the Pt and Al contacts on an *n-i-p* sample of set C, 2 s and 1000 s after the application of the 10 V/μm bias. At 2 s, the Pt contact produces a larger current, which would be expected if hole injection is dominant as Pt has a larger work function than Al, providing a smaller barrier to hole injection. After 1000 s, the current levels are much closer, possibly due to a decreased relative contribution of holes to the dark current, as electrons will face the same barrier to injection in both cases.

It is unfortunate that the concentrations of the deep hole traps had to be altered between simulations at different fields to get closer matches. However, there is a reasonable explanation for this. While both the deep hole trap level concentrations were increased as the field was increased, the amount of increase was much larger for the shallower deep traps. For example, the 10 V/μm simulation required  $2 \times 10^{15} \text{ cm}^{-3}$  more hole traps at a depth of 0.78 eV than the 3 V/μm simulation, whereas the 10 V/μm simulation required only  $2.45 \times 10^{14} \text{ cm}^{-3}$  more deep hole traps at a depth of 0.9 eV than the 3 V/μm simulation. This could be viewed as a general shifting of the trap depths towards the valence band edge at higher fields, something that could be occurring if at least some of the holes are being trapped in charged centers so that the effective trap depth can be lowered by the Poole-Frenkel effect.

Figure 5.13 (a) shows the experimental result at 10 V/μm where the temporary plateau appears, as is common of all samples of set C at high fields.  $\phi_e$  was decreased from 0.86 eV to 0.81 eV with the hope that a higher electron current would account for the plateau. The

experimental result is compared with the total simulated current as well as the simulated hole and electron currents in Fig. 5.15. It is clear that the simulated transient does not accurately predict the plateau and subsequent decay. It is likely that several finely tuned deep hole trap levels are required to model this high field effect.

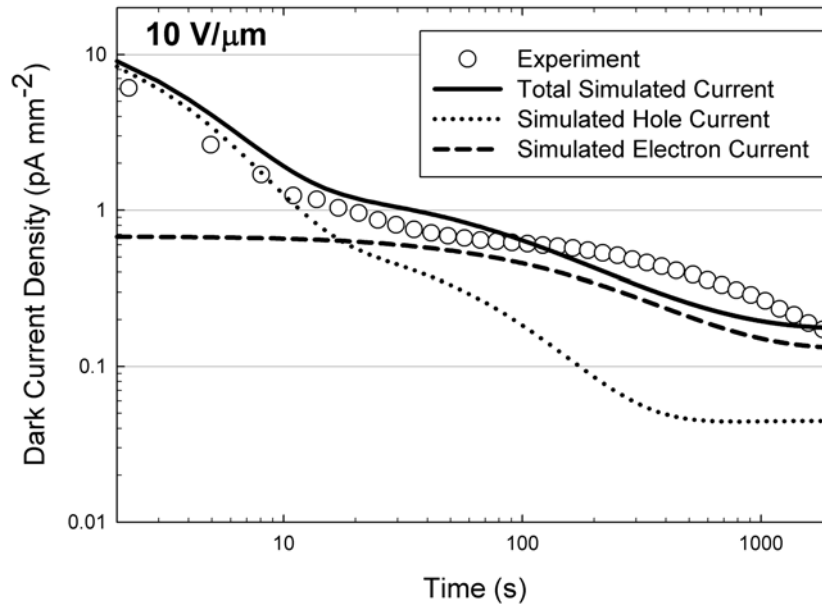


**Figure 5.15** Dark current density transients experimentally measured (circles) and simulated (lines) for the Pt contact on an *n-i-p* sample of set C at  $10 \text{ V}/\mu\text{m}$ . The temporary plateau exhibited experimentally is not well reproduced by the model.

## 5.4 Conclusion

Given the large number of variables which must be accounted for (and are not well defined for a-Se), it is clear that modeling the dark current transients produced by a-Se sandwich structures is no small task. It has been shown that while modeling such transients with pure and modified Monte Carlo simulations is possible, the computational times are simply too long to allow for the multiple iterations needed to fit the simulation results to experimental results by adjusting the variable parameters. The published model by Mahmood and Kabir, though greatly simplified, has shown promise and has been applied here, with some success, to model the dark current transients produced by an *n-i-p* sample which did not reach a steady-state. As discussed, there are adjustments which could make the model more accurate and useful, such as the division of the simulated sample into dimensional slices. This would allow for the modeling of structures

which do not include one or either of the blocking layers. Perhaps with future improvements in computing power, these adjustments could be implemented in a reasonable fashion. For now, the model, as presented, offers a reasonable explanation that the dark current in a-Se sandwich structures is due almost entirely to the injection of charge carriers from the contacts and gives a good description of these transients at varying applied fields. This conclusion is supported by the wealth of experimental results presented in Chapter 4 of this thesis.

# 6. MODELING OF X-RAY SENSITIVITY IN AMORPHOUS SELENIUM FILMS

## 6.1 Previous Model

The Monte Carlo based x-ray sensitivity modeling presented here is an extension of the work done by Yunus at the University of Saskatchewan [2]. That model considered the following factors:

a) Deep trapping of carriers:

Some drifting holes and electrons will be trapped in deep states. This trapping depends on the concentration of deep trap centers,  $N_t$ , within the a-Se.

b) Recombination between drifting carriers:

A positively charged hole and a negatively charged electron, drifting in opposite directions due to the applied electric field, can be drawn together by Coulombic attraction and recombine, essentially eliminating both carriers. This recombination depends on the concentration of drifting carriers and this concentration is very small when compared to the concentration of trapped carriers. Therefore, the type of recombination discussed in c) is dominant and recombination between drifting carriers can be ignored [63].

c) Recombination between trapped and drifting carriers:

Coordination defects in a-Se can appear over-all charge neutral (as discussed in Section 3.3.2.3), but can still trap a drifting hole or electron. When this occurs, the trap center then has an associated charge and can attract a drifting carrier of the opposite charge to recombine with the trapped carrier.

This recombination is governed by the Langevin recombination mechanism [243] which states that the rate of recombination is defined as follows:

$$R = C_L c_t c \quad (6.1)$$

where  $c$  is the drifting carrier concentration,  $c_t$  is the oppositely charged, trapped carrier concentration and  $C_L$  is the Langevin recombination coefficient, defined as:

$$C_L = \frac{e\mu}{\varepsilon_0 \varepsilon_r} \quad (6.2)$$

However, a deep trap center that is originally charged will still trap a traveling carrier of the opposite charge but will then appear neutral and will not contribute to recombination. Therefore, only a fraction,  $f_{recomb}$ , of the trapped carrier concentration should be considered in the Langevin equation and this fraction can only be determined through trial and error calibration [63].

d) Trap filling effects:

As drifting carriers are trapped by deep trap states, the number of available deep traps decreases. In effect, the deep traps are filled up. As this occurs, the probability of a carrier being trapped goes down and the effective lifetime increases as

$$\tau = \frac{\tau_0}{(1 - n_t / N_t)} \quad (6.3)$$

where  $\tau_0$  is the original carrier lifetime,  $n_t$  is the trapped carrier concentration and  $N_t$  is the original deep trap concentration [2].

e) Non-uniform electric field effects:

Drifting and trapped carriers within the a-Se build up a space charge density which affects the value of the electric field throughout the thickness of the a-Se. The concentration of drifting carriers is very small with respect to the concentration of trapped carriers, so the charge density is given by

$$\rho(x) = e(p_t - n_t) \quad (6.4)$$

This charge density is used to calculate the electric field at a given point in the a-Se layer using Poisson's equation:

$$\frac{dF(x)}{dx} = \frac{\rho(x)}{\epsilon_0 \epsilon_r} \quad (6.5)$$

with the boundary condition:

$$\int_0^L F(x) dx = V \quad (6.6)$$

where V is the applied voltage.

This altered field distribution will affect both the drift velocity of carriers at different points in the a-Se and the efficiency of EHP creation, as  $W_{\pm}$  depends inversely on the electric field [2].

f) Effects of x-ray induced deep trap generation:

It has been shown that amorphous chalcogens, such as a-Se, can contain metastable deep trap centers created by exposure to radiation [181,244,245]. The exact mechanism by which this occurs is not fully understood, but the metastable trap center concentration is taken to be

$$N_{x_t} = N_{x_0} \left[ 1 - \exp\left(-\frac{X}{a_X}\right) \right] \quad (6.7)$$

where  $N_{x_0}$  is the saturation value of the x-ray induced deep trap center concentration,  $a_X$  is an irradiation dependant constant of about 0.4 R (determined through trail and error model calibration), and  $X$  is the cumulative exposure [2].

This new deep trap center concentration will change the effective carrier lifetimes as follows:

$$\tau = \frac{\tau_0}{1 + (N_{x_t} - n_t) / N_t} \quad (6.8)$$

having a counter-effect to the trap filling phenomenon.

g) Release of trapped carriers:

The deep trap release time of electrons has been shown to be several hours so, for any practical purpose, a trapped electron can be considered lost forever. However, the release time of a hole is on the order of minutes [65]. Several minutes may pass between successive exposures in clinical use so it becomes important to include a probability-based representation of the effect of trapped hole release.

The results of computer simulations based on the factors mentioned above, as each of those factors were considered one at a time, can be found in reference [2]. The model presented here also includes all of these factors. In addition, it includes the effects on x-ray sensitivity of the blocking layers used to diminish the dark current and the effect of the non-uniform electric field distribution due to the trapping of charge carriers injected into the blocking layers due to the flow of dark current before each x-ray exposure.

## 6.2 Present Model

As with the dark current Monte Carlo simulations discussed in Section 5.1, the modeled sample is divided into dimensional slices with a width  $\Delta x$ , as shown in Fig. 6.1. Parameters such as  $F$ ,  $W_{\pm}$ , and the number of trapped carriers are stored for each slice. In the new, multilayer model, the deep trap concentrations and carrier lifetimes are altered appropriately in the slices corresponding to the blocking layers. Several slices are binned together for field calculations and array searches to improve efficiency. Arrays of holes and electrons are used to store drifting carrier locations in the sample. While the total number of carriers generated in an x-ray exposure in the diagnostic range can be  $10^{15}$ , it is not possible to track this many carriers. It has been shown that in simulations of this nature, tracking  $10^5$  carriers is feasible and sufficient for accurate results [2].

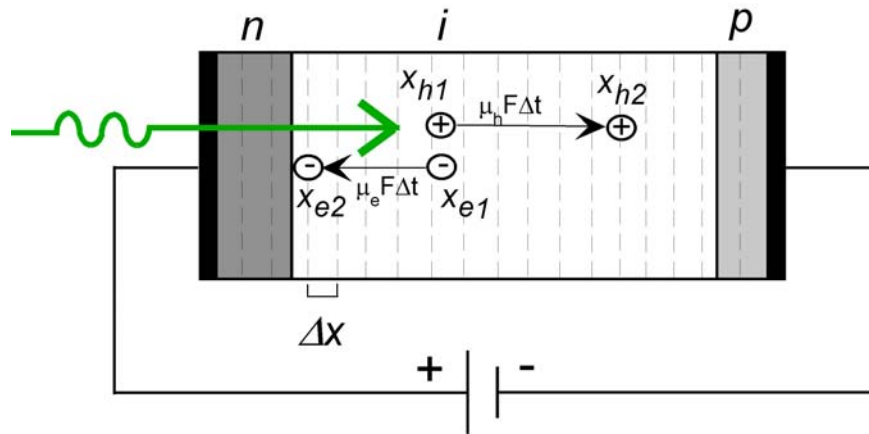


**Figure 6.1** An illustration of an *n-i-p* sample divided into dimensional slices, with holes and electrons drifting from their point of photogeneration due to the applied field.

At the start of the simulation, all carrier and dimensional arrays are initialized and values that will not change during the simulation are calculated, including the energy deposited in the a-Se by the x-ray beam. For a given simulated exposure, the incident x-ray photon fluence per  $m^2$  is given by [61]

$$N_0 = \frac{5.45 \times 10^{16} X}{E_{ph}(\alpha_{en} / \rho)_{air}} \quad (6.9)$$

where  $X$  is the exposure in R,  $E_{ph}$  is photon or beam energy in eV and  $(\alpha_{en}/\rho)_{air}$  is the mass absorption coefficient for air ( $0.539 \text{ cm}^2 \text{ g}^{-1}$  at 20 keV [66]). This means that the energy absorbed by the a-Se per unit area for a given exposure is the product of  $N_0$ , the quantum efficiency, QE, and the energy absorbed per attenuated photon as:

$$E_{abs} = N_0 [1 - \exp(-\alpha L)] \frac{\alpha_{en}}{\alpha} E_{ph} \quad (6.10)$$

where  $L$  is the thickness of the a-Se layer.

The remainder of the simulation is broken into time steps,  $\Delta t$ . Each time step, the following calculations are performed: First, the carrier generation profile must be calculated and is given by

$$c(x) = C_0 \exp(-\alpha x) \quad (6.11)$$

where  $C_0$  is a constant. The significance of Eq. 6.11 is shown in Fig. 6.2. To determine the initial position of each photogenerated EHP, the probability density function (PDF) for carrier generation at a position in the sample,  $x$ , must be calculated. The PDF is essentially the ratio of charge generated up to  $x$  (the hashed area under the graph of  $c(x)$  in Fig. 6.2) to the charge generated in the entire sample (the entire area under  $c(x)$ ) and is given by

$$PDF = \frac{\int_0^x C_0 \exp(-\alpha x) dx}{\int_0^L C_0 \exp(-\alpha x) dx} \quad (6.12)$$

where  $x$  can be solved for and is given by

$$x = -\frac{1}{\alpha} \ln\{1 - r[1 - \exp(-\alpha L)]\} \quad (6.13)$$

where  $r$  is a random number in the range [0-1] and is generated by the same random number generator described in Section 5.2.8. Unfortunately, this matter is complicated by the fact that  $F$  will not be uniform throughout the simulation due to the deep trapping of drifting charge carriers. Therefore, the  $W_{\pm}(x)$  profile becomes important in determining the carrier photogeneration profile:

$$c(x) = \frac{C_1}{W_{\pm}(x)} \exp(-\alpha x) \quad (6.14)$$

where  $C_1$  is a constant. The PDF is now given by

$$PDF = \frac{\int_0^x \frac{C_1}{W_{\pm}(x)} \exp(-\alpha x) dx}{\int_0^L \frac{C_1}{W_{\pm}(x)} \exp(-\alpha x) dx} \quad (6.15)$$

giving

$$r \int_0^L \frac{1}{W_{\pm}(x)} \exp(-\alpha x) dx = \int_0^x \frac{1}{W_{\pm}(x)} \exp(-\alpha x) dx \quad (6.16)$$

which is solved numerically in each time step.  $W_{\pm}$  must also be calculated for each dimensional slice and the equation used to do so is

$$W_{\pm}(x) = \left( 6 + \frac{15 \times 10^6}{F(x)^{0.8}} \right) \left( 0.72 + 0.56 \exp\left( -\frac{E_{ph}}{62700} \right) \right) \quad (6.17)$$

where  $E_{ph}$  is the mean energy of the x-ray beam in eV and  $F(x)$  is the electric field at  $x$  in V/m. Equation 6.17 was developed by Yunus [2] to fit the x-ray energy and electric field dependence data of Blevis *et al.* [78], shown in Fig. 2.5.

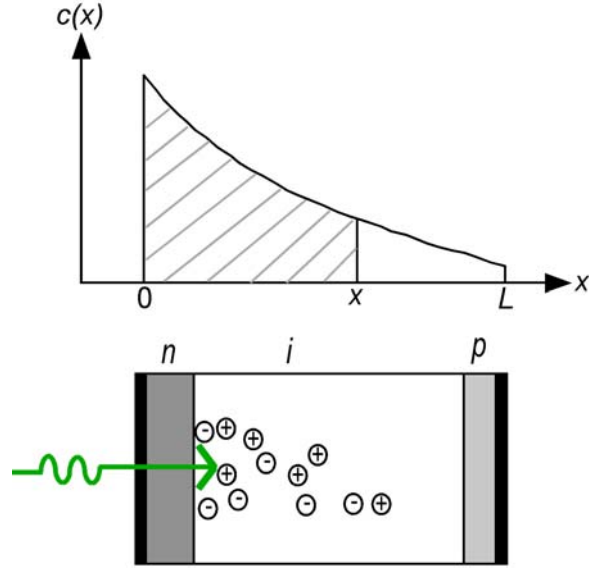


**Figure 6.2** The exponentially decaying carrier generation profile results in the majority of photogenerated carriers being created near the radiation receiving electrode.

For each time step, the drift of each carrier, regardless of whether it was generated on the current time step or a previous one, is calculated. This is shown diagrammatically in Fig. 6.1. Initially, the generated hole and electron are at  $x_{hl}$  and  $x_{el}$ , respectively. The distance that the carriers would drift in one time step, if they are not lost, is calculated and their destinations are given as  $x_{h2} = x_{hl} + \Delta t \mu_h F(x_{hl})$  and  $x_{e2} = x_{el} - \Delta t \mu_e F(x_{el})$ . The total trapped oppositely charged carrier concentration and deep trap concentration over that range is calculated and used to determine the probability that the carrier will be deeply trapped or recombine with a trapped oppositely charged carrier, taking into account trap filling effects, Langevin governed recombination and x-ray generated deep traps as discussed in Section 6.1. These probabilities are given by

$$prob\_trap = 1 - \exp\left\{-\frac{\Delta t(1 + (N_{x_i} - n_i)/N_t)}{\tau_0}\right\} \quad (6.18)$$

$$prob\_recomb = 1 - \exp(-\Delta t C_L c_i) \quad (6.19)$$

The total probability of a carrier being lost is then given by the summation of Eqs. 6.18 and 6.19 as  $prob\_lost = prob\_trap + prob\_recomb$ . A random number between zero and one is generated and if it is less than  $prob\_lost$ , then the carrier is lost. A second random number is then generated and if it is less than the ratio of  $prob\_trap$  to  $prob\_lost$ , the carrier is lost to trapping and is added as a trapped carrier to a slice between  $x_1$  and  $x_2$ , chosen randomly, and the trapped carrier is deleted from the array of drifting carriers. It should be noted that due to the memory constraints discussed previously, each carrier represents many in the simulation and so in the case of a trapped carrier, many trapped carriers are added to the value for that slice. Just how many carriers each simulated carrier represents is determined by a multiplication factor which is the ratio of the area under the charge generation profile (the total number of carriers that would be created for a given exposure) to the actual number of carriers simulated.

If the carrier is lost to recombination, many trapped, oppositely charged carriers are removed from a slice between  $x_1$  and  $x_2$ , also chosen randomly, and the recombined carrier is deleted from the array of drifting carriers. In the previous model used by Yunus [2], it was found that a field dependant fitting factor,  $f_{recomb}$ , was needed in the recombination calculations to match experimental results. This arises from the fact that only a trap center which is initially charge neutral (and hence charged after trapping a carrier) will contribute to recombination. That is, a filled trap which was initially charged will be neutral and will experience no coulombic interaction with other drifting carriers. As a result,  $f_{recomb}$  was found to be less than one. However, to match experimental results, it was also found that  $f_{recomb}$  needed to decrease with the applied field. The inclusion of this factor is acceptable, as the true nature of charge trapping in a-Se is not fully understood, as discussed in Section 3.3.2.3. The only explanation given by Yunus for the field dependence of  $f_{recomb}$ , was that at low fields, where the carrier schubwegs are short, perhaps so much trapping occurs that deeply trapped holes and electrons start to recombine with one another. However, this is unlikely and the following explanation may be more realistic:  $f_{recomb}$  represents the fraction of total trapped carriers which are trapped in centers which were initially charge neutral (charged after trapping) and can therefore contribute to recombination. If the concentration of carriers trapped in these initially neutral centers is denoted as  $N_{neutral}$  and the concentration of carriers trapped in initially charged centers as  $N_{charged}$ , then  $f_{recomb} = N_{neutral} / (N_{neutral} + N_{charged})$ . At higher applied fields, carriers trapped in initially charged centers will

experience a shorter release time as the applied field will counteract the coulombic attraction between the carrier and the trap, reducing the barrier to release. This means that at a higher applied field,  $N_{charged}$  will be smaller at a given time and therefore  $f_{recomb}$  will have a higher value at higher fields. In Section 6.4, it will be shown that a field dependent  $f_{recomb}$  was also required to match experimental results in this work.

If a carrier is not lost, it moves on to  $x_2$ . In this case, if  $x_2$  is outside of the photoconductor, then the carrier is considered collected. Once the drift distance is calculated for each carrier in the arrays, the field at each dimensional slice, due to the applied field and the space charge created by trapped carriers, is calculated by solving Poisson's equation as described in Section 6.1.

Finally, the current due to all of the drifting carriers is calculated using the Shockley-Ramo theorem [246,247] as

$$i_e = \frac{eN_e\mu_e F}{L} \text{ and } i_h = \frac{eN_h\mu_h F}{L} \quad (6.20)$$

where  $N_e$  and  $N_h$  are the total number of drifting electrons and holes, respectively, and the total current is given by  $i_{tot} = i_e + i_h$ . However, in the case of a non-uniform field distribution, the electron and hole current are given by

$$i_e = \frac{e\mu_e}{L} \sum_{j=0}^{N_e} F_j(x_j) \text{ and } i_h = \frac{e\mu_h}{L} \sum_{j=0}^{N_h} F_j(x_j) \quad (6.21)$$

where  $F_j(x_j)$  is the field experienced by a carrier,  $j$ , at a location,  $x_j$ .

For each x-ray exposure, the current is integrated to determine the total collected charge,

$$Q_{coll} = \int_0^T i_{tot} dt \quad (6.22)$$

where  $T$  is the time length of the exposure.  $Q_{coll}$  is divided by the total charge generated to determine the CCE for the exposure. The relative sensitivity is then calculated as the product of the QE, the CCE and the PGR as in Eq. 2.14.

## 6.3 Simulation Results

For all of the results presented in this section, the simulated exposure consisted of 30 exposures of 12 mR lasting 200 ms each with a 2 minute rest interval between each exposure. This gives a total cumulative exposure of 0.36 R after roughly 60 minutes. The mean photon energy of the radiation was taken as 20 keV and was modeled as a monoenergetic beam of 20 keV where the linear attenuation coefficient of a-Se,  $\alpha$ , is  $206.45 \text{ cm}^{-1}$  and the linear absorption coefficient,  $\alpha_{en}$ , is  $143.69 \text{ cm}^{-1}$  [66].

### 6.3.1 Results for Single Layer Structures

Initial sensitivity simulations were carried out considering only the factors included in the previous model used by Yunus [2]. The  $i$ -layer sample modeled here is shown in Fig. 6.3. The sample is positively biased, *i.e.*, the radiation receiving electrode is positive with respect to the other electrode, so that photogenerated holes are drifted across the sample since the majority of photogeneration will occur near the positive electrode. The sample was a 200  $\mu\text{m}$  thick  $i$ -layer with an applied field of 10 V/ $\mu\text{m}$ . The important material property values used in the simulation are summarized in Table 6.1.

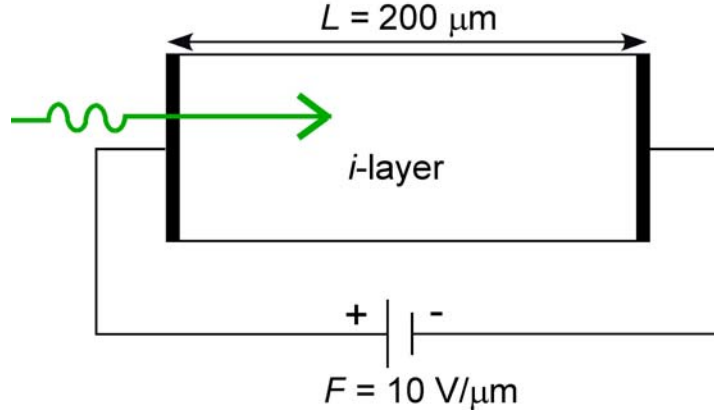


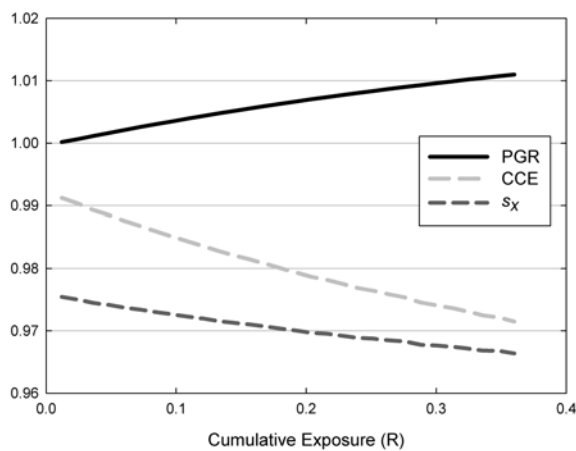
Figure 6.3 Single *i*-layer sample used in initial sensitivity simulations.

Table 6.1 Important material properties assumed in the initial x-ray sensitivity results. Deep trap concentrations are denoted as  $N_{th(e)}$  for holes (electrons),  $\tau_{0h(e)}$  are the carrier lifetimes,  $\tau_{rh(e)}$  are the release times and  $N_{x_{0h(e)}}$  are the constants used in calculating x-ray generated metastable traps.

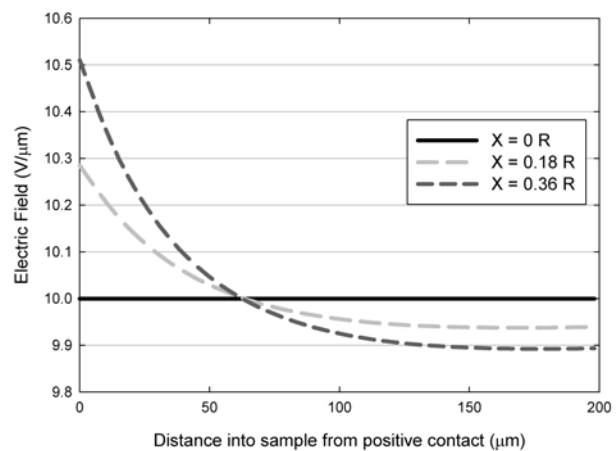
Property	Assumed Value	Property	Assumed Value
$\mu_h$	$0.12 \text{ cm}^2 \text{ V}^{-1} \text{ s}^{-1}$	$\mu_e$	$0.0035 \text{ cm}^2 \text{ V}^{-1} \text{ s}^{-1}$
$N_{th}$	$2.6 \times 10^{13} \text{ cm}^{-3}$	$N_{te}$	$1.3 \times 10^{13} \text{ cm}^{-3}$
$\tau_{0h}$	$47.5 \text{ } \mu\text{s}$	$\tau_{0e}$	$200 \text{ } \mu\text{s}$
$\tau_{rh}$	$100 \text{ s}$	$\tau_{re}$	$\infty$
$N_{x_{0h}}$	$9 \times 10^{12} \text{ cm}^{-3}$	$N_{x_{0e}}$	$9 \times 10^{12} \text{ cm}^{-3}$

These single layer results show the same decrease in sensitivity as observed by Yunus [2]. The value of the quantum efficiency will remain constant throughout the simulation, but as can be seen in Figure 6.4 (a), the PGR increases slightly while the CCE decreases slightly. This results in the normalized sensitivity decreasing without any real saturation throughout the simulation. These results are similar to those obtained in previous work [2]. To explain these phenomena, one must examine the change in the electric field distribution after all of the exposures. This is shown in Figure 6.4 (b). The electric field ends up higher than the initial field at the positive electrode and lower at the negative electrode. Most of the incident radiation will be absorbed very close to the positive electrode. Here the electric field is high, thus lowering the EHP creation energy and causing the PGR to increase as the difference in the electric field from the uniform initial case increases.

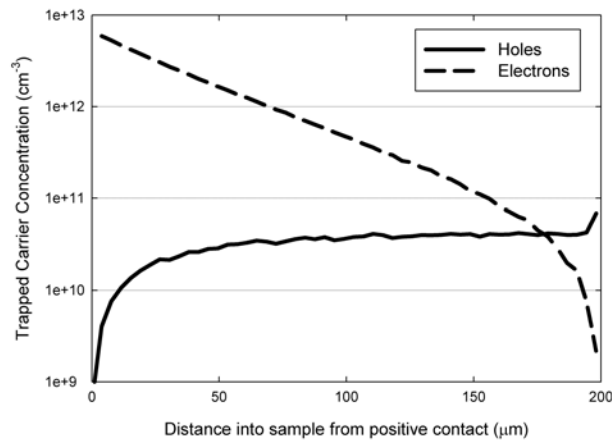
Figure 6.4 (c) shows that the concentration of trapped electrons is much higher than that of trapped holes, and this is expected as electrons have a shorter schubweg in a-Se. The trapped electron concentration is lower away from the positive electrode as most of the EHPs will be created close to the positive electrode and electrons will drift towards the positive electrode. Photogenerated holes will drift towards the negative electrode and thus the trapped hole concentration grows towards the negative electrode. Although the deep trap centers start to become full, x-ray exposure continually creates new deep trap centers, so carrier trapping continues to cause the CCE to fall. Also, the high concentration of trapped carriers leads to a higher and higher rate of recombination with drifting carriers. As a result, in this case, the CCE decreases more than the PGR increases and the sensitivity shows an overall decrease. Because of the x-ray generated trap centers, the increase in PGR and decrease in CCE continues and at a total cumulative exposure of 1 R, the value of  $s_x$  is actually higher than the value of the CCE.



(a)



(b)



(c)

Figure 6.4 (a) The CCE, PGR and normalized sensitivity as a function of cumulative exposure, (b) initial, mid-simulation and final electric field distribution and (c) final trapped carrier concentration distributions for a mammographic exposure, single layer simulation. The PGR increases with cumulative exposure due to trapped electrons near the positive contact which increase the electric field in that region, lowering  $W_{\pm}$ . However,  $s_x$  decreases with cumulative exposure as the CCE decreases more than the PGR increases due to the continued creation of x-ray induced, metastable trap states.

### 6.3.2 Results for $n-i$ and $n-i-p$ Structures

Yunus' model has been extended to include the effects on x-ray sensitivity of the thin blocking layers used to reduce the dark current due to injected carriers at the electrodes. In this model, a thin  $n$ -like layer (10  $\mu\text{m}$ ) is located between the positive contact and the  $i$ -layer and a thin  $p$ -like layer (2  $\mu\text{m}$ ) is located between the negative contact and the  $i$ -layer, as shown in Fig. 6.5. All material properties and beam energies have been kept consistent with those shown in Table 6.1. Important material properties of the blocking layers differing from that of the  $i$ -layer are shown in Table 6.2.

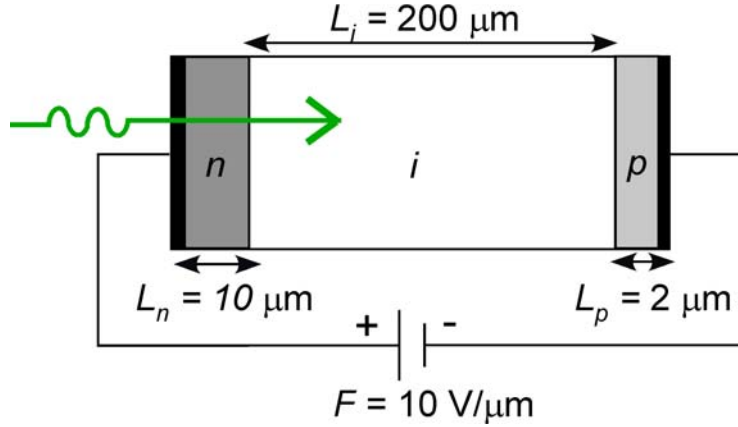


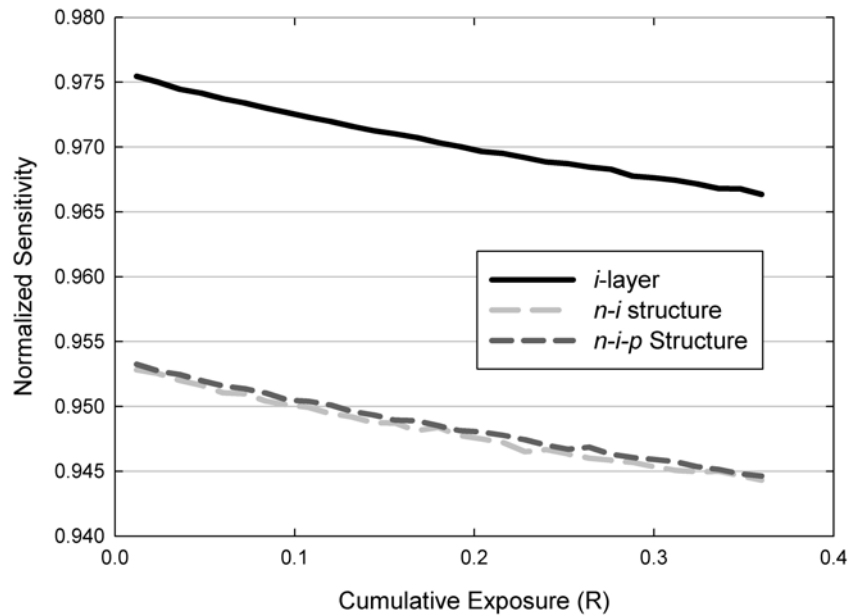
Figure 6.5 Three layer, *n-i-p* structured sample used in sensitivity simulations involving blocking layers. *n-i* structure results use the same structure with no *p*-layer.

Table 6.2 Material properties of the *n*- and *p*-like blocking layers. A double subscript of *n* refers to properties in the *n*-like layer, while a double subscript of *p* refers to properties in the *p*-like layer.

Property	Assumed Value	Property	Assumed Value
$N_{th_n}$	$2.6 \times 10^{15} \text{ cm}^{-3}$	$N_{te_n}$	$1.3 \times 10^{13} \text{ cm}^{-3}$
$N_{th_p}$	$2.6 \times 10^{13} \text{ cm}^{-3}$	$N_{te_p}$	$1.3 \times 10^{15} \text{ cm}^{-3}$
$\tau_{0h_n}$	0.48 $\mu\text{s}$	$\tau_{0e_n}$	200 $\mu\text{s}$
$\tau_{0h_p}$	47.5 $\mu\text{s}$	$\tau_{0e_p}$	2 $\mu\text{s}$

### 6.3.2.1 *n-i* Structure

Simulations were first carried out assuming a two layer, *n-i* structure, as the *p*-layer is relatively thin in mammographic detectors and its location (opposite the radiation receiving electrode) suggests that it will have little effect on the sensitivity. Figure 6.6 shows a comparison of  $s_x$  for the single, two layer and three layer structures. It can be seen that the addition of an *n*-layer does not change the rate at which the sensitivity decreases but it does give an overall lower sensitivity response (a decrease of about 2% at any given cumulative exposure). This is exactly the change noticed in the numerical calculation work done by Kabir *et al.* [59] when an *n*-like blocking layer was added to the *i*-layer model, as shown in Fig. 2.11.



**Figure 6.6 Comparison of normalized x-ray sensitivity vs. cumulative exposure for *i*-layer, *n-i* and *n-i-p* structures.  $s_x$  decreases at the same rate for all structures but is roughly 2% lower at any given cumulative exposure for the *n-i* and *n-i-p* structures than for the *i*-layer structure. The addition of the *p*-layer makes very little difference in the result.**

The lower  $s_x$  is mostly due to a lower CCE which results from much higher levels of hole trapping in the *n*-layer due to the increased value of hole trap concentration and decreased value of hole lifetime in the *n*-layer when compared with the *i*-layer. Furthermore, a lot of the photons will be absorbed in the *n*-layer, so many photogenerated holes will be trapped there before they even have a chance to drift into the *i*-layer. This increased hole trapping in the *n*-layer can be seen in Fig. 6.7. However, the concentration of trapped holes in the *n*-layer is still far below that of trapped electrons and therefore there is little change in the electric field distribution and hence the change in the PGR with cumulative exposure is almost identical in the *i*-layer and *n-i* structures.

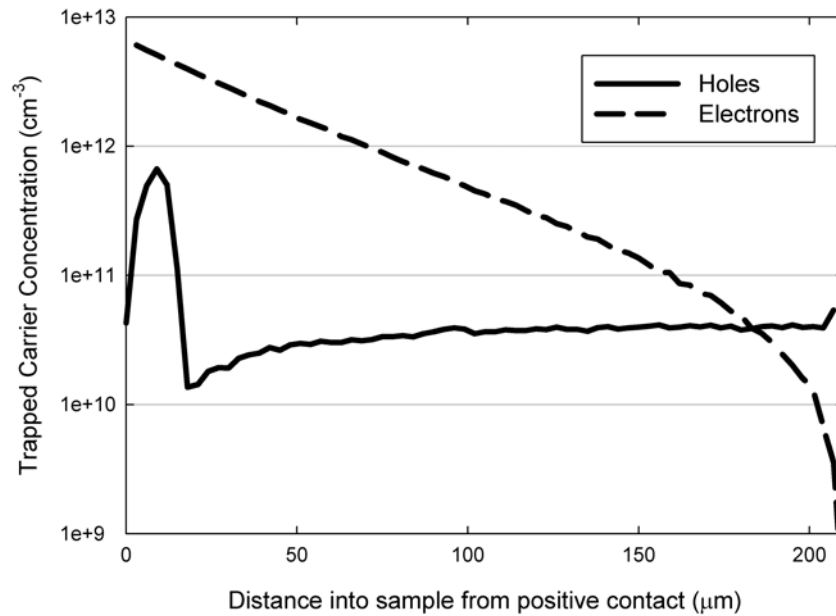


**Figure 6.7** Trapped hole and electron concentration distributions in the *n-i* sample after 0.36 R of exposure. The area of the sample between 0 and 10  $\mu\text{m}$  where there is increased hole trapping is the *n*-layer.

### 6.3.2.2 *n-i-p* Structure

As shown in Fig. 6.6, the trend and level in  $s_x$  is almost exactly the same between the *n-i* and *n-i-p* structures. This is because the addition of the *p*-layer is of little consequence to the charge collection in the positive bias. Holes drifting towards the negative electrode, and hence through the *p*-layer, will, by design, experience no decrease in transport in the *p*-layer. Drifting electrons would be trapped more easily in the *p*-layer but very few electrons will ever interact with the *p*-layer, as very little radiation will be absorbed that far into the structure and electrons generated in the *i*-layer will drift in the other direction.

#### 6.3.2.2.1 Effect of *p*-layer Thickness

While a 2  $\mu\text{m}$  thick *p*-layer is typical of the mammographic structures used in Chapter 4, the effect of varying the thickness of the *p*-layer on  $s_x$  has been modeled and is shown in Fig. 6.8. It can be seen that there is virtually no change in x-ray sensitivity when the thickness of the *p*-

layer is varied from 1 to 6  $\mu\text{m}$  in a positively biased mammographic structure. Again, this lack of a significant role in  $s_x$  is due to the position of the  $p$ -layer in this situation.

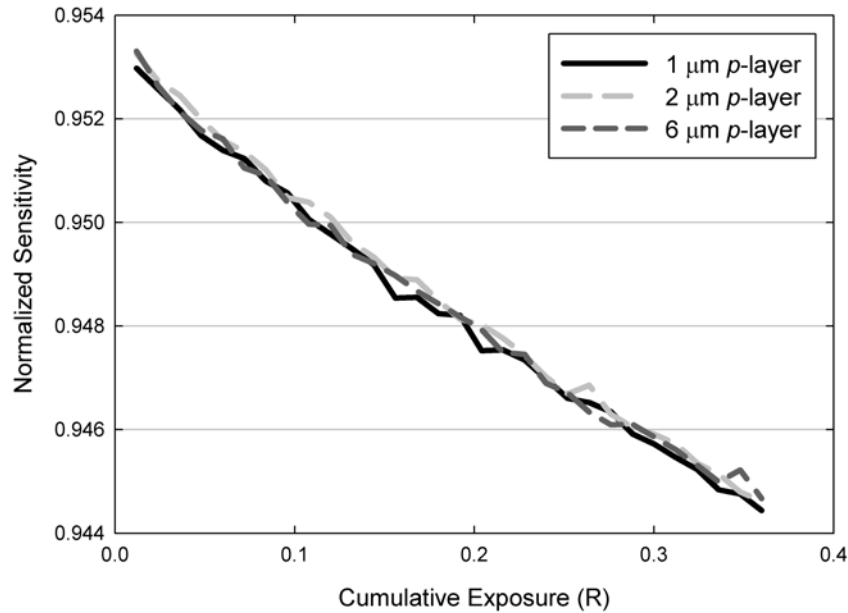


**Figure 6.8 Normalized x-ray sensitivity vs. cumulative exposure for an  $n$ - $i$ - $p$  mammographic structure with three different thicknesses of  $p$ -layer. Due to the positive bias, the thickness of the  $p$ -layer has almost no effect on  $s_x$ .**

### 6.3.2.2.2 Effect of $n$ -layer Thickness

As apparent from the results shown in Fig. 6.6, the addition of the  $n$ -layer causes a significant reduction in the normalized sensitivity when compared with a single  $i$ -layer structure. It is intuitive, since this decrease in sensitivity is due to a reduction in the CCE because of increased hole trapping in the  $n$ -layer, that the thickness of the  $n$ -layer would have a substantial impact on the sensitivity. This turns out to be the case, as shown in Fig. 6.9 where  $s_x$  is compared for 5, 10 and 20  $\mu\text{m}$  thick  $n$ -layers, with the rest of the structure remaining the same. While the rate of decrease in sensitivity with exposure remains independent of  $n$ -layer thickness, the overall sensitivity decreases as the thickness of the  $n$ -layer increases. An increase in  $n$ -layer thickness of 4 times (5 to 20  $\mu\text{m}$ ) results in a decrease in  $s_x$  of 5.5%.  $s_x$  decreases linearly with increasing  $n$ -layer thickness as the effect of decreasing CCE is simply due to more holes being generated in the  $n$ -layer where they are much more likely to be deeply trapped than in the  $i$ -layer.

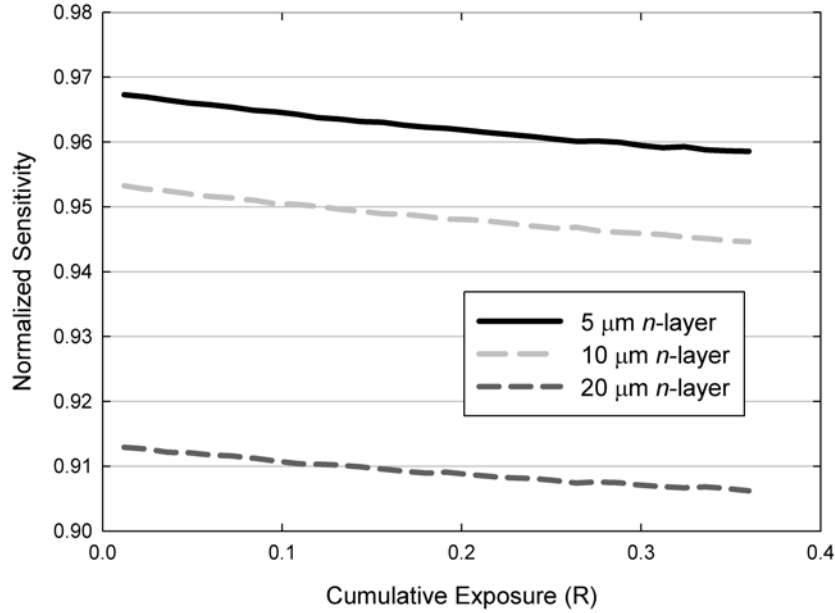


**Figure 6.9** Normalized sensitivity vs. cumulative exposure for an *n-i-p* structure in which the thickness of the *n*-layer varied from 5 to 20  $\mu\text{m}$ .  $s_x$  decreases linearly with increasing *n*-layer thickness.

### 6.3.2.2.3 Effect of Hole Lifetime in the *n*-layer

While the hole lifetime in the *n*-layer assumed in the above simulations was reasonable and quite small (0.48  $\mu\text{s}$ ), it is interesting to determine the effect of different hole lifetime values in the *n*-layer. Two additional scenarios were considered. First, the hole lifetime in the *n*-layer was increased by an order of magnitude to 4.8  $\mu\text{s}$ . As governed by Eq. 5.7, an increase in *n*-layer hole lifetime by an order of magnitude must correspond to an order of magnitude decrease in *n*-layer deep hole trap concentration. Therefore,  $N_{th_n}$  was also decreased from  $2.6 \times 10^{15} \text{ cm}^{-3}$  to  $2.6 \times 10^{14} \text{ cm}^{-3}$ . All other parameters were constant between the two simulations and are summarized in Tables 6.1 and 6.2. The resulting  $s_x$  can be seen in Fig. 6.10, compared with *n-i-p* results from Fig. 6.6 where  $\tau_{0h_n} = 0.48 \mu\text{s}$ . It can be seen that the sensitivity increases by  $\sim 2\%$  when the hole lifetime increases by an order of magnitude. This is due entirely to an increase in the CCE, as the PGR remains unchanged. The decrease in trapped hole concentration in the *n*-layer has little effect on the electric field due to the fact that the large concentration of electrons trapped there dominates the space charge density. Due to the decreased value of  $N_{th_n}$ , the trap

filling effect is more significant and the CCE increases as more holes photogenerated in the  $n$ -layer will be collected.

The second consideration is the case where the  $n$ -layer is ideal and all holes are immediately trapped there. This corresponds to a hole lifetime in the  $n$ -layer of 0 s and an effectively infinite concentration of deep hole traps. This was accounted for in the simulation by always setting the probability that a hole would be trapped in the  $n$ -layer to 1. It should be noted that this ideal case is obviously not the reality, as the dark current would then be nearly non-existent. The result of this simulation can also be seen in Fig. 6.10. The rate of decrease of  $s_x$  with cumulative exposure barely changes, but the overall level of  $s_x$  is decreased by  $\sim 16\%$ . This is due entirely to a decrease in CCE, as the PGR remains almost unchanged. The average concentration of trapped holes in the  $n$ -layer increased from  $3.9 \times 10^{11} \text{ cm}^{-3}$  in the case of  $\tau_{0h_n} = 0.48 \text{ } \mu\text{s}$  to  $2.8 \times 10^{12} \text{ cm}^{-3}$  when the lifetime was 0 s. Even so, this value remains relatively small when compared with the average concentration of trapped electrons in the  $n$ -layer ( $5.2 \times 10^{12} \text{ cm}^{-3}$ ) so that the effect on the field distribution and hence the PGR is minimal. The large decrease in sensitivity observed when considering an ideal  $n$ -layer is not surprising, as much of the photogeneration will take place there in a positively biased detector. This will cause a large percentage of the photogenerated holes to be instantly trapped and lost from the signal.

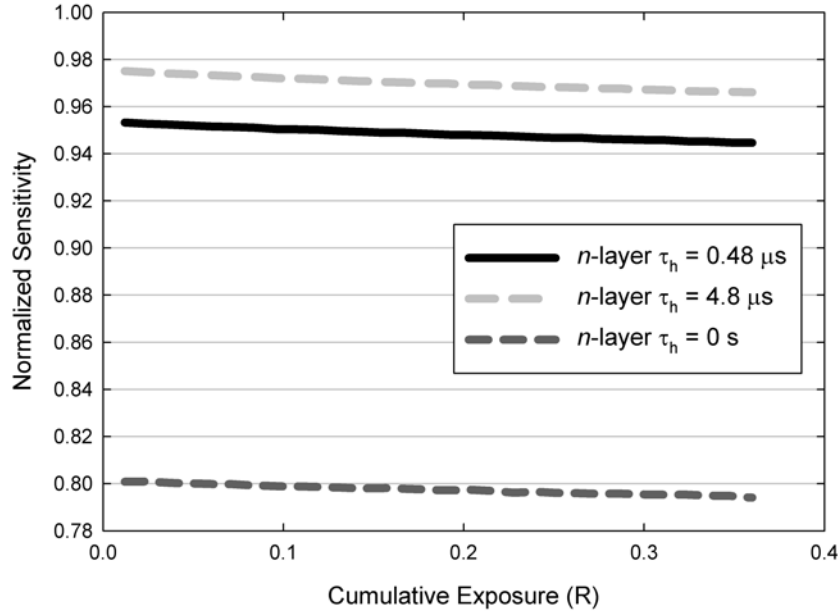


**Figure 6.10 Comparison of normalized sensitivity vs. cumulative exposure for *n-i-p* structures with a hole lifetime in the *n*-layer of 4.8  $\mu\text{s}$ , 0.48  $\mu\text{s}$  and 0 s. The shorter the hole lifetime in the *n*-layer, the lower the overall sensitivity. An ideal *n*-layer, with a hole lifetime of 0 s, produces a very low normalized sensitivity due to the immediate trapping of all holes photogenerated in the *n*-layer, next to the radiation receiving electrode.**

#### 6.3.2.2.4 Effect of Electron Lifetime in the *n*-layer

It is often not only the hole transport properties which are degraded in the *n*-layer but also those of electrons. Ideally, electrons would easily drift through the *n*-layer to be collected at the positive electrode, however, in reality, this is not always the case. To model this, the electron lifetime in the *n*-layer was decreased by one order of magnitude from its value in the *i*-layer to 20  $\mu\text{s}$  and  $N_{te_n}$  was increased from  $1.3 \times 10^{13} \text{ cm}^{-3}$  to  $1.3 \times 10^{14} \text{ cm}^{-3}$ . The result of this change in an *n-i-p* structure with an *n*-layer of 10  $\mu\text{m}$  can be seen in Fig. 6.11 compared with the *n-i-p* result from Fig. 6.6. Both electrons generated in the *n*-layer and electrons generated in the *i*-layer which end up drifting through the *n*-layer, will be more likely to be trapped, resulting in an overall decrease in sensitivity by  $\sim 0.4\%$ , depending on the exposure accumulated. This is a fairly insignificant result, but it is interesting that  $s_x$  decreases more quickly with accumulating exposure when the electron lifetime in the *n*-layer is lower. The CCE decreases at a greater rate when the electron lifetime is lower and this is mostly due to the fact that the increased

concentration of electron traps in the  $n$ -layer reduces the trap filling effect. The CCE is actually  $\sim 1\%$  lower after 0.36 R of exposure in the case of low electron lifetime, but the magnitude of this difference is lessened in  $s_x$  due to a PGR which increases slightly faster with cumulative exposure. The cause of this can be seen in Fig. 6.12, where the electric field increases next to the positive contact, with respect to the lower trapping situation, due to an increased trapped electron concentration in the  $n$ -layer. Since a large amount of photogeneration will occur in the  $n$ -layer, this sharp increase in field will have a strong positive effect on the PGR.

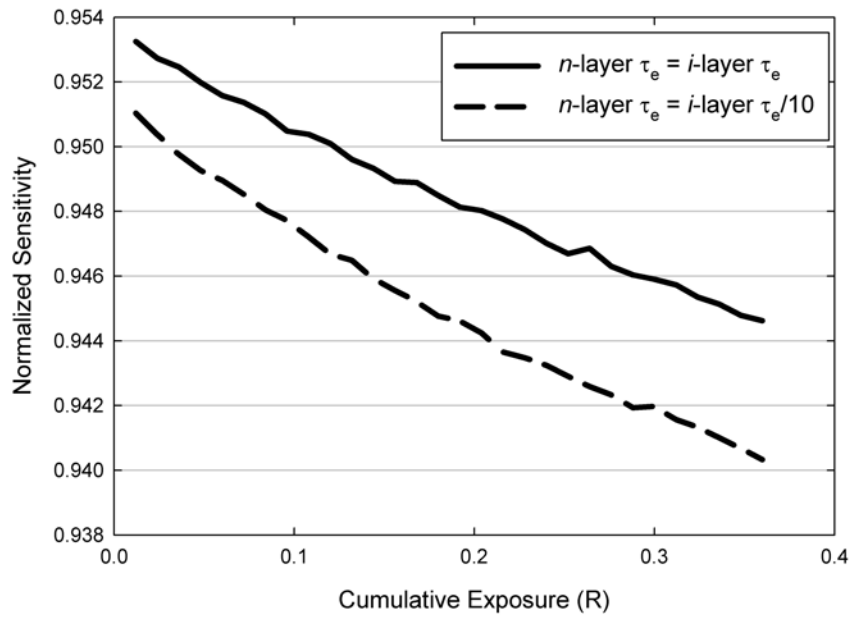


**Figure 6.11 Comparison of normalized sensitivity vs. cumulative exposure for two  $n$ - $i$ - $p$  structures with different electron lifetimes in the  $n$ -layer.  $s_x$  is reduced by only 0.4% after 0.36 R of exposure when the electron lifetime in the  $n$ -layer is decreased by one order of magnitude.**

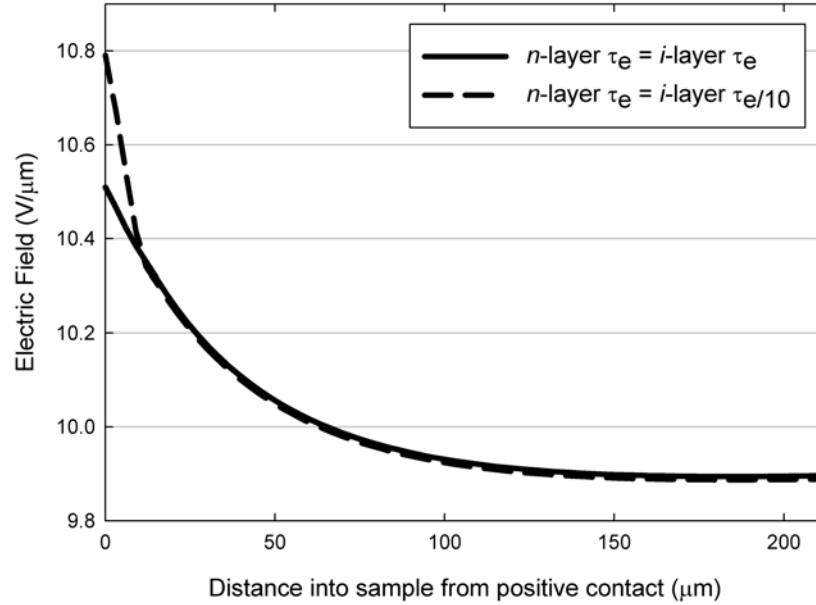


**Figure 6.12** The electric field distribution after 0.36 R for an *n-i-p* structure. When the electron lifetime in the *n*-layer is decreased by an order of magnitude, the increased trapped electron concentration near the positive contact causes a sharp increase in the electric field.

### 6.3.3 Results for Negatively Biased Structures

Though practical mammographic detectors are typically biased positively, it is interesting to see how the multilayer model performs when the structure is negatively biased, as shown in Fig. 6.13. The effects of cumulative x-ray exposure on  $s_x$  are quite different in this case and both the case of a single *i*-layer structure and a three layer, *p-i-n* structure will be considered. It should be noted that the terminology of using *p-i-n* in place of *n-i-p* simply refers to the fact that the *p*-layer is now next to the radiation receiving electrode as shown in Fig. 6.13.

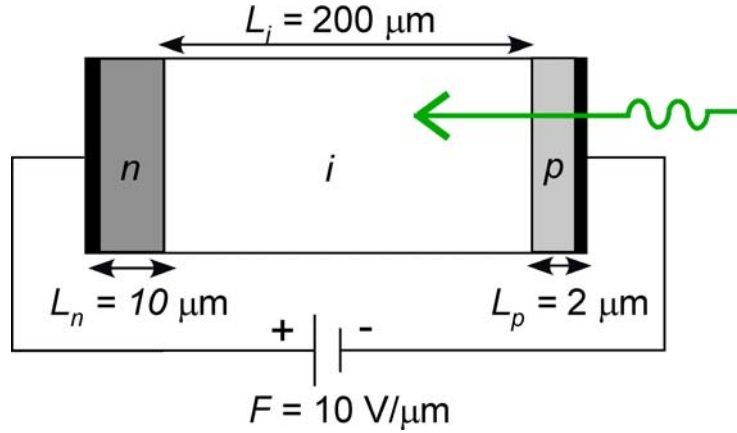


**Figure 6.13** Example of a negatively biased *p-i-n* sample used in sensitivity simulations. Single *i*-layer simulations use the same set up, without the *p*- and *n*-like blocking layers.

### 6.3.3.1 Results for *i*-layer Structures

Initial negative bias simulations were carried out considering a single *i*-layer. Figure 6.14 shows a comparison of simulated PGR, CCE and  $s_x$  for a single layer sample, both positively and negatively biased. In the case of the negatively biased sample, the normalized sensitivity decreases slightly faster with accumulating exposure than in the case of the positively biased sample and is  $\sim 9\%$  lower after 0.36 R of exposure. The different rate of decrease is due to the fact that the CCE is now relatively constant throughout the simulation while the PGR decreases with exposure instead of increasing. With a negative bias, the majority of photogeneration will now take place near the negative electrode. This means that now electrons, instead of holes, will need to drift across the sample to be collected. As electrons have the lower schubweg, there will be much more electron trapping throughout the sample, as shown in Fig. 6.15, and much less hole trapping than in the positive bias case. The greater proportion of trapped electrons will have a large effect on the electric field distribution driving the field very low near the negative contact where much of the photogeneration occurs, as seen in Fig. 6.16. The electric field becomes much more skewed across the sample than in the case of positive bias and hence  $W_{\pm}$  will increase in the region of strongest photogeneration in negative bias more than it would decrease in the region of strongest photogeneration in the case of positive bias. Hence, the PGR decreases more in negative bias than it increases in positive bias.

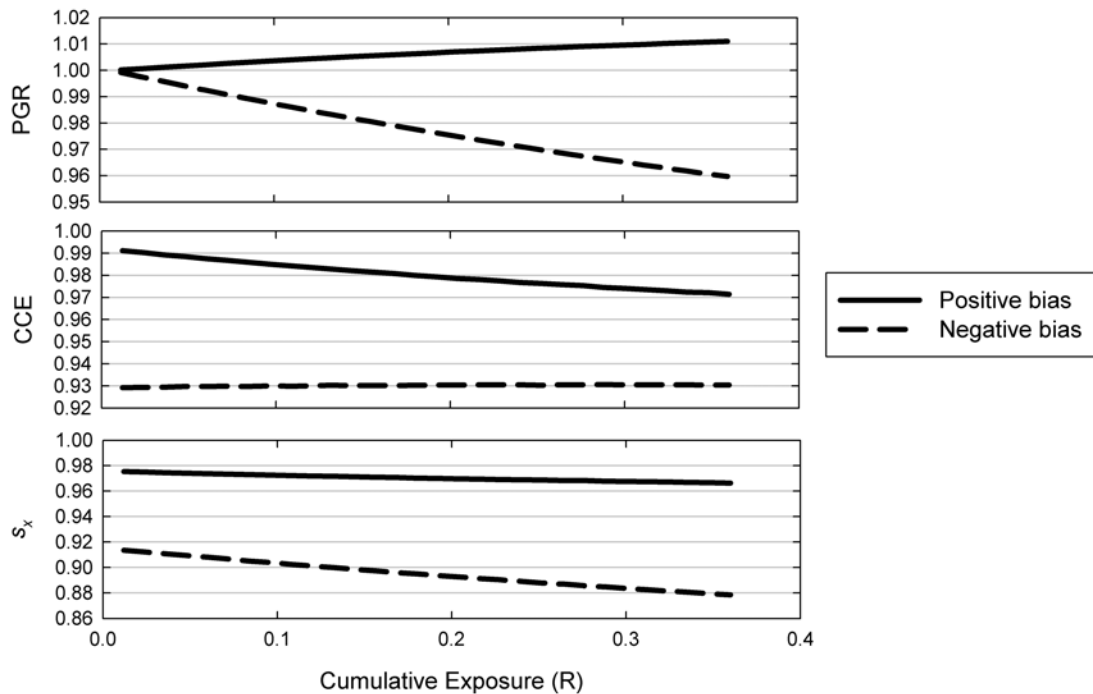


**Figure 6.14** A comparison of PGR, CCE and  $s_x$  vs. cumulative exposure for a single  $i$ -layer sample when biased either positively or negatively. The notation of bias refers to the polarity of the top, radiation receiving contact with respect to the substrate, *i.e.* negative bias refers to the case where the radiation receiving electrode is negative with respect to the substrate electrode as shown in Fig. 6.13. The normalized sensitivity of the positively biased sample is considerably higher and more consistent with exposure.

The middle graph in Fig. 6.14 shows that although the CCE starts much lower for the negative bias, it does not degrade with accumulated exposure. A lower overall CCE would be expected simply because electrons, which are less mobile than holes in a-Se, are now the carrier which, on average, must drift the farthest after photogeneration to be collected. While there is some trapping of holes throughout the sample, the level of trapped holes is very low ( $\sim 1 \times 10^8$  cm<sup>-3</sup> at the positive contact) and therefore there will be very little increase in recombination of drifting electrons with trapped holes as exposure is accumulated. If the effects of electron trap filling and new electron trap creation, due to irradiation, roughly cancel each other out, which appears to be the case, then the CCE would stay roughly consistent as exposure builds up.

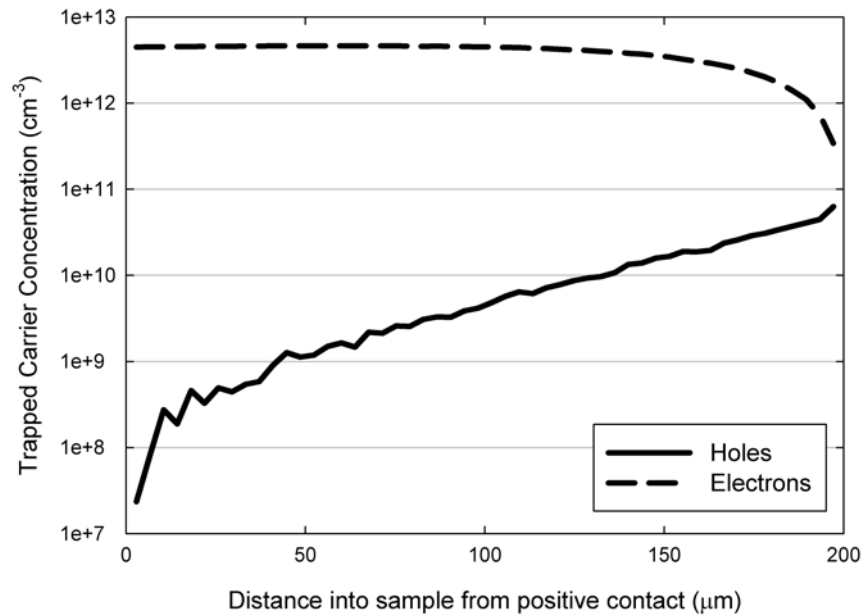


Figure 6.15 Trapped hole and electron concentrations across an *i*-layer sample biased negatively after 0.36 R of exposure. Trapped electron concentration increases away from the negative contact (right of graph), as most of the photogeneration will take place there and electrons will drift to the positive contact (left of graph). Holes will drift to the negative contact and few will be generated close to the positive contact leading to an increasing trapped hole concentration near the negative contact.

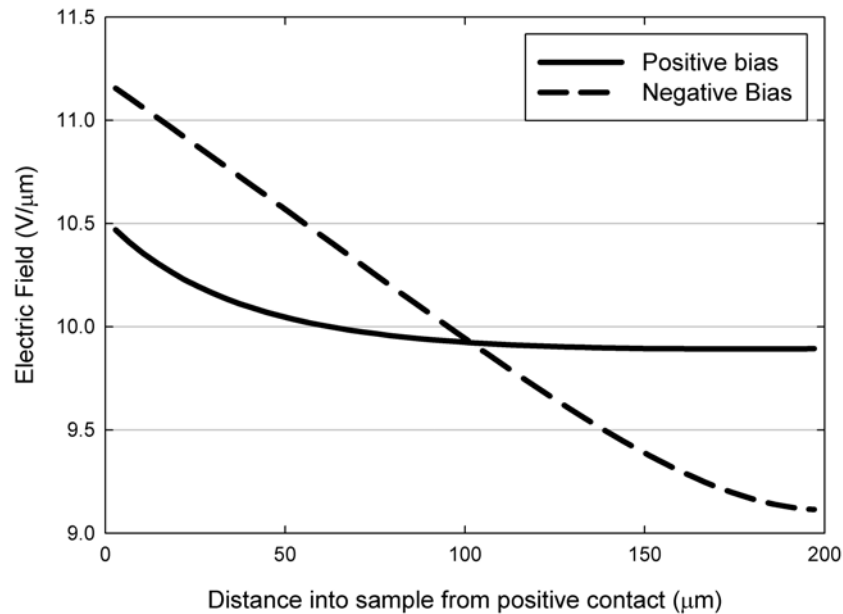
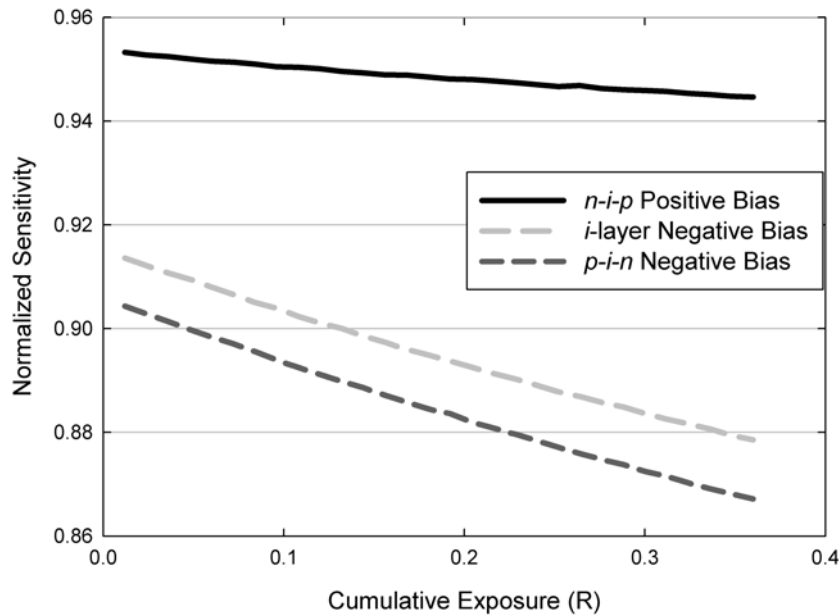


Figure 6.16 A comparison of the electric field distribution across an *i*-layer sample biased either positively or negatively after 0.36 R of exposure. In the case of positive bias, the electric field

increases near the positive contact (region of most photogeneration for positive bias), increasing the PGR. In the case of negative bias, the electric field decreases near the negative contact (region of most photogeneration for negative bias), decreasing the PGR.

### 6.3.3.2 Results for *p-i-n* Structures

A three layer, *p-i-n* structure shown in Fig. 6.13 was also modeled and the results compared to both an *n-i-p* sample and the negatively biased *i*-layer sample discussed in the previous sub-section. A comparison of the normalized sensitivity for these three situations is shown in Fig. 6.17. Much as in the case of the single layer comparison,  $s_x$  decreases more quickly with accumulating exposure for a negatively biased sample and is  $\sim 8\%$  lower than for the positively biased sample after 0.36 R of exposure. As discussed in Section 6.3.2, for the positively biased sample,  $s_x$  decreased by  $\sim 2\%$  when the blocking layers were added to the model and this decrease was due to a decrease in the CCE because of increased hole trapping immediately following photogeneration in the *n*-layer. This is also the case in the negatively biased sample, as the addition of the blocking layers results in a  $\sim 1.5\%$  decrease in  $s_x$  and this is also almost entirely due to a decrease in CCE. However, in this case it is due to the increased trapping of electrons immediately after photogeneration in the *p*-layer. The lesser decrease in the negatively biased case is expected as the *p*-layer considered is thinner than the *n*-layer considered. It should be noted that the *n*-layer electron lifetime used in this simulation is the same as the *i*-layer electron lifetime. Decreasing the electron lifetime in the *n*-layer, as done in Section 6.3.2.2.4, would likely decrease the CCE slightly due to greater electron trapping in the *n*-layer as the electrons drift through it, but since the effect noticed in Section 6.3.2.2.4 was so small (0.4%), this was not done here.



**Figure 6.17** A comparison of normalized sensitivity vs. cumulative exposure between a negatively biased, single layer sample, a negatively biased, three layer sample and a positively biased, three layer sample. Regardless of structure, the positively biased sample has a higher normalized sensitivity which is more consistent with cumulative exposure when compared with the negatively biased samples.

### 6.3.4 Effects of Dark Current

#### 6.3.4.1 Effects of a Non-uniform Initial Electric Field Distribution

When considering the operation of a practical FPXI, it is obvious that the electric field must be applied across the photoconductive layer some finite amount of time before the detector can be exposed to radiation. Therefore, during this time, the dark current which flows due to the application of the bias will accumulate trapped charge carriers in the photoconductive layer, altering the initially uniform electric field distribution. In the case of a single *i*-layer sample, the amount of trapped charge will be relatively small. Further, both injected holes and electrons will be trapped throughout the sample, reducing the resultant net space charge and the effect on the field distribution. For this reason, the model will only consider the effect of the non-uniform initial field on a three layer, *n-i-p* sample where the initial rush of dark current will result in a large amount of holes being trapped in the *n*-layer and electrons in the *p*-layer, altering the field distribution as shown in Fig. 6.18.

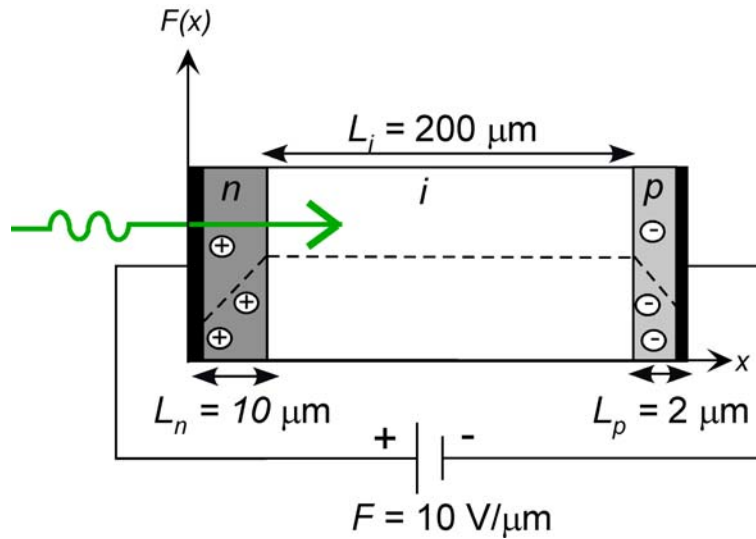


**Figure 6.18** Example of a positively biased, *n-i-p* sample with a non-uniform initial electric field distribution used in the simulation. The field (shown as a dashed line) at both the positive and negative contacts is reduced by the trapping of holes in the *n*-layer and electrons in the *p*-layer due to the initial rush of dark current after the bias is applied.

To model this initially non-uniform field, the simulation was initialized with a large concentration of holes trapped in the *n*-layer ( $3.4 \times 10^{14} \text{ cm}^{-3}$ ) and a large concentration of electrons trapped in the *p*-layer ( $1.17 \times 10^{15} \text{ cm}^{-3}$ ). These values were determined by simulating the dark current in the sample shown in Fig. 6.18 for 1000 s using the methods described in Section 5.3.3. For this simulation, only one deep hole trap state was assumed in the *n*-layer (at a depth of 0.78 eV above  $E_v$ ) and its concentration was the same as that used in the sensitivity simulations,  $2.6 \times 10^{15} \text{ cm}^{-3}$ . The deep electron trap state was assumed to have the same concentration as in the sensitivity simulations,  $1.3 \times 10^{15} \text{ cm}^{-3}$ , with release from these traps taking an infinitely long time.

Figure 6.19 compares the PGR, CCE and  $s_x$  for an *n-i-p* sample simulation with the non-uniform initial field distribution shown in Fig. 6.18 to the results obtained when a uniform initial field is assumed. It can be seen that the normalized sensitivity in the case of the non-uniform initial field starts about 6% lower but then quickly increases and within a few exposures follows the decreasing trend of the simulation which considered a uniform initial field. The main reason for this initially lower  $s_x$  is a lower value of PGR due to the initially lower field, and hence higher  $W_{\pm}$ , near the positive contact, where the majority of photogeneration takes place. The CCE also

starts slightly lower in the non-uniform initial field simulation due to the recombination of photogenerated electrons with trapped holes in the  $n$ -layer and the recombination of photogenerated holes with trapped electrons in the  $p$ -layer as they drift through on their way to collection. As the x-ray exposure accumulates, photogenerated charges quickly recombine with the trapped carriers in the blocking layers and the trapped charge profile soon becomes identical to that in the uniform initial field simulation. Clearly the amount of charge built up in the blocking layers during the initial rush of dark current is small when compared with the amount of charge cumulatively photogenerated during several x-ray exposures.

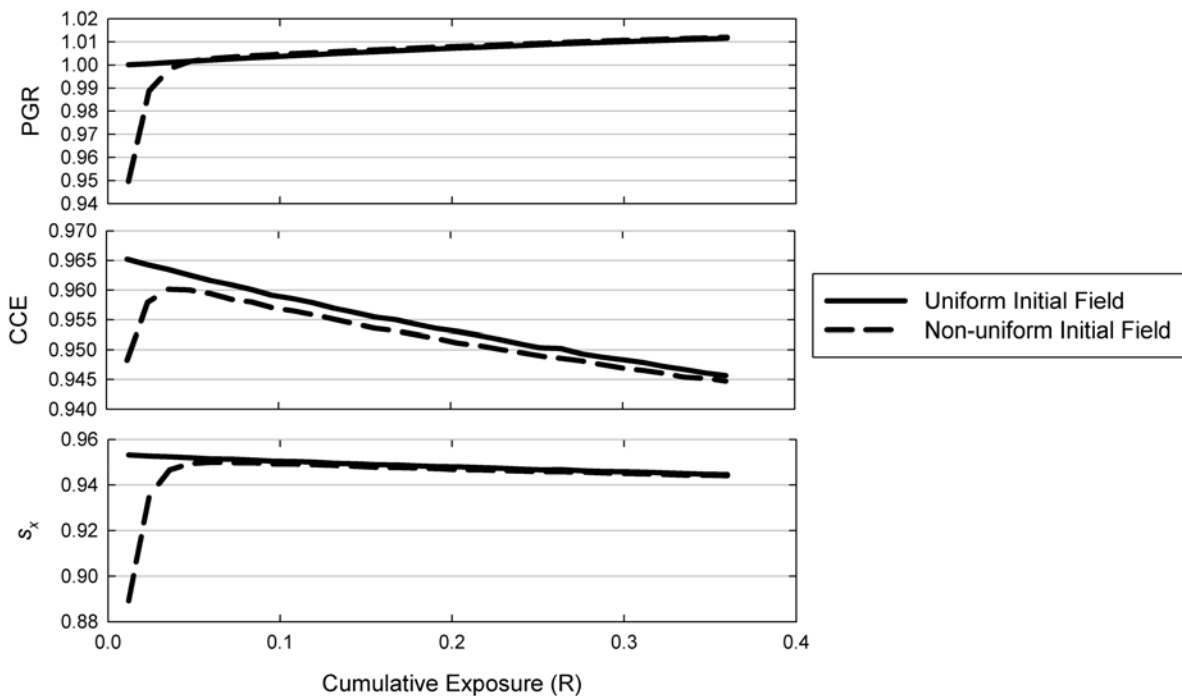


**Figure 6.19** PGR, CCE and  $s_x$  vs. cumulative exposure for an  $n$ - $i$ - $p$  structure resulting from both a simulation which considers a non-uniform initial electric field distribution due to dark current and one which does not (assumes an initially uniform electric field distribution). The initial reduction in sensitivity due to the trapped holes in the  $n$ -layer and trapped electrons in the  $p$ -layer is quickly neutralized by recombination with drifting photogenerated carriers.

It should be noted that any change in sensitivity of an FPXI, not just a decrease, can lead to ghosting. Certain FPXIs have presented results which indicate “positive ghosting”, where the ghosting was attributed to an increase in sensitivity [248], as seen initially in the results in Fig. 6.19.

### 6.3.4.2 Effects of Dark Current Flowing Between X-ray Exposures

Obviously, the dark current will not only be flowing before the first x-ray exposure, but in between exposures and during the exposures themselves. The effect of the dark current will be small during the exposures as the photogenerated current will be much larger and the time of the exposures is very short (200 ms). However, the effect of the dark current flowing during the 2 minutes between exposures could reduce the sensitivity, as it did initially in the previous sub-section. Unfortunately, as discussed in Chapter 5, modeling this in a pure Monte Carlo simulation would take an unreasonably long time. An attempt to include this effect has been made by resetting the trapped hole concentration in the  $n$ -layer and the trapped electron concentration in the  $p$ -layer to that produced by a numerical simulation of 120 s of dark current using the methods described in Section 5.3.3, before each exposure (including the first). This is a crude approximation, as the values determined by the dark current simulation are for 120 s of dark current flow, starting with a uniform field. This would not be the case, as the field distribution across the sample would be altered by each exposure. Furthermore, this approach does not take the x-ray induced deep trap states in the blocking layers into account when calculating the dark current. However, the results produced by this approximation are reasonable and they are presented in Fig. 6.20. The values predicted by the dark current simulation included concentrations of  $3.4 \times 10^{14} \text{ cm}^{-3}$  for trapped holes in the  $n$ -layer and  $4.6 \times 10^{14} \text{ cm}^{-3}$  for trapped electrons in the  $p$ -layer. Trapped hole concentrations in the  $i$ - and  $p$ -layer are reduced before each exposure due to release, as before.

The increase in PGR and decrease in CCE and  $s_x$  with cumulative exposure is similar to that for the case where the effects of dark current are ignored, however the overall levels of each are reduced. The  $s_x$  is reduced by roughly 6% over the simulation due to a decrease in CCE and an even larger decrease in the PGR, as discussed in the previous sub-section. Figure 6.21 shows that due to the trapping of holes injected into the  $n$ -layer by the flow of dark current between exposures, the electric field is not allowed to increase near the positive contact, as is observed when the dark current effects are ignored. However, the field throughout most of the rest of the sample (except for in the  $p$ -layer) is slightly higher, leading to a PGR which increases slightly more with cumulative exposure than when the dark current effects are ignored. As a result,

though the sensitivity is lower when the effect of the dark current is considered, the decrease in sensitivity with cumulative exposure is slightly less, as seen in Fig. 6.20.

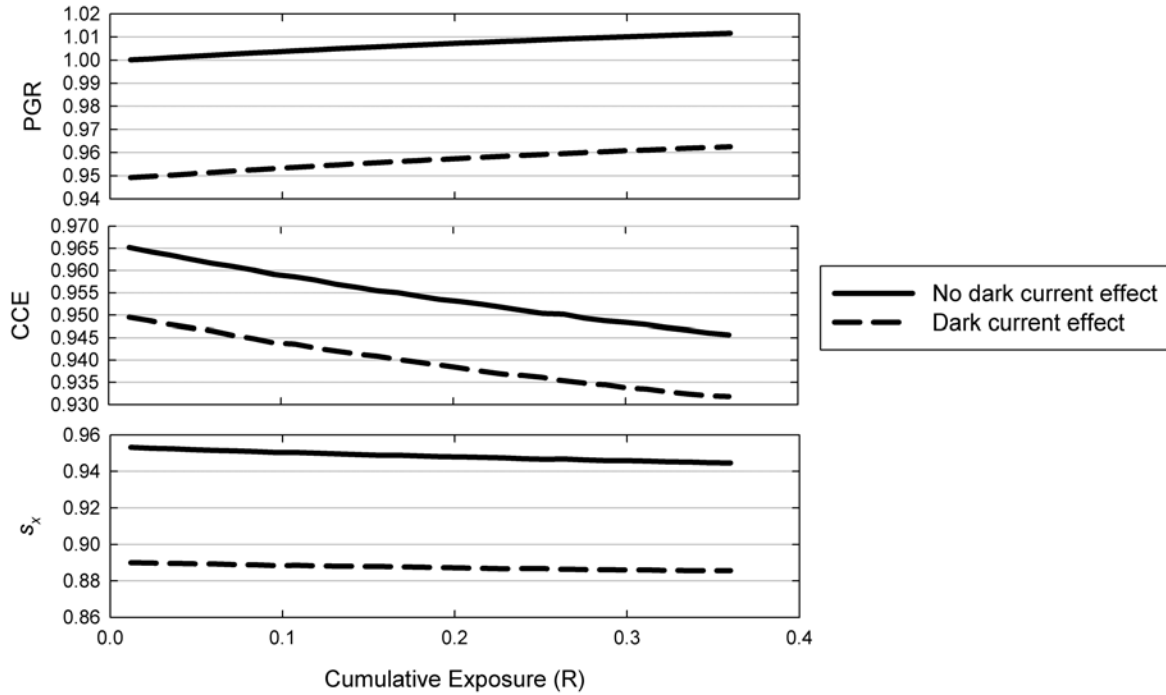


**Figure 6.20** PGR, CCE and  $s_x$  vs. cumulative exposure for an  $n-i-p$  structure resulting from simulations which assume no dark current (solid lines) and trapped holes in the  $n$ -layer and trapped electrons in the  $p$ -layer before each exposure as a result of the flow of dark current (dashed lines). The effect of the dark current flowing between each exposure is an overall reduction in the normalized sensitivity.

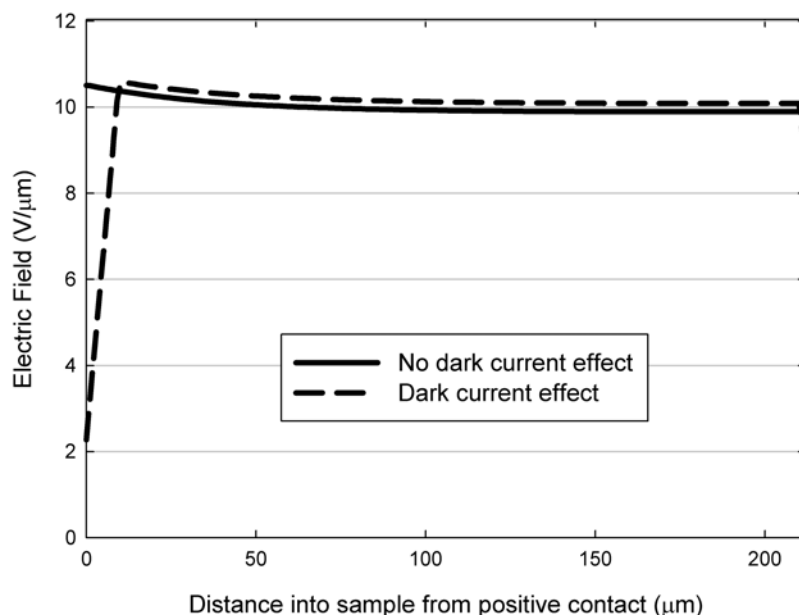


**Figure 6.21 Comparison of the electric field distribution across an *n-i-p* sample after 0.36 R of exposure simulated both with and without the effect of dark current flowing between exposures. The field is greatly reduced at the contacts when the dark current effects are considered due to trapped holes in the *n*-layer and trapped electrons in the *p*-layer.**

In order to improve the approximation to the effect of the dark current on the x-ray sensitivity, the trapped carrier concentrations in the blocking layers after one exposure in the above simulation were used as the initial conditions for a dark current calculation. 120 s of dark current data were simulated as before, but now with trapped electrons and holes in both blocking layers initially. The carriers injected during the dark current simulation could now be trapped or recombine with a trapped carrier of opposite charge in the blocking layer into which they were injected. This was modeled as a Langevin governed process as described by Eq. 6.2. As the trapped hole concentration in the *p*-layer and the trapped electron concentration in the *n*-layer were relatively low, there was almost no change in trapped hole concentration in the *n*-layer or trapped electron concentration in the *p*-layer when compared against the previous dark current calculation which assumed an initially uniform field. However, the trapped hole concentration in the *p*-layer was reduced by about 10% due to recombination with injected electrons and the trapped electron concentration in the *n*-layer was reduced by about 90% due to recombination with injected holes. As a result, the x-ray sensitivity simulation was modified so that not only were the trapped hole concentration in the *n*-layer and the trapped electron concentration in the *p*-

layer reset before each exposure, but the trapped hole concentration in the  $p$ -layer was reduced by 10% and the trapped electron concentration in the  $n$ -layer was reduced by 90% before each exposure. The results, compared against the previous simulation, which neglected this recombination effect can be seen in Fig. 6.22. There is very little difference, save for the fact that the PGR increases slightly more slowly, as 90% of the electrons trapped in the  $n$ -layer are removed between exposures due to recombination with holes injected by the dark current. This creates a more positive space charge in the  $n$ -layer, leading to a greater reduction in field at the positive, radiation receiving electrode, and hence a slightly lower PGR.

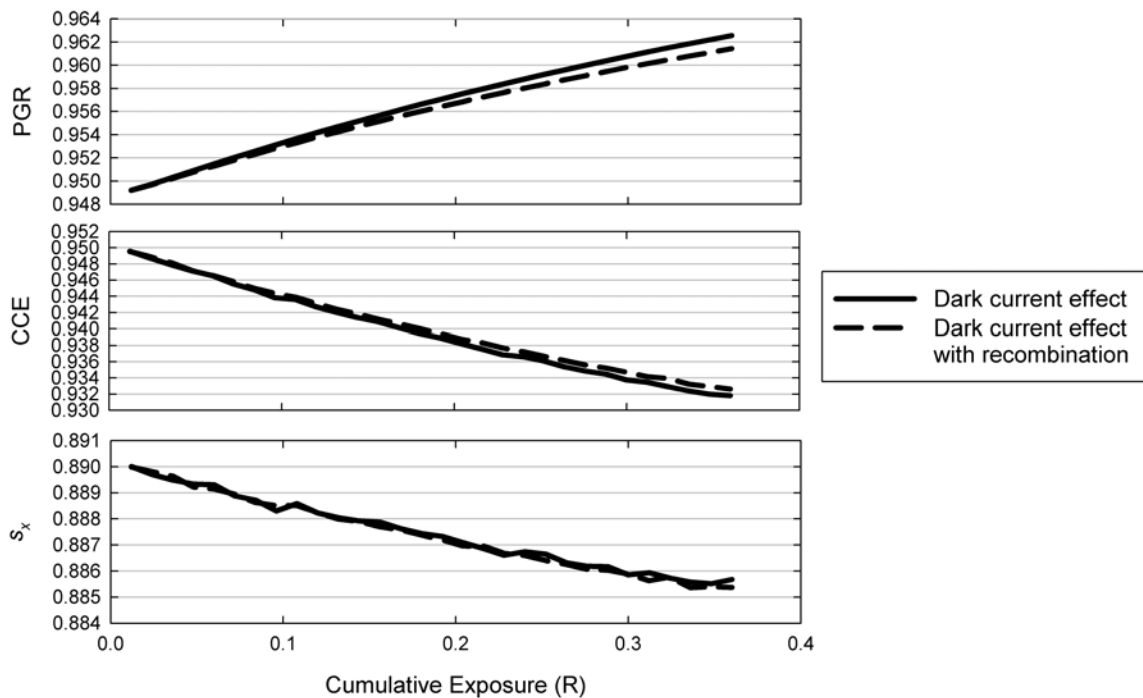


**Figure 6.22** PGR, CCE and  $s_x$  vs. cumulative exposure for an  $n$ - $i$ - $p$  structure resulting from a simulation which assumes trapped holes in the  $n$ -layer and trapped electrons in the  $p$ -layer before each exposure as a result of the flow of dark current (solid lines) and a simulation which also assumes recombination of injected carriers with oppositely charged carriers trapped in the blocking layers (dashed lines). The inclusion of the recombination effect makes very little difference.

## 6.4 Matching Experimental Results

In order to test the multilayer x-ray sensitivity model, a series of x-ray sensitivity experiments were carried out in industrial laboratories, the results of which would be used to

calibrate the model presented thus far. Experimental results gathered from a  $\sim 1$  mm thick *p-i-n* sample, negatively biased at different fields were chosen for matching.

#### 6.4.1 Experimental Procedure

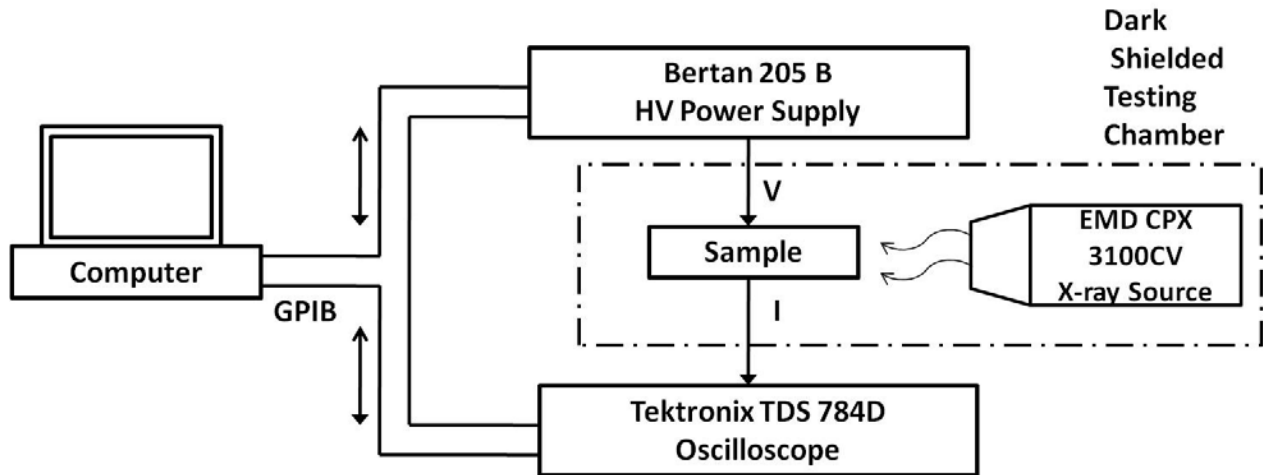


**Figure 6.23** Schematic diagram of the x-ray sensitivity data acquisition system. The 80 kVp X-ray source provided a spectrum with a mean beam energy of 54.5 keV and had an intrinsic filtration of 23.5 mm Al.

X-ray sensitivity experiments were carried out to determine the level of sensitivity reduction that would occur for a controlled series of exposures followed by a sensitivity recovery period. The system used to measure the x-ray sensitivity consisted of a high voltage power supply capable of providing voltages above 10 kV, allowing for fields of  $10 \text{ V}/\mu\text{m}$  on even 1000  $\mu\text{m}$  thick samples. Current values were captured using an oscilloscope connected to a computer and integrated using data acquisition software, as shown in Fig. 6.23. The x-rays used in all experiments had an average energy of 54.5 keV and were from an 80 kVp source with 23.5 mm Al filtration. Figure 6.24 shows the exposure sequence used in the experiments. Very low level “read” doses were given in order to determine the sample’s sensitivity without creating enough EHPs to alter it. These doses were only  $85 \mu\text{R}$  and only 20 ms in duration. These doses were given twenty seconds before a “ghost” dose of 31 mR and 200 ms duration. These “ghost” doses caused decreases in sensitivity. The “ghost” doses were given at 2 minute intervals. A series of 30 ghost doses were given followed by a 3 hour recovery period of just “read” doses every 2 minutes.

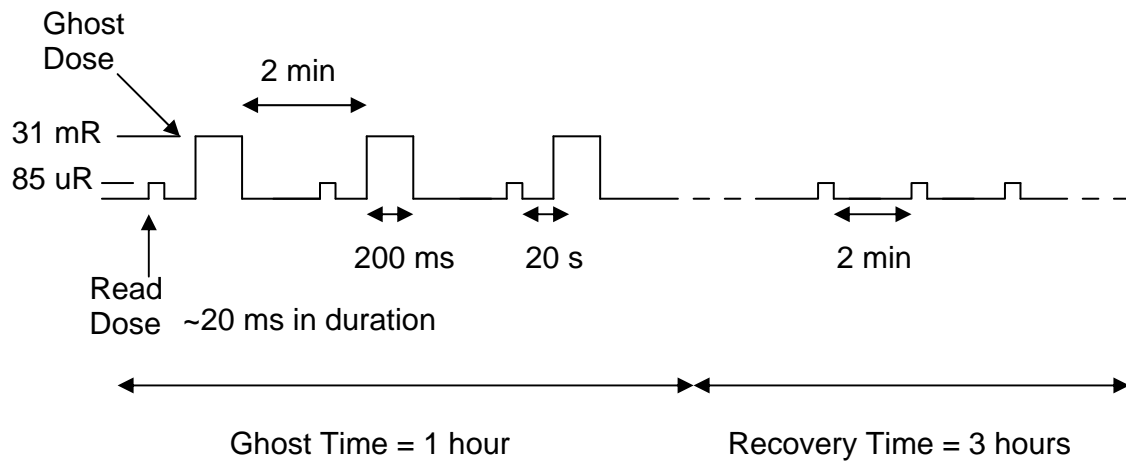


**Figure 6.24 X-ray sensitivity experimental sequencing.** The 200 ms ghost doses will create enough charge within the sample to cause ghosting through a decrease in the x-ray sensitivity. The 20 ms read doses will be small enough to allow for a measurement of the sensitivity without affecting it. Therefore, once the ghosting period ends, only read doses will be administered and sensitivity recovery should be observed.

The sample used was sample 553-5, a *p-i-n* structure from sample set E, and is shown schematically in Fig. 6.25. The *n*-layer is 20  $\mu\text{m}$  thick and is made of alkali-doped, stabilized a-Se, while the *p*-layer is made of a-As<sub>2</sub>Se<sub>3</sub> and is 5  $\mu\text{m}$  thick. The *i*-layer is roughly 1 mm thick and is made of a non-chlorinated alloy with hole and electron schubwegs of 5.9 mm and 4.8 mm, respectively. This is a sample more typical of the photoconductive layer used in general radiography FPXIs. The bottom, positive contact was ITO coated glass and the top, negative contact was Cr. Both had a surface area of 21 cm<sup>2</sup>.

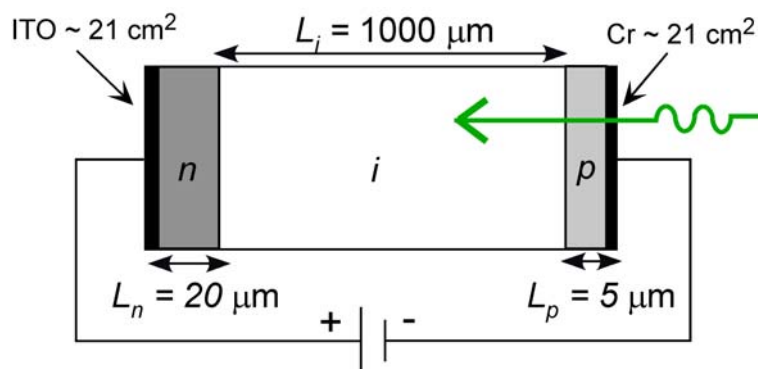


**Figure 6.25 *p-i-n* sample used in x-ray sensitivity experiments.**

## 6.4.2 Simulation Parameters

The layer thicknesses were set to match those of the sample and material properties of the  $i$ -layer were chosen to match the sample, given the measured schubwegs, by assuming  $0.12 \text{ cm}^2 \text{ V}^{-1} \text{ s}^{-1}$  for hole mobility and  $0.0035 \text{ cm}^2 \text{ V}^{-1} \text{ s}^{-1}$  for electron mobility. Trial and error fitting found that at  $10 \text{ V}/\mu\text{m}$ ,  $f_{recomb} = 1$ , but at  $5 \text{ V}/\mu\text{m}$ ,  $f_{recomb} = 0.8$  and at  $3 \text{ V}/\mu\text{m}$ ,  $f_{recomb} = 0.5$ , similar to the results reported by Yunus [2]. The other important material property values used in the simulation are summarized in Table 6.3. The mean photon energy of the radiation was taken as 54 keV and was modeled as a monoenergetic beam of 54 keV where the linear attenuation coefficient of a-Se is  $129 \text{ cm}^{-1}$  and the linear absorption coefficient is  $104 \text{ cm}^{-1}$  [66]. During the ghosting phase, 200 ms doses of 31 mR every two minutes were simulated. During the recovery phase, 20 ms doses of 81  $\mu\text{R}$  every two minutes were simulated. The simulations included the approximate effect of the dark current before and between exposures as described in Section 6.3.4.2.

**Table 6.3 Material properties assumed for the simulations done to match x-ray sensitivity experimental results. A double subscript of  $n$  refers to properties in the  $n$ -like layer, while a double subscript of  $p$  refers to properties in the  $p$ -like layer and a double subscript of  $i$  refers to properties in the  $i$ -layer.**

Property	Assumed Value	Property	Assumed Value
$\mu_h$	$0.12 \text{ cm}^2 \text{ V}^{-1} \text{ s}^{-1}$	$\mu_e$	$0.0035 \text{ cm}^2 \text{ V}^{-1} \text{ s}^{-1}$
$N_{th_p}$	$5.8 \times 10^{11} \text{ cm}^{-3}$	$N_{te_p}$	$2.4 \times 10^{14} \text{ cm}^{-3}$
$N_{th_i}$	$5.8 \times 10^{11} \text{ cm}^{-3}$	$N_{te_i}$	$2.4 \times 10^{11} \text{ cm}^{-3}$
$N_{th_n}$	$5.8 \times 10^{14} \text{ cm}^{-3}$	$N_{te_n}$	$2.4 \times 10^{12} \text{ cm}^{-3}$
$N_{x_{0h}}$	$9 \times 10^{11} \text{ cm}^{-3}$	$N_{x_{0e}}$	$9 \times 10^{11} \text{ cm}^{-3}$
$\tau_{rh}$	100 s	$\tau_{re}$	$\infty$
$\tau_{0h_p}$	49.2 $\mu\text{s}$	$\tau_{0e_p}$	1.37 $\mu\text{s}$
$\tau_{0h_i}$	49.2 $\mu\text{s}$	$\tau_{0e_i}$	1370 $\mu\text{s}$
$\tau_{0e_n}$	137 $\mu\text{s}$	$\tau_{0e_n}$	137 $\mu\text{s}$

### 6.4.3 Results

Obviously, these simulations give results in terms of normalized sensitivity, while the experimental results will be absolute sensitivity in SI units of  $C\ m^{-2}\ R^{-1}$ . To allow a comparison, the normalized sensitivity,  $s_x$ , must be converted to an absolute sensitivity value,  $S_x$ , through the relation  $S_x = s_x S_0$ , where  $S_0$ , as stated in Eq. 2.10, is given by

$$S_0 = \left( \frac{5.45 \times 10^{13} e}{(\alpha_{en} / \rho)_{air} W_{\pm}} \right) \times \left( \frac{\alpha_{en}}{\alpha} \right) \quad (6.23)$$

At a mean photon energy of 54 keV,  $\alpha_{en}/\alpha$  for a-Se is 0.81 and the mass absorption coefficient for air is  $0.0347\ cm^2\ g^{-1}$  [66].  $W_{\pm}$  is calculated using Eq. 6.15 with  $E_{ph} = 54\ keV$ . To achieve a close match, at 3 and 5 V/ $\mu m$  the field dependence of  $W_{\pm}$  is taken as  $F^{-0.8}$ , as shown in Eq. 6.17, but at 10 V/ $\mu m$  it was taken as  $F^{-0.795}$ . This yields values for  $W_{\pm}$  of 45, 68 and 100 eV at applied fields of 10, 5 and 3 V/ $\mu m$ , respectively. Calculating  $S_0$  at each field and  $S_x$  for each simulated point yields the results shown in Fig. 6.26. Here  $S_x$  is given as a function of time instead of accumulated exposure. A good match is achieved between the simulated results and the results of the experiment during the ghosting phase of the experiment. It can be seen that a higher applied field greatly increases sensitivity. This is due to the much greater schubwegs of photogenerated carriers, which will lead to less trapping and a higher CCE. The experimentally measured sensitivity increases roughly linearly with the applied field. There is also a lower percentage reduction in sensitivity at higher fields (approximately 18% at 3 V/ $\mu m$ , 10% at 5 V/ $\mu m$  and 4% at 10 V/ $\mu m$ ).

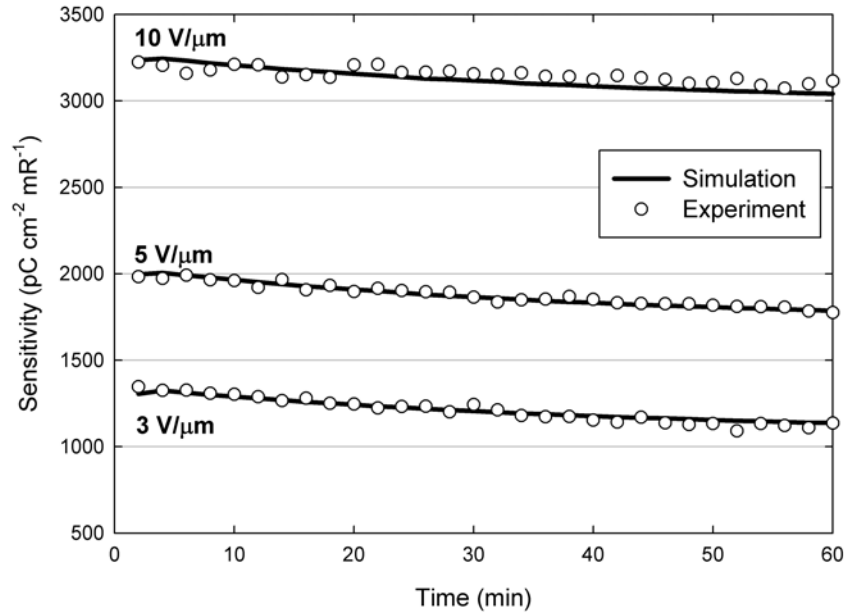


**Figure 6.26** A comparison of experimentally measured and simulated values of x-ray sensitivity vs. time, during the ghosting phase, for three different applied electric fields with the sample described in Fig. 6.25 with the simulation parameters listed in Table 6.3.

Figure 6.27 shows a closer look at the results at 5 V/μm. The simulation result from Fig. 6.26 is shown where  $f_{recomb} = 0.8$ , as well as simulations where  $f_{recomb} = 0.9$  and 1. Decreasing  $f_{recomb}$  results in less recombination of photogenerated carriers with oppositely charged trapped carriers, increasing the CCE and overall sensitivity. A value of 0.8 gives the best result. As found by Yunus [2], the value of  $f_{recomb}$  needed to match the experimental results decreases with the applied field. At 3 V/μm, the optimum value for  $f_{recomb}$  was found to be 0.5.

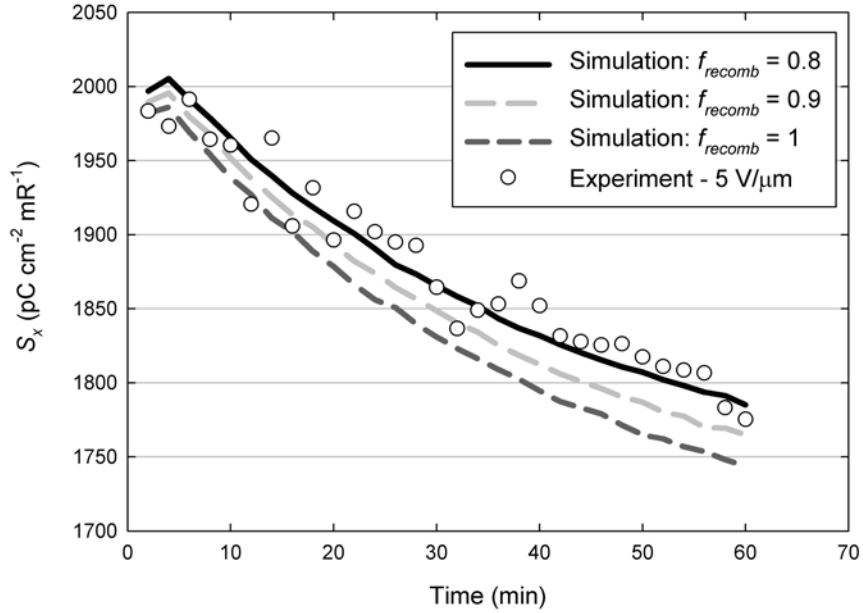


**Figure 6.27** A comparison of experimentally measured and simulated values of x-ray sensitivity vs. time, during the ghosting phase, at an applied field of 5 V/ $\mu\text{m}$ , for 3 different values of  $f_{recomb}$ . A value of 0.8 gives the best result.

Figure 6.28 shows both the ghosting and recovery phases at 5 V/ $\mu\text{m}$ . In the experimental results, the beginning of a sensitivity recovery is observed after 60 minutes when the ghost doses are no longer applied. However, this is not the case for the simulations described above, as very little recovery is observed. In the simulations, the only thing that is changing during the recovery period is that holes which were trapped during the ghosting phase are being released and the trapped carrier concentrations in the blocking layers are constantly being reset due to the dark current effect. The small read doses which are simulated have little effect. However, Fig. 6.28 also shows that strong sensitivity recovery is observed if the relaxation of the metastable traps created by x-ray exposure is considered. It has been shown that the electronic properties of a-Se, such as carrier lifetime, relax with time following a stretched exponential of the form [249]

$$\tau = \tau_{\infty} + (\tau_0 - \tau_{\infty}) \exp \left[ - \left( \frac{t}{\tau_{sr}} \right)^{\beta} \right] \quad (6.24)$$

where  $\tau_\infty$  is the fully relaxed lifetime,  $\tau_0$  is the initial lifetime,  $\tau_{sr}$  is the structural relaxation time constant and  $\beta$  is the stretching factor. The relaxation rates are similar for both hole and electron properties with  $\tau_{sr}$  ranging from  $\sim 15$  to 22 hours and a  $\beta$  of 0.6 – 0.7. The relaxation of the metastable x-ray induced trap centers during recovery is modeled in this way, such that for each simulated point during the recovery period, the concentration of both x-ray generated hole and electron traps is reduced as

$$N_{x_i} = N_{x_i} \exp \left[ - \left( \frac{t}{\tau_{sr}} \right)^\beta \right] \quad (6.25)$$

where  $t$  is the time since the beginning of the recovery period and  $\beta$  and  $\tau_{sr}$  are taken as 0.5 and 10 hours respectively.

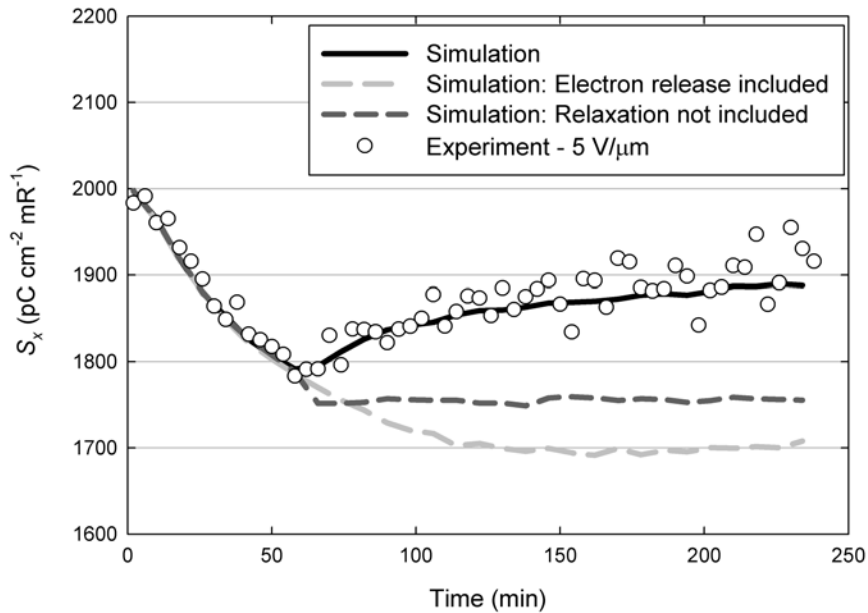


**Figure 6.28** A comparison of experimentally measured and simulated values of x-ray sensitivity vs. time, during both the ghosting and recovery phases, at an applied field of 5 V/ $\mu\text{m}$ . Simulated results are shown with and without relaxation of metastable deep traps and with and without electron release with  $\tau_{re} = 1$  hour. Significant recovery is observed only if the relaxation effect is considered and electron release is ignored.

There is little recovery observed if the relaxation of the metastable deep traps is not considered in the model. The effect of trapped hole release and the dark current cause very little

recovery. Numerical calculations of x-ray sensitivity recovery done by Manouchehri *et al.* [82] showed that the effect of the dark current on recovery was more substantial, but due to the numerical nature of both their dark current and sensitivity calculations, they were able to include a more realistic approximation to the effect of the dark current than in the work completed here. It should also be noted that they assumed a metastable deep trap relaxation that was purely exponential in nature while the experiments by Allen *et al.* [249] clearly showed that the relaxation of the properties of a-Se follow a stretched exponential as described in Eq. 6.24. The values assumed for  $\beta$  and  $\tau_{sr}$  in the work presented here were both slightly lower than those calculated by Allen (0.5 and 10 hours assumed here, compared to ranges of 0.6 – 0.7 and 15 to 22 hours). Again, the need for these lower values could stem from the crudeness of the approximation to the effect of the dark current used.

Figure 6.28 also shows the simulated result if the release of electrons is considered throughout the simulation, with a release time,  $\tau_{re}$ , of 1 hour. This is a rather low value for the release time, corresponding to a trap depth of  $\sim 0.92$  eV from the conduction band edge. The inclusion of electron release actually prevents any recovery. During the recovery phase, the release of trapped holes and electrons, along with the relaxation of metastable traps, gradually returns the field distribution to what it was originally, restoring the decayed PGR, as shown in Fig. 6.29. However, the newly empty electron traps can now trap photogenerated electrons, greatly decreasing the CCE and also the overall sensitivity. If electron release is ignored, the recovery is due to the improvement in the CCE with the release of trapped holes and relaxation of metastable trap states, while the PGR actually decreases as the space charge in the sample becomes increasingly negative (holes are released and electrons are not), driving the field lower near the negative contact, increasing  $W_{\pm}$  where much of the photogeneration takes place. This evolution of the field distribution across the sample can be seen in Fig. 6.30.

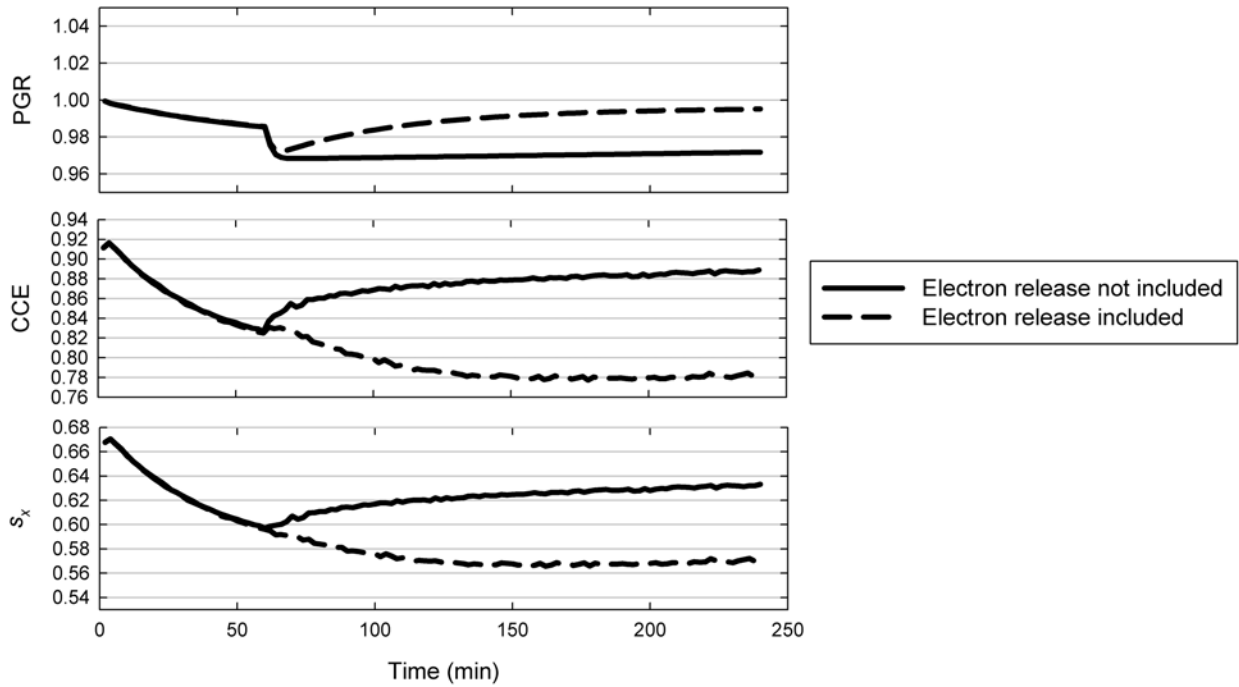


Figure 6.29 Simulated PGR, CCE and  $s_x$  vs. cumulative exposure ignoring the release of trapped electrons (solid lines) and including the release of trapped electrons with a release time of 1 hour (dashed lines). The inclusion of electron release causes recovery in the PGR but prevents recovery in the CCE.

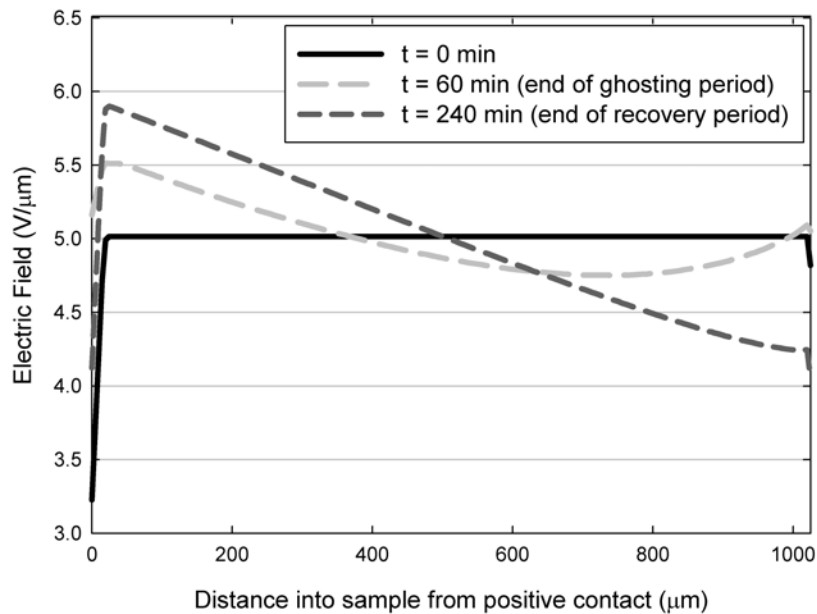
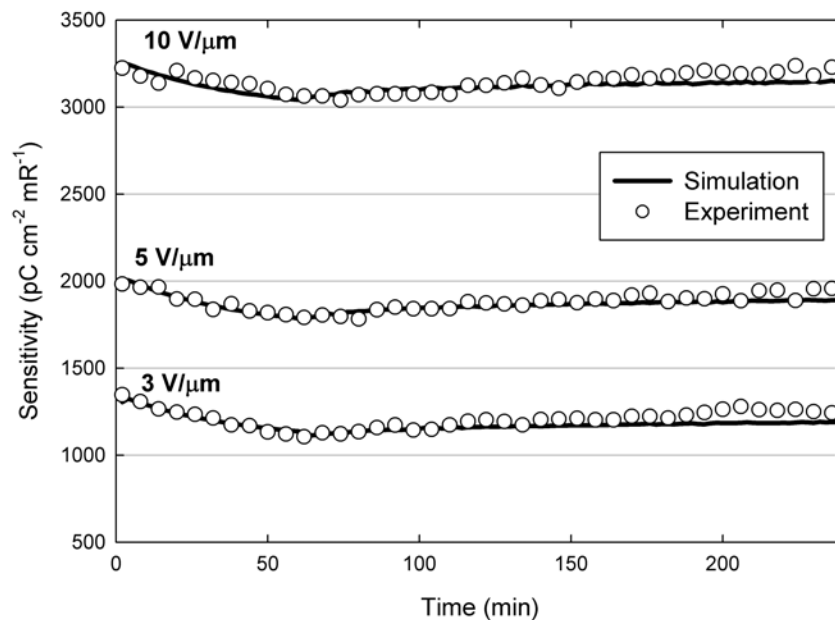


Figure 6.30 Simulated electric field distribution across the  $p$ - $i$ - $n$  sample initially, at the end of the ghosting period and at the end of the recovery period. The applied electric field was 5 V/ $\mu\text{m}$ .

Metastable deep trap relaxation was included in the simulation but electron release was not. As trapped holes are released, the space charge throughout the sample becomes increasingly negative, driving the field lower near the negative contact. This prevents substantial recovery of the PGR as shown in Fig. 6.29.

The numerical calculations performed by Manouchehri *et al.* [82] determined that a great deal of the sensitivity recovery was actually due to the release of trapped electrons. Once again, this discrepancy likely stems from their integrated simulation of the dark current between exposures. The realization of a time efficient, accurate and realistic manner of including the dark current effect in these Monte Carlo simulations would be a valuable future contribution, especially when simulating sensitivity recovery. Even so, the model presented here, without considering electron release, provides a very close match to the experimental results, both during the ghosting and recovery phases, as shown in Fig. 6.31.



**Figure 6.31** A comparison of experimentally measured and simulated values of x-ray sensitivity vs. time, during both the ghosting and recovery phases, for three different applied electric fields with the sample described in Fig. 6.25. Good agreement is achieved at all three fields, however the reasons behind the occurrence of the recovery in sensitivity differ from those found by Manouchehri *et al.* [82]. All simulation parameters are the same as those listed in Table 6.3. Equation 6.23 was used to model the relaxation of the metastable x-ray induced trap states with  $\beta = 0.5$  and  $\tau_{sr} = 10$  hours.

## 6.5 Conclusion

The Monte Carlo based modeling of x-ray sensitivity of a-Se, mammographic photoconductive layers presented in the chapter has shown good agreement with the results of the previous model [2], which this model was based on. It has shown that the x-ray sensitivity of the a-Se layer is slightly lower when the blocking layers are considered as compared to when a single *i*-layer is assumed. However, the rate of decrease in sensitivity with cumulative exposure is very similar between the two cases. The model has also shown that a negatively biased layer, where the *p*-layer is next to the radiation receiving electrode, exhibits significantly lower normalized sensitivity than a positively biased layer and the sensitivity in the negatively biased layer decreases more with cumulative exposure. This is likely one of the reasons that mammographic FPXIs use a positively biased multilayer structure.

In the case of positively biased, multilayer simulations, it has been shown that the thickness of the *p*-layer has little effect on the x-ray sensitivity as it is usually relatively thin and little photogeneration occurs near it. However, the model has shown that the thickness and the electrical properties of the *n*-layer have a large impact on the sensitivity, as much of the photogeneration will occur in that layer.

Experimentally measured sensitivity results from a negatively biased *p-i-n* sample, typical of the photoconductive layer in a-Se FPXIs used for general radiography, have been matched using this model. The simulations give a close match, both during the ghosting phase and the recovery phase of the experiment. The reasons for sensitivity recovery displayed by the simulations are not in agreement with the similar numerical work done by Manouchehri *et al.* [82] but still provide a close match with experiment. The effect of the dark current flowing between exposures may be underestimated by the model presented here. As discussed in Chapter 5, pure Monte Carlo simulations are not practical for simulating the dark current and a way of more accurately predicting the effect of the dark current within the framework of these simulations would allow for more reliable modeling of sensitivity recovery.

# 7. SUMMARY, CONCLUSIONS AND RECOMMENDATIONS

## 7.1 Introduction

The research presented in this thesis has provided an exhaustive study of the dark current in stabilized a-Se sandwich structures used in direct conversion x-ray image detectors. This work, both experimental and theoretical, has been focused on characterizing the dark current in these structures as a function of time, applied voltage, sample structure, sample thickness and contact metal. The resulting analysis has allowed for definite conclusions on whether carrier injection from the contacts or bulk thermal generation of carriers is the true dominant source of the dark current in these structures.

This research has also focused on expanding and improving previous models of the x-ray sensitivity of stabilized a-Se sandwich structures. This new model has allowed for the inclusion of the effects of the dark current reducing blocking layers and the flow of dark current between x-ray exposures. The x-ray sensitivity has been modeled as a function of cumulative exposure, sample structure and applied field with results matching newly acquired experimental data quite closely.

## 7.2 Dark Current

Chapter 4 of this thesis featured the experimental study of the dark current in five separate sets of a-Se samples with some steady-state modeling while Chapter 5 included modeling of the dark current transients.

## 7.2.1 Experimental Work

Dark current measurements were performed on samples created in both the University of Saskatchewan laboratories and by industry. Measurements were performed in both labs with different measurement systems producing similar results, speaking to the authenticity of the work done.

### 7.2.1.1 Dark Current as a Function of Time

As found in previously published measurements of dark current in a-Se sandwich structures, the dark current measured in this work decayed with time following the application of the bias. The level and shape of these transients depend on sample structure, contact metal and the magnitude of the applied field. In the case of transients measured for 1000 s or longer, it was found that samples needed to be rested for a minimum of 12 hours, short-circuited in the dark for transient reproducibility better than 90%.

Many samples, though not all, experienced a non-reproducible initial transient, giving evidence of a “contact formation process” with the initial application of a sufficiently high bias for a sufficiently long period of time. Subsequent, reproducible transients at the same field were always lower than these initial measurements and these initial values were never used for analysis or comparison.

The long term reproducibility of the dark current transients was also studied. Most sample structures displayed an increase in the dark current level of one order of magnitude or less over a 3 year period. *n-i-p* samples of set A displayed an increase of 4 orders of magnitude over this period and this has been attributed to crystallization of the *n*-layer with time.

### 7.2.1.2 Dark Current as a Function of Sample Structure

Sample set A was used to explore the effect of *n*- and *p*-type blocking layers on the dark current. It was confirmed that simple *i*-layer samples give dark current levels too high for detector operation. The addition of a *p*-type blocking layer next to the negative contact has little to no effect on the dark current level, though it will trap the majority of injected electrons. The addition of an *n*-type blocking layer next to the positive contact was shown to decrease the dark current level significantly (by as much as 3 orders of magnitude) due to the trapping of injected holes. These results suggest that injected holes are the main contributor to the dark current. The addition of both blocking layers simultaneously, resulting in an *n-i-p* or *p-i-n* structure, produces a further reduction in the dark current when compared to the case of an *n-i* or *i-n* structure. This is perhaps due to the trapping of the injected electrons in the *p*-layer of the three layer structure which would drift through the *i*-layer and recombine with trapped holes in the *n*-layer in the case of the two layer structure.

It was shown that the current levels through these samples are not symmetric with respect to positive and negative applied fields. A negatively biased *i*-layer sample produces dark current levels over 2 orders of magnitude greater than a positively biased *i*-layer sample. Negative bias refers to the case where the top contact is biased negatively with respect to the substrate. This could be due to fractionation during evaporation, causing a non-uniform distribution of hole traps across the sample. Samples with blocking layers produce a transient with a hump when forward biased which occurs at an earlier time at higher applied fields. These humps are possibly due to a trapped carrier profile across the sample which causes a temporary increase of the field at the contacts, coupled with the release of holes deeply trapped during the large initial rush of dark current. These conclusions drawn from the work on sample set A were all supported by evidence from work with sample set E.

Direct evidence of the accumulation of space charge in the a-Se samples was provided by voltage step measurements which showed that the samples developed regions of space charge great enough to absorb the change in the electric field at low voltages when the applied voltage was doubled. This effect was much more prominent in samples with blocking layers. Discharge

measurements showed that while samples with blocking layers tend to store slightly larger amounts of trapped carriers than *i*-layer samples, there is not a direct correlation between trapped charge and a sample's ability to reduce the dark current. It is actually the location of the trapped charge (near the contacts, in the blocking layers) that is most important in terms of efficiently reducing the dark current levels. These findings further support the theory that the dark current is dominated by the injection of carriers from the contacts and provide a reliable method to test for the proper functionality of blocking layers.

### **7.2.1.3 Dark Current as a Function of Applied Field**

It was found that the addition of blocking layers greatly reduced the dependence of the dark current on the applied field, with some three layer samples demonstrating a sub-ohmic relationship. It was also found that the field dependence always decreases with time after the application of the bias. This reduction with time is much greater in samples with blocking layers, supporting the idea that the build up of trapped charge in the blocking layers with time causes the decay transients. Some three layer samples were shown to have *J-F* characteristics that could initially be described quite accurately by carrier injection from the contacts over a Schottky barrier. However, after some time, two distinct regions of field dependence emerged in these samples and the Schottky barrier relation underestimated the field dependence at higher fields.

Analysis of the natural log of the dark current plotted as a function of the square root of the applied field yielded inconclusive results. For most samples, the slope of the resulting plot was too great to be indicative of Schottky emission or Poole-Frenkel enhanced bulk thermal generation.

### **7.2.1.4 Dark Current as a Function of *i*-layer Thickness**

Work with sample sets C and D showed very little dependence of the dark current on the thickness of the *i*-layer of an *n-i-p* sample. However, there was an observed decrease of 1 order of magnitude for every 2  $\mu\text{m}$  increase in *n*-layer thickness. These results strongly support the

conclusion that hole injection from the positive contact is the dominant source of dark current while thermal generation in the bulk is negligible.

Work with sample set B showed a strong increase in dark current with increasing *i*-layer thickness at high applied fields, much stronger than would be expected in the case of bulk thermal generation (an  $L^{3.3}$  dependence in some cases). These results were explained with the “leaky *n*-layer model”, as it was determined that the alloy used to create the *n*-layers in sample set B had poor hole trapping properties. This model required the assumption that electron injection current was significant and work with sample sets C and E showed that this may be the case at long times after the application of the bias.

#### **7.2.1.5 Dark Current as a Function of Contact Metal**

Reliable measurements with sample sets C and D consistently showed that a positive contact of Pt gave a higher dark current than Al. This would be expected if the dominant source of the dark current is hole injection over a Schottky barrier as Pt has a higher work function than Al. An opposite result was observed in sample set B, but once again, the data produced by this sample set was unreliable. The observed effect of a dependence of the dark current on the contact metal supports the theory that carrier injection is the most significant source of dark current.

#### **7.2.2 Modeling of Dark Current Transients**

The initial focus of this work was to model the dark current transients at different fields in different sample structures. Initial computer simulations using pure Monte Carlo and modified Monte Carlo simulation techniques gave promising results, but the very long computational times made matching of experimental results through trial and error adjustment of the many variable parameters exceedingly difficult. As a result, attempts at modeling the dark current as a function of sample structure were abandoned and simplified simulation techniques, published concurrently with the work done here, were adopted. The published results were matched and experimental results from sample set C were used for calibration.

The dark current transients in *n-i-p* samples at different applied fields were closely matched using the assumption that the dark current is entirely due to the injection of carriers from the contacts over a Schottky barrier and the trapping of the injected carriers in the blocking layers produces a space charge which reduces the field at the contacts, reducing carrier injection and, hence, the dark current, with time. It was found that to match dark current transients which decay for more than 1000 s, two levels of deep hole traps were needed and dark current after about 100 s was dominated by electron injection. The continued decay after this point is due to the filling of very deep electron traps.

### **7.2.3 Conclusions on Dark Current**

The wealth of experimental data collected and analyzed in Chapter 4 of this work has conclusively shown that the dominant source of dark current in a-Se sandwich structures is the injection of charge carriers from the contacts, predominantly holes injected from the positive contact, and thermal generation of carriers in the bulk is indeed negligible. This conclusion is supported by the success of the computer simulations described in Chapter 5 in matching experimental results by assuming only carrier injection. The simulations do suggest that electron injection becomes dominant at later times during the decay, however, a similar result could be produced by reducing the assumed electron contribution and assuming significant hole trap concentrations at deeper levels than predicted by the currently accepted DOS of a-Se.

## **7.3 X-ray Sensitivity**

The focus of the work on x-ray sensitivity presented in Chapter 6 was the modeling of the decrease in sensitivity with cumulative exposure, the suspected phenomenon behind ghosting. The model used Monte Carlo simulations and was based on a previous model considering deep trapping of carriers, recombination between trapped and drifting carriers, trap filling effects, non-uniform electric field effects, effects of x-ray induced metastable deep trap generation and release of trapped carriers. Normalized sensitivity was calculated as the product of the quantum efficiency, the photogeneration ratio and the charge collection efficiency. The new model

expanded upon the previous model by including the effects of the addition of blocking layers to the sample structure and the dark current.

### 7.3.1 Effect of Blocking Layers on X-ray Sensitivity

In the case of a positively biased sample, the effect of adding a 10  $\mu\text{m}$   $n$ -layer to a 200  $\mu\text{m}$   $i$ -layer sample reduced the normalized sensitivity by  $\sim 2\%$  due to increased hole trapping in the  $n$ -layer immediately after photogeneration.  $s_x$  decreases roughly linearly with increasing thickness of the  $n$ -layer over a range of 5 – 20  $\mu\text{m}$ . Increasing the lifetime of holes in the  $n$ -layer by one order of magnitude increased  $s_x$  by  $\sim 2\%$ , due to less trapping of holes photogenerated in the  $n$ -layer, while decreasing the hole lifetime in the  $n$ -layer to 0 s (as in the case of an ideal  $n$ -layer) decreased  $s_x$  by  $\sim 16\%$ . Decreasing the lifetime of electrons in the  $n$ -layer increases the number of photogenerated electrons that are trapped as they drift through the  $n$ -layer. However, this only decreases  $s_x$  by  $\sim 0.4\%$ . The addition of a thin  $p$ -layer has very little effect on  $s_x$  even when the thickness of the  $p$ -layer is varied between 1 and 6  $\mu\text{m}$ .

In the case of negatively biased single layer samples,  $s_x$  is 9% lower than in the positively biased case, as photogenerated electrons must now, on average, travel farther than photogenerated holes, leading to a lower CCE. Photogenerated electrons trapped near the negative contact drive the field down in that region, increasing  $W_{\pm}$  and causing the PGR to decrease significantly with accumulating exposure. As a result,  $s_x$  decreases more with accumulating exposure in the case of negative bias than positive bias. The addition of the blocking layers decreases  $s_x$  by  $\sim 1.5\%$  in the negatively biased case due to increased trapping of photogenerated electrons in the  $p$ -layer immediately after photogeneration.

### 7.3.2 Effect of Dark Current on X-ray Sensitivity

The effect of the dark current flowing before the first exposure and between subsequent exposures was modeled by resetting the concentrations of trapped carriers in the blocking layers to those predicted by numerical dark current calculations over the rest period between exposures, including Langevin governed recombination of injected holes with trapped electrons in the  $n$ -

layer and injected electrons with trapped holes in the  $p$ -layer. While this is a crude approximation, it resulted in simulated  $s_x$  values  $\sim 6\%$  lower when compared to those simulated without considering this effect. This is the result of a lower CCE but is also due to a decreased PGR due to a lower field at the positive contact where most of the photogeneration takes place.

### 7.3.3 Matching X-ray Sensitivity Experiments

Sensitivity experiments were conducted over a ghosting phase of 1 hour and a recovery phase of 3 hours on a  $\sim 1$  mm thick  $p-i-n$  sample at three applied fields. The results were simulated with the Monte Carlo model and good agreement was obtained at all fields during the ghosting phase when a field dependent recombination fitting factor of 1 at  $10$  V/ $\mu\text{m}$ , 0.8 at  $5$  V/ $\mu\text{m}$  and 0.5 at  $3$  V/ $\mu\text{m}$  was included. To achieve good matching during the recovery period, consideration of the relaxation of metastable x-ray generated traps with time in a stretched exponential manner was required. While good matching was achieved, it was found that the effect of metastable trap relaxation was the dominant factor in sensitivity recovery. Published numerical calculations done concurrently with the work presented here have predicted that the recovery is primarily due to dark current effects and the release of trapped carriers.

### 7.3.4 Conclusions on X-ray Sensitivity

The effects of blocking layers and dark current were successfully added to the previous Monte Carlo model. Excellent agreement was achieved with experimental results both in ghosting and sensitivity recovery. However, the crudeness of the approximation to the effect of the dark current flowing between exposures leaves room for improvement.

## 7.4 Recommendations for Future Work

While the experimental study of dark current in a-Se sandwich structures presented in this thesis was rather exhaustive, there are other experiments which would also be beneficial. It would be interesting to study the dark current transients as a function of operating temperature. To do these measurements properly, a measurement chamber which can be purged with inert gas

to avoid condensation problems during cooling below 0 °C will be needed. Furthermore, care must be taken when cooling the samples as they can experience cracking of the substrate and peeling of the a-Se off of the substrate at temperatures below 0 °C. These measurements probably would not give any new information as to the source of the dark current, as both injection current and bulk thermal generation current should scale with temperature in the same manner. However, it would be very interesting to determine if lowered temperature would result in dramatically lower dark current. This could allow for much higher applied fields, leading to much improved x-ray sensitivity, if an FPXI is operated at a lower temperature.

It would also be interesting to measure the dark current during x-ray exposure. While the photogenerated current will dominate the dark current during exposure, the signal immediately after the exposure could be compared to the signal immediately before exposure and to the same transient measured without any exposure. Theoretically, the trapped charge distribution across the sample will change during exposure, altering the dark current thereafter.

The creation of sample set D (*n-i-p* samples with two thicknesses of *i*-layer on one sample with all other properties remaining constant) would allow for precise measurement of the dependence of the noise in the dark current on the *i*-layer thickness. This could help to determine if the dominant source of noise is due to the contact or the bulk of the a-Se.

It would be a significant achievement to calibrate either the Monte Carlo or modified Monte Carlo dark current simulation models discussed in Chapter 5 with experimental data. These modeling techniques could be used to model the dark current in structures other than *n-i-p* and *p-i-n* but would probably require significant improvements in computing power or further optimization of the computing efficiency of the model.

In the case of the x-ray simulation modeling, it would be ideal if the dark current between exposures could be modeled in a purely Monte Carlo method, so those calculations could be done during the x-ray sensitivity simulations. Again, this could require greatly enhanced computing power. Alternatively, numerical simulations of the dark current could be built directly into the

sensitivity simulations. The result of this work should be compared against the work presented in this thesis to judge the approximation of the dark current effect utilized here.

Further, it would be interesting to use the current x-ray sensitivity model to simulate the change in the sensitivity with accumulating exposure in positively biased *n-i-p* mammographic samples at mammographic x-ray energies. To do this, sensitivity experiments similar to the ones described in Chapter 6 should be carried out. It is important that the approximate electronic properties of the sample studied be known so that the modeling done is as realistic as possible.

# APPENDIX

## Simplified Field Formula Derivation

Many of the models of the dark current in a-Se sandwich structures presented in this thesis require a calculation of the electric field at both the positive and negative contacts of the structure. These fields can be due to both the applied field and the space charge density created by charge carriers trapped within the structure. In the case of the Monte Carlo x-ray sensitivity simulations presented in Chapter 6, the field across the structure was calculated by solving Poisson's equation:

$$\frac{dF(x)}{dx} = \frac{\rho(x)}{\epsilon_0 \epsilon_r} \quad (\text{A.1})$$

with the boundary condition

$$\int_0^L F(x) dx = V_0 \quad (\text{A.2})$$

through numerical integration. Here  $\rho$  is the space charge density due to trapped carriers,  $L$  is the thickness of the sample and  $V_0$  is the applied voltage. This method can be used to find the electric field at any point within the structure.

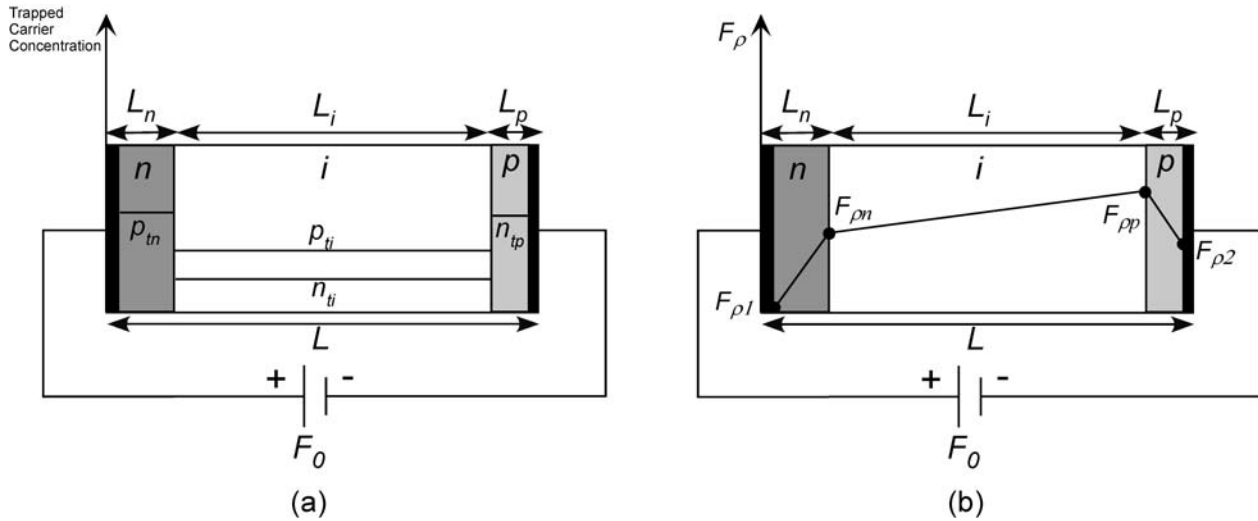


**Figure A.1 (a)** The trapped carrier concentration in each layer of a multilayer a-Se sandwich structure. Uniform trapped carrier concentrations are assumed in each layer. Trapped hole concentrations in the  $n$ -layer and  $i$ -layer are given by  $p_{tn}$  and  $p_{ti}$ , respectively and trapped electron concentrations in the  $i$ -layer and  $p$ -layer are given by  $n_{ti}$  and  $n_{tp}$ , respectively. **(b)** The electric field distribution across the structure due only to the trapped carrier concentrations. The field at the positive contact is denoted as  $F_{\rho 1}$ , the field at the  $n$ - and  $i$ -layer interface is  $F_{\rho n}$ , the field at the  $i$ - and  $p$ -layer interface is  $F_{\rho p}$  and the field at the negative contact is  $F_{\rho 2}$ .

The leaky  $n$ -layer model presented in Chapter 4 and the numerical calculations of dark current presented in Chapter 5 only require the value of the electric field at the positive and negative contact. If one assumes uniform trapped carrier concentrations within each layer of a multilayer structure, as shown in Fig. A.1, a more efficient calculation of the electric field is possible and these expressions are given in Eqs. 4.3, 4.4, 5.17, 5.18, 5.21 and 5.22. Figure A.1 (a) shows that holes injected from the positive contact are uniformly trapped in the  $n$ -layer while electrons injected from the negative contact are uniformly trapped in the  $p$ -layer with some of each carrier making their way into the  $i$ -layer and being uniformly trapped there. Here, it is assumed that there is a greater concentration of trapped holes than trapped electrons in the  $i$ -layer, but this will not make a difference in the derivation. Figure A.1 (b) shows the electric field distribution across the structure due only to the trapped charge in the structure,  $F_\rho$ . The values of  $F_\rho$  at the contacts and layer interfaces can be found by integrating the area under the trapped carrier concentration profile shown in Fig. A.1 (a). Obviously,  $F_{\rho 1}$  is 0. The simple integration yields the following expressions for the other fields:

$$F_{\rho n} = \frac{p_m e}{\varepsilon} L_n \quad (\text{A.3})$$

$$F_{\rho p} = F_{\rho n} + \frac{(p_{ii} - n_{ii})e}{\varepsilon} L_i = \frac{e}{\varepsilon} (p_m L_n + (p_{ii} - n_{ii})L_i) \quad (\text{A.4})$$

$$F_{\rho 2} = F_{\rho p} - \frac{n_{tp} e}{\varepsilon} L_p = \frac{e}{\varepsilon} (p_m L_n + (p_{ii} - n_{ii})L_i - n_{tp} L_p) \quad (\text{A.5})$$

where  $e$  is the elementary charge and  $\varepsilon$  is the permittivity of the a-Se ( $\varepsilon_0 \varepsilon_r$ ). The voltage across the structure due to the trapped charge,  $V_\rho$ , can be found by integrating the area under the  $F_\rho$  profile in Fig. A.2 (b), such that

$$V_\rho = \frac{F_{\rho 1} + F_{\rho n}}{2} L_n + \frac{F_{\rho n} + F_{\rho p}}{2} L_i + \frac{F_{\rho p} + F_{\rho 2}}{2} L_p \quad (\text{A.6})$$

The average field across the structure, which is also the field at the positive contact,  $F_1$ , due to both the trapped carriers within the structure and applied field,  $F_0$ , can then be found as

$$F_1 = \frac{V_0 - V_\rho}{L} \quad (\text{A.7})$$

where  $F_0 = V_0/L$ . Substituting Eqs. A3 – A6 into Eq. A7, gathering terms and substituting for  $L_i$  in terms of the other layer thicknesses ( $L_i = L - L_n - L_p$ ) yields the following expression for  $F_1$ :

$$F_1 = F_0 - \frac{e}{\varepsilon_r \varepsilon_0} \left[ \left( L_n - \frac{L_n^2}{2L} \right) p_m + \left( \frac{L_n^2 - L_p^2}{2L} - L_n + \frac{L}{2} \right) (p_{ii} - n_{ii}) - \frac{L_p^2}{2L} n_{tp} \right] \quad (\text{A.8})$$

If only trapped holes in the  $n$ -layer are considered, Eq. A.8 simplifies to

$$F_1 = F_0 - \frac{e}{\varepsilon} \left( L_n - \frac{L_n^2}{2L} \right) p_m \quad (\text{A.9})$$

Similarly, the field at the negative contact due to the trapped charge and applied field,  $F_2$ , is given by

$$F_2 = F_1 + F_{\rho_2} \quad (\text{A.10})$$

so that

$$F_2 = F_0 - \frac{e}{\varepsilon_r \varepsilon_0} \left[ -\frac{L_n^2}{2L} p_m + \left( \frac{L_n^2 - L_p^2}{2L} + L_p - \frac{L}{2} \right) (p_{ti} - n_{ti}) + \left( L_p - \frac{L_p^2}{2L} \right) n_{tp} \right] \quad (\text{A.11})$$

If only trapped holes in the  $n$ -layer are considered, Eq. A.11 simplifies to

$$F_2 = F_0 + \frac{e}{\varepsilon} \frac{L_n^2}{2L} p_m \quad (\text{A.12})$$

## REFERENCES

- [1] W. R. Hendee and E. R. Ritenour, "Medical Imaging Physics", 4th Edition, John Wiley and Sons, New York, USA, 2002.
- [2] M. Yunus, "Monte Carlo Modeling of the Sensitivity of x-Ray Photoconductors", M. Sc. Thesis, University of Saskatchewan, Saskatoon, Canada, 2005.
- [3] A. Poulos and G. Llewellyn, "Mammographic Discomfort: A Holistic Perspective Derived from Women's Experiences", *Radiography*, **11**, 1, pp. 17, 2005.
- [4] A. Jemal, R. Siegel, E. Ward, Y. Hao, J. Xu, and M. Thun, "Cancer Statistics, 2009", *A Cancer Journal for Clinicians*, **59**, pp. 225, 2009.
- [5] K. Kerlikoswe, D. Grady, S. M. Rubin, C. Sandrock, and V. Ernster, "Efficacy of Screening Mammography", *Journal of the American Medical Association*, **273**, 2, pp. 149, 1995.
- [6] D. M. Hunter, G. Belev, G. DeCresenzo, S. O. Kasap, J. G. Mainprize, G. Mawdsley, J. A. Rowlands, C. Smith, T. O. Tumer, and V. Verpakhovski, "High-Resolution (20 cycles/mm) Digital X-Ray Mammography using Amorphous Selenium Directly Coupled to CCD Readout Devices", *Proceedings of SPIE*, **5368**, pp. 466, 2004.
- [7] G. S. Belev, "Electrical Properties of Amorphous Selenium Based Photoconductive Devices for Application in X-Ray Image Detectors", Ph. D. Thesis, University of Saskatchewan, Saskatoon, Canada, 2007.
- [8] D. J. Brenner and E. J. Hall, "Computed tomography—an Increasing Source of Radiation Exposure", *New England Journal of Medicine*, **357**, 22, pp. 2277, 2007.
- [9] C. Westbrook, "MRI at a Glance", Wiley-Blackwell, Chichester, UK; Malden, USA, 2009.
- [10] D. G. Assimos and D. J. Vining, "Virtual Endoscopy", *Journal of Endourology*, **15**, 1, pp. 47, 2001.
- [11] J. A. Rowlands and J. Yorkston, "Flat Panel Detectors for Digital Radiography", in: J. Beutel, H. L. Kundel and R. L. Van Metters (Eds.), "Handbook of Medical Imaging", 1st Edition, SPIE, Washington, DC, 2000.
- [12] U. Neitzel, I. Maack, and S. Günther-Kohfahl, "Image Quality of a Digital Chest Radiography System Based on a Selenium Detector", *Medical Physics*, **21**, pp. 509, 1994.
- [13] S. Kasap, J. B. Frey, G. Belev, O. Tousignant, H. Mani, L. Laperriere, A. Reznik, and J. A. Rowlands, "Amorphous Selenium and its Alloys from Early Xeroradiography to High Resolution X-Ray Image Detectors and Ultrasensitive Imaging Tubes", *Physica Status Solidi (b)*, **246**, 8, pp. 1794, 2009.
- [14] S. O. Kasap and J. A. Rowlands, "Direct-Conversion Flat-Panel X-Ray Image Sensors for Digital Radiography", *Proceedings of the IEEE*, **90**, 4, pp. 591, 2002.

- [15] S. O. Kasap and J. A. Rowlands, "Direct-Conversion Flat-Panel X-Ray Image Detectors", *Circuits, Devices and Systems, IEE Proceedings*, **149**, 2, pp. 85, 2002.
- [16] H. K. Kim, I. A. Cunningham, Z. Yin, and G. Cho, "On the Development of Digital Radiography Detectors: A Review", *International Journal of Precision Engineering and Manufacturing*, **9**, pp. 86, 2008.
- [17] A. J. Shah, J. Wang, T. Yamada, and L. L. Fajardo, "Digital Mammography: A Review of Technical Development and Clinical Applications", *Clinical Breast Cancer*, **4**, 1, pp. 63, 2003.
- [18] A. Noel and F. Thibault, "Digital Detectors for Mammography: The Technical Challenges", *European Radiology*, **14**, 11, pp. 1990, 2004.
- [19] U. Neitzel, "Status and Prospects of Digital Detector Technology for CR and DR", *Radiation Protection Dosimetry*, **114**, 1-3, pp. 32, 2005.
- [20] J. A. Seibert, "Flat-Panel Detectors: How Much Better are they?", *Pediatric Radiology*, **36**, pp. 173, 2006.
- [21] M. Hoheisel, "Review of Medical Imaging with Emphasis on X-Ray Detectors", *Nuclear Instruments and Methods in Physics Research Section A: Accelerators, Spectrometers, Detectors and Associated Equipment*, **563**, 1, pp. 215, 2006.
- [22] W. A. Kalender and Y. Kyriakou, "Flat-Detector Computed Tomography (FD-CT)", *European Radiology*, **17**, 11, pp. 2767, 2007.
- [23] M. Körner, C. H. Weber, S. Wirth, K. J. Pfeifer, M. F. Reiser, and M. Treitl, "Advances in Digital Radiography: Physical Principles and System Overview", *Radiographics*, **27**, 3, pp. 675, 2007.
- [24] J. Yorkston, "Recent Developments in Digital Radiography Detectors", *Nuclear Instruments and Methods in Physics Research Section A: Accelerators, Spectrometers, Detectors and Associated Equipment*, **580**, 2, pp. 974, 2007.
- [25] R. Fahrig, A. Ganguly, P. Lillaney, J. Bracken, J. A. Rowlands, Z. Wen, H. Yu, V. Rieke, J. M. Santos, and K. B. Pauly, "Design, Performance, and Applications of a Hybrid x-ray/MR System for Interventional Guidance", *Proceedings of the IEEE*, **96**, 3, pp. 468, 2008.
- [26] M. Spahn, "Flat Detectors and their Clinical Applications", *European Radiology*, **15**, 9, pp. 1934, 2005.
- [27] Y. El-Mohri, L. E. Antonuk, Q. Zhao, Y. Wang, Y. Li, H. Du, and A. Sawant, "Performance of a High Fill Factor, Indirect Detection Prototype Flat-Panel Imager for Mammography", *Medical Physics*, **34**, pp. 315, 2007.
- [28] M. Overdick, C. Baumer, K. J. Engel, J. Fink, C. Herrmann, H. Kruger, M. Simon, R. Steadman, and G. Zeitler, "Status of Direct Conversion Detectors for Medical Imaging with X-Rays", *IEEE Transactions on Nuclear Science*, **56**, pp. 1800, 2009.
- [29] S. O. Kasap, M. Z. Kabir, and J. A. Rowlands, "Recent Advances in X-Ray Photoconductors for Direct Conversion X-Ray Image Detectors", *Current Applied Physics*, **6**, pp. 288, 2006.

- [30] J. Rowlands and S. Kasap, "Amorphous Semiconductors Usher in Digital x-Ray Imaging", *Physics Today*, **50**, 11, pp. 24, 1997.
- [31] T. P. Brody, "The Birth and Early Childhood of Active matrix—a Personal Memoir", *Journal of the Society for Information Display*, **4**, pp. 113, 1996.
- [32] W. Zhao and J. A. Rowlands, "X-Ray Imaging using Amorphous Selenium: Feasibility of a Flat Panel Self-Scanned Detector for Digital Radiology", *Medical Physics*, **22**, pp. 1595, 1995.
- [33] W. Zhao, J. A. Rowlands, S. Germann, D. F. Waechter, and Z. Huang, "Digital Radiology using Self-Scanned Readout of Amorphous Selenium: Design Considerations for Mammography", *Proceedings of SPIE*, **2432**, pp. 250, 1995.
- [34] M. J. Yaffe and J. A. Rowlands, "X-Ray Detectors for Digital Radiography", *Physics in Medicine and Biology*, **42**, 1, pp. 1, 1997.
- [35] W. Zhao, I. Blevis, S. Germann, J. A. Rowlands, D. Waechter, and Z. Huang, "Digital Radiology using Active Matrix Readout of Amorphous Selenium: Construction and Evaluation of a Prototype Real-Time Detector", *Medical Physics*, **24**, pp. 1834, 1997.
- [36] J. A. Rowlands, W. Zhao, I. M. Blevis, D. F. Waechter, and Z. Huang, "Flat-Panel Digital Radiology with Amorphous Selenium and Active-Matrix Readout.", *Radiographics*, **17**, 3, pp. 753, 1997.
- [37] D. L. Y. Lee, L. K. Cheung, and L. S. Jeromin, "New Digital Detector for Projection Radiography", *Proceedings of SPIE*, **2432**, pp. 237, 1995.
- [38] D. L. Y. Lee, L. K. Cheung, E. F. Palecki, and L. S. Jeromin, "Discussion on Resolution and Dynamic Range of Se-TFT Direct Digital Radiographic Detector", *Proceedings of SPIE*, **2708**, pp. 511, 1996.
- [39] S. O. Kasap, C. Haugen, M. Nesdoly, and J. A. Rowlands, "Properties of a-Se for use in Flat Panel X-Ray Image Detectors", *Journal of Non-Crystalline Solids*, **266**, pp. 1163, 2000.
- [40] T. O. Tümer, S. Yin, V. Cajipe, H. Flores, J. Mainprize, G. Mawdsley, J. A. Rowlands, M. J. Yaffe, E. E. Gordon, and W. J. Hamilton, "High-Resolution Pixel Detectors for Second Generation Digital Mammography", *Nuclear Instruments and Methods in Physics Research Section A: Accelerators, Spectrometers, Detectors and Associated Equipment*, **497**, 1, pp. 21, 2003.
- [41] G. Belev, S. Kasap, J. A. Rowlands, D. Hunter, and M. Yaffe, "Dependence of the Electrical Properties of Stabilized a-Se on the Preparation Conditions and the Development of a Double Layer X-Ray Detector Structure", *Current Applied Physics*, **8**, 3-4, pp. 383, 2008.
- [42] K. S. Karim, A. Nathan, and J. A. Rowlands, "Amorphous Silicon Active Pixel Sensor Readout Circuit for Digital Imaging", *IEEE Transactions on Electron Devices*, **50**, 1, pp. 200, 2003.
- [43] M. H. Izadi and K. S. Karim, "High Dynamic Range Pixel Architecture for Advanced Diagnostic Medical X-Ray Imaging Applications", *Journal of Vacuum Science & Technology A: Vacuum, Surfaces, and Films*, **24**, 3, pp. 846, 2006.

- [44] M. H. Izadi, K. S. Karim, A. Nathan, and J. A. Rowlands, "Low-Noise Pixel Architecture for Advanced Diagnostic Medical x-Ray Imaging Applications", *Proceedings of SPIE*, **6142**, pp. 61420T, 2006.
- [45] F. Taghibakhsh and K. S. Karim, "Two-Transistor Active Pixel Sensor Readout Circuits in Amorphous Silicon Technology for High-Resolution Digital Imaging Applications", *IEEE Transactions on Electron Devices*, **55**, 8, pp. 2121, 2008.
- [46] A. Mercha, J. Rhayem, L. Pichon, M. Valenza, J. M. Routoure, R. Carin, O. Bonnaud, and D. Rigaud, "Low-Frequency Noise in Low Temperature Unhydrogenated Polysilicon Thin Film Transistors", *Microelectronics Reliability*, **40**, 11, pp. 1891, 2000.
- [47] M. H. Izadi, O. Tousignant, M. F. Mokam, and K. S. Karim, "An a-Si Active Pixel Sensor (APS) Array for Medical X-Ray Imaging", *IEEE Transactions on Electron Devices*, **57**, 11, pp. 3020, 2010.
- [48] A. Sultana, M. M. Wronski, K. S. Karim, and J. A. Rowlands, "Digital X-Ray Imaging using Avalanche a-Se Photoconductor", *IEEE Sensors Journal*, **10**, 2, pp. 347, 2010.
- [49] S. Kasap, J. A. Rowlands, S. D. Baranovskii, and K. Tanioka, "Lucky Drift Impact Ionization in Amorphous Semiconductors", *Journal of Applied Physics*, **96**, pp. 2037, 2004.
- [50] A. Reznik, S. D. Baranovskii, O. Rubel, G. Juska, S. O. Kasap, Y. Ohkawa, K. Tanioka, and J. A. Rowlands, "Avalanche Multiplication Phenomenon in Amorphous Semiconductors: Amorphous Selenium Versus Hydrogenated Amorphous Silicon", *Journal of Applied Physics*, **102**, pp. 053711, 2007.
- [51] K. Jandieri, O. Rubel, S. D. Baranovskii, A. Reznik, J. A. Rowlands, and S. O. Kasap, "Lucky-Drift Model for Impact Ionization in Amorphous Semiconductors", *Journal of Materials Science: Materials in Electronics*, **20**, pp. 221, 2009.
- [52] O. Rubel, A. Potvin, and D. Laughton, "Generalized Lucky-Drift Model for Impact Ionization in Semiconductors with Disorder", *Journal of Physics: Condensed Matter*, **23**, pp. 055802, 2011.
- [53] Y. Ohkawa, K. Miyakawa, T. Matsubara, K. Kikuchi, S. Suzuki, M. Kubota, N. Egami, and A. Kobayashi, "Temperature Dependence of Carrier Traps in High Sensitivity HARP Photoconductive Film", *Physica Status Solidi (c)*, **6**, S1, pp. S224, 2009.
- [54] M. M. Wronski, W. Zhao, A. Reznik, K. Tanioka, G. DeCrescenzo, and J. A. Rowlands, "A Solid-State Amorphous Selenium Avalanche Technology for Low Photon Flux Imaging Applications", *Medical Physics*, **37**, pp. 4982, 2010.
- [55] R. E. Johanson, S. O. Kasap, J. Rowlands, and B. Polischuk, "Metallic Electrical Contacts to Stabilized Amorphous Selenium for use in X-Ray Image Detectors", *Journal of Non-Crystalline Solids*, **227**, pp. 1359, 1998.
- [56] S. O. Kasap and G. Belev, "Progress in the Science and Technology of Direct Conversion X-Ray Image Detectors: The Development of a Double Layer a-Se Based Detector", *Journal of Optoelectronics and Advanced Materials*, **9**, 1, pp. 1, 2007.

- [57] S. Mahmood, M. Kabir, O. Tousignant, H. Mani, J. Greenspan, and P. Botka, "Dark Current in Multilayer Amorphous Selenium x-Ray Imaging Detectors", *Applied Physics Letters*, **92**, 22, pp. 223506, 2008.
- [58] B. T. Polischuk and A. Jean, "Multilayer plate for x-ray imaging and method of producing same", US Patent 5,880,472, 1999.
- [59] M. Z. Kabir, F. Manouchehri, S. A. Mahmood, V. K. Devabhaktuni, O. Tousignant, H. Mani, J. Greenspan, and P. Botka, "Modeling of Dark Current and Ghosting in Multilayer Amorphous Selenium x-Ray Detectors", *Proceedings of SPIE*, **6913**, pp. 69133U, 2008.
- [60] C. Haugen, S. O. Kasap, and J. Rowlands, "Charge Transport and Electron-Hole-Pair Creation Energy in Stabilized a-Se x-Ray Photoconductors", *Journal of Physics D: Applied Physics*, **32**, pp. 200, 1999.
- [61] M. Yunus, M. Z. Kabir, and S. O. Kasap, "Sensitivity Reduction Mechanisms in Amorphous Selenium Photoconductive x-Ray Image Detectors", *Applied Physics Letters*, **85**, pp. 6430, 2004.
- [62] M. Z. Kabir, M. Yunus, S. Kasap, O. Tousignant, H. Mani, and P. Gauthier, "Sensitivity of Stabilized a-Se Based x-Ray Photoconductors", *Current Applied Physics*, **6**, 3, pp. 393, 2006.
- [63] M. Z. Kabir, "Modeling of x-Ray Photoconductors for x-Ray Image Detectors", Ph. D. Thesis, University of Saskatchewan, Saskatoon, Canada, 2005.
- [64] M. Z. Kabir, S. O. Kasap, and J. A. Rowlands, "Photoconductors for X-ray Image Detectors", in: S. O. Kasap and P. Capper (Eds.), "The Springer Handbook of Electronic and Photonic Materials", Springer, Heidelberg, Germany, 2006.
- [65] S. Kasap and J. Rowlands, "Review X-Ray Photoconductors and Stabilized a-Se for Direct Conversion Digital Flat-Panel X-Ray Image-Detectors", *Journal of Materials Science: Materials in Electronics*, **11**, 3, pp. 179, 2000.
- [66] <http://physics.nist.gov/PhysRefData/>.
- [67] J. M. Boone, "X-ray production, interaction, and detection in diagnostic imaging", in: J. Beutel, H. L. Kundel and R. L. Van Metter (Eds.), "Handbook of Medical Imaging Volume 1", SPIE Press, Washington, USA, 2000.
- [68] C. A. Klein, "Bandgap Dependence and Related Features of Radiation Ionization Energies in Semiconductors", *Journal of Applied Physics*, **39**, 4, pp. 2029, 1968.
- [69] R. C. Alig and S. Bloom, "Electron-Hole-Pair Creation Energies in Semiconductors", *Physical Review Letters*, **35**, 22, pp. 1522, 1975.
- [70] W. Que and J. A. Rowlands, "X-Ray Photogeneration in Amorphous Selenium: Geminate Versus Columnar Recombination", *Physical Review B*, **51**, 16, pp. 10500, 1995.
- [71] S. O. Kasap, V. Aiyah, B. Polischuk, and A. Baillie, "X-Ray Sensitivity of a-Se for x-Ray Imaging with Electrostatic Readout", *Journal of Applied Physics*, **83**, pp. 2879, 1998.

- [72] D. M. Pai and R. C. Enck, "Onsager Mechanism of Photogeneration in Amorphous Selenium", *Physical Review B*, **11**, 12, pp. 5163, 1975.
- [73] G. Jaffe, "On the Theory of Ionization in Columns", *Annalen Der Physik*, **42**, pp. 303, 1913.
- [74] J. Hirsch and H. Jahankhani, "The Carrier Yield in a-Se Under Electron Bombardment", *Journal of Physics: Condensed Matter*, **1**, pp. 8789, 1989.
- [75] D. Mah, J. A. Rowlands, and J. A. Rawlinson, "Sensitivity of Amorphous Selenium to x Rays from 40 kVp to 18 MV: Measurements and Implications for Portal Imaging", *Medical Physics*, **25**, pp. 444, 1998.
- [76] M. R. V. Sahyun, "Monte Carlo Modeling of Electrophotographic x - ray Detectors", *Journal of Applied Physics*, **53**, 9, pp. 6253, 1982.
- [77] J. A. Rowlands, G. DeCrescenzo, and N. Araj, "X-Ray Imaging using Amorphous Selenium: Determination of x-Ray Sensitivity by Pulse Height Spectroscopy", *Medical Physics*, **19**, pp. 1065, 1992.
- [78] I. M. Blevis, D. C. Hunt, and J. A. Rowlands, "Measurement of x-Ray Photogeneration in Amorphous Selenium", *Journal of Applied Physics*, **85**, pp. 7958, 1999.
- [79] G. Belev and S. O. Kasap, "Amorphous Selenium as an X-Ray Photoconductor", *Journal of Non-Crystalline Solids*, **345**, pp. 484, 2004.
- [80] M. Z. Kabir and S. O. Kasap, "Charge Collection and Absorption-Limited x-Ray Sensitivity of Pixellated x-Ray Detectors", *Journal of Vacuum Science & Technology A: Vacuum, Surfaces, and Films*, **22**, pp. 975, 2004.
- [81] M. Z. Kabir, S. O. Kasap, W. Zhao, and J. A. Rowlands, "Direct Conversion X-Ray Sensors: Sensitivity, DQE and MTF", *Circuits, Devices and Systems, IEE Proceedings*, **150**, 4, pp. 258, 2003.
- [82] F. Manouchehri, M. Z. Kabir, O. Tousignant, H. Mani, and V. K. Devabhaktuni, "Time and Exposure Dependent x-Ray Sensitivity in Multilayer Amorphous Selenium Detectors", *Journal of Physics D: Applied Physics*, **41**, pp. 235106, 2008.
- [83] M. Choquette, Y. Demers, Z. Shukri, O. Tousignant, K. Aoki, M. Honda, A. Takahashi, and A. Tsukamoto, "Performance of a Real-Time Selenium-Based x-Ray Detector for Fluoroscopy", *Proceedings of SPIE*, **4320**, pp. 501, 2001.
- [84] W. Zhao, G. DeCrescenzo, and J. A. Rowlands, "Investigation of Lag and Ghosting in Amorphous Selenium Flat-Panel x-Ray Detectors", *Proceedings of SPIE*, **4682**, pp. 9, 2002.
- [85] W. Zhao, G. DeCrescenzo, S. O. Kasap, and J. A. Rowlands, "Ghosting Caused by Bulk Charge Trapping in Direct Conversion Flat-Panel Detectors using Amorphous Selenium", *Medical Physics*, **32**, pp. 488, 2005.
- [86] J. Kalade, E. Montrimas, and J. Rakauskas, "The Mechanism of Sensitivity Reduction in Selenium Layers Irradiated by X-Rays", *Physica Status Solidi (a)*, **25**, 2, pp. 629, 1974.
- [87] H. G. Chotas, C. E. Floyd, and C. E. Ravin, "Memory Artifact Related to Selenium-Based Digital Radiography Systems.", *Radiology*, **203**, 3, pp. 881, 1997.

- [88] A. V. Oppenheim, R. W. Schaffer, and J. R. Buck, "Discrete-Time Signal Processing", 2nd Edition, Prentice-Hall, Upper Saddle River, USA, 1999.
- [89] S. O. Kasap, H. Ruda, and Y. Boucher, "Cambridge Illustrated Handbook of Optoelectronics and Photonics", Cambridge University Press, Cambridge, 2009.
- [90] O. Tousignant, Y. Demers, L. Laperriere, and S. Marcovici, "a-Se Flat Panel Detectors for Medical Applications", *Proceedings of the 2007 IEEE Sensors Applications Symposium, SAS*, pp. 1, 2007.
- [91] M. Lachaine and B. G. Fallone, "Monte Carlo Simulations of x-Ray Induced Recombination in Amorphous Selenium", *Journal of Physics D: Applied Physics*, **33**, pp. 1417, 2000.
- [92] L. del Risco Norrild, C. Rönqvist, K. Fransson, R. Brenner, L. Gustafsson, F. Edling, and S. Kullander, "Calculation of the Modulation Transfer Function for the X-Ray Imaging Detector DIXI using Monte Carlo Simulation Data", *Nuclear Instruments and Methods in Physics Research Section A: Accelerators, Spectrometers, Detectors and Associated Equipment*, **466**, 1, pp. 209, 2001.
- [93] A. G. Kozorezov, J. K. Wigmore, A. Owens, R. Den Hartog, and A. Peacock, "The Effect of Carrier Diffusion on the Characteristics of Semiconductor Imaging Arrays", *Nuclear Instruments and Methods in Physics Research Section A: Accelerators, Spectrometers, Detectors and Associated Equipment*, **531**, 1-2, pp. 52, 2004.
- [94] M. Z. Kabir and S. O. Kasap, "Modulation Transfer Function of Photoconductive x-Ray Image Detectors: Effects of Charge Carrier Trapping", *Journal of Physics D: Applied Physics*, **36**, pp. 2352, 2003.
- [95] M. Z. Kabir, L. Chowdhury, G. DeCrescenzo, O. Tousignant, S. O. Kasap, and J. A. Rowlands, "Effect of Repeated x-Ray Exposure on the Resolution of Amorphous Selenium Based x-Ray Imagers", *Medical Physics*, **37**, pp. 1339, 2010.
- [96] M. Z. Kabir and S. O. Kasap, "DQE of Photoconductive x-Ray Image Detectors: Application to a-Se", *Journal of Physics D: Applied Physics*, **35**, 21, pp. 2735, 2002.
- [97] W. Zhao, W. G. Ji, and J. A. Rowlands, "Effects of Characteristic x Rays on the Noise Power Spectra and Detective Quantum Efficiency of Photoconductive x-Ray Detectors", *Medical Physics*, **28**, pp. 2039, 2001.
- [98] A. Cunningham, in: J. Beutel, H. L. Kundel and R. L. van Metter (Eds.), "Handbook of Medical Imaging", SPIE Press, Washington, 2000.
- [99] M. Rabbani, R. Shaw, and R. Van Metter, "Detective Quantum Efficiency of Imaging Systems with Amplifying and Scattering Mechanisms", *Journal of the Optical Society of America A*, **4**, 5, pp. 895–901, 1987.
- [100] J. G. Mainprize, D. C. Hunt, and M. J. Yaffe, "Direct Conversion Detectors: The Effect of Incomplete Charge Collection on Detective Quantum Efficiency", *Medical Physics*, **29**, pp. 976, 2002.
- [101] M. Z. Kabir, "Effects of Charge Carrier Trapping on Polycrystalline PbO X-Ray Imaging Detectors", *Journal of Applied Physics*, **104**, pp. 074506, 2008.

- [102] K. C. Kao, "Dielectric Phenomena in Solids", 1st Edition, Elsevier Academic Press, San Diego, USA, 2004.
- [103] S. M. Sze, "Physics of Semiconductor Devices", 2nd Edition, Wiley, New York, USA, 1981.
- [104] K. C. Kao and W. Hwang, "Electrical Transport in Solids", Pergamon Press, Oxford, England, 1981.
- [105] S. O. Kasap, "Principles of Electronic Materials and Devices", Revised Edition, McGraw-Hill, Boston, USA, 2002.
- [106] S. A. Mahmood and M. Z. Kabir, "Dark Current Mechanisms in Stabilized Amorphous Selenium Based n-i Detectors for x-Ray Imaging Applications", *Journal of Vacuum Science & Technology A: Vacuum, Surfaces, and Films*, **29**, pp. 031603, 2011.
- [107] R. A. Street, "Thermal Generation Currents in Hydrogenated Amorphous Silicon p - i - n Structures", *Applied Physics Letters*, **57**, pp. 1334, 1990.
- [108] R. A. Street, "Long-Time Transient Conduction in a-Si:H p-i-n Devices", *Philosophical Magazine B*, **63**, 6, pp. 1343, 1991.
- [109] S. A. Mahmood and M. Z. Kabir, "Modeling of Transient and Steady-State Dark Current in Amorphous Silicon Pin Photodiodes", *Current Applied Physics*, **9**, 6, pp. 1393, 2009.
- [110] L. B. Schein, "Charge Generation from Band-Gap States in Amorphous Selenium Films", *Physical Review B*, **10**, 8, pp. 3451, 1974.
- [111] J. L. Hartke, "The Three - Dimensional Poole - Frenkel Effect", *Journal of Applied Physics*, **39**, 10, pp. 4871, 1968.
- [112] T. Meyer, R. Johanson, and S. Kasap, "The Effect of 1/f Noise in Integrating Sensors and Detectors", *IET Circuits, Devices & Systems*, **5**, 3, pp. 177, 2011.
- [113] J. L. Hartke, "Drift Mobilities of Electrons and Holes and Space-Charge-Limited Currents in Amorphous Selenium Films", *Physical Review*, **125**, 4, pp. 1177, 1962.
- [114] H. P. D. Lanyon, "Electrical and Optical Properties of Vitreous Selenium", *Physical Review*, **130**, 1, pp. 134, 1963.
- [115] G. Pfister and A. I. Lakatos, "One-Carrier and Two-Carrier Steady-State Space-Charge-Limited Currents in Amorphous Selenium Films", *Physical Review B*, **6**, 8, pp. 3012, 1972.
- [116] J. Mort and A. I. Lakatos, "Steady State and Transient Photoemission into Amorphous Insulators", *Journal of Non-Crystalline Solids*, **4**, pp. 117, 1970.
- [117] L. Müller and M. Müller, "Current-Voltage Characteristics at High Fields in Amorphous Selenium Thin Layers", *Journal of Non-Crystalline Solids*, **4**, pp. 504, 1970.
- [118] S. O. Kasap, in: A. S. Diamond and D. S. Weiss (Eds.), "The Handbook of Imaging Materials", 2nd Edition, Marcel Dekker, New York, USA, 2002.
- [119] G. Belev and S. Kasap, "Reduction of the Dark Current in Stabilized a-Se Based X-Ray Detectors", *Journal of Non-Crystalline Solids*, **352**, 9-20F, pp. 1616, 2006.

- [120] H. Du, L. E. Antonuk, Y. El-Mohri, Q. Zhao, Z. Sul, J. Yamamoto, and Y. Wang, "Investigation of the Signal Behaviour at Diagnostic Energies of Prototype, Direct Detection, Active Matrix, Flat-Panel Imagers Incorporating Polycrystalline HgI<sub>2</sub>", *Physics in Medicine and Biology*, **53**, pp. 1325, 2010.
- [121] L. Fornaro, A. Cuna, A. Noguera, I. Aguiar, M. Perez, L. Mussio, and A. Gancharov, "Low Dark Current (001) Mercuric Iodide Thick Films for X-Ray Direct and Digital Imagers", *IEEE Transactions on Nuclear Science*, **52**, 6, pp. 3107, 2006.
- [122] R. A. Street, S. E. Ready, K. Van Schuylenbergh, J. Ho, J. B. Boyce, P. Nylén, K. Shah, L. Melekhov, and H. Hermon, "Comparison of PbI and HgI for Direct Detection Active Matrix x-Ray Image Sensors", *Journal of Applied Physics*, **91**, pp. 3345, 2002.
- [123] M. Yun, S. Cho, R. Lee, G. Jang, Y. Kim, W. Shin, and S. Nam, "Investigation of PbI<sub>2</sub> Film Fabricated by a New Sedimentation Method as an X-Ray Conversion Material", *Japanese Journal of Applied Physics*, **49**, pp. 041801, 2010.
- [124] S. Tokuda, H. Kishihara, S. Adachi, and T. Sato, "Preparation and Characterization of Polycrystalline CdZnTe Films for Large-Area, High-Sensitivity X-Ray Detectors", *Journal of Materials Science: Materials in Electronics*, **15**, 1, pp. 1, 2004.
- [125] M. Simon, R. A. Ford, A. R. Franklin, S. P. Grabowski, B. Menser, G. Much, A. Nascetti, M. Overdick, M. J. Powell, and D. U. Wiechert, "PbO as Direct Conversion x-Ray Detector Material", *Proceedings of SPIE*, **5368**, pp. 188, 2004.
- [126] S. Cho, S. Kang, C. Kwon, M. Yun, J. Park, S. Park, J. Choi, C. Mun, H. Lee, and S. Nam, "Effect of Annealing on the X-Ray Detection Properties of Nano-Sized Polycrystalline Lead Oxide Films", *Japanese Journal of Applied Physics*, **47**, pp. 7393, 2008.
- [127] L. Fornaro, N. Sassen, M. Pérez, A. Noguera, and I. Aguiar, "Comparison of Mercuric Bromide and Lead Bromide Layers as Photoconductors for Direct X-Ray Imaging Applications", *IEEE Nuclear Science Symposium Conference Record*, pp. 3750, 2006.
- [128] I. Aguiar, S. Kröger, and L. Fornaro, "Bismuth Tri-Iodide Polycrystalline Films for X-Ray Direct and Digital Imagers", *Nuclear Instruments and Methods in Physics Research A*, **610**, pp. 332, 2009.
- [129] P. J. Sellin, "Recent Advances in Compound Semiconductor Radiation Detectors", *Nuclear Instruments and Methods in Physics Research A*, **513**, pp. 332, 2003.
- [130] S. del Sordo, L. Abbene, A. M. Mancini, A. Zappettini, and P. Ubertini, "Progress in the Development of CdTe and CdZnTe Semiconductor Radiation Detectors for Astrophysical and Medical Applications", *Sensors*, **9**, pp. 3491, 2009.
- [131] K. Morigaki, "Physics of Amorphous Semiconductors", Imperial College Press, London, UK, 1999.
- [132] R. A. Street, "Hydrogenated Amorphous Silicon", Cambridge University Press, New York, USA, 1991.
- [133] G. Lucovsky, in: E. Gerlach and P. Grosse (Eds.), "Physics of Selenium and Tellurium", Springer-Verlag, New York, USA, 1979.

- [134] A. Feltz, "Amorphous Inorganic Materials and Glasses", VCH Publishers Inc., New York, USA, 1993.
- [135] V. Minaev, S. Timoshenkov, and V. Kalugin, "Structural and Phase Transformations in Condensed Selenium", *Journal of Optoelectronics and Advanced Materials*, **7**, 4, pp. 1717, 2005.
- [136] Y. Miyamoto, "Structure and Phase Transformation of Rhombohedral Selenium Composed of Se<sub>6</sub> Molecules", *Japanese Journal of Applied Physics*, **19**, 10, pp. 1813, 1980.
- [137] C. Juhasz, V. Gembala, and S. O. Kasap, "Growth Characteristics of Vacuum Coated Thick a-Se Films for Device Applications", *Journal of Vacuum Science and Technology A*, **18**, 2, pp. 665, 2000.
- [138] T. Takahashi, K. Ohno, and Y. Harada, "Highly Disordered Amorphous Selenium Studied by Ultraviolet Photoemission Spectroscopy", *Physical Review B*, **21**, 8, pp. 3399, 1980.
- [139] G. Lucovsky and F. L. Galeener, "Intermediate Range Order in Amorphous Solids", *Journal of Non-Crystalline Solids*, **35**, pp. 1209, 1980.
- [140] M. Abkowitz, "Density of States in a-Se from Combined Analysis of Xerographic Potentials and Transient Transport Data", *Philosophical Magazine Letters*, **58**, 1, pp. 53, 1988.
- [141] M. Long, P. Galison, R. Alben, and G. A. N. Connell, "Model for the Structure of Amorphous Selenium and Tellurium", *Physical Review B*, **13**, 4, pp. 1821, 1976.
- [142] P. E. Meek, "Vibrational Spectra and Topological Structure of Tetrahedrally Bonded Amorphous Semiconductors", *Philosophical Magazine*, **33**, 6, pp. 897, 1976.
- [143] J. Robertson, "A New Model for the Structure of Amorphous Selenium", *Philosophical Magazine*, **34**, 1, pp. 13, 1976.
- [144] P. Nielsen, "Density of States of Amorphous Selenium by Vacuum Photoemission", *Physical Review B*, **6**, 10, pp. 3739, 1972.
- [145] F. Greuter, "Electronic Surface Properties of a Liquid Semiconductor: Selenium", *Journal of Physics C: Solid State Physics*, **28**, pp. 2527, 1985.
- [146] A. E. Owen and J. M. Marshall, *Proceedings of the Seventh International Conference on Amorphous and Liquid Semiconductors, Edinburgh*, pp. 529, 1977.
- [147] S. Kasap and C. Juhasz, "Time-of-Flight Drift Mobility Measurements on Chlorine-Doped Amorphous Selenium Films", *Journal of Physics D: Applied Physics*, **18**, pp. 703, 1985.
- [148] W. E. Spear, "Transit Time Measurements of Charge Carriers in Amorphous Selenium Films", *Proceedings of the Physical Society (London)*, **B70**, pp. 669, 1957.
- [149] M. Abkowitz and D. M. Pai, "Photoelectronic Behavior of a-Se and some a-Se: As Alloys in their Glass Transition Regions", *Physical Review B*, **18**, 4, pp. 1741, 1978.
- [150] S. O. Kasap, V. Aiyah, B. Polischuk, A. Bhattacharyya, and Z. Liang, "Deep-Trapping Kinematics of Charge Carriers in Amorphous Semiconductors: A Theoretical and Experimental Study", *Physical Review B*, **43**, 8, pp. 6691, 1991.

- [151] G. Juška, A. Matulionis, and J. Viscakas, "Measurement of Thermal Release and Transit Time in Case of Multiple Trapping", *Physica Status Solidi (b)*, **33**, 2, pp. 533, 1969.
- [152] T. E. Orlowski and M. Abowitz, "Microstripline Transient Photocurrents in a-Se: Structure Resolved in Shallow Band-Tail States", *Solid State Communications*, **59**, 10, pp. 665, 1986.
- [153] R. Blakney and H. Grunwald, "Trapping Process in Amorphous Selenium", *Physical Review*, **159**, 3, pp. 664, 1967.
- [154] T. Yasar, "Transient Polarization Currents in Amorphous Selenium", Ph. D. Thesis, Princeton University, Princeton, USA, 1968.
- [155] J. Noolandi, "Multiple-Trapping Model of Anomalous Transit-Time Dispersion in a-Se", *Physical Review B*, **16**, pp. 4466, 1977.
- [156] M. Benkhedir, M. Brinza, and G. Adriaenssens, "Electronic Density of States in Amorphous Selenium", *Journal of Physics: Condensed Matter*, **16**, 5253, pp. 5264, 2004.
- [157] M. Benkhedir, M. Aida, and G. Adriaenssens, "Defect Levels in the Band Gap of Amorphous Selenium", *Journal of Non-Crystalline Solids*, **344**, 4, pp. 193, 2004.
- [158] N. F. Mott and E. A. Davis, "Electronic Processes in Non-Crystalline Materials", 2nd Edition, Oxford University Press, Oxford, UK, 1979.
- [159] H. Z. Song, G. J. Adriaenssens, E. V. Emelianova, and V. I. Arkhipov, "Distribution of Gap States in Amorphous Selenium Thin Films", *Physical Review B*, **59**, 16, pp. 10607, 1999.
- [160] K. V. Koughia, B. Fogal, G. Belev, R. E. Johanson, and S. O. Kasap, "Density of States in the Mobility Gap of Stabilized a-Se from Electron Time-of-Flight Photocurrent Analysis", *Journal of Non-Crystalline Solids*, **338**, pp. 569, 2004.
- [161] K. Koughia, Z. Shakoor, S. Kasap, and J. Marshall, "Density of Localized Electronic States in a-Se from Electron Time-of-Flight Photocurrent Analysis", *Journal of Applied Physics*, **97**, 3, pp. 033706-1, 2005.
- [162] K. Koughia and S. O. Kasap, "Density of States of a-Se Near the Valence Band", *Journal of Non-Crystalline Solids*, **352**, 9-20F, pp. 1539, 2006.
- [163] H. Naito, T. Iwai, M. Okuda, T. Matsushita, and A. Sugimura, "Computer Simulation Study of Tail State Distribution in Amorphous Selenium", *Journal of Non-Crystalline Solids*, **114**, pp. 112, 1986.
- [164] P. C. Taylor and K. L. Ngai, "Transient Electrical Transport in Pure and Doped Chalcogenide Glasses", *Solid State Communications*, **40**, 5, pp. 525, 1981.
- [165] G. Pfister and H. Scher, "Dispersive (Non-Gaussian) Transient Transport in Disordered Solids", *Advances in Physics*, **27**, 5, pp. 747, 1978.
- [166] G. Pfister, "Dispersive Low-Temperature Transport in a-Selenium", *Physical Review Letters*, **36**, 5, pp. 271, 1976.
- [167] F. K. Dolezalek and W. E. Spear, "Electronic Transport Properties of some Low Mobility Solids Under High Pressure", *Journal of Non-Crystalline Solids*, **4**, pp. 97, 1970.

- [168] M. Abkowitz, "Evidence for the Defect Origin of States which Control Photoelectronic Behavior of Amorphous Chalcogenides", *Journal of Non-Crystalline Solids*, **66**, 1-2, pp. 315, 1984.
- [169] M. Abkowitz, in: M. A. Kastner, G. A. Thomas and S. R. Ovshinsky (Eds.), "Disordered Semiconductors", Plenum Publishing Co., New York, USA, 1987.
- [170] P. W. Anderson, "Model for the Electronic Structure of Amorphous Semiconductors", *Physical Review Letters*, **34**, 15, pp. 953, 1975.
- [171] R. A. Street and N. F. Mott, "States in the Gap in Glassy Semiconductors", *Physical Review Letters*, **35**, 19, pp. 1293, 1975.
- [172] M. Kastner, D. Adler, and H. Fritzsche, "Valence-Alternation Model for Localized Gap States in Lone-Pair Semiconductors", *Physical Review Letters*, **37**, 22, pp. 1504, 1976.
- [173] M. Kastner, "Defect Chemistry and States in the Gap of Lone-Pair Semiconductors", *Journal of Non-Crystalline Solids*, **31**, 1-2, pp. 223, 1978.
- [174] D. Adler, "Amorphous-Semiconductor Devices", *Scientific American*, **236**, pp. 36, 1977.
- [175] H. Fritzsche, "The Nature of Localized States and the Effect of Doping in Amorphous Semiconductors", *Chinese Journal of Physics*, **15**, 2, pp. 73, 1977.
- [176] S. O. Kasap, V. Aiyah, B. Polischuk, and M. A. Abkowitz, "Determination of the Deep-Hole Capture Cross-Section in a-Se Via Xerographic and Interrupted-Field Time-of-Flight Techniques", *Philosophical Magazine Letters*, **62**, 5, pp. 377, 1990.
- [177] M. Abkowitz, "On the Question of Chain-End ESR in Amorphous Selenium", *Journal of Chemical Physics*, **46**, pp. 4537, 1967.
- [178] S. C. Agarwal, "Nature of Localized States in Amorphous Semiconductors—A Study by Electron Spin Resonance", *Physical Review B*, **7**, 2, pp. 685, 1973.
- [179] D. Carles, G. Lefrançois, and J. P. Larmagnac, "A Model for Steady-State Photoconductivity in Amorphous Selenium", *Journal De Physique Lettres*, **45**, 18, pp. 901, 1984.
- [180] X. Zhang and D. A. Drabold, "Evidence for Valence Alternation, and a New Structural Model of Amorphous Selenium", *Journal of Non-Crystalline Solids*, **241**, 2-3, pp. 195, 1998.
- [181] A. V. Kolobov, H. Oyanagi, K. Tanaka, and K. Tanaka, "Structural Study of Amorphous Selenium by in Situ EXAFS: Observation of Photoinduced Bond Alternation", *Physical Review B*, **55**, 2, pp. 726, 1997.
- [182] D. Vanderbilt and J. D. Joannopoulos, "Total Energies in Se. III. Defects in the Glass", *Physical Review B*, **27**, 10, pp. 6311, 1983.
- [183] R. Steudel, "Hypervalent Defects in Amorphous Selenium and Similar Lone-Pair Semiconductors", *Journal of Non-Crystalline Solids*, **83**, 1-2, pp. 63, 1986.

- [184] A. S. Zyubin, F. V. Grigor'ev, and S. A. Dembovskii, "Quantum-Chemical Simulation of the Influence of Defects on the Infrared Spectrum and the Electronic Structure of a-Se", *Semiconductors*, **37**, 5, pp. 598, 2003.
- [185] D. Hohl and R. O. Jones, "First-Principles Molecular-Dynamics Simulation of Liquid and Amorphous Selenium", *Physical Review B*, **43**, 5, pp. 3856, 1991.
- [186] E. Montrimas and B. Petrétis, "The Relation between Deep Trapping Levels and the Structure of Se Layers", *Journal of Non-Crystalline Solids*, **15**, pp. 96, 1974.
- [187] A. G. Sigai, "Open-Boat Evaporation of Se", *Journal of Vacuum Science and Technology*, **12**, pp. 958, 1975.
- [188] M. Hordon, *Proceedings of the Fourth International Symposium on Uses of Selenium and Tellurium*, pp. 156, 1990.
- [189] S. O. Kasap, K. V. Koughia, B. Fogal, G. Belev, and R. E. Johanson, "The Influence of Deposition Conditions and Alloying on the Electronic Properties of Amorphous Selenium", *Semiconductors*, **37**, 7, pp. 789, 2003.
- [190] G. S. Belev, B. Fogal, K. V. Koughia, R. E. Johanson, and S. O. Kasap, "Dependence of Charge-Carrier Ranges in Stabilized a-Se on Preparation Conditions and Alloying", *Journal of Materials Science: Materials in Electronics*, **14**, 10, pp. 841, 2003.
- [191] S. O. Kasap and B. Polischuk, "Application of the Interrupted Field Time-of-Flight Transient Photoconductivity Technique to Investigating Sample Inhomogeneities: Cl-Doped Amorphous Se: Te and Se: As Films", *Canadian Journal of Physics*, **73**, 1-2, pp. 96, 1995.
- [192] G. Belev, D. Tonchev, B. Fogal, C. Allen, and S. O. Kasap, "Effects of Oxygen and Chlorine on Charge Transport in Vacuum Deposited Pure a-Se Films", *Journal of Physics and Chemistry of Solids*, **68**, pp. 972, 2007.
- [193] O. Oda, A. Onozuka, and I. Tsuboya, "Effect of Oxygen on Electrophotographic Properties of Selenium", *Journal of Non-Crystalline Solids*, **83**, 1-2, pp. 49, 1986.
- [194] M. Abkowitz, "Structure and Mobility in Molecular and Atomic Glasses", *Annals of New York Academy of Science*, **371**, pp. 170, 1981.
- [195] J. Schottmiller, M. Tabak, G. Lucovsky, and A. Ward, "The Effects of Valency on Transport Properties in Vitreous Binary Alloys of Selenium", *Journal of Non-Crystalline Solids*, **4**, pp. 80, 1970.
- [196] P. J. Sellin, "Thick Film Compound Semiconductors for X-Ray Imaging Applications", *Nuclear Instruments and Methods in Physics Research Section A: Accelerators, Spectrometers, Detectors and Associated Equipment*, **563**, pp. 1, 2006.
- [197] M. Schieber, H. Hermon, A. Zuck, A. Vilensky, L. Melekhov, R. Shatunovsky, E. Meerson, Y. Saado, M. Sukach, E. Pinkhasy, S. E. Ready, and R. A. Street, "Thick Films of X-Ray Polycrystalline Mercuric Iodide Detectors", *Journal of Crystal Growth*, **225**, pp. 118, 2001.

- [198] M. Schieber, A. Zuck, M. Braiman, J. Nissenbaum, R. Turchetta, W. Dulinski, D. Husson, and J. L. Riester, "Polycrystalline Mercuric Iodide Detectors", *IEEE Transactions on Nuclear Science*, **NS-44**, pp. 2571, 1997.
- [199] M. Schieber, H. Hermon, A. Zuck, A. Vilensky, L. Melekhov, R. Shatunovsky, and R. Turketa, "High-Flux x-Ray Response of Composite Mercuric Iodide Detectors", *Proceedings of SPIE*, **3768**, pp. 296, 1999.
- [200] A. V. Sukack, V. V. Tetyorkin, and N. M. Krolevec, "Mechanisms of Carrier Transport in CdTe Polycrystalline Films", *Semiconductors Physics, Quantum Electronics & Optoelectronics*, **13**, 2, pp. 221, 2010.
- [201] D. S. McGregor and H. Hermon, "Room-Temperature Compound Semiconductor Radiation Detectors", *Nuclear Instruments and Methods in Physics Research Section A: Accelerators, Spectrometers, Detectors and Associated Equipment*, **395**, pp. 101, 1997.
- [202] G. Pang, D. L. Lee, and J. A. Rowlands, "Investigation of a Direct Conversion Flat Panel Imager for Portal Imaging", *Medical Physics*, **28**, pp. 2121, 2001.
- [203] R. A. Street, S. E. Ready, F. Lemmi, K. S. Shah, P. Bennett, and Y. Dmitriyev, "Electronic Transport in Polycrystalline PbI Films", *Journal of Applied Physics*, **86**, pp. 2660, 1999.
- [204] N. Destefano and M. Mulato, "Influence of Multi-Depositions on the Final Properties of Thermally Evaporated TlBr Films", *Nuclear Instruments and Methods in Physics Research Section A: Accelerators, Spectrometers, Detectors and Associated Equipment*, **624**, pp. 114, 2010.
- [205] F. Olschner, K. S. Shah, J. C. Lund, J. Zhang, K. Daley, S. Medrick, and M. R. Squillante, "Thallium Bromide Semiconductor X-Ray and  $\gamma$ -Ray Detectors", *Nuclear Instruments and Methods in Physics Research Section A: Accelerators, Spectrometers, Detectors and Associated Equipment*, **322**, 3, pp. 504, 1992.
- [206] G. Zentai, L. Partain, R. Pavlyuchkova, C. Proano, B. N. Breen, A. Taieb, O. Dagan, M. Schieber, H. Gilboa, and J. Thomas, "Mercuric Iodide Medical Imagers for Low Exposure Radiography and Fluoroscopy", *Proceedings of SPIE*, **5368**, pp. 200, 2004.
- [207] M. Z. Kabir and S. O. Kasap, "Charge Collection and Absorption-Limited Sensitivity of X-Ray Photoconductors: Applications to a-Se and HgI<sub>2</sub>", *Applied Physics Letters*, **80**, pp. 1664, 2002.
- [208] A. Zuck, M. Schieber, O. Khakhan, and Z. Burshtein, "Near Single-Crystal Electrical Properties of Polycrystalline HgI<sub>2</sub> Produced by Physical Vapor Deposition", *IEEE Transactions on Nuclear Science*, **50**, pp. 991, 2003.
- [209] R. C. Whited and L. Van den Berg, "Native Defect Compensation in HgI<sub>2</sub> Crystals", *IEEE Transactions on Nuclear Science*, **NS-24**, pp. 165, 1977.
- [210] N. E. Hartsough, J. S. Iwanczyk, E. Nygard, N. Malakhov, W. C. Barber, and T. Gandhi, "Polycrystalline Mercuric Iodide Films on CMOS Readout Arrays", *IEEE Transactions on Nuclear Science*, **56**, 4, pp. 1810, 2009.
- [211] G. Zentai, L. Partain, R. Pavlyuchkova, C. Proano, G. Virshup, L. Melekhov, A. Zuck, B. N. Breen, O. Dagan, and A. Vilensky, "Mercuric Iodide and Lead Iodide x-Ray Detectors

- for Radiographic and Fluoroscopic Medical Imaging", *Proceedings of SPIE*, **5030**, pp. 77, 2003.
- [212] K. Oh, M. Yun, S. Cho, M. Kim, Y. Kim, Y. Kim, J. Sin, and S. Nam, "Laminate Structure Detectors for Low Dark Current with Photoconductors in Digital X-Ray Imaging", *Nuclear Instruments and Methods in Physics Research Section A: Accelerators, Spectrometers, Detectors and Associated Equipment*, **607**, pp. 158, 2009.
- [213] S. Tokuda, H. Kishihara, S. Adachi, and T. Sato, "Improvement of Temporal Response and Output Uniformity of Polycrystalline CdZnTe Films for High-Sensitivity x-Ray Imaging", *Proceedings of SPIE*, **5030**, pp. 861, 2003.
- [214] Y. Eisen and A. Shor, "CdTe and CdZnTe Room-Temperature X-Ray and Gamma Ray Detectors and Imaging Systems", *Materials Research Society Symposium Proceedings*, **487**, pp. 129, 1997.
- [215] M. Arques, S. Renet, A. F. Brambilla G., A. Gasse, N. Billon-Pierron, M. Jolliot, and L. Mathieu, "Fluoroscopic X-Ray Demonstrator using a CdTe Polycrystalline Layer Coupled to a CMOS Readout Chip", *Proceedings of SPIE*, **7622**, pp. 76221K, 2010.
- [216] K. M. Garadkara, S. J. Pawarb, P. P. Hankarea, and A. A. Patil, "Effect of Annealing on Chemically Deposited Polycrystalline CdTe Thin Films", *Journal of Alloys and Compounds*, **491**, pp. 77, 2010.
- [217] B. Schumm, H. Althues, and S. Kaskel, "CdTe Nanoparticles for the Deposition of CdTe Films using Clost Spaced Sublimation", *Journal of Crystal Growth*, **312**, pp. 2449, 2010.
- [218] V. A. Gnatyuk, O. I. Vlasenko, L. A. Kosyachenko, O. L. Maslyanchuk, V. M. Sklyarchuk, E. V. Grushko, and T. Aoki, "CdTe-Based Schottky Diode X-Ray Detectors for Medical Imaging", *Proceedings of SPIE*, **7008**, pp. 70081Z, 2008.
- [219] J. Kang, E. Parsai, D. Albin, V. G. Karpov, and D. Shvydkal, "From Photovoltaics to Medical Imaging: Applications of Thin-Film CdTe-Based Schottky Diode X-Ray Detectors for Medical Imaging", *Applied Physics Letters*, **93**, pp. 223507, 2008.
- [220] D. Shvydkal, E. Parsai, J. Kang, D. Pearson, and J. Feldmeier, "Patient Scatter Analysis for a New Generation of Portal Imaging Sensors Based on Thin-Film Cadmium Telluride", *Medical Physics*, **35**, pp. 2711, 2008.
- [221] E. I. Parsai, D. Shvydkal, and J. Kang, "Design and Optimization of Large Area Thin-Film CdTe Detector for Radiation Therapy Imaging Applications", *Medical Physics*, **37**, 8, pp. 3980, 2010.
- [222] R. Sorgenfrei, D. Greiffenberg, and M. Fiederle, "Investigation of Growth Conditions of CdTe Thick Films on Properties and Demands for X-Ray Detector Applications", *IEEE Transactions on Nuclear Science*, **56**, 4, pp. 1768, 2009.
- [223] R. Sorgenfrei, A. Zwerger, C. Disch, K. H. Bachem, and M. Fiederle, "Direct Growth of CdTe Thick Films on the Medipix2 Pixel Detector Chip", *Journal of Applied Physics*, **108**, pp. 094504, 2010.
- [224] A. Brauers and U. Schiebel, "X-ray Image Sensor", US Patent 5,729,021, 1998.

- [225] J. C. Schottmiller, "Photoconductivity in Tetragonal and Orthorhombic Lead Monoxide Layers", *Journal of Applied Physics*, **37**, 9, pp. 3505, 1966.
- [226] Y. Ma, "Study of the Oxygen-Sensitive Behaviour of Yellow Lead Oxide by Defect Chemistry", *Journal of Applied Physics*, **76**, 5, pp. 2860, 1994.
- [227] D. R. Ouimetter, S. Nudelman, and R. Aikens, "New Large-Area X-Ray Image Sensor", *Proceedings of SPIE*, **3336**, pp. 470, 1998.
- [228] L. Fornaro, E. Saucedo, L. Mussio, A. Gancharov, and A. Cuña, "Bismuth Tri-Iodide Polycrystalline Films for Digital X-Ray Radiography Applications", *IEEE Transactions on Nuclear Science*, **51**, pp. 96, 2004.
- [229] A. Cuña, I. Aguiar, A. Gancharov, M. Pérez, and L. Fornaro, "Correlation between Growth Orientation and Growth Temperature for Bismuth Tri-Iodide Films", *Crystal Research and Technology*, **39**, 10, pp. 899, 2004.
- [230] M. Ikeda, Y. Oka, K. Mori, and M. Atsuta, "Study of Dark Current Blocking Layer for BiI<sub>3</sub> X-Ray Detector Film", *IEEE Nuclear Science Symposium Conference Record*, **7**, pp. 4520, 2004.
- [231] S. Kasap, J. B. Frey, G. Belev, O. Tousignant, H. Mani, J. Greenspan, L. Laperriere, O. Bubon, A. Reznik, G. DeCrescenzo, K. S. Karim, and J. A. Rowlands, "Amorphous and Polycrystalline Photoconductors for Direct Conversion Flat Panel X-Ray Image Sensors", *Sensors*, **11**, pp. 5112, 2011.
- [232] J. B. Frey, G. Belev, O. Tousignant, H. Mani, and S. O. Kasap, "Dark Current in Multilayer Stabilized Amorphous Selenium X-Ray Photoconductors", *Physica Status Solidi (c)*, **6**, pp. S251, 2009.
- [233] S. Touihri, G. Safoula, and J. C. Bernède, "Diode Devices Based on Amorphous Selenium Films", *Physica Status Solidi (a)*, **159**, 2, pp. 569, 1997.
- [234] J. C. Bernede, S. Touihri, and G. Safoula, "Electrical Characteristics of an aluminum/amorphous Selenium Rectifying Contact", *Solid-State Electronics*, **42**, 10, pp. 1775, 1998.
- [235] H. B. Michaelson, "The Work Function of the Elements and its Periodicity", *Journal of Applied Physics*, **48**, pp. 4729, 1977.
- [236] F. Jansen, "Effects of Oxygen and Chlorine on the Interfacial Crystallization of Amorphous Selenium Films", *Journal of Vacuum Science Technology*, **18**, 2, pp. 215, 1981.
- [237] H. Kim, C. Gilmore, A. Piqué, J. Horwitz, H. Mattoussi, H. Murata, Z. Kafafi, and D. Chrisey, "Electrical, Optical, and Structural Properties of indium–tin–oxide Thin Films for Organic Light-Emitting Devices", *Journal of Applied Physics*, **86**, pp. 6451, 1999.
- [238] S. H. Majid and R. E. Johanson, "Excess Noise in Amorphous Selenium p - i - n Devices", *Physica Status Solidi (c)*, **7**, 3 - 4, pp. 873, 2010.

- [239] M. D. Tabak and M. E. Scharfe, "Transition from Emission - Limited to Space - Charge - Limited Photoconductivity", *Journal of Applied Physics*, **41**, 5, pp. 2114, 1970.
- [240] J. G. Simmons and G. W. Taylor, "Dielectric Relaxation and its Effect on the Isothermal Electrical Characteristics of Defect Insulators", *Physical Review B*, **6**, 12, pp. 4793, 1972.
- [241] E. Montrimas and B. Petrétis, "The Structure of Vacuum-Evaporated Selenium Layers", *Physica Status Solidi (a)*, **15**, pp. 361, 1973.
- [242] K. Antoine, H. Jain, and M. Vlcek, "Optical Spectroscopy of a-As<sub>2</sub>Se<sub>3</sub> Under in Situ Laser Irradiation", *Journal of Non-Crystalline Solids*, **352**, 6-7, pp. 595, 2006.
- [243] S. O. Kasap, B. Fogal, M. Z. Kabir, R. E. Johanson, and S. K. O'Leary, "Recombination of Drifting Holes with Trapped Electrons in Stabilized a-Se Photoconductors: Langevin Recombination", *Applied Physics Letters*, **84**, pp. 1991, 2004.
- [244] M. Abkowitz and R. C. Enck, "Photoenhanced Metastable Deep Trapping in Amorphous Chalcogenides Near Room Temperature", *Physical Review B*, **27**, 12, pp. 7402, 1983.
- [245] D. K. Biegelsen and R. A. Street, "Photoinduced Defects in Chalcogenide Glasses", *Physical Review Letters*, **44**, 12, pp. 803, 1980.
- [246] W. Shockley, "Currents to Conductors Induced by a Moving Point Charge", *Journal of Applied Physics*, **9**, pp. 635, 1938.
- [247] S. Ramo, "Currents Induced by Electron Motion", *Proceedings of the IRE*, **27**, 9, pp. 584, 1939.
- [248] A. K. Bloomquist, M. J. Yaffe, G. E. Mawdsley, D. M. Hunter, and D. J. Beideck, "Lag and Ghosting in a Clinical Flat-Panel Selenium Digital Mammography System", *Medical Physics*, **33**, pp. 2998, 2006.
- [249] C. Allen, G. Belev, R. Johanson, and S. O. Kasap, "Relaxation of Electrical Properties of Stabilized Amorphous Selenium Based Photoconductors", *Journal of Non-Crystalline Solids*, **354**, 19-25, pp. 2711, 2008.